

ACTA DE EVALUACIÓN DE LA TESIS DOCTORAL
(FOR EVALUATION OF THE ACT DOCTORAL THESIS)

Año académico (academic year): 2018/19

DOCTORANDO (candidate PHD): **MORIANO MARTÍN, JAVIER**

D.N.I./PASAPORTE (Id.Passport): ******2342C**

PROGRAMA DE DOCTORADO (Academic Committee of the Programme): **D441-ELECTRÓNICA: SISTEMAS ELECTRÓNICAS AVANZADOS. SISTEMAS INTELIGENTES**

DPTO. COORDINADOR DEL PROGRAMA (Department): **ELECTRÓNICA**

TITULACIÓN DE DOCTOR EN (Phd title): **DOCTOR/A POR LA UNIVERSIDAD DE ALCALÁ**

En el día de hoy 30/11/18, reunido el tribunal de evaluación, constituido por los miembros que suscriben el presente Acta, el aspirante defendió su Tesis Doctoral **con Mención Internacional** (In today assessment met the court, consisting of the members who signed this Act, the candidate defended his doctoral thesis with mention as International Doctorate), elaborada bajo la dirección de (prepared under the direction of) **MARIO RIZO MORENTE // EMILIO JOSÉ BUENO PEÑA**.

Sobre el siguiente tema (Title of the doctoral thesis): **CONTRIBUTIONS TO THE MULTI-FREQUENCY CONTROL OF GRID-TIED VOLTAGE SOURCE CONVERTERS**

Finalizada la defensa y discusión de la tesis, el tribunal acordó otorgar la CALIFICACIÓN GLOBAL³ de (**no apto, aprobado, notable y sobresaliente**) (After the defense and defense of the thesis, the court agreed to grant the GLOBAL RATING (fail, pass, good and excellent): **EXCELLENT**

Alcalá de Henares, a 30 de Noviembre de 2018

Fdo. (Signed): Paolo Martelli

Fdo. (Signed): Ortiz Gami

Fdo. (Signed): Lennart Itenber

FIRMA DEL ALUMNO (candidate's signature),

Fdo. (Signed): Javier Moriano

Con fecha 17 de diciembre de 2018, la Comisión Delegada de la Comisión de Estudios Oficiales de Posgrado, a la vista de los votos emitidos de manera anónima por el tribunal que ha juzgado la tesis, resuelve:

- ☒ Conceder la Mención de "Cum Laude"
☐ No conceder la Mención de "Cum Laude"

La Secretaria de la Comisión Delegada

³ La calificación podrá ser "no apto" "aprobado" "notable" y "sobresaliente". El tribunal podrá otorgar la mención de "cum laude" si la calificación global es de sobresaliente y se emite en tal sentido el voto secreto positivo por unanimidad. (The grade may be "fail" "pass" "good" or "excellent". The panel may confer the distinction of "cum laude" if the overall grade is "Excellent" and has been awarded unanimously as such after secret voting.).

INCIDENCIAS / OBSERVACIONES:
(Incidents / Comments)



En aplicación del art. 14.7 del RD. 99/2011 y el art. 14 del Reglamento de Elaboración, Autorización y Defensa de la Tesis Doctoral, la Comisión Delegada de la Comisión de Estudios Oficiales de Posgrado y Doctorado, en sesión pública de fecha 17 de diciembre, procedió al escrutinio de los votos emitidos por los miembros del tribunal de la tesis defendida por *MORIANO MARTÍN, JAVIER*, el día 30 de noviembre de 2018, titulada *CONTRIBUTIONS TO THE MULTI-FREQUENCY CONTROL OF GRID-TIED VOLTAGE SOURCE CONVERTERS*, para determinar, si a la misma, se le concede la mención "cum laude", arrojando como resultado el voto favorable de todos los miembros del tribunal.

Por lo tanto, la Comisión de Estudios Oficiales de Posgrado **resuelve otorgar** a dicha tesis la

MENCIÓN "CUM LAUDE"

Alcalá de Henares, 18 de diciembre de 2018
EL VICERRECTOR DE INVESTIGACIÓN Y TRANSFERENCIA



F. Javier de la Mata

F. Javier de la Mata de la Mata

Copia por e-mail a:

Doctorando: MORIANO MARTÍN, JAVIER

Secretario del Tribunal: ORIOL GOMIS BELLMUNT

Directores de Tesis: MARIO RIZO MORENTE // EMILIO JOSÉ BUENO PEÑA



Universidad
de Alcalá

ESCUELA DE DOCTORADO
Servicio de Estudios Oficiales de
Posgrado

DILIGENCIA DE DEPÓSITO DE TESIS.

Comprobado que el expediente académico de D./D^a _____
reúne los requisitos exigidos para la presentación de la Tesis, de acuerdo a la normativa vigente, y habiendo
presentado la misma en formato: ☐ soporte electrónico ☐ impreso en papel, para el depósito de la
misma, en el Servicio de Estudios Oficiales de Posgrado, con el nº de páginas: _____ se procede, con
fecha de hoy a registrar el depósito de la tesis.

Alcalá de Henares a _____ de _____ de 20____



Fdo. El Funcionario



PhD. Program in Electronics: Advanced Electronic
Systems. Intelligent Systems

Contributions to the multifrequency control of grid-tied voltage source converters

PhD. Thesis Presented by
Javier Moriano Martin

2018



PhD. Program in Electronics: Advanced Electronic Systems. Intelligent
Systems

CONTRIBUTIONS TO THE MULTIFREQUENCY CONTROL OF GRID-TIED VOLTAGE SOURCE CONVERTERS

PhD. Thesis Presented by
Javier Moriano Martín

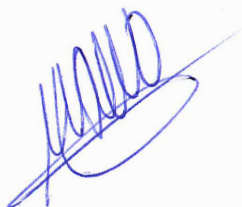
Advisors:
Dr. Mario Rizo Morente
Dr. Emilio José Bueno Peña

Alcalá de Henares, 2018

Dr. Mario Rizo Morente, Doctor por la Universidad de Alcalá e Ingeniero de Control de Siemens Gamesa, y

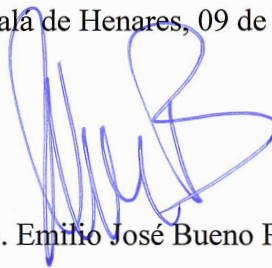
Dr. Emilio José Bueno Peña, Profesor Titular de la Universidad de Alcalá,

INFORMAN: Que la Tesis Doctoral titulada “**Contributions to the multifrequency control of grid-tied voltage source converters**” presentada por D. Javier Moriano Martín, y realizada bajo la dirección de los doctores D. Mario Rizo Morente y D. Emilio José Bueno Peña, dentro del campo de la aplicación de los VSCs como interfaces entre la red eléctrica y sistemas de generación de energía eléctrica, reúne los méritos de calidad y originalidad para optar al Grado de Doctor.



Fdo. Mario Rizo Morente

Alcalá de Henares, 09 de Septiembre de 2018



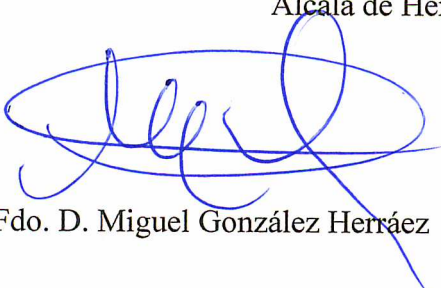
Fdo. Emilio José Bueno Peña

Dr. Miguel González Herráez, Coordinador de la Comisión Académica del Programa de Doctorado del Departamento de Electrónica de la Universidad de Alcalá,

INFORMA: Que la Tesis Doctoral titulada “**Contributions to the multifrequency control of grid-tied voltage source converters**” presentada por D. Javier Moriano Martín, y dirigida por los doctores D. Mario Rizo Morente y D. Emilio José Bueno Peña, cumple con todos los requisitos científicos y metodológicos, para ser defendida ante un Tribunal, según lo indicado por la Comisión Académica del Programa de Doctorado.



Alcalá de Henares, 03 de Septiembre de 2018



Fdo. D. Miguel González Herráez

**A mis padres y a mi hermano
por su apoyo incondicional**

“The energy of the mind is the essence of the life”
Aristotle

Agradecimientos

Tras un proceso tan largo se hace difícil recordar a todos los que agradecer sin olvidarse de gente que haya contribuido de forma directa o indirecta en este proceso.

Para empezar los que más directamente han contribuido en esta tesis. A Emilio Bueno por la confianza que tuvo en mi desde el primer momento y por siempre estar dispuesto a prestar su ayuda. A Mario Rizo por el enorme esfuerzo de dirigir una tesis sacando tiempo de donde no había y por el genial trato personal.

También agradecer a Martin Ordonez por su acogida durante mi estancia en la UBC y a los profesores de la UAH Francisco Javier Rodriguez, Pedro Martín y Raúl Mateos.

Al grupo GEISER por permitirme realizar esta tesis y por haber podido conocer a buenos compañeros como Miguel, Javi Serrano, Inés, Jorge, Carlos, Paco, Tomás y Rafael Peña. También a los compañeros del grupo GRIFO con los que he compartido despacho durante este tiempo Marco, Arancha, Laura Monroy y Laura Monteagudo.

A los grandes amigos que he hecho durante mis 8 años en la Universidad de Alcalá, a Pilar, Andrés, Bailón, Guille, Nico, Bernabé, Esther. A Rubén Izquierdo por todos los desayunos y las vueltas investigadoras.

A todos los que me hicieron sentirme parte de su grupo y de su familia durante mi estancia en la UBC. A Franco, Nacho, Pancho, Celeste, Andrés, Abbash, Hamed, Ali, Teresa, Daniel, Luca.

Fuera de la universidad agradecer a los chavales que se encargan de la tarea de desconexión de la tesis, de pasar buenos momentos y de hacer que todo sea más sencillo: a Adri, Marta, Bravo, Álvaro, Samanta, Rodel, Miguel, Dani, Alberto.

Especial mención merece Rocío Martín quién fue mi compañera desde la entrada a la universidad, amiga fuera y parte de GEISER. Una pena no haber podido completar este camino también juntos, pero como decimos, no todo puede ser ideal.

Al igual que en los anteriores TFG y TFM, a la persona que me sigue acompañando en este viaje, a Laura. Todo es más fácil a tu lado y me alegro de haber compartido todo este tiempo contigo y espero seguir compartiéndolo. Muchas gracias por aguantarme y por ayudarme con esta tesis (aún no siendo tu tema). Me alegro de que vinieses conmigo hasta Vancouver y que siempre seas mi gran apoyo.

Por último, la parte más importante, a la familia, que tan de cerca me ha apoyado y me ha dado los medios durante este tiempo. A mi padre Juan Carlos, a mi madre María Jesús y a mi hermano Raúl. Habeis sido una gran influencia de como con trabajo, con humildad y sin rendirse nunca, se pueden conseguir grandes cosas.

*Confía en el tiempo, que suele dar dulces salidas a
muchas amargas dificultades.*

Miguel de Cervantes Saavedra

Resumen

El interés por la producción de energía limpia está en aumento y la generación de este tipo de energía se puede fomentar mediante la instalación de generadores locales. Dichos generadores son conectados a la red de distribución a través de convertidores de potencia. Al mismo tiempo el número de cargas conectadas a la red está incrementando y con ello el número de cargas no lineales. Estas últimas consumen corrientes armónicas y esto provoca distorsión armónica a la red.

En esta tesis se estudia y se presentan contribuciones en el control de los convertidores de potencia para que al mismo tiempo que se inyecta potencia, el convertidor sea capaz de actuar adecuadamente frente a la distorsión armónica del voltaje de la red (control multifrecuencial). En primer lugar, esta tesis cubrirá el estudio de las diferentes técnicas de control de corrientes armónicas y también de las diferentes técnicas de sincronización y detección de componentes armónicas de tensión presentes en la red.

En cuanto al cálculo de referencias de corrientes armónicas, se explican las principales variantes dependiendo de la funcionalidad deseada y se estudia la entrega de potencia instantánea constante incluso con red distorsionada. Además, se propone un nuevo método de cálculo para eliminar las principales oscilaciones de potencia sin exceder las limitaciones de distorsión de corrientes.

También se describen las limitaciones del convertidor cuando se trabaja con componentes fundamentales y armónicas. Se analizan los principales saturadores multifrecuenciales para evitar la sobremodulación y se propone un nuevo saturador que no empeora la dinámica total del sistema y siempre consigue el mínimo THD de corriente.

Por último, se aborda la problemática de la distorsión armónica del voltaje de red. Primero se estudia la compensación de las corrientes consumidas por cargas locales y después se propone la compensación directa de la tensión del PCC.

En esta tesis se intenta incrementar el número de funcionalidades que puede desempeñar el convertidor para que además de entregar potencia, sea capaz de mejorar la calidad de la red, sin exceder las limitaciones físicas del convertidor. Cada una de las contribuciones es validada mediante resultados de simulación y experimentales.

Palabras clave: Multifrecuencia, Saturacion, Calidad de red, Control armónico.

Abstract

The interest in renewable energy is increasing and it can be enhanced through the connection of local generators. These generators are connected to the distribution grid by means of power converters. Meanwhile, the number of loads connected to the grid is also increasing and with this, the number of non-linear loads, which consume harmonic currents and provoke grid voltage harmonic distortion.

In this thesis, the multifrequency control of power converter is studied and different contributions are made in this regard. Multifrequency control consists on at the same time injecting power and being able to deal with the grid harmonic voltage distortion. First, this thesis covers the study of the different current control techniques and the different grid synchronization and grid voltage harmonic components detection.

Regarding the harmonic current references calculation, the main possibilities are described depending on the pursued functionality. Among them the functionality of delivering constant power even with a distorted grid is highlighted. Then, a new method is proposed where the most important components are reduced without exceeding the current THD limitations.

In addition, the converter limitations are also studied when both harmonic and fundamental current components are dealt together. The most important multifrequency distortion-free saturators are analysed and a new distortion free saturator is proposed, which does not worsen the whole system dynamic and always delivers the minimum possible THD.

Finally, the problem of the grid harmonic voltage distortion is directly tackled. First, the compensation of the currents consumed by non-linear loads (Active power filter) is studied. Then, the compensation of the grid voltage harmonic components is directly focused and a new strategy is proposed.

Therefore, in this thesis, the number of functionalities has been increased. In this context, in addition to the power delivering, it is also tried to improve the power quality, without exceeding the physical converter limitations. Each one of the previous mentioned contributions has been validated through simulated and experimental results.

Keywords: Multifrequency, Saturation, Power Quality, Harmonic control.

Contents

Resumen	XIII
Abstract	XV
Contents	XVII
List of Figures	XXIII
List of Tables	XXVII
List of Acronyms	XXIX
1. Introduction	1
1.1. Framework	1
1.1.1. Renewable Energies	2
1.1.2. Distributed generation	3
1.1.3. Power Quality	4
1.2. Motivation and objectives	5
1.3. List of publications	8
1.3.1. Journal Publications	8
1.3.2. Conference Publications	8
1.3.3. Additional journal publications	9
1.4. Document structure	9
2. State of the art	11
2.1. Background	11
2.1.1. Multifrequency and harmonic control	11
2.1.1.1. Complex Space Vectors	12

2.1.1.2.	Complex transfer functions	12
2.1.2.	Grid synchronization and harmonic detection	13
2.1.2.1.	Phase detection	13
2.1.2.2.	Fundamental and Harmonic sequences detection	14
2.1.3.	Current reference calculation	14
2.1.3.1.	Current THD reduction	14
2.1.3.2.	Active Power Filters	15
2.1.3.3.	Instantaneous Power	15
2.1.4.	Saturators	16
2.1.5.	Harmonic Compensation	17
2.1.5.1.	Active Power Filters	17
2.1.5.2.	PCC harmonic voltage reduction	18
2.2.	Review of Contributions	19
3.	Multifrequency Control of grid-tied Voltage Source Converters	23
3.1.	Introduction	23
3.2.	Vector representation of three-phase variables	23
3.2.1.	$\alpha\beta$ Stationary reference frame	24
3.2.2.	Three-phase Unbalance	25
3.2.3.	Harmonic distortion	25
3.2.4.	dq Synchronous reference frame	26
3.3.	Controllers for $\alpha\beta$ and dq reference frames	28
3.3.1.	Proportional Resonant Controllers (PRC)	28
3.3.2.	Second Order Generalized Integrator (SOGI)	29
3.3.3.	Reduced Order Generalized Integrator (ROGI)	29
3.3.4.	SOGI vs ROGI	33
3.4.	Grid synchronization and Sequence Detector	34
3.4.1.	Phase Locked Loop (PLL)	35
3.4.2.	Sequence detection with PRCs	36
3.4.2.1.	Sequence detection with SOGIs	36
3.4.2.2.	Sequence detection with ROGIs	38
3.5.	Multifrequency Current Control	40
3.5.1.	Gains empirical adjustment	43

3.5.2. Plant pole cancellation	44
3.5.3. Multifrequency control in state variables	48
3.5.3.1. Ackermann's Formula poles location	50
3.5.3.2. Linear - quadratic regulator (LQR) gains adjustment	50
3.6. Conclusions	53
4. Instantaneous Active Power Multifrequency Control	55
4.1. Introduction	55
4.2. The Instantaneous Power Theory	55
4.3. Harmonic Power Ripple	57
4.4. Current References Calculation for Power Ripple elimination	60
4.4.1. FPS current control without power ripple elimination	63
4.4.2. FPS and FNS current control for power ripple elimination	63
4.4.3. Multifrequency current control for power fluctuations elimination	64
4.5. CRC for Power Ripple elimination with THD optimization	65
4.6. Simulation Results	69
4.7. Conclusions	71
5. Current controller saturators under multifrequency operation	73
5.1. Introduction	73
5.2. VSC DC voltage limitations	75
5.3. Harmonic trajectory shapes	77
5.4. Multifrequency Current Controller Saturators	80
5.4.1. Distortion Free Equally weighted Saturator	80
5.4.2. Maximum Power Distortion Free Saturator	82
5.4.3. Distortion free Instantaneous Multifrequency Saturator (DFIMS)	83
5.4.3.1. DFIMS with positive and negative sequences	84
5.4.3.2. Multifrequency sequences saturator	86
5.4.3.2.1. DFIMS Algorithm Description:	88
5.4.3.2.2. Deterministic system obtainment	89
5.4.3.2.3. Algorithm Completion:	90
5.4.3.2.4. Simplified implementation:	91
5.4.3.2.5. Antiwindup algorithm description:	94
5.4.3.2.6. DFIMS transient analysis	95

5.5.	VSC current references saturators	97
5.5.1.	RMS current Saturator	98
5.5.2.	Maximum peak current value Saturator	99
5.6.	Simulation Results	101
5.7.	Conclusions	104
6.	Multifrequency control for PCC voltage distortion compensation	105
6.1.	Introduction	105
6.2.	VSC with Active Power Filter (APF) functionality	106
6.2.1.	VSIs for Distributed generators with APF capabilities	107
6.2.2.	Parallel operation of VSIs for DGs with APF capabilities	108
6.2.3.	Proposed strategy for maximum power extraction during Parallel operation of VSIs for DGs with APF capabilities	108
6.3.	Harmonic PCC voltage reduction	113
6.3.1.	Grid Impedance	115
6.3.1.1.	Grid impedance in multifrequency context	118
6.3.1.2.	Grid Inductance estimation based on Generalized Integra- tors (GIGI)	119
6.3.2.	Saturation for harmonic PCC voltage	126
6.3.2.1.	PCC harmonic voltage mathematical model	127
6.3.2.2.	PCC harmonic voltage controller	129
6.3.2.3.	PCC harmonic voltage saturation algorithm	131
6.4.	Simulation Results	137
6.4.1.	Parallel Active Power Filters	137
6.4.2.	Harmonic PCC voltage reduction	140
6.5.	Conclusions	141
7.	Experimental Results	143
7.1.	Introduction	143
7.2.	Experimental set-up	143
7.2.1.	Power Converter	143
7.2.2.	Control electronic system	144
7.2.3.	Auxiliary equipment	145
7.3.	Instantaneous Active Power Multifrequency Control	147

7.3.1. Matrix LU Decomposition	149
7.4. Distortion Free Instantaneous Multifrequency Saturator	151
7.5. PCC Harmonic Voltage Control	154
7.5.1. Parallel Active Power Filters	155
7.5.2. PCC Harmonic Voltage Control	158
7.6. Conclusions	161
8. Conclusions and future works	163
8.1. Conclusions	163
8.2. Future work	165
8.2.1. Fastest current controller	165
8.2.2. Instantaneous Active Power	166
8.2.3. Current Multifrequency Saturation	166
8.2.4. PCC adaptative controller to L_g variations	166
8.2.5. PCC harmonic voltage control with parallel shunt VSCs	167
Bibliography	169

List of Figures

1.1. Global energy consumption	1
1.2. World CO ₂ emissions	2
1.3. Electricity generation by different renewable sources	3
1.4. Top five EU MS in solar electricity and wind power installed capacity . . .	4
1.5. Current waveform and harmonic spectrum for a non-linear load	5
2.1. Comparison of fundamental and multifrequency trajectories	17
2.2. Conventional Shunt APF and sensorless APF topologies.	18
2.3. Graphical representation of thesis contributions.	21
3.1. Simplified control scheme with the basic control blocks.	24
3.2. Positive, negative and zero decomposition	25
3.3. Bode of SOGI closed loop - Magnitude	29
3.4. Bode of ROGI closed loop - Magnitude	31
3.5. Positive, negative and zero decomposition	32
3.6. PLL structure scheme.	35
3.7. SRF-PLL structure scheme.	36
3.8. Grid synchronization and sequence detection MSOGI scheme	37
3.9. Bode diagram of the MSOGI transfer function.	38
3.10. Grid synchronization and sequence detection MROGI scheme	39
3.11. Synchronization MROGI bode transfer function	40
3.12. MROGI grid synchronization and sequences detector.	41
3.13. ROGI based current controller	42
3.14. Closed loop transient response for the empirical adjustment of the gains . .	44
3.15. Transient response for the plant pole cancellation	47
3.16. Zeros and Poles of the closed loop transfer function	48

3.17. Closed loop transient response for +1 and -5	48
3.18. Multifrequency current control in state variables	49
3.19. Transient response and poles location of LQR multifrequency controller . .	52
4.1. Anti-aliasing filter transfer function bode	61
4.2. Graphical description of the whole system	62
4.3. Current reference calculation for P and Q references	63
4.4. Current reference calculation for power ripple elimination (2 nd)	64
4.5. Current reference calculation for power ripple elimination (2 nd , 4 th , 6 th) . .	65
4.6. Current reference calculation for power ripple elimination (2 nd , 6 th) and THD optimization	68
4.7. FFT of instantaneous active power	70
4.8. FFT of dc-bus voltage with different CRC methods	70
4.9. Complex FFT of exchanged currents ($\vec{i}_{\alpha\beta}$) with different CRC methods . .	70
5.1. Schematics of current and voltage saturators in a current control.	74
5.2. 2-levels VSC	75
5.3. 2-levels and 3-levels Neutral Point Clamped (NPC) converters states and limiting hexagon	76
5.4. Different $\vec{u}_{\alpha\beta}$ trajectories including different positive and negative sequences	77
5.5. Examples of two different types of roulette: (a) Epitrochoid and (b) Hy- potrochoid. Both of them with $R=6$, $r=1$ and $d=0.5$	78
5.6. Comparison of mathematical curves with the $\vec{u}_{\alpha\beta}$ trajectory	79
5.7. Distortion Free Equally weighted Saturator algorithm representation. . . .	80
5.8. Maximum Power Distortion Free Saturator algorithm representation. . . .	83
5.9. (a) Positive and negative overmodulation trajectory example and (b) Re- duced positive and negative trajectory after DFIMS application.	84
5.10. Trajectory rotation process example.	87
5.11. Approximation to the non-linear functions by third order polynomial. . . .	92
5.12. Graphical description of simplified implementation of DFIMS	93
5.13. Scheme of the antiwindup plus saturator algorithm.	95
5.14. Step response of closed loop transfer function with $\hat{L} = L$ and $\hat{R} = R$. . .	96
5.15. Step response of closed loop transfer function with $\hat{L} \neq L$	96
5.16. Current limitations in stationary $\alpha\beta$ axis for amplitude saturation.	100

5.17. Comparison of saturators in steady state.	103
5.18. Comparison of saturators during transients for an step response	104
6.1. APF electric scheme	106
6.2. Application of Parallel VSIs with APF Capabilities.	109
6.3. Strategy for paralleling VSIs.	110
6.4. Scheme of the employed saturation strategy for parallel connected distributed generators.	112
6.5. General case with non-linear loads up and downstream from the PCC and its equivalence.	113
6.6. Required converter output voltage under different situations	114
6.7. PCC Harmonic voltage control representation.	116
6.8. Example of strong grid with loads and distributed generators	117
6.9. Example of weak grid with loads and distributed generators	118
6.10. Grid estimation variation	120
6.11. GIGI electrical simplified scheme	120
6.12. GIGI system graphical description.	121
6.13. GIGI SOGIs closed loop transfer function	122
6.14. Bode magnitude of MAF	123
6.15. Bode response of MROGI and MSOGI current controllers	124
6.16. Graphical description of harmonic injection	125
6.17. Simulation results of GIGI	126
6.18. Plant of the PCC voltage harmonic control	128
6.19. Simplified plant of the PCC voltage harmonic control	129
6.20. Output PCC voltage for closed loop transfer function	130
6.21. Actuation current signals for desired PCC voltage	131
6.22. Schematics of control of PCC voltage containing the different subsystems. .	132
6.23. Scheme of PCC Harmonic control with DFIMS saturator plus antiwindup. .	137
6.24. Parallel APFs operation while dc-bus saturation	138
6.25. P and Q comparison while dc-bus saturation	139
6.26. Harmonic PCC voltage control under different conditions	140
7.1. CONDOR Converter.	144
7.2. Control electronic system.	145

7.3. User interface for power converter.	145
7.4. Regatron® TopCom ACS 3-phase programmable Power Supply.	146
7.5. AMREL® SPS 800-18 dc voltage source.	146
7.6. Generated unbalance and distorted grid voltage waveform	147
7.7. Waveform of instantaneous active power for different CRC methods	148
7.8. FFT of instantaneous active power for different CRC methods	148
7.9. FFT of exchanged currents with 8×8 and 8×8 Opt	149
7.10. Experimental obtained waveforms with DFIMS and literature saturator	153
7.11. Current FFT with literature saturator and DFIMS in steady state	153
7.12. Transient analysis of literature saturator and DFIMS	154
7.13. Hardware in the loop set-up	156
7.14. Experimental set-up	156
7.15. Reference output voltages ($\vec{u}_{\alpha\beta}$) during saturation	157
7.16. Voltage, currents and powers measured at PCC comparison	157
7.17. FFT of the different exchanged currents	158
7.18. Experimental set-up for PCC harmonic voltage compensation	159
7.19. PCC Harmonic voltage sequences with PCC control	160
7.20. PCC voltage waveform comparison with and without PCC control	160

List of Tables

3.1. Comparative overview between SOGI and ROGI	34
3.2. Controller Gains calculated for $t_{set} = 10$ ms and $t_{set} = 30$ ms.	47
4.1. Power ripple from combination of different voltage and current sequences .	66
4.2. Power oscillation control: simulation parameters description	69
4.3. Simulation results	71
5.1. Voltage values depending on state	75
5.2. Coefficients for polynomial approximation of non linear functions	92
5.3. Limiting $\vec{i}_{\alpha\beta}$ values	99
5.4. Simulation parameters description	101
5.5. Simulation Results	102
6.1. Simulation parameters	138
7.1. Runtime for different CRC methods	147
7.2. Instantaneous Active Power Experimental results	149
7.3. Parameters for the instantaneous active power experimental test	152
7.4. Experimental Results for DFIMS and literature Saturators	153
7.5. Experimental set-up parameters for parallel APFs	157
7.6. Experimental parameters description for PCC control	158
7.7. Experimental Results of PCC control	160

List of Acronyms

APF	Active Power Filter
CCF	Complex-coefficient Filter
CLC	Capacity Limitation Control
CMC	Centre Mode Control
CRC	Current References Calculator
DFIG	Doubly Feed Induction Generator
DFIMS	Distortion Free Instantaneous Multifrequency Saturator
DG	Distributed Generation
DGs	Distributed Generators
DSP	Digital Signal Processor
DVR	Dynamic Voltage Restorer
ESS	Energy Storage System
FFT	Fast Fourier Transform
FNS	Fundamental Negative Sequence
FOH	First Order Hold
FPGA	Field-programmable gate array
FPS	Fundamental Positive Sequence
FS	Frequency Splitting
HD	Harmonic Distortion
LVRT	Low Voltage Ride-Through
MAF	Moving Average Filter
MCCF	Multiple Complex-coefficient filter
MMC	Modular Multilevel Converter
MPPT	Maximum Power Point Tracking

NDC	Non-detection Zone
NPC	Neutral Point Clamped
OCV	Open Circuit Voltage
PCC	Point of common coupling
PLL	Phase Locked Loop
PI	Proportional Integrator
PRC	Proportional-Resonant Controller
PS	Power Splitting
PV	Photovoltaic
PWM	Pulse-width Modulation
RES	Renewable Energy Sources
RMS	Root Mean Square
ROGI	Reduced Order Generalized integrator
SCR	Short-circuit Ratio
SOC	State of Charge
SOGI	Second Order Generalized Integrator
SRF	Synchronous Reference Frame
STATCOM	Static Compensator
SVM	Space Vector Modulation
THD	Total Harmonic Distortion
VCO	Voltage Controlled oscillator
VSC	Voltage Source Converter
VSI	Voltage Source Inverter
ZOH	Zero Order Hold

Chapter 1

Introduction

1.1. Framework

The global economy and the energy consumption has followed an increasing trend during last years [1]. Both of them are usually related and the variations of the first, are commonly reflected on the second. In fact, year by year the global consumption of energy has continuously increased since 1990. As shown in Figure 1.1, This tendency has just been broken during the period between 2008 and 2009, directly related with the global economical crisis.

The relationship between the economy and energy has always been supposed to have a close effect among them. In [2], the relationship between the energy consumption and the country GDP was analysed, showing a high correlation, especially in developed countries. Furthermore, in absolute terms, different forecasts indicate that the energy consumption is going to continue increasing during the next years [3].

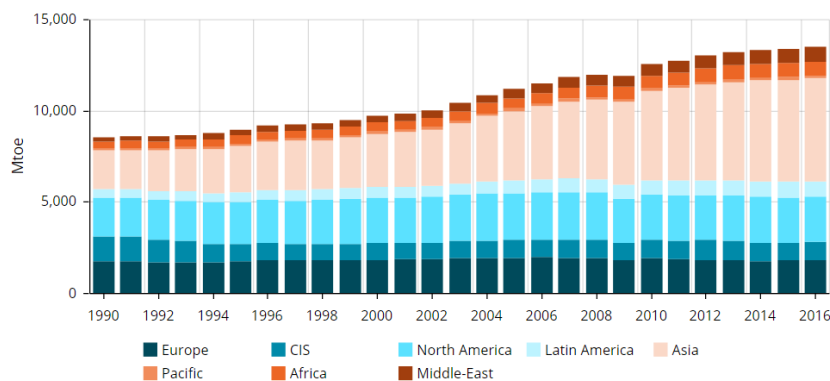


Figure 1.1: Global energy consumption trend from 1990 until 2016 and the corresponding breakdown by energy (2016). Source: Enerdata.

All these facts together make energy one of the most interesting topics, nowadays, for countries and governments. In addition to the evolution of the energy consumption during the years, the source where the energy comes from is another remarkable topic.

The energy can be split in the different available resources, among the most important ones are still the ones based on fossil fuels: Oil, Coal, Gas.

These resources provoke an increment on the greenhouse gases and it is highly remarkable how from 1800 to our days, the population has increased by 7, the yearly energy use by 50 and the CO₂ emissions by 150 [4]. The increment in greenhouse gases emissions is the main cause of climate change, and that fact has brought the emissions reduction as one of the priorities of the world [5].

Splitting the emissions by sector, as shown in Fig. 1.2, the 65 % of the total emissions are concentrated into two sectors: Electricity & Heat (42 %) and transportation (23 %) [6]. Furthermore, these sectors are linked and in the future, with the development of the electric vehicle [7], part of the emission related with transportation, could be transferred to the electrical sector. This implies even more interest on reducing the CO₂ emissions in the electricity sectors. Therefore, instead of employing the conventional sources of energy, the world is trying to move toward clean and renewable sources of energies.

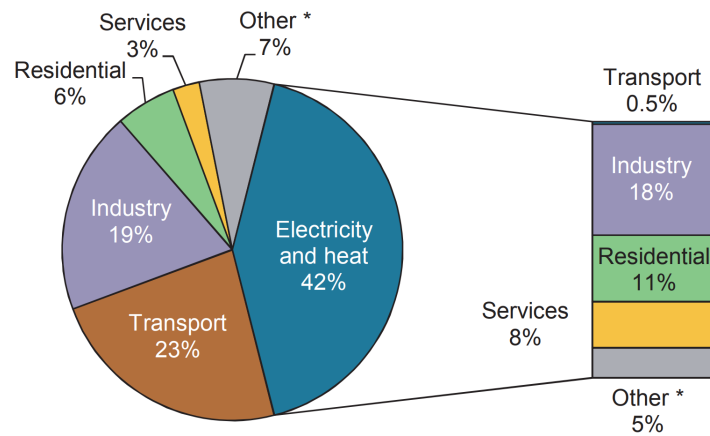


Figure 1.2: World CO₂ emissions by fuel combustion by sector in 2014. Source: International Energy Agency.

1.1.1. Renewable Energies

During the 1990s, energy policy changes appear all around the world in order to improve economic, environmental, security and social concerns [8]. In Europe, this policy was mainly focused on research and development (R&D) and then, these R&D policies gradually shifted to the market [9]. In 1997, a White Paper was published by the European Commission. This paper established the first target for renewable energies in the EU (from 5.4% in 1997 to 12% in 2010) [10]. According to the UE in those years, although the energy resources were abundantly available and the economic potential was considerable the contribution to the energy consumption was disappointingly small. Therefore, a joint effort was requested to the Community and to the Member States' level in order to meet the renewable integration target. In the same way, indicative targets were set for electric-

ity. In [11] national targets for each member country are set in order to achieve a global target of 22,1% of *Renewable Energy Sources (RES)* from the total shared electricity by 2010.

In 2014, the European Commission set the new targets for the climate change [5]. In addition to the greenhouse gas reduction of a 40 % (relative to emissions of 1990), a 27 % renewable target is set for energy consumption. It shows how, against the conventional fuel fossil resources, renewable energies appeared as unlimited, clean and sustainable resources. These advantages boosted the interest on improving those technologies and different countries has increased renewable generation [12], as depicted for in Fig. 1.3.

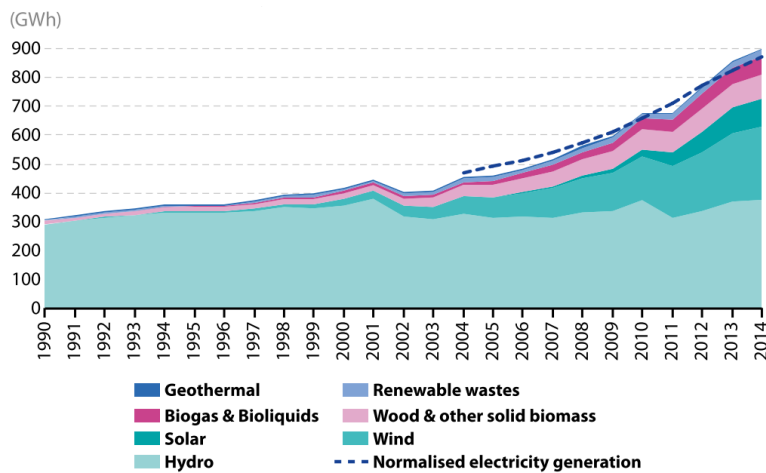


Figure 1.3: Electricity generation showing different renewable sources (1990-2014). Source: Eurostat.

In November 2016, in order to maintain the EU competitive in the clean energy transition, different measures were proposed in [13]. One of the key points was to achieve the global leadership in renewable energies. In one of the last reports, released in 2017 [14] (data up to 2015), it showed that the progress toward the 2020 renewable energy targets are on track.

Between the different RES, two technologies are the predominant ones. In 2015, in Europe, wind power and solar photovoltaic represented one quarter of the total EU electricity capacity. Wind power being the leading RES with more than one half of the new renewable electricity capacity installed and one third for the photovoltaic. It can be seen that Spain is one of the top five countries in both technologies, as showed in Fig. 1.4.

1.1.2. Distributed generation

The concept of the grid electric system has been for long time seen within the centralized model. In this model, different generation points at certain locations generate the energy for all the consumption points. This model is the most employed, under the classic vision of big generators that reduce the marginal cost of energy production. In addition, the size of these generators brought them out of the cities where the space limitation was

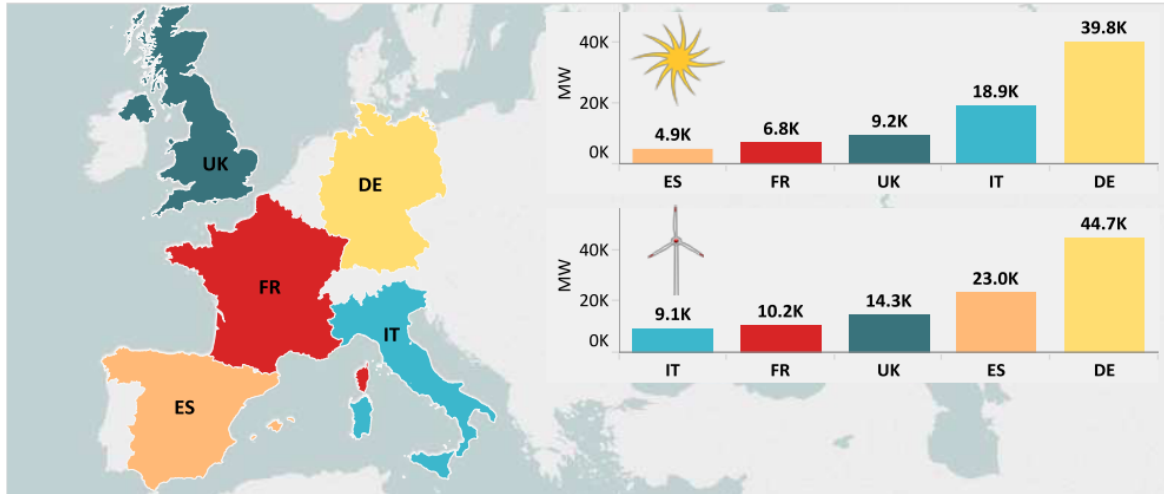


Figure 1.4: Top five EU MS in solar electricity and wind power installed capacity, 2015 [14]

not a constraint and great advances were carried out over electricity transportation and losses reduction.

However, with the appearance of new energies and the interest in increasing the energy efficiency a different model called distributed generation arised. Although this model appeared with an unclear definition, a definition was aimed in [15]. Distributed generation is an electric power source, which is directly connected to the distribution network.

In difference with the centralized one the distributed generation presents some benefits as stated in [16]. First, the smaller size of distributed generators allows more flexibility to adapt to the changing economic environment. Second, it allows a flexible reaction to electricity prices fluctuations and it could also contribute to power quality. It can locally perform voltage support and power factor corrections within other features [17]. Third, from the point of view of the system operators, when an investment is needed in extending the capacity of distribution and transportation lines, distributed generation can be employed for feeding local loads and in this way reducing losses.

1.1.3. Power Quality

Power quality is a general term that contains a variety of electromagnetic phenomena that define the voltage and currents at a certain time and a certain power system location [18]. As the number of electronic equipment has increased and it can cause electromagnetic disturbance, power quality has become an interesting issue.

Between the different phenomena contained in the power quality, it can be highlighted voltage fluctuations, voltage dips and interruptions, voltage imbalance, power-frequency variations and harmonics and interharmonics. Of special interest is the steady-state waveform distortion, which is described as the deviation from an ideal sinusoid.

Concretely, one of the most typical waveform distortion is due to the harmonics. Harmonics are sinusoidal voltage or current with a frequency that is an integer multiple of the fundamental frequency (typically 50 Hz or 60 Hz). The harmonic distortion exists due to the non-linear nature of different devices and loads of the power system.

Many customers and at the same time overall power system is being more and more concerned about the harmonic distortion. The main harmonics contributors to the power system are the power electronic equipment. These devices, when connected to the grid, inject harmonic currents into the grid, as depicted in Fig. 1.5. As these currents provoke voltage droops, due to the system impedance, voltage distortion occurs.

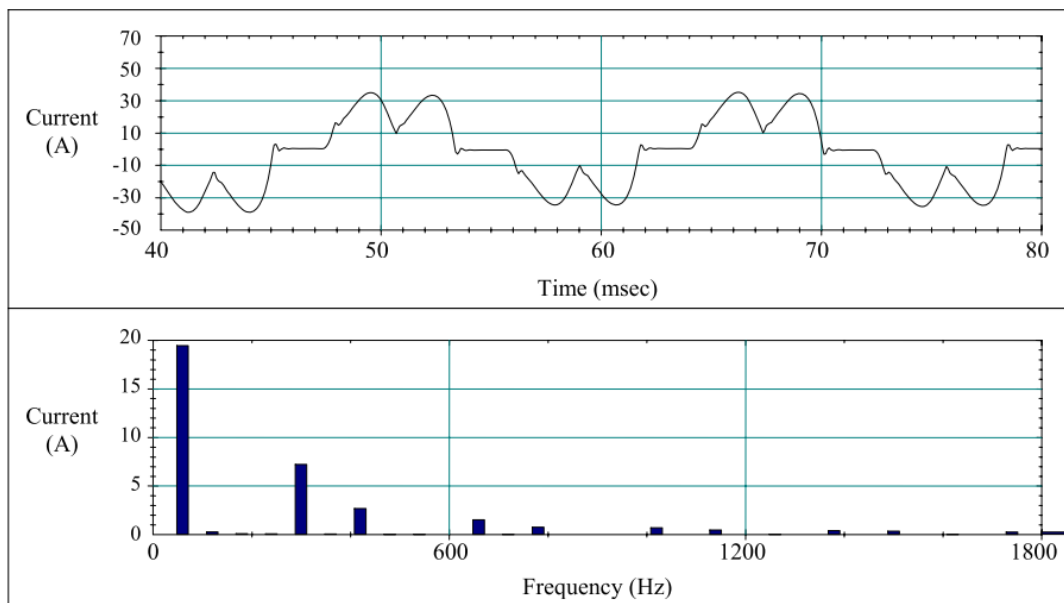


Figure 1.5: Current waveform and harmonic spectrum for a non-linear load [18]

1.2. Motivation and objectives

Within the previous described context, the increment of energy in the world and the interest on reducing the greenhouse emissions has increased the importance of the renewable energies. As it has been described the world is trying to move to an scenario with a significant presence of renewable energy. In this framework, different targets had been set and accomplished in the previous years. Similarly, more ambitious targets have been set for the next coming years.

In the same way, due to several benefits, the increment of renewable energies comes together with the idea of the distributed generation. The local generation for local loads consumption leads to a reduction of the line losses and reducing the capacity stress of the transport lines. In addition, the connection of the renewable energy to the distribution grid through a *Voltage-source converter (VSC)* allows to contribute to the grid power quality.

As previously stated, one of the phenomena within the power quality topic is the harmonic distortion. Due to the increment of non-linear loads, the concern over it has increased. The distortion of the grid is something that needs to be taken into account when the VSC works connected to the grid. It needs to be noted that if the grid is distorted and no compensation is carried out, harmonic currents are automatically injected to the grid.

Taking into account the previous described context, this thesis will focus on the multi-frequency control of VSC connected to a distorted distribution grid, typically for renewable energy power injection. Multifrequency control is based on in addition to control the fundamental frequency also perform the control at the most common harmonic frequencies.

For performing the control of the harmonic currents in addition to the fundamental ones, several tools are needed. Between the different parts that make possible the multi-frequency control, this thesis will contribute in several of them. The different steps for a multifrequency control can be divided in:

- Grid synchronization and Harmonic detection.
- Multifrequency Current Reference Calculation.
- Multifrequency Controller.
- Multifrequency Saturators.

Although this thesis will deal with all the different parts of the multifrequency control, the main contribution of this thesis will be mainly focused on two of them: multifrequency current references calculation and multifrequency saturators.

Regarding to the multifrequency current references calculation, different applications can be achieved from each one of the strategies. The harmonic current references can be mainly calculated for three different purposes:

- First, current reference calculations can be set to zero in order to do not exchange any harmonic current with the grid and maintain the current *Total Harmonic Distortion (THD)* as low as possible.
- Second, when the grid is distorted, the cross effect between the fundamental current component and the harmonic voltage components are translated into power oscillations. The harmonic references can be calculated in order to compensate the power oscillations (power filtering).
- Third, the current harmonic references can be calculated in order to compensate the harmonic currents that are being consumed by different non-linear loads. In this way, the harmonic voltage THD at the point where the VSC is connected (*Point of Common Coupling (PCC)*) can be reduced.

The three different strategies will be studied along the thesis for different applications and the control system will be optimized for them. This thesis, in particular, will contribute to the current references calculation for one of the aforementioned applications. This application is the second one, where power filtering is desired. A novel reference calculation strategy will be proposed where the most important fluctuations of the active power are compensated but at the same time the smaller THDi is injected to the grid.

Meanwhile, for the multifrequency control, one of the main objective of this thesis will be to develop a multifrequency saturator. With the increment of capabilities (harmonic control), the actuation signals could reach easier the physical limitations. In this way, reaching the limitations can incur into a different set of problems as THDi increment and in the worst case even leading the control system to an unstable situation. In this way, the available multifrequency saturators will be studied and the different weaknesses will be analysed. An objective of this thesis will be to develop a distortion free instantaneous multifrequency saturator (DFIMS) that is able to calculate the maximum achievable operation point without exceeding the limitations. Furthermore, the proposed saturator will be able to choose the priority of harmonic or fundamental operation.

With the proposed DFIMS, the optimization of the first and the third applications can be achieved. First, DFIMS will be developed for achieving the minimum THDi. In this context, even when the converter limitation is reached, the inverter will be able to deliver zero harmonic currents. Then, for the grid harmonic voltages compensation, DFIMS will be applied in order to perform the maximum possible compensation without exceeding limitations. This problem is crucial and it had been reported in previous work and a solution will be provided in this thesis.

As secondary objective, for grid synchronization and harmonic sequences detection, a novel method based in reduced order generalized integrators (ROGI) will be proposed. This method allows independent gain for each sequence to be detected and a dynamic analysis of the detection time will be carried out. Another secondary object will be carried out within the topic of grid harmonic voltage compensations. Within this topic, the grid plays a key role and the grid inductance value is the most important parameter. A novel method based on harmonic injection for grid inductance estimation will be also presented.

In conclusion, this thesis will deal with the multifrequency control of shunt VSCs connected to the grid. Enhancements in the different steps of multifrequency control will be proposed, implemented and validated. The enhancements will be found in grid harmonic detection, multifrequency current references calculation, multifrequency saturation and grid inductance detection. In addition, the three most common multifrequency applications will be studied and optimized as minimum THDi delivering, constant active power delivering with minimum THDi injection and harmonic currents from non linear load and grid harmonic voltage compensation.

1.3. List of publications

The objectives pursued on this thesis have resulted into contributions that have been published in different journal and national and international conferences. In addition during the PhD process, different collaborations and projects have been carried out that has also resulted into additional journal publications.

1.3.1. Journal Publications

J. Moriano, M. Rizo, E. Bueno, R. Martin and F. J. Rodriguez, “A Novel Multi-frequency Current Reference Calculation to Mitigate Active Power Fluctuations,” *Industrial Electronics, IEEE Transactions on*, vol. 65, no.1, pp. 810-818, Jan. 2018.

J. Moriano, M. Rizo, E. Bueno, R. Sendra and R. Mateos, “Distortion-Free Instantaneous Multifrequency Saturator for THD current reduction,” *Industrial Electronics, IEEE Transactions on*, Submitted (Minor revisions).

J. Moriano, M. Ordonez, M. Rizo and E. Bueno, “Harmonic Compensation Optimization for Multiple Parallel Distributed Generators,” *Power Electronics, IEEE Transactions on*, Submitted (Major revisions).

J. Moriano, M. Rizo, E. Bueno, “Harmonic voltage compensation by grid supporting shunt controlled distributed generators,” *Industrial Electronics, IEEE Transactions on*, Pending of submission.

1.3.2. Conference Publications

J. Moriano, M. Rizo, E. Bueno, R. Martin and F. J. Rodriguez, “Multi-frequency stationary frame grid synchronization using multiple reduced order generalized integrators,” *IECON 2016 - 42nd Annual Conference of the IEEE Industrial Electronics Society*, pp. 2349-2354, 2016.

J. Moriano, V. Bermejo, E. Bueno, M. Rizo and A. Rodriguez, “A novel approach to the grid inductance estimation based on second order generalized integrators,” *2017 IEEE Energy Conversion Congress and Exposition (ECCE)*, Cincinnati, OH, USA, 2017, pp. 1794-1801.

J. Moriano, M. Rizo, E. Bueno, and M. Moranchel, “Harmonic voltage compensation by grid supporting controlled distributed generators,” *2018 IEEE International Conference on Industrial Technology (ICIT)*, Lyon, 2018, pp. 1920-1925.

J. Moriano, M. Rizo, E. Bueno, R. Martin and F. J. Rodriguez, “Sincronización con la Red Eléctrica mediante Integradores Generalizados de Orden Reducido” *Sextas Jornadas de Jóvenes Investigadores de la Universidad de Alcalá (Ciencias e ingenierías)*, pp. 249-255.

1.3.3. Additional journal publications

J. Moriano, F.J. Rodríguez, P. Martín; J.A. Jiménez, B. Vuksanovic, “A New Approach to Detection of Systematic Errors in Secondary Substation Monitoring Equipment Based on Short Term Load Forecasting,” *Sensors*, 2016, 16, 85.

I. Sanz, M. Moranchel, J. Moriano, F. J. Rodriguez, S. Fernandez, “Reconfiguration Algorithm to Reduce Power Losses in Offshore HVDC Transmission Lines,” *Power Electronics, IEEE Transactions on*, vol. 33, no.4, pp. 3034-3043, 2017.

1.4. Document structure

The document of this Thesis is organized in eight chapters.

After this first introductory chapter, Chapter 2 performs a review of the knowledge of the most relevant work related with the thesis content. The knowledge review starts from the complex control of power converters and study different methods for current calculation, converter saturation and grid support through harmonic voltage control.

Chapter 3 introduces the control of harmonic sequences in addition to the fundamental components (multifrequency control). Most common controllers are described including those controllers for specific frequencies. In order to perform grid connected VSC control, this chapter also deals with the diverse methods of grid synchronization. At the end of the chapter, different techniques for the multifrequency control are presented.

Chapter 4 focuses on the current reference calculation in order to reduce the power fluctuations when the grid is distorted. A novel reference calculation method is proposed that reduces active power oscillations through the exchange of harmonic currents with the grid. In this novel method, the power oscillation compensation is made exclusively over the most significant components while the minimum THD is delivered to the grid.

Chapter 5 deals with a common problem within the VSC, the actuation limitation. The voltage that a VSC can generate at the ac-side is limited by the available voltage at the dc-side. In this context, with the inclusion of controlled sequences (harmonics), this limitation can be reached sooner. Here the different multifrequency saturators are analysed and a new one, with instantaneous capability is proposed.

Chapter 6 discusses one of the most powerful applications of the multifrequency control, the harmonic compensation. Firstly, it starts with the compensation of harmonic currents generated by local non linear loads. The injected harmonic currents are measured and then, they are locally compensated by the controlled VSC. The second part of the chapter analyses the compensation of harmonic voltages without additional measurements. Through the analysis of the harmonic grid voltages, currents are injected until completely reducing the distortion. However, as it is unthinkable that an only VSC can

compensate the total grid distortion, the saturator proposed in previous chapter allows to perform the compensation up to the maximum without exceeding saturation.

Chapter 7 contains the description of the experimental set-up employed for testing the proposed algorithms and the consequent obtained results.

Finally, Chapter 8 summarizes the conclusion extracted from the thesis and describes the possible future lines that could continue the developed work on this thesis.

Chapter 2

State of the art

This thesis is mainly focused on the research of control algorithms for the control extension from fundamental components (± 50 Hz and ± 60 Hz) to the most common harmonic components. This chapter makes a review of the previous work related with multifrequency, the different applications and control elements. Then, the thesis objectives and contributions within the multifrequency control are described in the last part of the chapter.

2.1. Background

2.1.1. Multifrequency and harmonic control

VSC is the element employed for the connection of *Distributed Generators (DGs)* to the distribution grid. The injected currents to the grid are defined by the current control strategy. The basis of the control strategy is to employ a controller that presents infinite gain at the desired frequency, which a zero error between the controlled variable and the reference signal wants to be achieved.

The most typical employed controller is the PI, that presents zero error for dc signals. However, the controlled variable in the VSC are of sinusoidal nature with a frequency of 50 or 60 Hz. For the employment of PI with this kind of signals, the signals have been typically transformed to a synchronous reference frame that is rotating at the fundamental frequency (ω_0) [19]. In addition to the control of the fundamental positive sequence ($+\omega_0$), another transformation can be carried out with a rotating axis at ($-\omega_0$). This transformation converts the negative component into a dc signal and PI can be employed [20]. The same process can be carried out for harmonic components (rotating axes at $-5\omega_0$ or $+7\omega_0$) as seen in [21].

The disadvantage of this control strategy is the detection of the grid phase (θ) and the requirement of transforming the measured signals into the new synchronous axes and then, the anti-transformation of the actuation signals. In this regard, new controllers

were employed that presents infinite gain at the fundamental frequency (SOGI) [22]. In addition, multiple SOGIs can be configured in order to present infinite gain at the most common harmonic components and in this regard, control those components [23].

Anyhow, the SOGI presents infinite gain at both positive and negative sequences of the desired harmonic. In this context, +1 and -1 sequences can be controlled at the same time with the particularity of having the same dynamic for both. Meanwhile, regarding harmonic components, in normal conditions just one of the sequences (negative or positive) is the interesting one to be controlled. A different option for exclusively controlling the interesting sequences of each harmonic is to transform the signals to the synchronous axis rotating at the fundamental frequency ($+\omega_0$). In this regard, the most common harmonic components ($h = (-6k + 1)$, $h = (6k + 1)$) are converted to the positive and negative components of a different harmonic ($h = \pm 6k$) [24].

However, once again, if exclusively the fundamental or negative sequence wants to be addressed and no transformation are desired, a possible option is to work in the complex space vector, employing complex transfer functions.

2.1.1.1. Complex Space Vectors

Three-phase dynamic systems has been widely studied during several years. First, the three-phase quantities can be expressed as two-phase quantities if the zero sequence is disregarded following the Clarke transformation [25]. Then, these two-phase signals can be treated as a complex signal, as described in [26]:

$$u_s = u_\alpha + ju_\beta = \frac{2K}{3} (u_a + e^{j2\pi/3}u_b + e^{j4\pi/3}u_c). \quad (2.1)$$

In the same way that the three-phase signals can be expressed as complex signals, the same occurs with the transfer functions. As it had been described for ac machines in [27], the relationship amount voltage and current magnitudes can be expressed in a complex notation, where the voltage is expressed as $\vec{u}_s = u_{s\alpha} + ju_{s\beta}$ and the current as $\vec{i}_s = i_{s\alpha} + ji_{s\beta}$:

$$\vec{u}_s = r_s \vec{i}_s + l_s \frac{d\vec{i}_s}{dt} + \vec{u}_e \quad (2.2)$$

In this regard, for complex space vector notation, the complex transfer function can be described with complex coefficients, the complex poles do not need to have a conjugated and the frequencies responses are not necessarily symmetric [28].

2.1.1.2. Complex transfer functions

In this context, a transfer function with unsymmetrical transfer function could present infinite gain exclusively in one of the sequences of the desired harmonic. The complex

filters were proposed in [29], but the proliferation was not until several years after [28]. This type of *Complex-coefficient Filter (CCF)*, described by the following transfer function:

$$CCF(s) = \frac{\omega_c}{s - j\omega_0 + \omega_c}, \quad (2.3)$$

was employed for three-phase grid-interfaced converters in [30]. They were employed for the grid synchronization and harmonic detection in a structure of *Multiple complex-coefficient filter (MCCF)*, that will be described in Subsection 2.1.2. Then, regarding to the control topic, Busada in [31] proposed an structure denominated as ROGI

$$ROGI(s) = \frac{k}{s - jh\omega_0}, \quad (2.4)$$

which was employed for the fundamental and harmonic current control. With this structure, it was possible to set independent control dynamics for each one of the sequences. In addition, the control of those sequence was possible without performing any dq transformation and therefore, without the necessity of grid phase detection.

2.1.2. Grid synchronization and harmonic detection

A step that is typically related with the current control is the synchronization algorithm. Historically, as previously described during the multifrequency control, the knowledge of the grid condition has been of extreme importance. This knowledge is mainly based on knowing the amplitude, phase and frequency of the fundamental grid component. Especial importance is given to the phase that is required for transformation to synchronous reference axis. In this thesis one of the most important features resides on the grid voltage harmonic detection. During this section the state of the art of synchronization and harmonic detection are described.

2.1.2.1. Phase detection

For the grid phase detection the most employed synchronization method is the *Phase Locked Loop (PLL)*. PLL was introduced by Appleton in 1923, but it was not until 1932 when H. de Bellescize developed the complete concept. PLL started to be employed for the reception of radio signals and then it was widely employed in industry. Finally, those techniques arrived to the power converters world, for synchronization with the power grid [32].

PLL systems are able to provide the angle and the frequency of the grid voltage. As previously stated, this information is usually employed for the conventional dq synchronization techniques through the (SRF-PLL) [33]. Several optimizations appeared for accurately grid phase detection even with unbalanced grid as Delayed Signal Cancellation (DSC-PLL) [34] or the Double Second Order Generalized Integrator (DSOGI-PLL) [35].

2.1.2.2. Fundamental and Harmonic sequences detection

The previously described systems are able to accurately determine the phase and frequency of the grid voltage. However, these systems are not able to extract enough information for reflecting the shape of the signal. This is of special importance when harmonic voltage is required for the control system [36]. Therefore, in order to extract the grid harmonic information, different algorithms have been proposed that extract the grid harmonic information through the *Fast Fourier Transform (FFT)* analysis [37], [38]; the implementation of parallel notch filters [39].

In this regard, a novel strategy able to extract simultaneously the positive and the negative harmonic sequences through the employment of multiple SOGIs has been proposed in [36], [40]. Finally, with the previously explained complex transfer functions, a harmonic sequences detection algorithm based in Multiple Complex Coefficients Filters is described in [30]. Then, in this thesis and also published in [41], a harmonic detection system based in ROGIs was proposed.

2.1.3. Current reference calculation

Although the current control is crucial in order to exchange the desired currents with the grid, there exists a previous step that determines the functionality of the power converter. This step is the current references calculation and these references can allow the converter to accomplish different functionalities.

For example, when just the fundamental frequency is taken into account, the algorithm for the current references calculation can accomplish the *Low voltage Ride Through (LVRT)* requirements for *Doubly Feed Induction Generator (DFIG)* [42] [43] or the *Maximum Power Point Tracking (MPPT)* for *Photovoltaic (PV)* systems [44] [45].

In a similar way, when the negative sequence related with unbalance is controlled in addition to the positive fundamental sequence, the reference calculation for these components also plays a key role. In 1996, Rioual was one of the first one on adding positive and negative sequences in the control actuation [46].

Finally, regarding the multifrequency context the reference for the harmonic current components determines the harmonic functionality. These functionality would be during the whole thesis divided in three:

2.1.3.1. Current THD reduction

The first strategy for selecting the value of the harmonic current references is the THD reduction. In this technique the objective is to deliver the minimum possible harmonic currents, specially when the grid is distorted. For achieving this purpose, the harmonic references can be directly set to zero. This is the strategy pursued in some previous works.

For example it is one of the strategies employed in [31], it is also the pursued strategy in [47] (even when the inverter is limited) and also in [48] with SOGIs based control.

2.1.3.2. Active Power Filters

The second strategy can be widely found in the literature. This strategy is employed for the compensation of local non-linear loads that are consuming harmonic currents. For obtaining the required references, the harmonic currents consumed by the non-linear loads are directly measured with current sensors. Then, these measured currents are set as references in order to be delivered by the power converter and in this way, reducing the THDi of the grid currents. This strategy can be seen in [49] and for example in [50] where the *Active Power Filter (APF)* capability is added to *Voltage Source Inverter (VSI)*s associated with renewable sources. This strategy is extended in Subsection 2.1.5, where the compensation of the harmonic voltages at the PCC, the parallelization of APFs and their limitations are analysed.

2.1.3.3. Instantaneous Power

The third strategy for current reference calculation has been deeper studied in this thesis. The harmonic voltage distortion implies that when a fundamental current is injected to the grid oscillations occurs over the delivered active and reactive powers.

Oscillations in the delivered powers imply also oscillations in DC ripple current. DC current ripple is harmful for different devices, such as batteries or capacitors. Battery current ripple, especially at low frequencies, increases battery heating and therefore, this effect can accelerate battery ageing [51]. Similar effect is provoked over capacitors, where the increment of RMS current carries temperature risen decreasing capacitor lifetime. For critical capacitors, some topologies have been proposed in order to avoid the high frequency current ripple to pass through them [52]. However, if low frequency ripple is not eliminated, it would increase RMS current affecting critical and expensive capacitors.

In addition to the dc current fluctuations, low frequency power oscillations, also provoke dc voltage ripple. Therefore, from that point of view, DC microgrids and grids are one of the main beneficiaries of power oscillations elimination, in order to provide a higher quality to the loads [53]. Furthermore, dc voltage ripple also affects induction machines in different ways, as electric losses, temperature increment and different noise problems related with torque fluctuations [54], [55].

The multifrequency control allows to reduce those power harmonic components if the proper current references are calculated. In [42] the multifrequency controller described in [30] is employed for improving the DFIG behaviour during harmonic voltage distortion. Different calculation methods are proposed in this paper including one for removing the active and reactive power oscillations at the six harmonic of the grid frequency. Then,

some enhancements are presented in [56] and in [57]. The different strategies are switched between reducing the different components of the active and reactive power ripple or to provide clean currents. In [58] and as one of the contributions of this thesis, a new method of references calculation is employed that reduce the most important components of the active power ripple and it is achieved with the minimum THDi.

2.1.4. Saturators

The two previous sections have showed the importance of the current controllers and the different functionalities that can be achieved with the current reference calculation. In order to achieve the desired currents, a control actuation (voltage) needs to be applied. However, it could occur that the required actuation exceeds the VSC rating, and in this context, the control actuation is needed to be limited.

The different saturation strategies can be divided in two categories: scalar and vector methods. The difference between scalar and vector saturation is mainly found in the fact that the scalar saturation would reduce each component independently. Meanwhile, the vector methods reduce both components of the vector at the same time [59].

An example of scalar saturation is the implicit limitation of the employment of the PWM technique [60]. With this technique the maximum actuation can be provided. However, this technique implies that at a some point, the overmodulation is reached and distortion occurs.

Most common vector saturations can be found in the literature as in [61], [62] or [63]. In all of them, when overmodulation is reached, the magnitude of the vector is reduced but the phase of the vector is kept. However, all of them, exclusively work with a trajectory that is shaped by the fundamental positive sequence.

The addition of controlled sequences complicates the strategy and it had been avoided until [59], where the *Fundamental Positive Sequence (FPS)* and the *Fundamental Negative Sequence (FNS)* are simultaneously dealt with. In addition, the importance of finding the proper reduction gain during the complete trajectory is highlighted. On contrary, if the gain is continuously varying, additional distortion is produced. Therefore, this kind of saturation strategy is named as distortion-free saturation. Two different methods are proposed depending on if a proportional saturation of both components is desired or if the maximum swept area is desired.

Then, the saturation topic was taken into a more complex dimension with the saturation when harmonic components are also dealt with, as shown in Fig. 2.1. A distortion-free saturator that was able to address all these sequences at the same time was proposed in [64] and some enhancements over the dynamics were proposed in [65]. Then, a modified saturator of the previous strategy was proposed in [66], where the harmonic currents reference to be delivered needs to be previously known and the saturator is able to deliver

maximum power and the dynamics are several times faster.

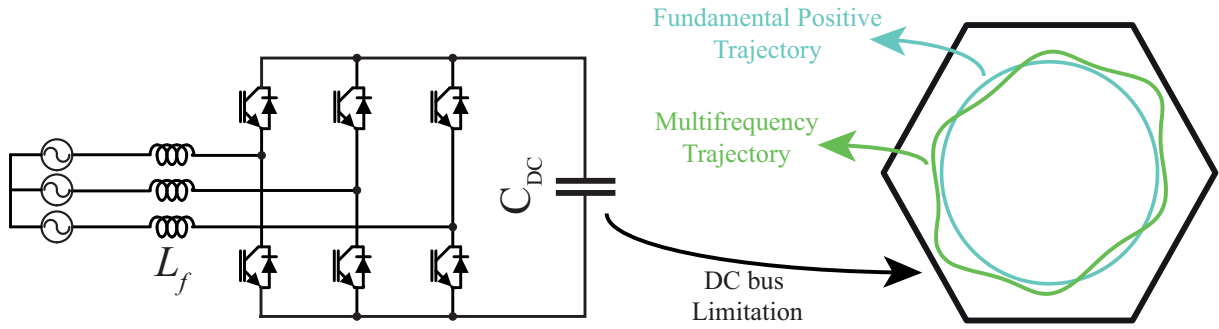


Figure 2.1: Comparison of trajectory with only fundamental positive sequence and with the inclusion of harmonic sequences inside the hexagon of DC-bus limitation.

Finally, in [47] a new multifrequency distortion free saturator is proposed, which is able to perform the saturation without inferring over the system dynamics. In this saturator the minimum THDi is always pursued.

2.1.5. Harmonic Compensation

During the last part of the thesis, the VSI harmonic currents are controlled in order to improve the power quality. The final objective is to reduce the voltage distortion of the electric grid. This voltage distortion is provoked by the propagation of the harmonic currents consumed by non-linear load. Therefore, two different strategies are analysed. The first strategy is to locally measuring the harmonic currents consumed by non-linear loads and compensating then (Active Power Filter). The second strategy consists on measuring the harmonic voltage content at the PCC and injecting harmonic currents until reducing the PCC harmonic voltage distortion.

2.1.5.1. Active Power Filters

APFs have been since long time studied in the literature as described in [67] and they have proliferated in the industry [68]. The APF is in charge of suppressing the harmonic currents consumed or generated by local devices. In this context, the electronics of the APF is the same that for any other VSC with the addition of a current sensor for measuring the current consumed by the load.

The increment of the number of non-linear loads, sometimes could require more than one converter in order to compensate all the harmonic currents. Different strategies could be employed for the parallel connection and control of different APFs [69]. As the total harmonic currents of the non-linear loads is distributed between the APFs different criteria can be employed. In the first strategies, the total harmonic current consumption is split regarding to the frequency component (*Frequency Splitting (FS)/Centre Mode Control (CMC)*) [70], [71]. In the second one, as a different approach the total harmonic

current is divided by the different APFs (*Power Splitting (PS)/ Distributed control*). Another possibility is to compensate according to the converter power rating (*Master-slave Control/Capacity Limitation Control (CLC)*): In this parallel working mode, each VSI is in charge to perform the maximum possible harmonic compensation regarding to its power rating [71].

In addition, due to the similarity of electronics topology between an APF and any other VSC, it is gaining importance the inclusion of the APF functionality in VSC associated with distributed generators [72]. However, the addition of functionalities implies that the limitations of the VSC can be sooner reached [50]. In this thesis, a new method is proposed for VSCs associated with distributed generators. In this case, an strategy is proposed for continuously providing the maximum active power while the harmonic compensation is achieved in a cooperative way during saturation state.

2.1.5.2. PCC harmonic voltage reduction

As previously described, the APF compensates the harmonic currents by setting the reference currents to the ones measured by the load. However, it would be interesting to be able to perform the harmonic current compensation without the necessity of an additional current sensor. In [73] a new topology is proposed in order to reduce the number of employed sensors. However, this topology does not fit with the common shunt APF topology, as shown in Fig. 2.2.

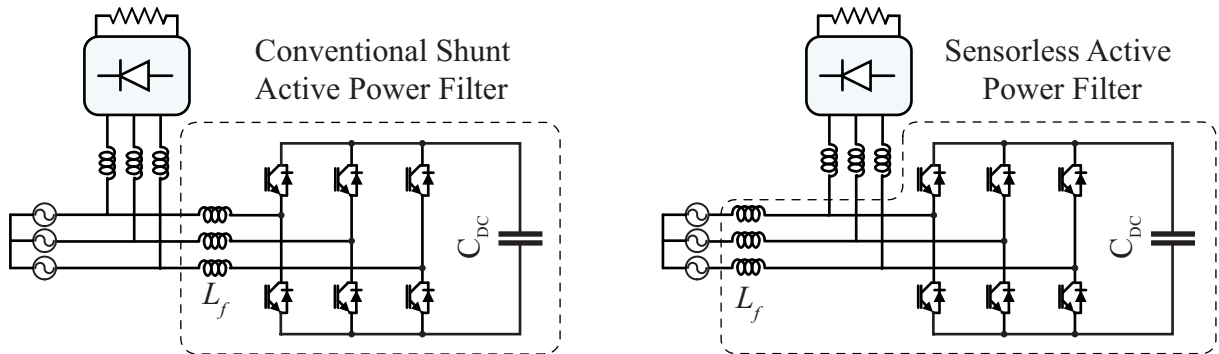


Figure 2.2: Conventional Shunt APF and sensorless APF topologies [73].

Keeping the shunt parallel connected topology and trying to reduce the harmonic voltage distortion, without the necessity of additional current sensors has not proliferated yet. However, this possibility has been described sometimes in the literature and a shunt APF can be able to compensate the harmonic voltages at the PCC and therefore, stop the harmonic propagation. In 1983, [74] described among one of the APF harmonic detection methods to measure the harmonic voltages at the PCC and deliver a proportional current. This type of strategy is also employed in [75]. Then, in [76] the harmonic voltage damping is implemented as an additional functionality in the control of VSIs for distributed generators. This strategy is also studied in [77], [78].

One of the parameters that have more influence in the harmonic PCC voltage reduction is the grid impedance. Although in some works the value of the grid impedance estimation is avoided [79], the knowledge of this parameter has a great influence on the PCC voltage controller dynamics. For the grid impedance estimation, different approaches have been carried out in the literature. The typical employed methods for the grid impedance detection are based on provoking a small disturbance over the grid and analysing the grid response. The most typical are injecting a current spike and performing an FFT analysis [80], [81]; Reference current phase angle alteration and grid reaction analysis [82]; Active (P) and reactive (Q) power variations [83], [84], [85], [86]; Frequency tone injection [87].

In this thesis, a new detection method for the grid inductance is proposed and published in [88]. In this method a frequency tone is injected and the variation over the PCC is analysed. Then, the grid inductance is estimated and it can be extrapolated for the interesting controlled harmonic components.

Therefore, once that the grid impedance is estimated, the PCC voltage harmonic components can be reduced and the controller dynamics can be set. However, as stated in [77] and more recently in [89], there exists a huge barrier for taking the PCC voltage compensation of shunt connected VSCs to the industrial world. This barrier is the dc voltage limitation that could limit the ac output trajectory. In this thesis, with the development of the distortion free multifrequency saturator this problem can be tackled and the PCC harmonic voltage can be controlled solving the saturation issue. An approach has been carried out in this thesis and it has been partially published in [90].

2.2. Review of Contributions

As stated along the chapter, different contributions have been made regarding the topic of the multifrequency control of power converters. At this point the contributions of the Thesis have been previously described and in this section all of them are summarized.

Between the different steps of the multifrequency control, a first contribution has been made over the synchronization. A novel structure based on the multiple ROGIs parallel connection and it has been published in [41].

In the multifrequency control, the different techniques for the tuning of the ROGIs have been described. Although it has not been published, some techniques that had not previously been employed for the ROGI controllers have been employed here.

Then, a novel references calculation method is proposed in order to reduce the power oscillations even when the grid presents voltage distortion. The novelty of the strategy falls on reducing the main oscillating component with the optimization of delivering the minimum current THDi. This strategy is described at the end of Chapter 4 and it has already been published in [58].

The next contributions are carried out over the saturation system. One of the most important contributions of this thesis is the proposed saturator that is able to keep the linear modulation range without incurring into additional distortion. This saturation is made over multifrequency trajectories and it is carried out without increasing the external control settling time. This proposed method is described in Section 5.4.3 and it has been submitted in [47]. In addition, although it remains pending of publication, the described DFIMS employed for voltage saturation could be employed in current saturations as described in Section 5.5.2.

Finally, contributions are made regarding to the topic of avoiding the propagation of harmonic currents that are usually consumed by non-linear loads. First, regarding to the cancellation of those harmonic components in a local way, a novel strategy is proposed for the cooperative compensation among VSIs interfacing distributed generators. The strategy allows that even under saturated situations the distributed generator are able to deliver the maximum power. This method has been described in 6.2.3 and submitted to Transactions on Power Electronics.

Continuing with this topic, in order to avoid the propagation of harmonic current components provoking voltage distortion another contribution is made. In this context, a PCC voltage control method is proposed that reduces the PCC harmonic distortion. This PCC voltage controller is tuned in accordance to the estimated grid impedance. As a key feature, this compensation is achieved as a secondary goal and then, in case of reaching converter limitations, the compensation is achieved as far as possible with the help of DFIMS. This strategy has been described in Section 6.3 and it has been partially published in [90], but still is pending of a journal publication with the addition of the described contributions.

As a secondary task in the regard of PCC voltage controller, it has been mentioned that the grid impedance estimation is needed in order to tuned the controller. In Section 6.3.1, a novel method for the grid impedance estimation optimized for harmonic inductance detection is proposed and it has been published in [88].

The previously summarized contributions are depicted in Fig. 2.3, where the main publications are highlighted. When the novelty has not been published yet, the chapter where it is described is referred.

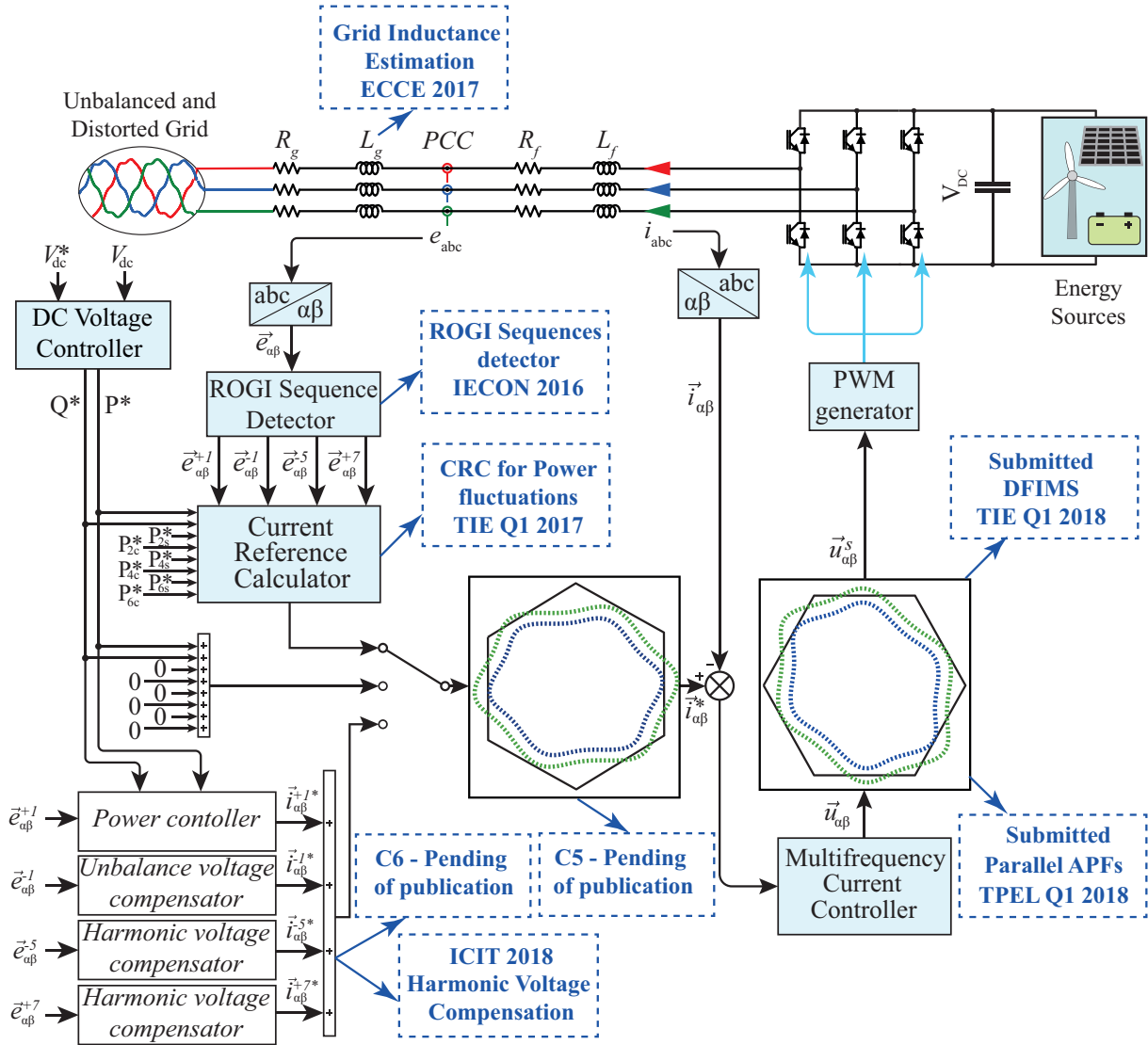


Figure 2.3: Graphical representation of thesis contributions.

Chapter 3

Multifrequency Control of grid-tied Voltage Source Converters

3.1. Introduction

This section gives an explanation of the multifrequency control of grid tied converters. In addition to perform the control over fundamental frequency (usually 50Hz), multifrequency control also deals with the harmonic components. This chapter is divided into different sections in order to show the up-to-date techniques for the basic steps of the multifrequency control process (grid synchronization and current control), as shown in Fig. 3.1.

The chapter starts in Section 3.2 with an overview of the representation of three phase signals in different stationary and synchronous reference frame including different grid distortion. Then, in Section 3.3 a study of the different controllers available for both, dc and sinusoidal signals, is carried out. The decomposition of the fundamental and harmonic grid voltage components and the converter-grid synchronization is studied in 3.4. Finally, the control structures for multifrequency current control and its design is described in Section 3.5.

3.2. Vector representation of three-phase variables

As previously stated, this thesis is based on the control of grid tied VSC converters. Concretely, the studied VSC performs a conversion between dc and three-phase ac. Therefore, the three-phase voltages of the grid and the three-phase currents that the converters exchange with the grid need to be measured and processed. In this regard, different transformations can be carried out in order to reduce the degrees of freedom and complexity of working with three-phase signals. The different transformations under different signal conditions are analysed in this section.

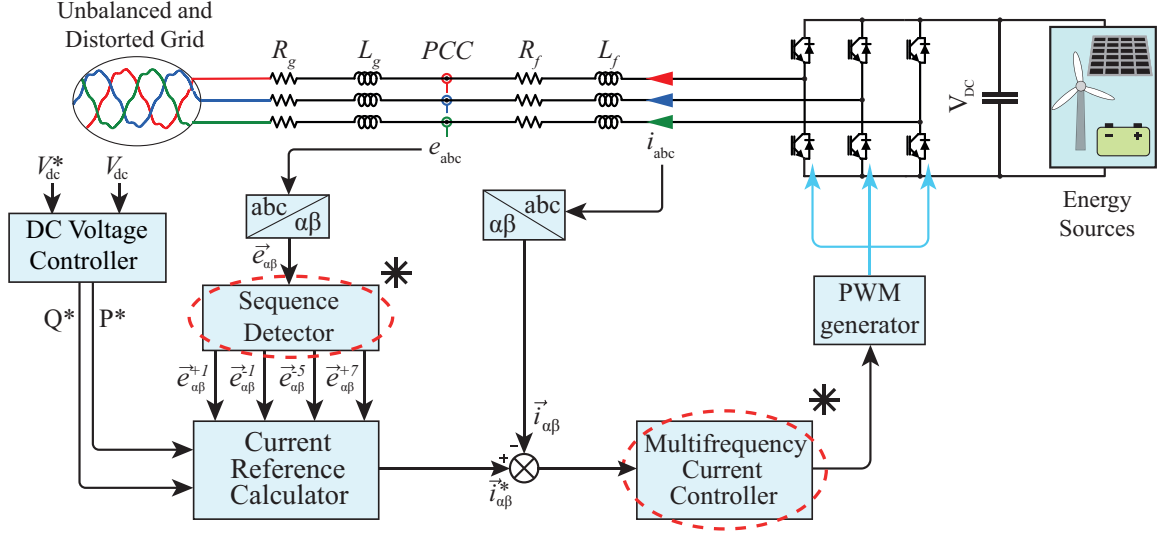


Figure 3.1: Simplified control scheme with the basic control blocks.

3.2.1. $\alpha\beta$ Stationary reference frame

Assuming a three-phase VSC, three-phase voltage (v_a, v_b, v_c) and three-phase currents (i_a, i_b, i_c) are measured. Ideally, these signals are symmetrical separated with 120° between them:

$$\begin{aligned} x_a &= X \cdot \sin(\omega t) \\ x_b &= X \cdot \sin(\omega t - 120^\circ) \\ x_c &= X \cdot \sin(\omega t + 120^\circ) \end{aligned} \quad (3.1)$$

where x can stand for both, voltage (v) or current (i). As it is well-known, the three degrees of freedom from the three phases measurements (both voltages and currents) can be transformed to a new three degrees of freedom $\alpha\beta\gamma$ stationary reference frame through the Clarke transformation. Depending on the selected gain, the transformation can be carried out in order to keep the same amplitude ($K = \frac{2}{3}$) or to maintain the power magnitudes ($K = \sqrt{\frac{2}{3}}$):

$$\begin{bmatrix} x_\alpha \\ x_\beta \\ x_\gamma \end{bmatrix} = K \begin{bmatrix} 1 & \frac{1}{2} & -\frac{1}{2} \\ 0 & \frac{\sqrt{3}}{2} & \frac{\sqrt{3}}{2} \\ \frac{1}{\sqrt{2}} & \frac{1}{\sqrt{2}} & \frac{1}{\sqrt{2}} \end{bmatrix} \begin{bmatrix} x_a \\ x_b \\ x_c \end{bmatrix} \quad (3.2)$$

In three-phase three-wire VSC there is no neutral wire and therefore, the γ component is equal to zero. Then, the $\alpha\beta\gamma$ reference frame is usually referred to as $\alpha\beta$. Therefore, this transformation reduces the control complexity to just two degrees of freedom. Furthermore, the new α and β axes are set orthogonal.

In this new reference frame, the two orthogonal axes describe a new plane where the α axis can be understood as the abscissa axis, while the β axis represents the ordinates.

This plane can also be seen as a complex plane where α is interpreted as the real part, and β represents the imaginary part. In this way, the three-phase voltage or current signals can be interpreted as only one $(x_\alpha + jx_\beta)$ complex signal [26].

3.2.2. Three-phase Unbalance

Unfortunately, the grid is not always as perfect as the one described at the beginning of the section. Under some circumstances, three-phase signals are not perfectly symmetrical, due to phase or magnitude differences. This situation is defined as unbalance and it increases the system complexity. Unbalanced systems are more difficult to analyse and to control than the balanced ones. The desire to always work with balanced systems brought a transformation that convert any unbalanced system, to three balanced systems. By the superposition principle, the solution is always the addition of three systems, divided into:

- Positive sequence
- Negative sequence
- Zero sequence

The transformation of a generic three phase system to the positive-, negative- and zero-sequence components is described as:

$$\begin{bmatrix} x_p \\ x_n \\ x_0 \end{bmatrix} = \frac{1}{3} \begin{bmatrix} 1 & \delta & \delta^2 \\ 1 & \delta^2 & \delta \\ 1 & 1 & 1 \end{bmatrix} \begin{bmatrix} x_a \\ x_b \\ x_c \end{bmatrix} \quad (3.3)$$

where δ is defined as $1_{\angle 120^\circ}$. The graphical transformation of an unbalanced system into positive, negative and zero sequences is shown in Fig. 3.2.

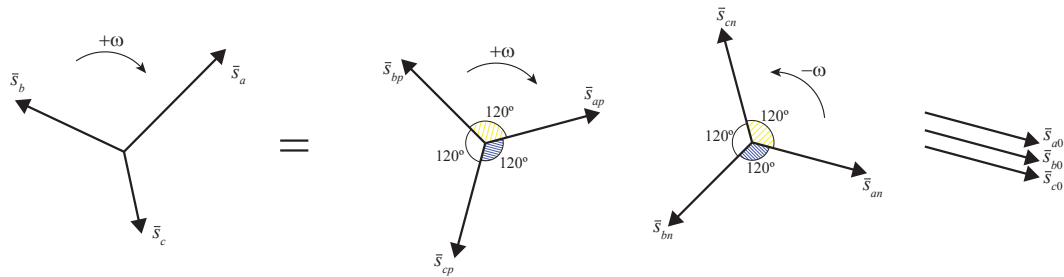


Figure 3.2: Decomposition example of three-phase unbalanced signals into positive negative and zero balanced systems.

3.2.3. Harmonic distortion

In addition to the unbalance, the grid can present other non-idealities and disturbances. The connection of different non linear loads to the grid provokes the increment of harmonic

current components, which can provoke harmonic voltage components at the PCC. Typical examples of non linear loads are found in computers, uncontrolled rectifiers for electric car charging or fluorescence lamps. The harmonic currents consumed by non linear loads can be analysed through the FFT and it can be appreciated that in addition to the fundamental component, it is also composed by odd harmonics (wave symmetry) that decrease in magnitude with the increment of harmonic order. When the amount of these kind of loads proliferates along the grid, the current consumption can be transformed in harmonic grid voltages. In three-phase three-wire power converters, the third multiple harmonics does not appear.

Following these premises, it can be deduced that the most harmful harmonic are the low odd non-triple harmonics, concretely 5 and 7. Therefore, converting the fifth harmonic effect over each one of the three-phase signal can be expressed as:

$$\begin{aligned} x_a^5 &= X_5 \cdot \sin(5(\omega t)) &= X_5 \cdot \sin(5\omega t) \\ x_b^5 &= X_5 \cdot \sin(5(\omega t - 120)) &= X_5 \cdot \sin(5\omega t + 120) \\ x_c^5 &= X_5 \cdot \sin(5(\omega t + 120)) &= X_5 \cdot \sin(5\omega t - 120). \end{aligned} \quad (3.4)$$

It can be seen how, when a fifth harmonic affects to the three-phase signals, x_b and x_c exchange their phases, which implies to be interpreted as a negative sequence. However, if the seventh harmonic is analysed, it can be seen that the phases are not altered:

$$\begin{aligned} x_a^7 &= X_7 \cdot \sin(7(\omega t)) &= X_7 \cdot \sin(7\omega t) \\ x_b^7 &= X_7 \cdot \sin(7(\omega t - 120)) &= X_7 \cdot \sin(7\omega t - 120) \\ x_c^7 &= X_7 \cdot \sin(7(\omega t + 120)) &= X_7 \cdot \sin(7\omega t + 120). \end{aligned} \quad (3.5)$$

Therefore, it can be interpreted as a positive sequence. The case of the 5th harmonic can be extended to the different $6k - 1$ harmonics, while the different $6k + 1$ harmonics are described as positive fundamental sequences, as it occurs with 7th harmonic.

3.2.4. dq Synchronous reference frame

A further step can be reached with a new transformation, where In difference with the previous $\alpha\beta$ transformation, the reference axes are continuously rotating. This further step is known as Park transformation and the previous $\alpha\beta$ variables are transformed to new dq axis. As previously described, stationary reference frame allows to represent the three-phase variables as a complex signal $\vec{x}_{\alpha\beta} = x_\alpha + jx_\beta$. Assuming a rotating frequency of ω , dq axes vary with time $\theta = \omega t$. The transformation from $\alpha\beta$ stationary frame to dq synchronous reference frame is described as:

$$\begin{bmatrix} s_d \\ s_q \\ s_0 \end{bmatrix} = \begin{bmatrix} \cos(\theta) & -\sin(\theta) & 0 \\ \sin(\theta) & \cos(\theta) & 0 \\ 0 & 0 & 1 \end{bmatrix} \begin{bmatrix} s_\alpha \\ s_\beta \\ s_\gamma \end{bmatrix}. \quad (3.6)$$

The transformation is equivalent to multiply the signal by $e^{-j\omega_r t}$, where ω_r stands for the axis rotation frequency. The FPS signal in stationary reference frame, can be described as:

$$\vec{x}_{\alpha\beta}^{+1} = X_{+1} \cdot e^{j(\omega t + \phi_1)}. \quad (3.7)$$

For the transformation, when the synchronous edges rotates at the same frequency that the signal frequency ($\omega_r = \omega$), the transformation can be expressed as:

$$\vec{x}_{dq}^{+1} = X_{+1} \cdot e^{j(\omega t + \phi_1)} \cdot e^{-j\omega t} = X_{+1} \cdot e^{j\phi_1} \quad (3.8)$$

resulting in a dc signal. The signals in $\alpha\beta$ stationary reference frame result into dc signals always that the rotating frequency is accurately detected and employed into the transformation. An example can be also seen if a harmonic component is converted to dq axis. In this case, the harmonic sequence corresponding to -5 can be converted with an axis rotation of $\omega_r = -5\omega$:

$$\vec{x}_{dq}^{-5} = X_{-5} \cdot e^{j(-5\omega t + \phi_{-5})} \cdot e^{+j5\omega t} = X_{+5} \cdot e^{j(\phi_{-5})}. \quad (3.9)$$

This transformation of harmonic components into dc signals, can exclusively be performed if the desired harmonic signal has been previously separated from the rest of components. A most common alternative is to directly perform the transformation of the total measured signal $\vec{x}_{\alpha\beta}$ which could contains different kind of sequences:

$$\begin{aligned} \vec{x}_{\alpha\beta} &= X_{+1} \cdot e^{j(\omega t + \phi_1)} + X_{-1} \cdot e^{j(-\omega t + \phi_{-1})} + X_{-5} \cdot e^{j(-5\omega t + \phi_{-5})} + X_{+7} \cdot e^{j(7\omega t + \phi_7)} \\ &+ \sum_2^n \left[X_{-6k+1} \cdot e^{j[(-6k+1)\omega t + \phi_{(-6k+1)}]} + X_{6k+1} \cdot e^{j[(6k+1)\omega t + \phi_{(6k+1)}]} \right] \end{aligned} \quad (3.10)$$

into the dq axis with a rotation of the natural frequency $\omega_r = \omega$, resulting in:

$$\begin{aligned} \vec{x}_{dq} &= \vec{x}_{\alpha\beta} \cdot e^{-j\omega t} = X_{+1} \cdot e^{j(\phi_1)} + X_{-1} \cdot e^{j(-2\omega t + \phi_{1m})} + X_{-5} \cdot e^{j(-6\omega t + \phi_{5m})} + X_{+7} \cdot e^{j(6\omega t + \phi_7)} \\ &+ \sum_2^n \left[X_{-6k+1} \cdot e^{j[-6k\omega t + \phi_{(-6k+1)}]} + X_{6k+1} \cdot e^{j[6k\omega t + \phi_{(6k+1)}]} \right] \end{aligned} \quad (3.11)$$

Through this conversion the FPS component is transformed into a constant signal and the most common harmonics sequences (-5 and $+7$) results in ± 6 harmonic components. Meanwhile, the negative sequence appears in dq axis as a second harmonic.

This transformation, in addition to the transformation operations, requires algorithms for phase and frequency detection (typically PLL), that are explained in Section 3.4. The main advantage of the synchronous reference frame is that it allows to work with dc signals for the FPS, allowing the employment of the control theory for dc signals.

3.3. Controllers for $\alpha\beta$ and dq reference frames

As described in previous section, sinusoidal voltages and currents are the physical magnitudes that need to be dealt with, regarding VSC topic. As explained during the last part, the magnitudes can be converted to dq synchronous reference frame where the FPS is transformed into a dc signal. This conversion has been widely employed, due to the facility to work with dc signals, instead of sinusoidal ones.

The preference of employment of dc signals has been especially appreciated in control. In order to control dc signals, a controller that achieves a zero error in steady state for zero frequency signals would perfectly fit. *Proportional Integrator (PI)* is the most common controller employed for this purpose and its transfer function in continuous domain is expressed as:

$$C(s) = k_p + \frac{k_i}{s} = \frac{k_p \cdot s + k_i}{s}. \quad (3.12)$$

As the PI controller in open loop presents an infinite gain for the zero frequency (dc signal) it achieves a zero error for that frequency. However, as it has been previously explained, in $\alpha\beta$ stationary reference frame or for rest of components in dq synchronous reference frame, the signals are sinusoidal with a certain frequency. In the previous described cases, the signals are of sinusoidal nature and therefore, if a zero error in steady state wants to be achieved, the transfer function needs to present a 0 dB gains in closed loop at the signal frequency. Therefore, if the desired controller is a PI, the bandwidth needs to be extended up to the signals frequencies. However, when the control wants to be carried out over a certain frequency, another possibility exists and it is to employ a *Proportional Resonant Controller (PRC)*.

3.3.1. Proportional Resonant Controllers (PRC)

PRC consists on a type of controller that presents infinite gain at the desired frequency. These kind of controllers are called PRC because they are composed by two parts, a proportional part and a resonant part that is in charge of the desired frequency. The

most common resonant controllers are the *Second Order Generalized Integrator (SOGI)* and the *Reduced order generalized integrator (ROGI)*.

3.3.2. Second Order Generalized Integrator (SOGI)

In this context, the SOGI appeared as a solution [91], whose transfer function is:

$$\frac{y(t)}{x(t)} = \frac{K_{SOGI} \cdot s}{s^2 + \omega_0^2} \quad (3.13)$$

where the gain k_{SOGI} determines the behavior of the transfer function in terms of selectivity (reduction of bandwith) and settling time. The transfer function has two poles, one of them at $s = +j\omega_0$ and the other one at $s = -j\omega_0$. That would achieve infinite gain in open loop for the desired ω_0 in both positive and negative sequences. The described transfer function of the SOGI in open loop, can be graphically depicted as shown in Fig. 3.3.

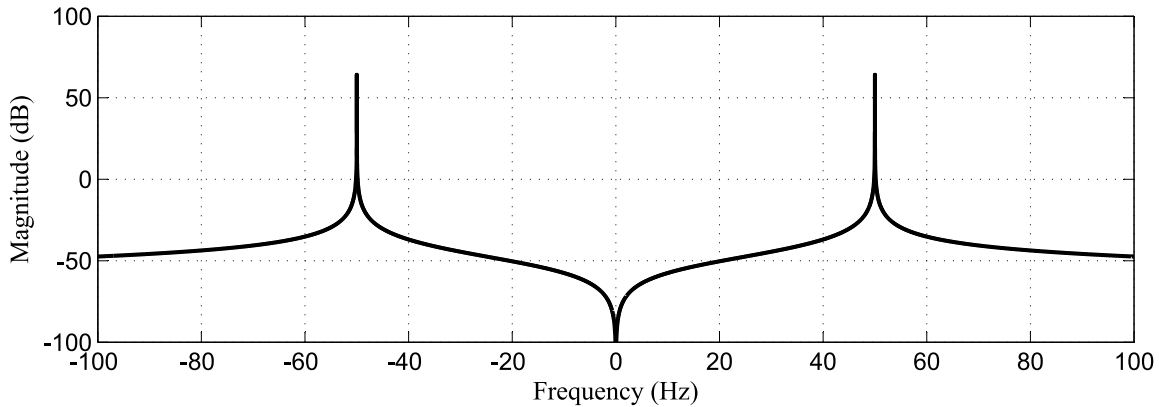


Figure 3.3: Bode representation of the magnitude of the SOGI transfer function open loop.

As seen in the depicted figure, SOGI presents infinite gain for the desired frequency to be controlled, e.g. 50 Hz, but in addition, desired or not, it also brings infinite gain at the opposite sequence frequency, e.g. -50 Hz. This fact is an advantage when both sequences want to be controlled, but exclusively, when the same dynamics wants to be obtained for both of them.

3.3.3. Reduced Order Generalized Integrator (ROGI)

Unlike SOGI, multiple-complex coefficient-filter-based is presented and described in [30]. This transfer function, latter generalized as ROGI [31] allows to have an infinite gain, exclusively, in the desired sequence. It means that the infinite gain is presented at the positive or negative sequence, exclusively, without a reflection effect on the opposite sequence. The ROGI transfer function is described in continuous domain as:

$$\frac{\vec{y}_{\alpha\beta}}{\vec{x}_{\alpha\beta}} = \frac{k_{ROGI}}{s - j\omega_0} \quad (3.14)$$

and as it occurred with the SOGI, the gain k_{ROGI} determines the behaviour in terms of selectivity and response time. The whole transfer function and the behaviour depending on the gain are shown in Fig. 3.4.

The ROGI is a resonant controller, which regardless of the input, provides a double output. One with the input frequency and another at the ROGI's tuned frequency. Both output signals have the same phase and the same amplitude, and they are dependent on the ROGI's transfer function. If the ROGI is tuned at a frequency ω_0 and a complex signal with an ω periodicity is introduced at the input, the output would result in:

$$y(s) = \frac{k_{ROGI}}{s - j\omega_0} \cdot x(s) = \frac{k_{ROGI}}{s - j\omega_0} \cdot \mathcal{L}\{A \cdot e^{j\omega t}\} = \frac{k_{ROGI}}{s - j\omega_0} \cdot \frac{A}{s - j\omega} \quad (3.15)$$

This could be written as the sum of two components, one at the tuned frequency and the other one at the input frequency:

$$y(s) = \frac{k_{ROGI} \cdot A}{j(\omega_0 - \omega)} \cdot \left[\frac{1}{s - j\omega_0} - \frac{1}{s - j\omega} \right] \quad (3.16)$$

with both of them having the same amplitude, that varies depending on $\omega_0 - \omega$. In the time domain, it can be expressed as:

$$y(t) = \mathcal{L}^{-1}\{y(s)\} = \frac{k_{ROGI} \cdot A}{j(\omega_0 - \omega)} \cdot [e^{j\omega_0 t} - e^{j\omega t}]. \quad (3.17)$$

Nevertheless, the implementation of controllers is carried out in commercial boards that are far from the continuous domain and require the discrete domain implementation. In order to express the continuous transfer function in discrete domain, different discretization methods can be employed. The basis of the ROGI, as previously described, is to present infinite open loop gain at the tuned frequency. Then, the discrete transfer function needs to present the same pole in z domain:

$$z = e^{s \cdot T_s} = e^{j(\omega_0 \cdot T_s)} \quad (3.18)$$

With the employment of different conventional conversion methods (*Zero Order Hold (ZOH)*, *First Order Hold (FOH)*, impulse-invariant mapping, Tustin with prewarping at ω_0 and Zero-Pole matching) the pole is placed at exactly the same value: $e^{j\omega_0 \cdot T_s}$. Therefore, the difference of discretization between the different methods are found in the numerator. The different discretization methods have been analysed and compared. For all of them the magnitude bode diagrams are equivalent, regardless of the employed discretization method and also for the continuous transfer function. Regarding to the

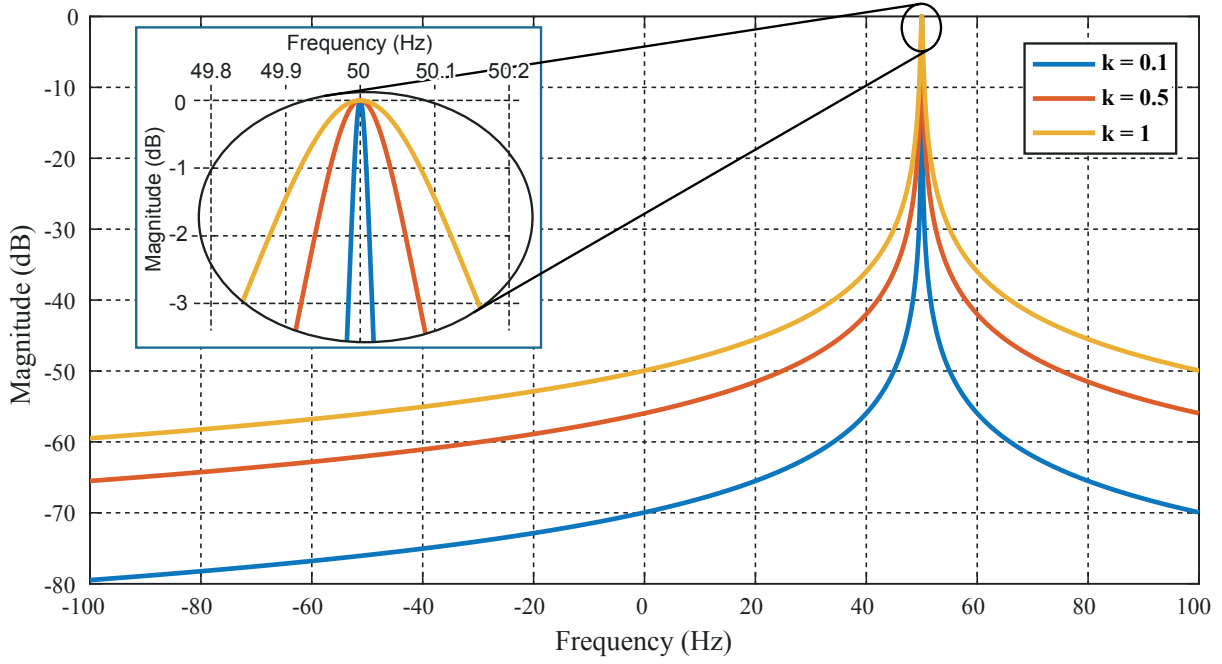


Figure 3.4: Bode representation of the magnitude of the ROGI transfer function closed loop. Bandwidth and bode comparison with different k_{ROGI} are shown.

phase matching, it is completely achieved for those that add an additional zero (FOH and Tustin). However, for the rest of methods, a variation in the phase occurs for the high frequency components (5° up to 1250 Hz for ROGI resonant frequency of 50 Hz), as it can be appreciated in Fig. 3.5. In this regard, as the phase variation is for frequencies that are not interesting for the control system, it has been preferred to employ those discretization methods that do not add additional zeros. Therefore, the ROGI transfer function in the discrete domain can be expressed as:

$$\frac{\vec{y}_{\alpha\beta}}{\vec{x}_{\alpha\beta}} = \frac{k_{ROGI(d)}}{z - e^{j\omega_0 T_s}} \quad (3.19)$$

Once that the position of the pole has been set, and it has been decided that no additional zeros are included, the discrete ROGI gain needs to be set. For example, through the pole matching discretization method, the gain could be adjusted in order to obtain the same magnitude for zero frequency:

$$\frac{k_{ROGI}}{-j\omega_0} = \frac{k_{ROGI(d)}}{1 - e^{j\omega_0 T_s}} \quad (3.20)$$

$$k_{ROGI(d)} = \frac{k_{ROGI}(1 - e^{j\omega_0 T_s})}{-j\omega_0} \quad (3.21)$$

However, the best option for achieving the desired dynamics in discrete domain, is to directly calculate the ROGI gain in discrete domain. The adjustment of the ROGI gains is dependent on the controlled plant. The different methods for gains calculation

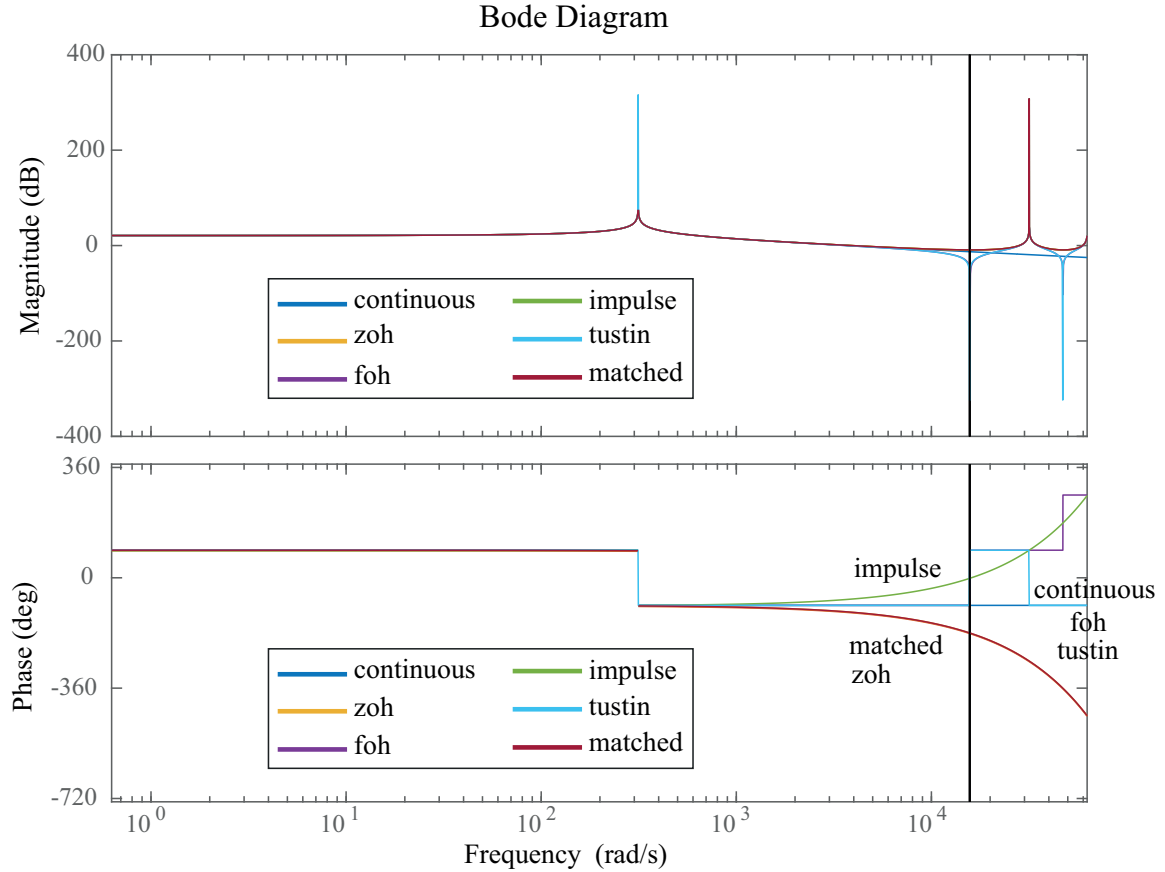


Figure 3.5: Decomposition example of three-phase unbalanced signals into positive negative and zero balanced systems.

are provided in Section 3.5.

Finally, once that the discretization methods have been analysed and the ROGI's transfer function in discrete domain has been obtained (3.19), the next step is the implementation over the DSP. For this purpose, in C programming, the complex signals and complex coefficients are treated as 2 elements arrays. Then, the basic operations with complex numbers are defined:

```
#define complexsum(cnum1,cnum2,cresult) \
    cresult[0]=cnum1[0]+cnum2[0]; \
    cresult[1]=cnum1[1]+cnum2[1];
```

```
#define complexmul(cnum1,cnum2,cresult) \
    cresult[0]=cnum1[0]*cnum2[0]-cnum1[1]*cnum2[1]; \
    cresult[1]=cnum1[0]*cnum2[1]+cnum1[1]*cnum2[0];
```

Working with (3.19) The obtained output of the ROGI, when a complex input is given, could be defined as:

$$\begin{aligned}\vec{y}_{\alpha\beta}(k) &= k_{ROGI(d)} \cdot \vec{x}_{\alpha\beta}(k) + \vec{y}_{\alpha\beta}(k-1) \cdot e^{jh\omega_0 T_s} \\ &= k_{ROGI(d)} \cdot \vec{x}_{\alpha\beta}(k) + \vec{y}_{\alpha\beta}(k-1) \cdot [\cos(h\omega_0 T_s) + j \sin(h\omega_0 T_s)]\end{aligned}\quad (3.22)$$

As it can be extracted from the previous formula, the complex constant ($e^{jh\omega_0 T_s}$) can be expressed in real and imaginary terms. For a defined resonant frequency of 50 Hz and a sampling time of 200 μ s the pre-stored values would be:

```
rogi_tf[0]=0.9980267; //cos(2*pi*50*200e-6)
rogi_tf[1]=0.0627905; //sin(2*pi*50*200e-6)
```

The implementation over the DSP for obtaining the complex output signal obtained from the ROGI when an input complex signal is applied could be expressed as:

```
complexmul(xab, krogi, aux1);
complexmul(yab_prev, rogi_tf, aux2);
complexsum(aux1, aux2, yab);

yab_prev[0]=yab[0]; yab_prev[1]=yab[1];
```

3.3.4. SOGI vs ROGI

Between the two previous described resonant controllers, depending on the pursued application, a choose needs to be made. Here, the different features, of both of them, are highlighted and compared, in order to make easier the decision.

It needs to be clarified, that with the connection of two ROGIs for the possitive and negative sequences connected in parallel, the SOGI transfer function can be obtained (if gains are the same):

$$\frac{\vec{y}_{\alpha\beta}}{\vec{x}_{\alpha\beta}} = \frac{k_{ROGI}}{s - j\omega_0} + \frac{k_{ROGI}}{s + j\omega_0} = \frac{k_{SOGI} \cdot s}{s^2 + \omega_0^2} \quad (3.23)$$

Therefore, the SOGI can be understood as a particularization of ROGIs structure, with the clear advantage of having scalar coefficients. Then, although the SOGI functionality can be achieved with ROGIs, in the cases where a SOGI is needed, its employment is preferable for the ease of implementation.

When positive and negative sequences want to be controlled, and in addition, the same behaviour is desired for both sequences, SOGI appears as the optimal solution. The symmetrical behaviour for positive and negative sequences, also brings the benefit of, if a switch between phases occurs (resulting in a negative sequence) it would also be controlled. As previously stated, this functionality also could be reached through the

employment of ROGIs. Then, in the described situation, the real coefficients and the ease of implementation makes the choose of SOGI preferable.

However, in some applications, the behaviour desired for the positive and negative sequences can be independently selected. This is a typical example, when the magnitude or priority difference between the two of them is considerable. In these cases, usually a faster control wants to be achieved for the most important one, and usually more selectivity for the small one. Then, different gains need to be selected and this can only be reached by means of ROGIs.

Furthermore, as described in (3.4) for $6k - 1$ harmonics, and in (3.5) for $6k + 1$ harmonics, when the stationary reference frame wants to be employed, the harmonic components are mainly found in exclusively one of the sequences. In this context, when harmonic sequences are dealt with, the employment of ROGIs allows to work without the necessity of θ detection.

As another advantage, when working with the dq-synchronous reference frame, one of the components could be desired to be released. In this case, if one of the components wants to be released while the other one is still controlled (e.g. control 5^{th} and no 7^{th}), ROGI appears as the optimal controller. This requirement could come from different parts (standards accomplishment, grid quality, etc).

Finally, the employment of complex coefficients makes that the transfer function is not symmetrical in negative and positive sides. This fact can be of high interest when a rejection rate for one sequence is desired higher than for the opposite sequence. An example can be seen when there exists an undesirable harmonic sequence that wants to be released by our controller.

An overview of the different properties for each controller are collected in Table 3.1.

Table 3.1: Comparative overview between SOGI and ROGI

PRC	SOGI	ROGI
Real coefficients and ease of implementation	✓	×
Control of both negative and positive sequences at once	✓	×
Immunity to sequence	✓	×
Independent gain selection (selectivity, response time, etc) for each sequence	×	✓
Unsymmetrical rejection rate to negative and positive sequences	×	✓
Complex transfer function and complex input and output signals	×	✓
θ detection and DQ transformation is not mandatory for harmonic control	×	✓
The control over one harmonic can be released (e.g. control 5^{th} and no 7^{th})	×	✓

3.4. Grid synchronization and Sequence Detector

Depending on the VSI functionality, they are often connected to the grid, in order to exchange active or reactive power, or performing grid supporting capabilities. In those cases, for grid connection it is crucial to detect the grid fundamental positive component

amplitude and phase. Furthermore, this detection needs to be carried out fast and accurately. It needs to be taken into account that when a change occurs over the grid, it needs to be detected several time faster than the controller settling time.

In order to carry out the synchronization with the grid, in a first approach the grid frequency can be assumed constant. With this premise, different approaches can be found in the literature, as instantaneous symmetrical components (ISC) [92], space vector filters (SVF) [93] or recursive weighted least-square estimation (WLSE) [94]. However, the frequency is not always constant and for meeting the desired functionality the employed synchronization system, needs to be able to adapt to frequency changes. In this context, PLL appears as one of the most extended solutions.

However, in some cases as in the one studied along this thesis, where multifrequency control is dealt, the information of the fundamental components (FPS and FNS) grid components is not enough information for the control system, and therefore, a synchronization system that is also able to detect the different harmonic sequences is needed.

3.4.1. Phase Locked Loop (PLL)

PLL has been an extensively employed method in order to phase grid detection. The PLL input is a sinusoidal signal. Then, the objective is to obtain at the output a signal, which has a phase and frequency equal to the input signal. The process is achieved by three different blocks: Phase detector (PD), Filter and *Voltage Controlled oscillator* (VCO). The phase detector is a nonlinear device that its output is proportional to the phase difference between the input and output sinusoidal signals. The filter is usually a first order low pass filter or PI controller which generates the control voltage for the VCO. Finally, the VCO is a nonlinear device that generates an oscillation, whose frequency is controlled by a lower frequency input voltage. The process with the different blocks is depicted in Fig. 3.6.

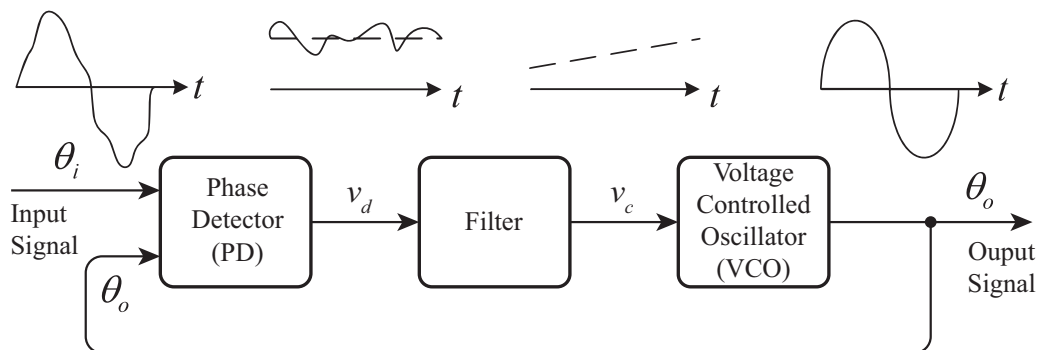


Figure 3.6: PLL structure scheme.

When the dq reference frame is employed, a common strategy is to perform the dq transformation with a θ that is generated through the output of the VCO. This is the

strategy for phase tracking of three-phase power systems in Synchronous reference frame and it is known as SRF-PLL [33]. The scheme of SRF-PLL is depicted in Fig. 3.7, where as it can be appreciated, the frequency, amplitude and phase of the three-phase signals are obtained.

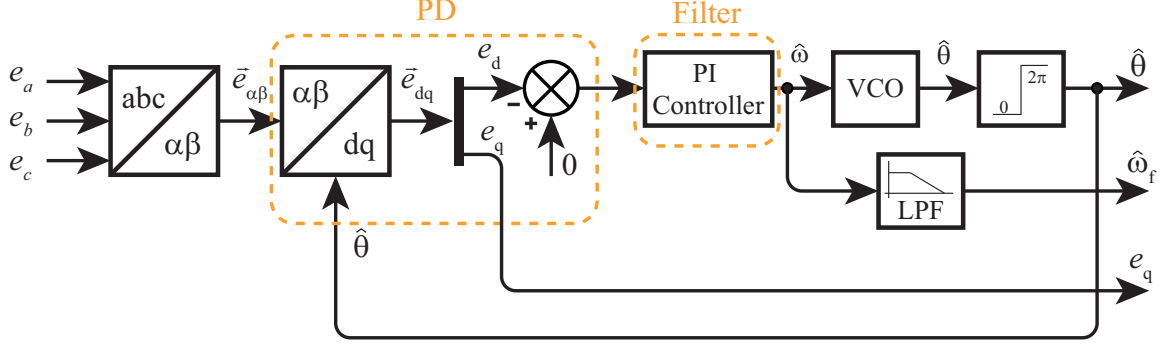


Figure 3.7: SRF-PLL structure scheme.

3.4.2. Sequence detection with PRCs

In order to extend the detection capabilities, the magnitude and phase detection of FPS can be expanded to the NFS and the principal harmonic components. PRCs described during section 3.3.1 can be employed for this purpose.

The employed strategy consists on implementing a closed loop where the input is the measured PCC voltage. The objective is to obtain several outputs where each of them is the filtered sequence that comes from each resonant controller. Therefore, a set of different resonant filters would allow to pass the different desired sequences (FPS, FNS and harmonics). Those sequences would be added among them, resulting in a combined signal that is sent back and compared with the input, which closes the loop.

Depending on the desired sequences and the chosen reference frame, a decision on the optimal resonant detector need to be made. Usually, the most common sequences are the FPS, the FNS and the low frequency, non-triple, odd harmonics.

3.4.2.1. Sequence detection with SOGIs

When *Synchronous Reference Frame (SRF)* is employed, the previously described interesting harmonics, usually 5th ($h = -5$) and 7th ($h = +7$) are converted into $h = \pm 6$. In these conditions, the resonant filter for the harmonics sequence detection is a SOGI which a transfer function equal to

$$\frac{y(t)}{x(t)} = \frac{K_{sogi} \cdot s}{s^2 + (6 \cdot \omega_0)^2} \quad (3.24)$$

where the same SOGI gain corresponds to both harmonic sequences components. In this case, SOGI appears as the optimal controller. Several SOGI structures have been proposed regarding to the detection of FPS and FNS in the $\alpha\beta$ stationary reference frame. As previously expressed, for sequence detection, the ± 1 sequences could be carried out in $\alpha\beta$ stationary reference frame and the -5 and $+7$ components could be referred to SRF and extracted with a SOGI at $h = \pm 6$. However, it is desirable to detect all the sequences in the same reference frame. For achieving this a topology was described in [36] where the SOGIs were placed at $h = 1$, $h = 5$ and $h = 7$ with the signals in $\alpha\beta$ reference frame. In this way, the θ calculation is avoided and the consequent Park transformations. The schematic of the proposed algorithm is depicted in Fig. 3.8.

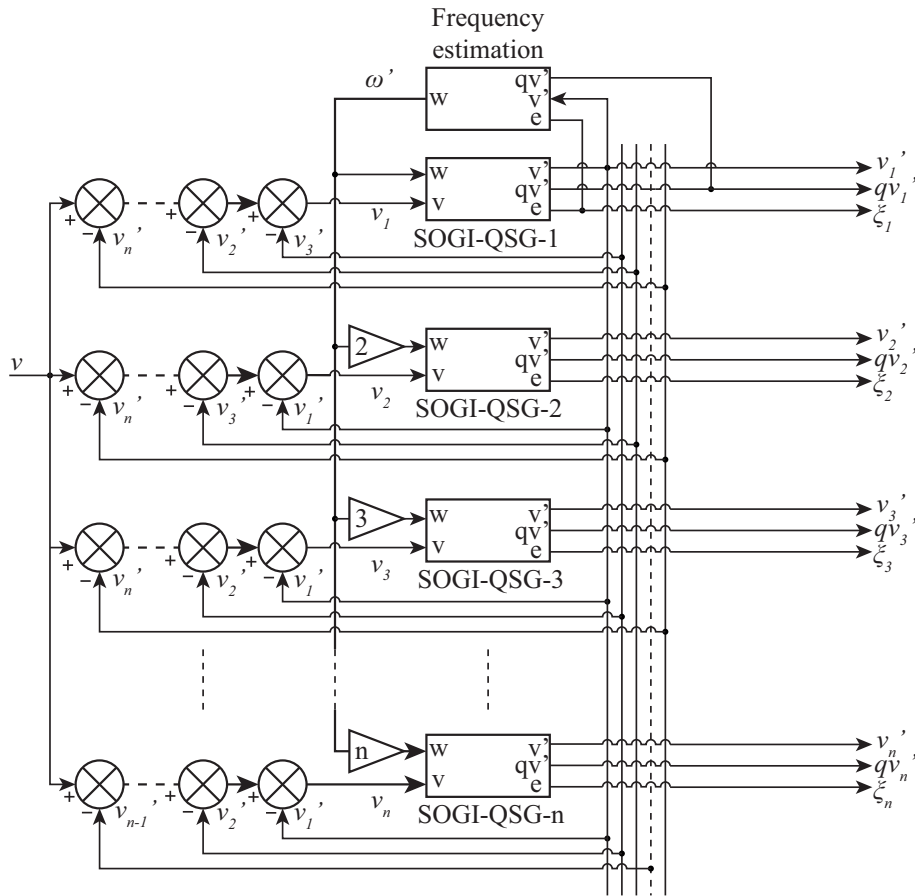


Figure 3.8: Grid synchronization and sequence detection MSOGI scheme [36].

This synchronization system is able to detect both, positive and negative sequences, due to the fact that a previously stated, the SOGI transfer function presents infinite gain for the positive and negative sequences of the interesting frequency. The global transfer function for the MSOGI system that performs the detection of 1, 5 and 7 harmonics is depicted in Fig. 3.9.

However, for the multifrequency current control that will be described in the next section and along the thesis, the different harmonic sequences want to be faced individually, and therefore, working in $\alpha\beta$ stationary reference frame, the ROGI appears as the op-

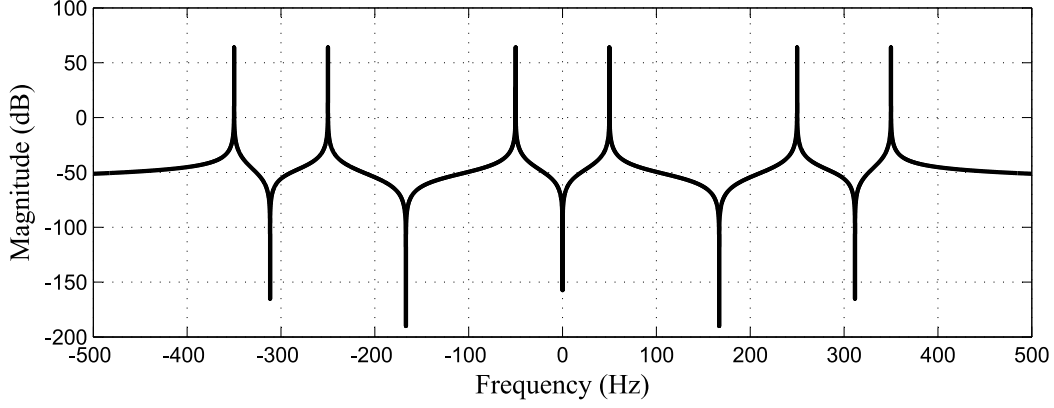


Figure 3.9: Bode diagram of the MSOGI transfer function.

timum controller, which is able to exclusively filter the desired sequence and assign an independent gain to each one.

3.4.2.2. Sequence detection with ROGIs

As it has been described before, when SRF is employed, the detection of harmonic sequences can be achieved with an only SOGI tuned at $6h$. However, for the synchronization with $h = \pm 1$ it should be carried out over $\alpha\beta$ and its detection could be carried out with another SOGI tuned at the fundamental frequency. However, as an inconvenience, the same gain is employed for FPS and NFS, which are totally different in magnitude.

In this regard, with the employment of multiple ROGIs, the synchronization can be directly carried out over the $\alpha\beta$ stationary reference frame. In addition, as the ROGI does exclusively presents infinite gain at positive or negative frequency, an independent gain can be assigned to each one of the ROGIs and get the desired behaviour for each sequence.

The main idea is to transform the measured PCC voltages (e_a, e_b, e_c) to the $\alpha\beta$ stationary reference frame $\vec{e}_{\alpha\beta}$. This voltage is the input of the sequence detector system, as depicted in Fig. 3.10. Then each ones of the input pass through each one of the ROGIs. Finally, the summation of every ROGI is performed, creating a signal that is the other input of the sequence detector [30] [41].

As previously described, the ROGI transfer function is defined as:

$$\frac{y(s)}{x(s)} = \frac{k_{ROGI}}{s - j\omega_0} \quad (3.25)$$

if a closed loop with exclusively one ROGI is carried out (with the plant equal to 1), the closed loop transfer function in continuous domain can be expressed as:

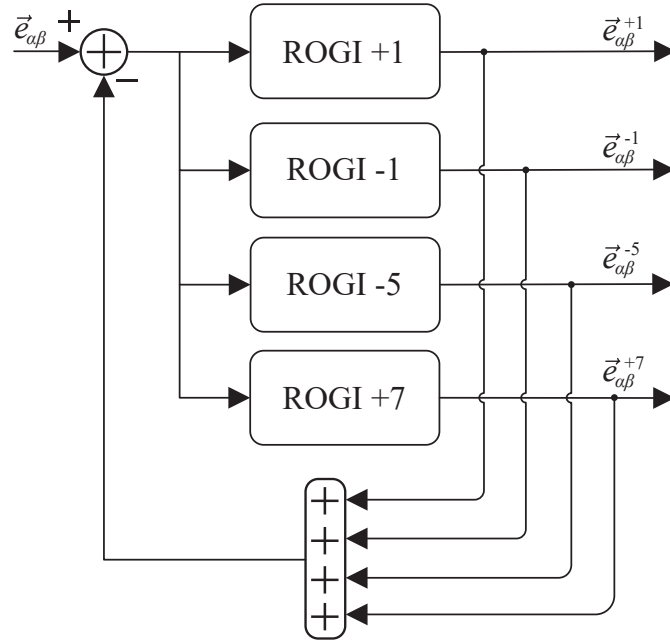


Figure 3.10: Grid synchronization and sequence detection MROGI scheme. [41]

$$\frac{y(s)}{x(s)} = \frac{k_{ROGI}}{s - (j\omega_0 - k_{ROGI})} \quad (3.26)$$

and assuming that the input is rotating at the tuned frequency ($x(t) = V \cdot e^{j\omega t}$), the output in continuous domain is defined as:

$$y(s) = \frac{V}{s - j\omega} \cdot \frac{k_{ROGI}}{s - (j\omega_0 - k_{ROGI})} = \frac{\frac{V \cdot k_{ROGI}}{j(\omega_0 - \omega) - k_{ROGI}}}{s - (j\omega_0 - k_{ROGI})} - \frac{\frac{V \cdot k_{ROGI}}{j(\omega_0 - \omega) - k_{ROGI}}}{s - j\omega}. \quad (3.27)$$

which in time domain can be expressed as:

$$y(t) = \frac{V \cdot k_R}{j(\omega_0 - \omega) - k_R} \cdot (e^{(j\omega_0 - k_R)t} - e^{j\omega t}) = \underbrace{\frac{V \cdot k_R}{k_R - j(\omega_0 - \omega)}}_{V \text{ when } \omega = \omega_0} \cdot \left(e^{j\omega t} - \underbrace{e^{j\omega_0 t} \cdot e^{-k_R t}}_{\text{Dissapear with time}} \right) \quad (3.28)$$

Therefore, it can be seen how when the input has a signal with a rotating frequency (ω) equal to the tuned ROGI frequency (ω_0) the output will be equal to the input. The transient until reaching the steady state value will be achieved in a time that is dependent with k_{ROGI} . Meanwhile, the ROGI gain (k_{ROGI}) also presents influence over the selectivity as it was showed in Fig. 3.4.

The complete transfer function of the MROGI, taking into account the transfer function for each independent ROGI, is described as:

$$\frac{y(s)}{x(s)} = \frac{k_{ROGI+1}}{s - j\omega_0} + \frac{k_{ROGI-1}}{s + j\omega_0} + \frac{k_{ROGI-5}}{s + j5\omega_0} + \frac{k_{ROGI+7}}{s - j7\omega_0} \quad (3.29)$$

and the Bode of the transfer function is depicted in Fig. 3.11.

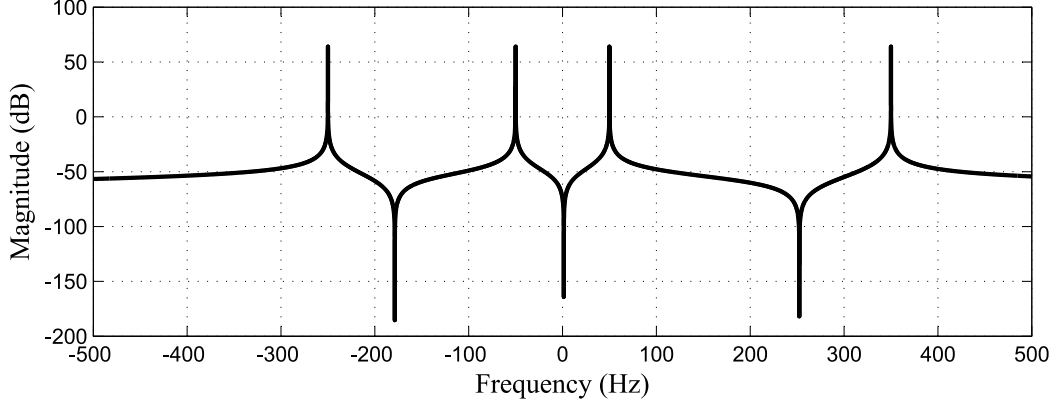


Figure 3.11: Synchronization MROGI bode transfer function [41].

As it can be appreciated, the transfer function of the MROGI structure, presents infinite gain for the interesting sequences and allowing independent gain selection for each sequence. In Fig. 3.12 the synchronization algorithm is applied over the *abc* voltage measurements of a real grid. It can be seen how, the +1 and -1 sequences are set with different gains in order to prioritize the short detection time for the first and accuracy for the second.

3.5. Multifrequency Current Control

Regarding to the control of VSCs, the current control have the objective to bring the actual currents, measured through current sensors, to the desired value of reference currents (control inputs). This control appears as the inner loop, and the input reference currents, are usually calculated by a previous outer loop.

In this context, multifrequency current control is in charge of, in addition to control FPS and FNS currents, also control the most common harmonic currents. The employment of a current control based on $\alpha\beta$ stationary reference frame was selected, avoiding the θ calculation and the consequent transformations. In order to perform the control of desired controlled frequencies, resonant controllers are selected for multifrequency, and concretely, ROGIs are selected in order to perform an independent control for each interesting sequence.

The error signal (E) is calculated as the difference between the total reference current ($\vec{i}_{\alpha\beta}^*$), including all sequences, and the total measured current ($\vec{i}_{\alpha\beta}$). This error signal passes through the cascade controller structure. The output is made up of the sum of

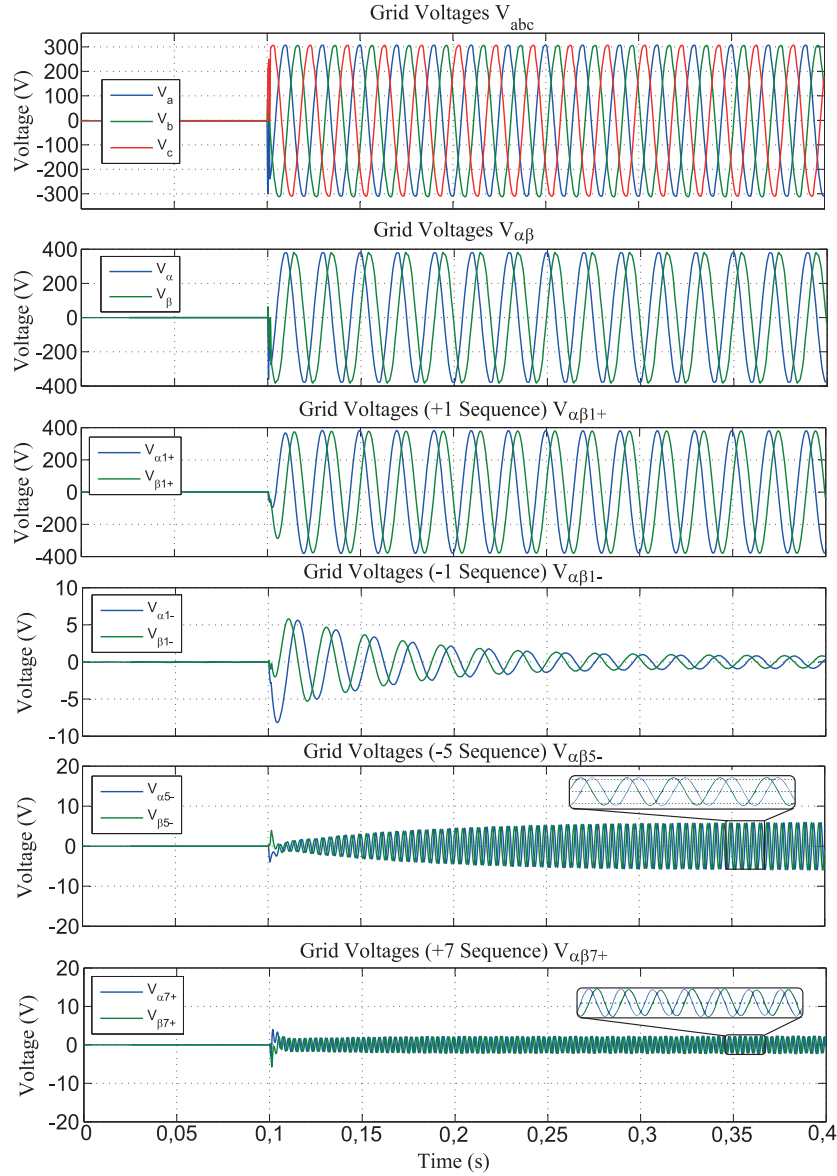


Figure 3.12: Three-phase grid voltage. The abc signals transformed into $\alpha\beta$ stationary reference frame and each one of the ROIGs outputs for sequence voltage detection. [41]

the different ROIGs outputs and the proportional part. This total output, which would be the voltage to apply at the AC side of the VSC, through the PWM generation block, results in:

$$v_{ref} = K_P \cdot E + \sum_{h \in H} \frac{K_{rh}}{s - jh\omega_0} \cdot E \quad (3.30)$$

where K_p is the proportional gain, ω_0 is the fundamental frequency, H stands for the different harmonic sequences to be controlled:

$$H = (+1, -1, -5, +7, -11, +13, \dots, h_m) \quad (3.31)$$

where h_m is the highest controlled harmonic order.

The plant to be controlled is composed by the filter of the VSC. This filter is usually an L filter, or a combination with a capacitor with small influence over the controlled frequencies (LC or LCL filter). The plant transfer function can be seen as

$$T(s) = \frac{\vec{i}_{\alpha\beta}(s)}{\vec{u}_{\alpha\beta}} = \frac{1}{R_f + L_f \cdot s} \quad (3.32)$$

which in discrete domain can be expressed as

$$T(z) = \frac{\frac{1}{R_1} \left(1 - e^{-\frac{R_1 T_s}{L_1}} \right) z^{-1}}{1 - e^{-\frac{R_1 T_s}{L_1}} z^{-1}} = \frac{b_{cc} \cdot z^{-1}}{1 - a_{cc} \cdot z^{-1}} = \frac{b_{cc}}{z - a_{cc}}. \quad (3.33)$$

Therefore, hereafter, $b_{cc} = \frac{1}{R_1} \left(1 - e^{-\frac{R_1 T_s}{L_1}} \right)$ and $a_{cc} = e^{-\frac{R_1 T_s}{L_1}}$. Assuming now, a graphical representation of the ROGI based multifrequency control system together with the plant transfer function is shown in Fig. 3.13.

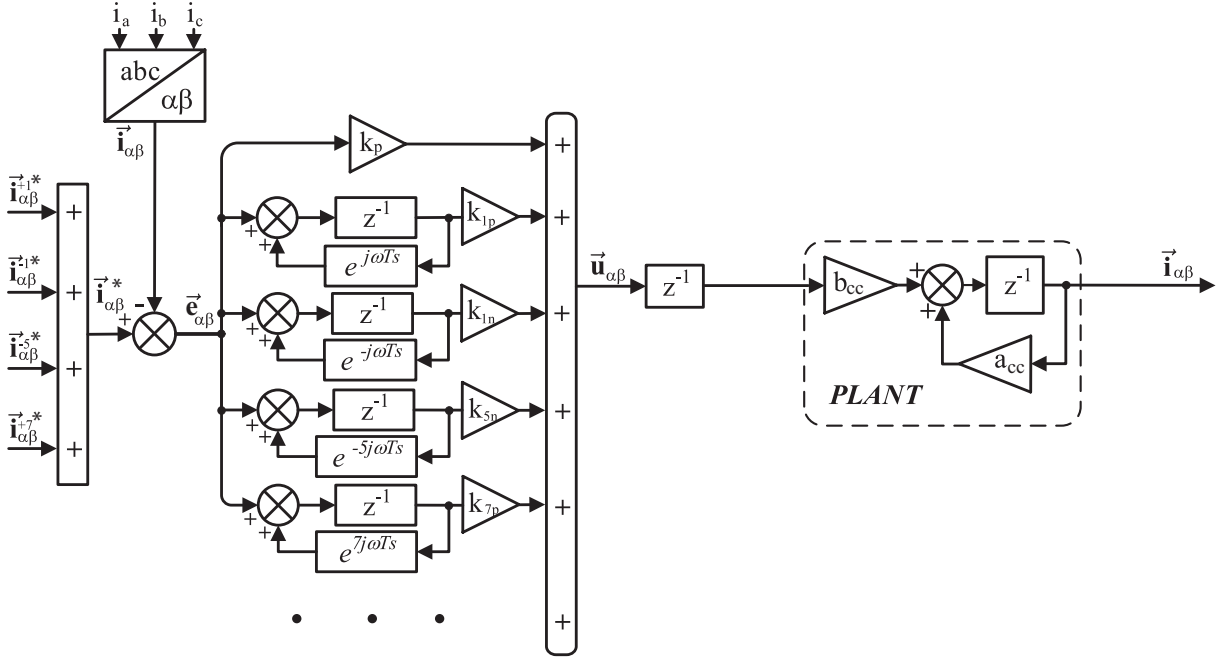


Figure 3.13: Control scheme with the proportional part and the ROGIs controllers for the most common harmonic sequences.

The transfer function of the controller in open loop expressed in the discrete domain is defined as:

$$\frac{\vec{u}_{\alpha\beta}(z)}{\vec{e}_{\alpha\beta}(z)} = k_p + \frac{k_{r1}}{z - e^{j\omega t}} + \frac{k_{rm1}}{z - e^{-j\omega t}} + \frac{k_{rm5}}{z - e^{-j5\omega t}} + \frac{k_{r7}}{z - e^{j7\omega t}}. \quad (3.34)$$

where $\vec{e}_{\alpha\beta}$ stands for the input error and $\vec{u}_{\alpha\beta}$ for the actuation voltage. Each one of the ROGIs has its own gain value (k_{rh}), namely k_{r1} , k_{rm1} , k_{rm5} , k_{r7} for the most common

harmonics in addition to the proportional gain k_p . This implies a total of five degrees of freedom for gain choosing. These gains would determine the location of the total five poles when the loop is closed with the plant (four ROGI controller poles and the plant pole).

Therefore, one of the main tasks of the multifrequency current controller is to correctly select these gains for achieving the stability and the dynamic desired.

3.5.1. Gains empirical adjustment

The first method for selecting the gains is empirical. It consists on calculating the output that comes out from the closed loop transfer function with the employment of different gains. The open loop transfer function of the previous described controller can be expressed as:

$$\frac{\vec{i}_{\alpha\beta}(s)}{\vec{e}_{\alpha\beta}(s)} = \left[k_p + \frac{k_{r1}}{s - j\omega_0} + \frac{k_{rm1}}{s + j\omega_0} + \frac{k_{rm5}}{s + j5\omega_0} + \frac{k_{r7}}{s - j7\omega_0} \right] \cdot \left[\frac{1}{Ls + R} \right]. \quad (3.35)$$

For the closed loop analysis, an approximation can be carried out for analysing the output when an input equal to the resonant frequency is applied. Therefore, when this occurs, the output of the rest of resonators could be neglected, resulting a closed loop transfer function expressed as:

$$\frac{\vec{i}_{\alpha\beta}^h(s)}{\vec{i}_{\alpha\beta}^{h*}(s)} = \frac{\left[k_p + \frac{k_{rh}}{s - jh\omega_0} \right] \left[\frac{1}{Ls + R} \right]}{1 + \left[k_p + \frac{k_{rh}}{s - jh\omega_0} \right] \left[\frac{1}{Ls + R} \right]} = \frac{(k_p)s + (k_{rh} - k_p(jh\omega_0))}{Ls^2 + (k_p - jh\omega_0 L + R)s + (k_{rh} - jk_p h\omega_0 - jRh\omega_0)}. \quad (3.36)$$

The difficulty of analysis of the obtained closed transfer function with a second order denominator with complex coefficient has lead to think on alternative approaches. In this context, it was decided to move to an empirical design method, where the design is directly carried out in discrete domain and taking into account the effect of all the different ROGIs at the same time. First, the value of k_p is decided by assigning a small gain to the rest of ROGI and by testing the output response obtained with a set of different proportional gains, as depicted in 3.14.a. Then, the preferred k_p is selected and a set of gains for the first ROGI are tested, while the rest of ROGIs are deactivated, in order to meet the FPS settling time requirements, as depicted in Fig. 3.14.b.

The same process continues for k_{rn1} and k_{rn5} in Fig. 3.14.c and 3.14.d. Finally, k_{r7} is selected among a set of gains in order to obtain the desired response for an input that contains all the different sequences, as depicted in Fig. 3.14.e.

Although this method is empirical, it allows to select the different gains while all the ROGIs are taken into account. The iterative designing method allows to set the desired

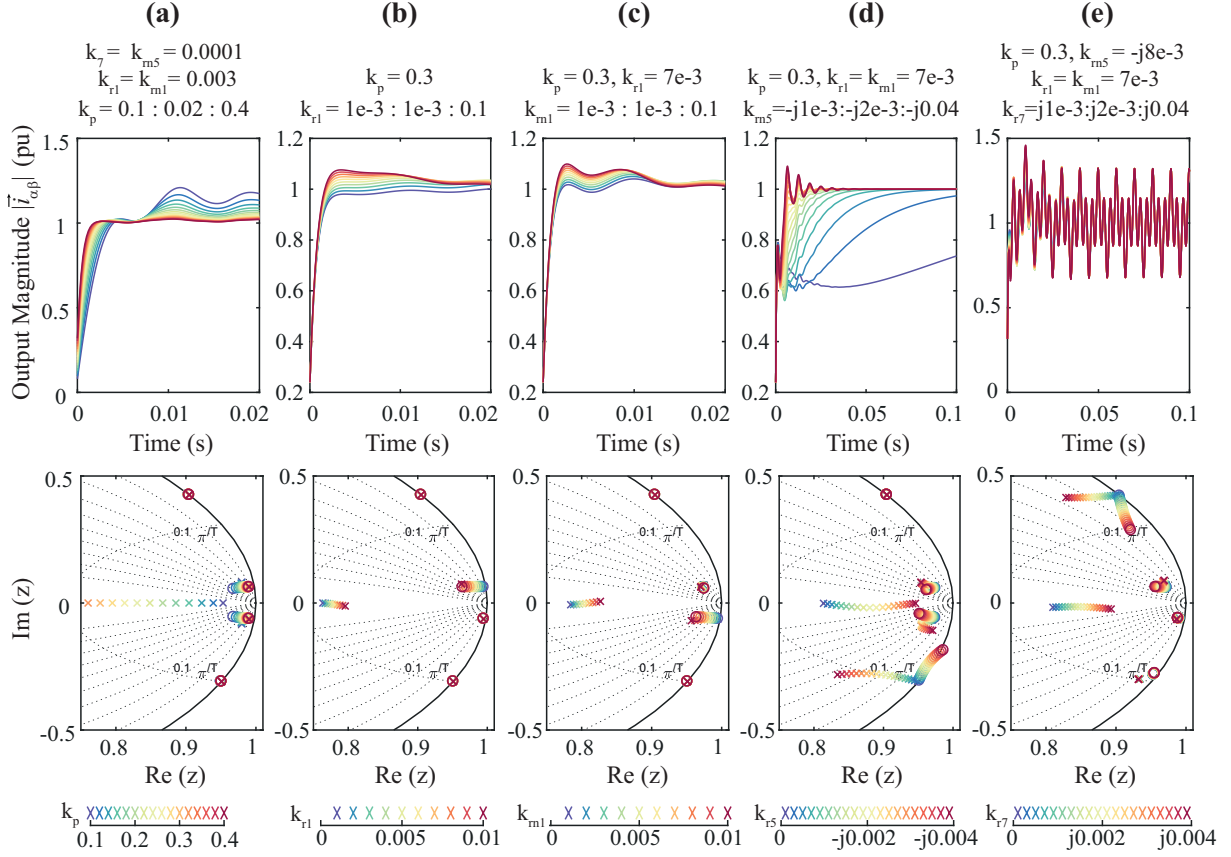


Figure 3.14: Closed loop transient response in discrete domain for the gains adjustment in an empirical way. (a) Different k_p are tested while a FPS input is applied. (b) k_p has been selected and different k_{r1} are tested while a FPS input is applied. (c) k_p and k_{r1} have been selected and different k_{rm1} are tested while a NFS input is applied. (d) k_p , k_{r1} and k_{rm1} have been selected and different k_{rm5} are tested while a 5th harmonic input is applied. (e) k_p , k_{r1} , k_{rm1} and k_{rm5} have been selected and different k_{r7} are tested while a combined input (with FPS, FNS, 5th and 7th harmonic sequenced) is applied.

settling time and controlling additional parameters as the overshoot. In this way the described method increases the tunable controller parameters in comparison with the following plant pole cancellation method.

3.5.2. Plant pole cancellation

The second method for selecting the gains is based on the plant pole cancellation strategy. This strategy is carried out in continuous domain and then, if desired, the result can be discretized. In open loop, the total transfer function including the controller and the plant, is described as:

$$\frac{\vec{i}_{\alpha\beta}(s)}{\vec{e}_{\alpha\beta}(s)} = \left[k_p + \frac{k_{r1}}{s - j\omega_0} + \frac{k_{rm1}}{s + j\omega_0} + \frac{k_{rm5}}{s + j5\omega_0} + \frac{k_{r7}}{s - j7\omega_0} \right] \cdot \left[\frac{1}{Ls + R} \right], \quad (3.37)$$

that could also be expressed as:

$$\frac{\vec{i}_{\alpha\beta}(s)}{\vec{e}_{\alpha\beta}(s)} = \frac{1}{L} \cdot \frac{k_p \cdot a \cdot b \cdot c \cdot d + k_{r1} \cdot b \cdot c \cdot d + k_{rn1} \cdot a \cdot c \cdot d + k_{rn5} \cdot a \cdot b \cdot d + k_{r7} \cdot a \cdot b \cdot c}{\underbrace{(s - j\omega_0)}_a \cdot \underbrace{(s + j\omega_0)}_b \cdot \underbrace{(s + j5\omega_0)}_c \cdot \underbrace{(s - j7\omega_0)}_d \cdot (s + R/L)}, \quad (3.38)$$

where it can be seen that the plant presents a pole at $s = -R/L$. The strategy carried out here is to set k_p as a combination of the rest of gains, in order to present a zero at the plant pole $s = -R/L$. Therefore, the numerator ($\text{num}(s)$) is evaluated for $-R/L$ and k_p is solved:

$$k_p = \frac{-k_{r1} \cdot B \cdot C \cdot D - k_{rn1} \cdot A \cdot C \cdot D - k_{rn5} \cdot A \cdot B \cdot D - k_{r7} \cdot A \cdot B \cdot C}{A \cdot B \cdot C \cdot D} \quad (3.39)$$

where $A = [(-R/L) - j\omega_0]$, $B = [(-R/L) + j\omega_0]$, $C = [(-R/L) + j5\omega_0]$ and $D = [(-R/L) - j7\omega_0]$. This equation could be simplified for obtaining the equation for the k_p calculation in pole plant cancellation:

$$k_p = -\frac{k_{r1}}{\underbrace{(-(R/L) - j\omega_0)}_A} - \frac{k_{rn1}}{\underbrace{(-(R/L) + j\omega_0)}_B} - \frac{k_{rn5}}{\underbrace{(-(R/L) + j5\omega_0)}_C} - \frac{k_{r7}}{\underbrace{(-(R/L) - j7\omega_0)}_D}. \quad (3.40)$$

If the worked out k_p is now substituted in (3.38), it can be splitted into four different summands:

$$\begin{aligned} \frac{\vec{i}_{\alpha\beta}(s)}{\vec{e}_{\alpha\beta}(s)} &= \frac{1}{L} \cdot \underbrace{\frac{-k_{r1} \cdot a \cdot b \cdot c \cdot d}{A} + k_{r1} \cdot b \cdot c \cdot d}_{y_1(s)/x_1(s)} + \frac{1}{L} \cdot \underbrace{\frac{-k_{rn1} \cdot a \cdot b \cdot c \cdot d}{B} + k_{rn1} \cdot a \cdot c \cdot d}_{y_2(s)/x_2(s)} \\ &\quad + \frac{1}{L} \cdot \underbrace{\frac{-k_{rn5} \cdot a \cdot b \cdot c \cdot d}{C} + k_{rn5} \cdot a \cdot b \cdot d}_{y_3(s)/x_3(s)} + \frac{1}{L} \cdot \underbrace{\frac{-k_{r7} \cdot a \cdot b \cdot c \cdot d}{D} + k_{r7} \cdot a \cdot b \cdot c}_{y_4(s)/x_4(s)}. \end{aligned} \quad (3.41)$$

Analysing the first one of the summands ($y_1(s)/x_1(s)$), it can be simplified as follows:

$$\frac{y_1(s)}{x_1(s)} = \frac{1}{L} \cdot \frac{-k_{r1} \cdot a \cdot b \cdot c \cdot d}{A} + k_{r1} \cdot b \cdot c \cdot d = \frac{1}{L \cdot A} \cdot k_{r1} \cdot \frac{A - a}{(a) \cdot (s + R/L)} = \frac{1}{R + jL\omega_0} \cdot \frac{k_{r1}}{s - j\omega_0}. \quad (3.42)$$

A similar process can be carried out with the other rest of summands ($y_2(s)/x_2(s)$, $y_3(s)/x_3(s)$, $y_4(s)/x_4(s)$). Therefore, the total open loop transfer function after the k_p

adjustment for the plant pole cancellation could be expressed as:

$$\frac{\vec{i}_{\alpha\beta}(s)}{\vec{e}_{\alpha\beta}(s)} = \frac{1}{R + jL\omega_0} \cdot \frac{k_{r1}}{s - j\omega_0} + \frac{1}{R - jL\omega_0} \cdot \frac{k_{rn1}}{s + j\omega_0} + \frac{1}{R - j5L\omega_0} \cdot \frac{k_{rn5}}{s + j5\omega_0} + \frac{1}{R + j7L\omega_0} \cdot \frac{k_{r7}}{s - j7\omega_0}. \quad (3.43)$$

As it can be appreciated in the previous equation, regardless of the input signal $x(s)$, the output signal in open loop would contain a part related with each one of the resonators. However, when the input signal frequency is close to the one of the resonator, the output signal is mainly composed by the output of the resonator for this frequency. In this context, in order to set the gains for obtaining the desired transient response, for analysing the response for a frequency that is found at a resonator, the output of the rest of resonators is neglected.

As an example, the behaviour of the system when a fifth harmonic signal wants to be controlled is studied. In this case, the approximated closed loop transfer function will be described as:

$$\frac{\vec{i}_{\alpha\beta}^{-5}(s)}{\vec{i}_{\alpha\beta}^{-5*}(s)} \approx \frac{\frac{k_{rn5}}{R - j5L\omega_0} \cdot \frac{1}{s + j5\omega_0}}{1 + \frac{k_{rn5}}{R - j5L\omega_0} \cdot \frac{1}{s + j5\omega_0}} = \frac{k' \cdot \frac{1}{s + j5\omega_0}}{1 + k' \cdot \frac{1}{s + j5\omega_0}} = \frac{k'}{s + (j5\omega_0) + k'}. \quad (3.44)$$

The output could be approximately defined as:

$$\vec{i}_{\alpha\beta}^{-5}(s) \approx \frac{k'}{s + (j5\omega_0) + k'} \cdot \frac{V}{s + j5\omega_0} = V \cdot \left[\frac{1}{s + j5\omega_0} - \frac{1}{s + j5\omega_0 + k'} \right] \quad (3.45)$$

and if it expressed in the time domain:

$$\vec{i}_{\alpha\beta}^{-5}(t) \approx V \cdot \left[e^{-j5\omega_0 t} - e^{-(j5\omega_0 + k')t} \right] = V \cdot e^{-j5\omega_0 t} \cdot \left[1 - e^{-k' \cdot t} \right] \quad (3.46)$$

where the settling time (t_{set}) can be worked out as:

$$t_{set} = \frac{4}{k'} \rightarrow k_{rn5} = \frac{4(R - j5L\omega_0)}{t_s}. \quad (3.47)$$

The described method for the multifrequency control design has been tested for a plant with an inductance of 750 μH . In this case, two tests have been carried out, one with the settling time for all the different gains have been set to 10 ms and another where the settling time is set to 30 ms. The different gains for each one of the cases are worked out with the previous equations (3.47) and (3.40), and their values are collected in Table 3.2.

Table 3.2: Controller Gains calculated for $t_{set} = 10$ ms and $t_{set} = 30$ ms.

Gain	$t_{set} = 10$ ms	$t_{set} = 30$ ms
k_p	1.2	0.4
k_{r1}	$9.42477796 + j 94.2477796$	$3.14159265 + j 31.4159265$
k_{rn1}	$9.42477796 - j 94.2477796$	$3.14159265 - j 31.4159265$
k_{rn5}	$9.42477796 - j 471.238898$	$3.14159265 - j 157.079632$
k_{r7}	$9.42477796 + j 659.734457$	$3.14159265 + j 219.911485$

The transient response when a rotating signal of the fifth harmonic is required at the reference is depicted in Fig. 3.15, for settling times of 10 and 30 ms. It can be appreciated the effect of the other controllers over the actuation signal that was previously neglected, and how it disappears with the time.

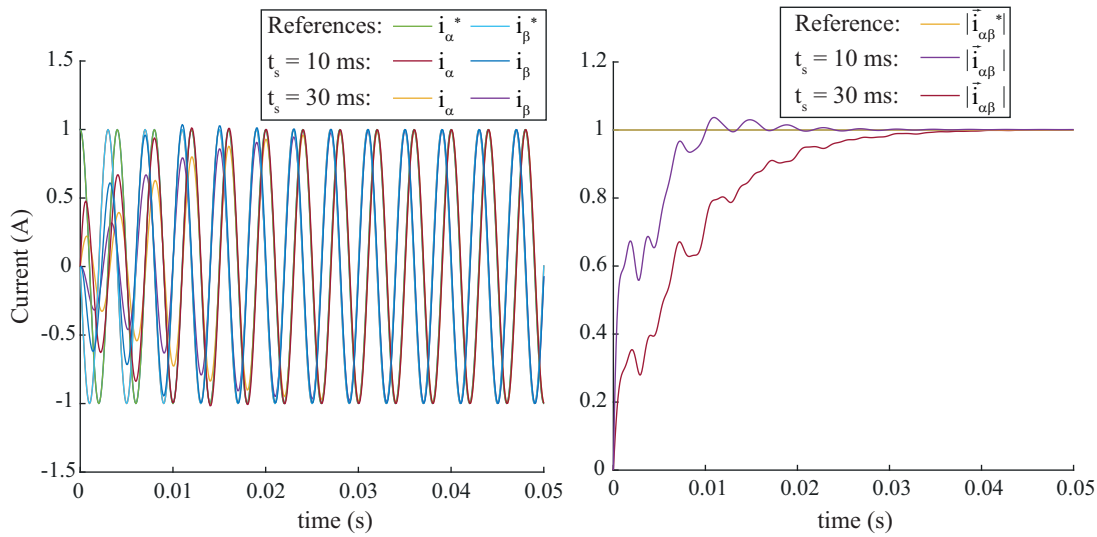


Figure 3.15: Transient response for the plant pole cancellation when a rotating input of the fifth harmonic is employed for settling times of 10 and 30 ms.

The location of the poles and zeros of the discretized closed loop system ($t_s = 100 \mu s$), when the controller with a settling time of 30 ms is employed, is depicted in Fig. 3.16. It can be appreciated that one of the zero has been placed over the plant pole, performing the plant pole cancellation.

Although the same settling time has been presented for the previous case, an independent settling time can be set for each one of the sequences. The different settling time assignment is usually interesting in order to relax the actuation over the harmonic sequences and avoid the actuator saturation. This is achieved by assigning a higher settling time for the harmonic components than for the FPS, as depicted in Fig. 3.17. These harmonic components demand a great actuation for low settling time values and in addition they are not as critical as the FPS one.

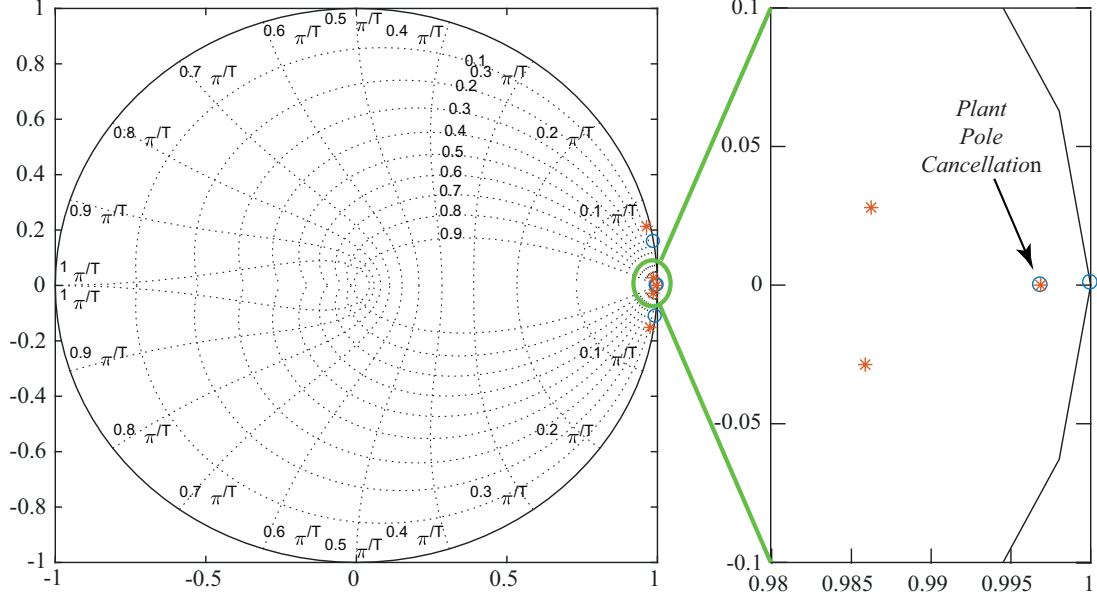


Figure 3.16: Zeros and Poles of the closed loop transfer function after the zero-pole matched discretization method by the employment of the plant pole cancellation method.

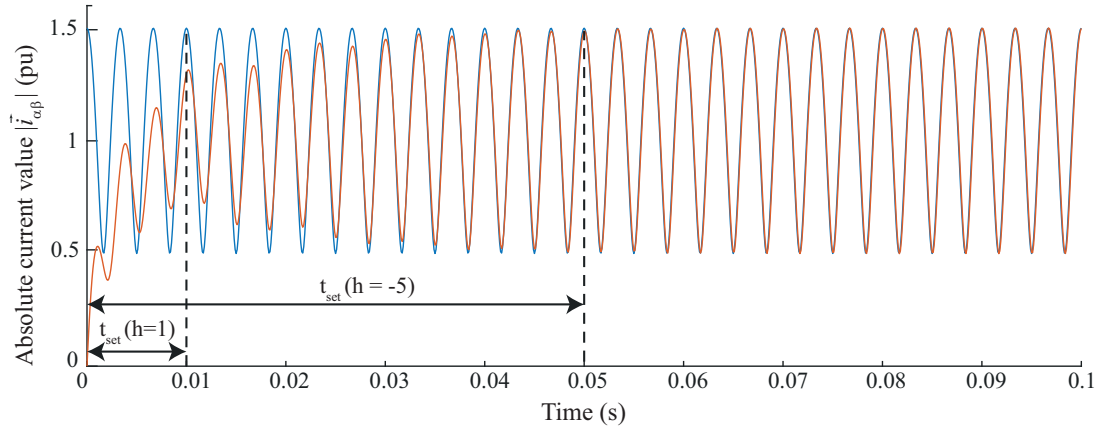


Figure 3.17: Closed loop transient response with an oscillating input (1 pu for +1 and 0.5 for -5 sequences). The settling times has been set as $t_{set} = 10\text{ms}$ for the FPS and $t_{set} = 50\text{ ms}$ for the rest of sequences.

3.5.3. Multifrequency control in state variables

As described in [31], the multifrequency controller in stationary $\alpha\beta$ reference frame, can be directly designed in the discrete time domain. In this way, the delay introduced by the DSP is taken into account in order to study the response of the controller and it is seen as an additional state of the system, as depicted in Fig. 3.18.

In the studied system, the delay is considered equal to the sampling time and the current vector $\vec{i}_{\alpha\beta}$ is also named as one of the states \vec{x}_a . In this way, if each ROGI's output is understood as an state, the system expression in state variable is described in (3.48) and (3.49).

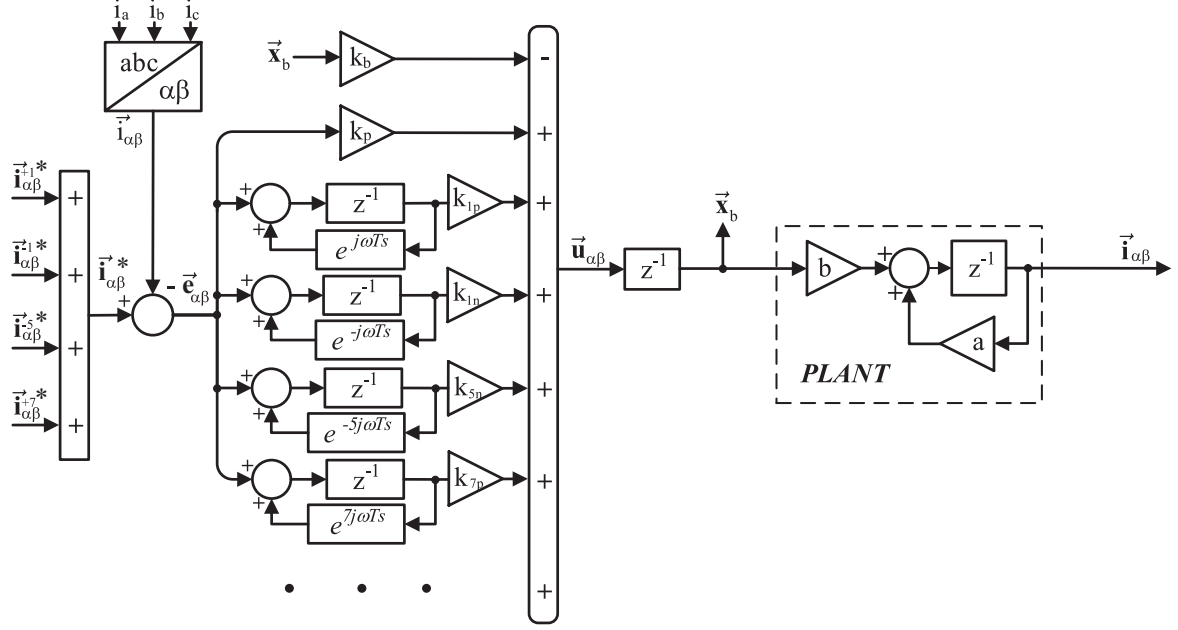


Figure 3.18: Multifrequency current control in state variables

$$\begin{bmatrix} \vec{x}_a(k+1) \\ \vec{x}_b(k+1) \\ \vec{x}_{1p}(k+1) \\ \vec{x}_{1n}(k+1) \\ \vec{x}_{5n}(k+1) \\ \vec{x}_{7p}(k+1) \end{bmatrix} = \underbrace{\begin{bmatrix} a_{cc} & b_{cc} & 0 & 0 & 0 & 0 \\ 0 & 0 & 0 & 0 & 0 & 0 \\ 1 & 0 & e^{j\omega_0 T_s} & 0 & 0 & 0 \\ 1 & 0 & 0 & e^{-j\omega_0 T_s} & 0 & 0 \\ 1 & 0 & 0 & 0 & e^{-j5\omega_0 T_s} & 0 \\ 1 & 0 & 0 & 0 & 0 & e^{j7\omega_0 T_s} \end{bmatrix}}_G \begin{bmatrix} \vec{x}_a(k) \\ \vec{x}_b(k) \\ \vec{x}_{1p}(k) \\ \vec{x}_{1n}(k) \\ \vec{x}_{5n}(k) \\ \vec{x}_{7p}(k) \end{bmatrix} + \underbrace{\begin{bmatrix} 0 \\ 1 \\ 0 \\ 0 \\ 0 \\ 0 \end{bmatrix}}_H \vec{u}_c^{\alpha\beta}(k). \quad (3.48)$$

$$y(k) = \underbrace{\begin{bmatrix} 1 & 0 & 0 & 0 & 0 & 0 \end{bmatrix}}_C \cdot \begin{bmatrix} \vec{x}_a(k) \\ \vec{x}_b(k) \\ \vec{x}_{1p}(k) \\ \vec{x}_{1n}(k) \\ \vec{x}_{5n}(k) \\ \vec{x}_{7p}(k) \end{bmatrix}. \quad (3.49)$$

The output of the controller is made up of the combined effect of the different states (\vec{x}_a , \vec{x}_b , \vec{x}_{1p} , \vec{x}_{1n} , \vec{x}_{5n} , \vec{x}_{7p}). Meanwhile, the total number of gains is composed by k_p , k_b and a gain for each resonant controller (typically k_{r1p} , k_{r1n} , k_{r5n} , k_{r7p}). The values of those gains determine the location of the poles in closed loop and therefore, they need to be carefully selected in order to get the desired stability and dynamic response.

3.5.3.1. Ackermann's Formula poles location

The place that the poles of the closed loop system take along the plane determines the stability, dynamic behaviour and required actuation vector. Once that the decision of where the poles want to be placed has been made, the vector gains K , can be worked out through the Ackermann's Formula [95].

The position of the poles of the closed loop system is determined by the characteristic polynomial (Δ):

$$\Delta(z) = \det(zI - G + HK) \quad (3.50)$$

Once that the position of the closed loop poles has been decided, the objective is to calculate the K matrix that bring the poles to the desired place. As complex gains are allowed, there is no constrain for positioning the poles. The characteristic equation, for the multifrequency control with six degrees of freedom can be written as:

$$\Delta(z) = (z - p_1)(z - p_2)(z - p_3)(z - p_4)(z - p_5)(z - p_6) \quad (3.51)$$

The Ackermann's formula establish that the vector gains can be worked out as:

$$K = [0 \ 0 \ \dots \ 0 \ 1] \mathcal{C}^{-1} \Delta(G) \quad (3.52)$$

where \mathcal{C} is the controllability matrix that can be defined as:

$$\mathcal{C} = \begin{bmatrix} H & GH & \dots & G^{m-1}H \end{bmatrix} \quad (3.53)$$

resulting in:

$$K = [0 \ 0 \ 0 \ 0 \ 0 \ 1] \begin{bmatrix} H & GH & G^2H & G^3H & G^4H & G^5H \end{bmatrix}^{-1} \cdot [(G - p_1)(G - p_2)(G - p_3)(G - p_4)(G - p_5)(G - p_6)] \quad (3.54)$$

3.5.3.2. Linear - quadratic regulator (LQR) gains adjustment

As the position of the poles is not easy to determine, different strategies appear that automatically tries to find the optimal position of the poles with the minimum cost. Linear-quadratic regulator (LQR) is an algorithm, which is able to calculate between all the possible gain matrix K , the one that minimizes the following quadratic cost function [96]:

$$J(u) = \sum_{n=1}^{\infty} (x[n]^T Q x[n] + u[n]^T R u[n]). \quad (3.55)$$

The LQR technique first find the solution for the Riccati equation, by solving S:

$$G^T S + S G - (S H) R^{-1} (H^T S) + Q = 0 \quad (3.56)$$

and then, the K matrix is calculated as:

$$K = R^{-1} (H^T S). \quad (3.57)$$

In this context, the matrices Q and R need to be defined in order to establish the weights for the cost function. As one of the main problems of the control design is to avoid the overmodulation, a smaller value is assigned to the Q matrix than to the R matrix. This technique also allows to design the control for controllers with a higher order and allowing the control of more harmonics.

As an example, controllers for the following most common harmonic components (-11 and +13) are added. Resulting in a 8×8 G matrix and a 8×1 H matrix:

$$G = \begin{bmatrix} a_{cc} & b_{cc} & 0 & 0 & 0 & 0 & 0 & 0 \\ 0 & 0 & 0 & 0 & 0 & 0 & 0 & 0 \\ 1 & 0 & e^{j\omega_0 T_s} & 0 & 0 & 0 & 0 & 0 \\ 1 & 0 & 0 & e^{-j\omega_0 T_s} & 0 & 0 & 0 & 0 \\ 1 & 0 & 0 & 0 & e^{-j5\omega_0 T_s} & 0 & 0 & 0 \\ 1 & 0 & 0 & 0 & 0 & e^{j7\omega_0 T_s} & 0 & 0 \\ 1 & 0 & 0 & 0 & 0 & 0 & e^{-j11\omega_0 T_s} & 0 \\ 1 & 0 & 0 & 0 & 0 & 0 & 0 & e^{j13\omega_0 T_s} \end{bmatrix} \quad H = \begin{bmatrix} 0 \\ 1 \\ 0 \\ 0 \\ 0 \\ 0 \\ 0 \\ 0 \end{bmatrix} \quad (3.58)$$

For this system, the position of 8 poles is needed to be found, and therefore LQR appears as a good solution. The values of Q and R are decided in order to reduce the actuator operation $\vec{u}_{\alpha\beta}$. For achieving this, the weights for the cost minimization function are set in order to give importance to $\vec{u}_{\alpha\beta}$:

$$Q = \begin{bmatrix} 0.001 & 0 & 0 & 0 & 0 & 0 & 0 & 0 \\ 0 & 0.001 & 0 & 0 & 0 & 0 & 0 & 0 \\ 0 & 0 & 0.001 & 0 & 0 & 0 & 0 & 0 \\ 0 & 0 & 0 & 0.001 & 0 & 0 & 0 & 0 \\ 0 & 0 & 0 & 0 & 0.001 & 0 & 0 & 0 \\ 0 & 0 & 0 & 0 & 0 & 0.001 & 0 & 0 \\ 0 & 0 & 0 & 0 & 0 & 0 & 0.001 & 0 \\ 0 & 0 & 0 & 0 & 0 & 0 & 0 & 0.001 \end{bmatrix} \quad R = [1] \quad (3.59)$$

With these premises, the worked out gains for a converter with an L filter of $750\mu H$ and an R of 0.0012Ω are the following:

$$K^T = \begin{bmatrix} 1.9862221 + j0.0027990 \\ 0.4876851 + j0.0028007 \\ 0.0753097 - j0.0150034 \\ 0.0767735 - j0.0015791 \\ 0.0325175 - j0.0695649 \\ -0.0152209 + j0.0752661 \\ -0.0635628 - j0.0430864 \\ -0.0757025 + j0.0128762 \end{bmatrix}. \quad (3.60)$$

The transient response of the controller system designed through the LQR technique is depicted in Fig. 3.19.a. The location of the poles and zeros is also depicted in Fig. 3.19.b.

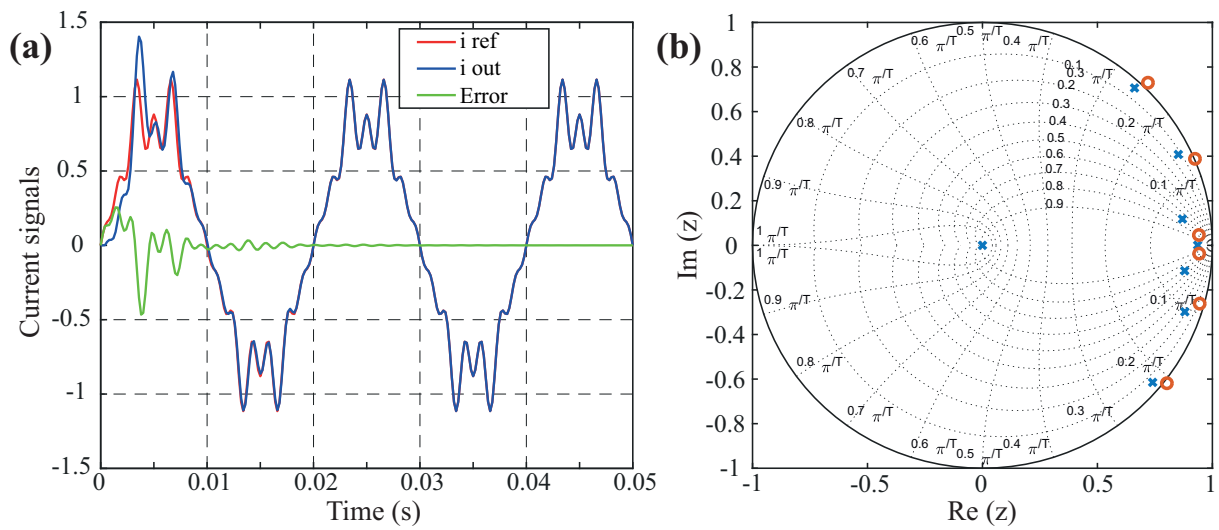


Figure 3.19: (a) Transient response of the multifrequency controller designed by the LQR technique ($t_{set} = 10$ ms) when an input (with FPS, NFS, 5^{th} , 7^{th} , 11^{th} and 13^{th} sequences) is applied at the input. (b) Poles and zeros location of the described controller

3.6. Conclusions

During this section the multifrequency control has been studied. From the basis of the three-phase signals up to the harmonic components analysis. In this regard, the fundamental and harmonic components are analysed in $\alpha\beta$ stationary reference frame and in dq synchronous reference frame.

Then, the grid synchronization and the grid harmonic detection are studied. In this context, a method based in ROGIs transfer function which is able to exclusively detect positive or negative sequences is proposed.

Finally, different techniques for the tuning of the multifrequency controllers are described in the last part of the chapter. Some of them as the zero-pole cancellation is for first time carried out in this thesis for the tuning of ROGIs.

Chapter 4

Instantaneous Active Power Multifrequency Control

4.1. Introduction

Between the different capabilities that a VSC can accomplish in a multifrequency control context, the most important ones can be divided in:

- Current THD reduction.
- Power ripple reduction.
- Harmonic voltage reduction.

The capability to satisfy any of the requirements is directly related with the selected current references that the current controller receives as input.

For the first situation, the harmonic reference currents are directly set to zero. The second capability for power ripple reduction is analysed along this chapter. Finally, third strategy is developed in [Chapter 6](#).

Assuming a non ideal grid, where unbalance and distortion can appear, the cross effect between the harmonic voltages and fundamental current components can imply fluctuations in the instantaneous power. As a solution, if harmonic currents are injected, the cross effect between the voltage and the harmonic current components could perform the compensation of the previously mentioned power oscillations.

4.2. The Instantaneous Power Theory

This section is focused on the p-q theory for three-wire three-phase systems. This theory analyses the instantaneous power in the time domain regardless of the voltage and current waveforms, and it has been extensively detailed in [\[97\]](#).

This theory was published with experimental verification in [98] and it is supported by previous work, as in [99] where it was shown that reactive power could be exchanged, without the necessity of storage elements. The term instantaneous reactive power was introduced in [100]. Furthermore, the inclusion of active ac power filters was described in [101].

The theory is developed in the $\alpha\beta\gamma$ stationary reference frame [102]. For three phase three wire system, the γ sequence can be neglected, and therefore three phase voltage (v_a, v_b, v_c) and currents (i_a, i_b, i_c) waveforms can be transformed to the $\alpha\beta$ stationary reference frame:

$$\begin{bmatrix} x_\alpha \\ x_\beta \end{bmatrix} = \frac{2}{3} \begin{bmatrix} 1 & \frac{1}{2} & -\frac{1}{2} \\ 0 & \frac{\sqrt{3}}{2} & -\frac{\sqrt{3}}{2} \end{bmatrix} \begin{bmatrix} x_a \\ x_b \\ x_c \end{bmatrix} \quad (4.1)$$

where x can be replaced for both, voltage or current.

The instantaneous active power, calculated from the three phase instantaneous values of phase voltages and line currents can be described as:

$$p(t) = v_a(t) \cdot i_a(t) + v_b(t) \cdot i_b(t) + v_c(t) \cdot i_c(t) \quad (4.2)$$

Meanwhile, by the employment of the Clarke transformation to $\alpha\beta$ (amplitude invariant), the instantaneous complex power (\vec{s}) can be defined as the product of the complex voltage vector ($\vec{v}_{\alpha\beta}$) and the conjugate of the current complex vector ($\vec{i}_{\alpha\beta}^*$).

$$\vec{s} = \frac{3}{2} (\vec{v}_{\alpha\beta} \cdot \vec{i}_{\alpha\beta}^*) = (p + jq) \quad (4.3)$$

Representing (4.3) in matrix form, it can be rewritten as

$$\begin{bmatrix} p \\ q \end{bmatrix} = \frac{3}{2} \begin{bmatrix} v_\alpha & v_\beta \\ -v_\beta & v_\alpha \end{bmatrix} \begin{bmatrix} i_\alpha \\ i_\beta \end{bmatrix}. \quad (4.4)$$

Furthermore, in a first approach to express the currents in relation with voltages and powers (real (p) and imaginary (q)), it can be written as

$$\begin{bmatrix} i_\alpha \\ i_\beta \end{bmatrix} = \frac{2}{3} \cdot \frac{1}{v_\alpha^2 + v_\beta^2} \begin{bmatrix} v_\alpha & v_\beta \\ v_\beta & -v_\alpha \end{bmatrix} \begin{bmatrix} p \\ q \end{bmatrix}. \quad (4.5)$$

This expression can be divided into two expressions regarding exclusively to the instantaneous real power (p) and to the instantaneous imaginary power (q)

$$\begin{bmatrix} i_\alpha \\ i_\beta \end{bmatrix} = \frac{2}{3} \cdot \frac{1}{v_\alpha^2 + v_\beta^2} \begin{bmatrix} v_\alpha & v_\beta \\ v_\beta & -v_\alpha \end{bmatrix} \left(\begin{bmatrix} p \\ 0 \end{bmatrix} + \begin{bmatrix} 0 \\ q \end{bmatrix} \right) = \begin{bmatrix} i_{\alpha p} \\ i_{\beta p} \end{bmatrix} + \begin{bmatrix} i_{\alpha q} \\ i_{\beta q} \end{bmatrix}. \quad (4.6)$$

Now, each current component ($i_{\alpha p}, i_{\beta p}, i_{\alpha q}, i_{\beta q}$) can be expressed as

$$i_{\alpha p} = \frac{2}{3} \cdot \frac{v_\alpha}{v_\alpha^2 + v_\beta^2} \cdot p \quad \text{and} \quad i_{\beta p} = \frac{2}{3} \cdot \frac{v_\beta}{v_\alpha^2 + v_\beta^2} \cdot p \quad (4.7)$$

$$i_{\alpha q} = \frac{2}{3} \cdot \frac{v_\beta}{v_\alpha^2 + v_\beta^2} \cdot q \quad \text{and} \quad i_{\beta q} = \frac{2}{3} \cdot \frac{-v_\alpha}{v_\alpha^2 + v_\beta^2} \cdot q \quad (4.8)$$

The active power associated with the two first current components is determined as:

$$p = \frac{3}{2} (v_\alpha \cdot i_{\alpha p} + v_\beta \cdot i_{\beta p}) = \frac{3}{2} \cdot \frac{2}{3} \cdot \frac{1}{v_\alpha^2 + v_\beta^2} (v_\alpha \cdot v_\alpha + v_\beta \cdot v_\beta) \cdot p = p \quad (4.9)$$

and therefore the active power associated with the second two currents components can be described as:

$$p = \frac{3}{2} (v_\alpha \cdot i_{\alpha q} + v_\beta \cdot i_{\beta q}) = \frac{3}{2} \cdot \frac{2}{3} \cdot \frac{1}{v_\alpha^2 + v_\beta^2} (v_\beta \cdot v_\alpha - v_\alpha \cdot v_\beta) \cdot q = 0 \quad (4.10)$$

Therefore, the components associated with imaginary power (q) is not involved in the energy exchange between the source and the load and hence, for the control or exchange of this kind of power, *Energy Storage System (ESS)* is therefore not required.

4.3. Harmonic Power Ripple

Assuming that the voltage at the PCC can show different non idealities, such as unbalance and distortion, the PCC voltage ($\vec{v}_{\alpha\beta}$) can be decomposed in all its different components:

$$\vec{v}_{\alpha\beta}(t) = \dots + \vec{v}_{\alpha\beta}^{-11}(t) + \vec{v}_{\alpha\beta}^{-5}(t) + \vec{v}_{\alpha\beta}^{-1}(t) + \vec{v}_{\alpha\beta}^{+1}(t) + \vec{v}_{\alpha\beta}^{+7}(t) + \vec{v}_{\alpha\beta}^{+13}(t) + \dots = \sum_{h \in H_s} \vec{v}_{\alpha\beta}^h(t) \quad (4.11)$$

where H stands for the subset of studied components $H_s = [\dots, -11, -5, -1, +1, +7, +13, \dots]$. In a similar way, the exchanged current with the grid ($\vec{i}_{\alpha\beta}$) can be divided in the different components:

$$\vec{i}_{\alpha\beta}(t) = \dots + \vec{i}_{\alpha\beta}^{-11}(t) + \vec{i}_{\alpha\beta}^{-5}(t) + \vec{i}_{\alpha\beta}^{-1}(t) + \vec{i}_{\alpha\beta}^{+1}(t) + \vec{i}_{\alpha\beta}^{+7}(t) + \vec{i}_{\alpha\beta}^{+13}(t) + \dots = \sum_{h \in H_s} \vec{i}_{\alpha\beta}^h(t) \quad (4.12)$$

Equations (4.11) and (4.12) can be expressed in dq synchronous reference frame through the Park transformation:

$$\vec{x}_{dq}^h(t) = \vec{x}_{\alpha\beta}^h(t)e^{-jh\omega_0 t}. \quad (4.13)$$

As described along the previous section, the instantaneous power ($\vec{s} = p + jq$) can be expressed as the instantaneous multiplication of $\alpha\beta$ voltage and the conjugate of the current vector. In synchronous dq reference frame with the different harmonic components, the instantaneous power can be expressed as:

$$\vec{s} = \frac{3}{2} \left(\sum_{h_1 \in H_s} \vec{v}_{dq}^{h_1} e^{jh_1\omega_0 t} \right) \left(\sum_{h_2 \in H_s} \vec{i}_{dq}^{h_2} e^{jh_2\omega_0 t} \right)^* \quad (4.14)$$

where $h_1 \in H_s$ and $h_2 \in H_s$ stand for the harmonic component which can be independent for voltage or current. Previous equation can be extended, resulting in a sum of different products (multiplication between the different voltage and current harmonic sequences). Regarding the general case, where h_1 and h_2 does not necessarily has the same value, the contribution of each product to the whole instantaneous power can be expressed as:

$$\vec{s}_{h_1 h_2} = \frac{3}{2} (\vec{v}_{dq}^{h_1} e^{jh_1\omega_0 t}) (\vec{i}_{dq}^{h_2} e^{jh_2\omega_0 t})^*. \quad (4.15)$$

At the same time, equation (4.15) can be split in the effect of the d and q components individually:

$$\vec{s}_{h_1 h_2} = \frac{3}{2} (v_d^{h_1} e^{jh_1\omega_0 t} + v_q^{h_1} e^{j(h_1\omega_0 t + \frac{\pi}{2})}) \cdot (i_d^{h_2} e^{-jh_2\omega_0 t} + i_q^{h_2} e^{-j(h_2\omega_0 t + \frac{\pi}{2})}). \quad (4.16)$$

If previous equation is now expanded, it results in a new one composed by four different summands, where each one of them can be seen as a phasor rotating at $(h_1 - h_2) \cdot \omega_0$

$$\vec{s}_{h_1 h_2} = \frac{3}{2} (v_d^{h_1} i_d^{h_2} e^{j(h_1-h_2)\omega_0 t} + v_d^{h_1} i_q^{h_2} e^{j((h_1-h_2)\omega_0 t - \frac{\pi}{2})} + v_q^{h_1} i_d^{h_2} e^{j((h_1-h_2)\omega_0 t + \frac{\pi}{2})} + v_q^{h_1} i_q^{h_2} e^{j(h_1-h_2)\omega_0 t}) \quad (4.17)$$

Hereafter, the rotating frequency of those summands is named as $k = h_1 - h_2$ and as it can be deduced from previous equations, it will be the power frequency ripple provoked by a voltage and current sequences. Previous equation can be rewritten in complex rectangular notation:

$$\vec{s}_{h_1 h_2} = \frac{3}{2} [(v_d^{h_1} i_d^{h_2} + v_q^{h_1} i_q^{h_2})(\cos(k\omega_0 t) + j \sin(k\omega_0 t)) + (v_d^{h_1} i_q^{h_2} - v_q^{h_1} i_d^{h_2})(\sin(k\omega_0 t) - j \cos(k\omega_0 t))] \quad (4.18)$$

Depending on the voltage and current harmonic sequences, k can adopt different values. Three particular cases can be highlighted and studied:

- No rotation: $k = 0$ ($h_1 = h_2$).
- Positive rotation: $k > 0$ ($h_1 > h_2$).
- Negative rotation: $k < 0$ ($h_1 < h_2$).

For the first case, where h_1 is equal to h_2 , k adopts zero value, which means that rotation is not produced. For that case, expanding Eq. 4.18 with $k = 0$, the two components $p(t)$ and $q(t)$ results into constant components:

$$\begin{bmatrix} P_0 \\ Q_0 \end{bmatrix} = \frac{3}{2} \begin{bmatrix} v_d^h & v_q^h \\ v_q^h & -v_d^h \end{bmatrix} \begin{bmatrix} i_d^h \\ i_q^h \end{bmatrix} \quad (4.19)$$

where harmonic sequence h substitutes both, voltage (h_1) and current (h_2) harmonic sequences. This first case is widely employed for the active or reactive power references achieved with the FPS current (i^{+1}) and the FPS voltage (v^{+1}). However, it also needs to be noted, that in addition to the cross effect of voltage and current FPS other components with the same rotating frequency contribute to this constant power values. Therefore, constant powers (P_0 and Q_0) also are influenced by the cross effect of NFS components (v^{-1} and i^{-1}) and harmonic components (v^{-5} and i^{-5} ; v^{+7} and i^{+7} ; ...).

The following cases describe the summands when the voltage (h_1) and current (h_2) sequences are not rotating at the same frequency, resulting in $k \neq 0$. As a consequence, in the next studied cases, their combination provokes ripple in p and q instantaneous powers.

It needs to be noted that from the instantaneous power theory, p and q , are the real and imaginary components of the complex \vec{s} power. It states that p and q belongs to the real numbers domain ($p \in \mathbb{R}$ and $q \in \mathbb{R}$). Therefore, the ripple harmonic sequence (k) provoked over p and q has a symmetrical effect over the positive and negative domain (real signals). Hence, in the two following cases k will be written as $|k|$, and it is divided in two different cases, when k is positive (second case) and when it is negative (third case).

The second case is suitable when h_1 is greater than h_2 and p and q components can be obtained from Eq. 4.18:

$$\begin{bmatrix} P_{|k|}^{cos} \\ P_{|k|}^{sin} \\ Q_{|k|}^{cos} \\ Q_{|k|}^{sin} \end{bmatrix} = \frac{3}{2} \begin{bmatrix} v_d^{h_1} & v_q^{h_1} \\ -v_q^{h_1} & v_d^{h_1} \\ v_q^{h_1} & -v_d^{h_1} \\ v_d^{h_1} & v_q^{h_1} \end{bmatrix} \begin{bmatrix} i_d^{h_2} \\ i_q^{h_2} \end{bmatrix}. \quad (4.20)$$

However, when k results in a negative number ($h_1 < h_2$), the p and q ripple components are governed by:

$$\begin{bmatrix} P_{|k|}^{cos} \\ P_{|k|}^{sin} \\ Q_{|k|}^{cos} \\ Q_{|k|}^{sin} \end{bmatrix} = \frac{3}{2} \begin{bmatrix} v_d^{h_1} & v_q^{h_1} \\ v_q^{h_1} & -v_d^{h_1} \\ v_q^{h_1} & -v_d^{h_1} \\ -v_d^{h_1} & -v_q^{h_1} \end{bmatrix} \begin{bmatrix} i_d^{h_2} \\ i_q^{h_2} \end{bmatrix}. \quad (4.21)$$

Previous analysis is suitable regardless of the number and order of harmonics. The employment of the synchronous reference frame makes possible to obtain a set of linear equations.

4.4. Current References Calculation for Power Ripple elimination

As described along the previous section, the appearance of harmonic voltage components at the voltage grid, provokes fluctuations in the delivered active and reactive powers. As the grid harmonics decrease their magnitude as their frequency increases, the main effect falls on the low frequency power ripple.

During this section, current references are calculated in order to reduce power ripple, which as detailed before is a desire that comes from different parts (clients and devices manufacturers) [103]. As explained during previous section, power oscillations are provoked by the combination between non fundamental voltage components (v_{-1} , v_{-5} , v_{+7} , v_{-11} , ...) and the fundamental current (i_{+1}). In the same way, if non fundamental currents are on purpose generated, power oscillations are also provoked by its combination with fundamental and harmonic voltage components (v_{+1} , v_{-1} , v_{-5} , v_{+7} , ...). These provoked power oscillations could compensate the undesired power oscillations and improve the power filtering.

First of all, it needs to be noticed that harmonic control implies a multifrequency control structure. The time consumption and the complexity level increases with the number of controlled frequencies. In this context, a decision usually needs to be made in order to select the controlled harmonics. Usually, the most critical harmonic sequences are selected for being controlled, and as the magnitude decreases with the frequency, -5 and +7 harmonic sequences are the ones typically selected.

Another important fact to take into account is that as described before, the power is the product of currents and voltages. Therefore, when voltages and currents are measured, if any kind of filter is applied (usually anti-aliasing), it is needed to carefully deal with the phase shifting at the different interesting frequencies. As depicted in Fig. 4.1.a, if an anti-aliasing filter is employed for acquisition, the cutoff frequency should be higher than the highest interesting frequency. Then, the phase shifting that appears for harmonic sequences (-5 & +7) is considerable and needs to be compensated.

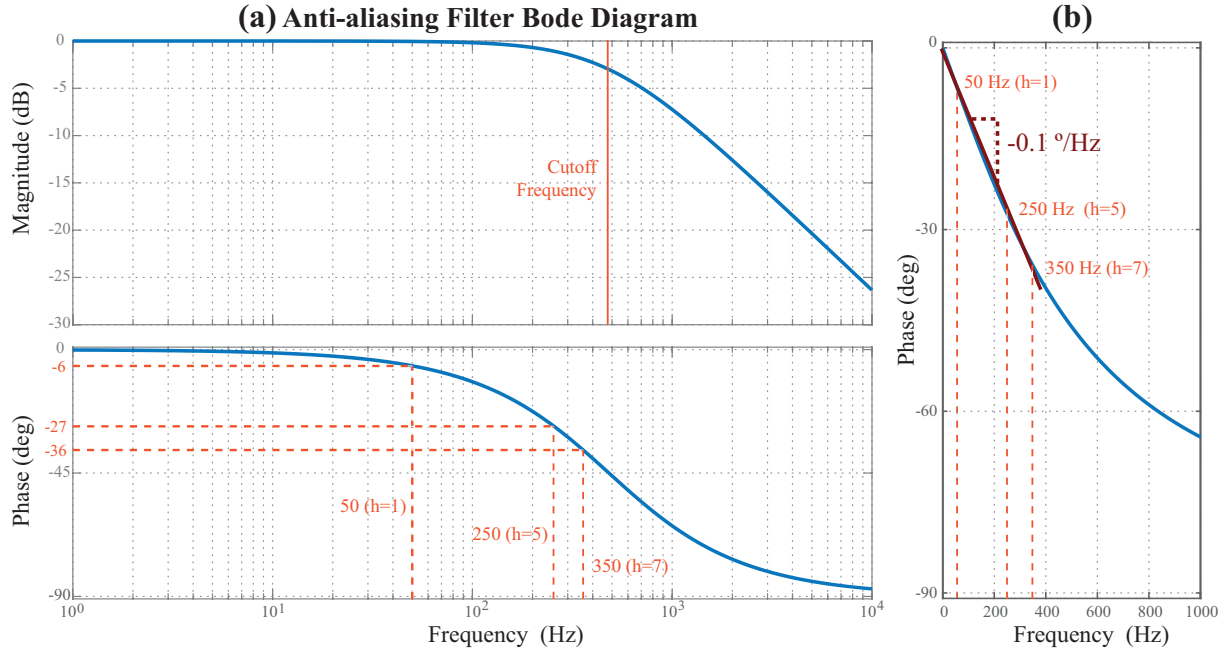


Figure 4.1: Anti-aliasing filter composed by a 100 Ω resistor and a 3.3 μF capacitor. It can be appreciated that in lower harmonic frequencies, the phase shifting can be linearised.

The compensation can be done by the multiplication of the measured variable by $e^{-j\theta_c}$, where θ_c is the phase delay provoked by the anti-aliasing filter.

$$x_{\alpha\beta}^h = \check{x}_{\alpha\beta}^h \cdot e^{-j\theta_c^h} \quad (4.22)$$

where $\check{x}_{\alpha\beta}^h$ is the obtained value (voltage or current) for the harmonic h after the anti-aliasing filter, and $x_{\alpha\beta}^h$ is the value obtained after the correction, that will be the one employed, hereafter. For knowing the value of θ_c^h , the filter can be theoretically described and the phase shifting for each interested frequency can be calculated offline and then pre-stored and corrected during the algorithm execution. In some cases, as in the one depicted in Fig. 4.1.b, composed by a 100 Ω resistor and a 3.3 μF capacitor, the phase shifting in the range of the studied harmonics ($f < 400$ Hz) varies linearly, and therefore, the phase variation slope can be worked out and applied for all the desired sequences:

$$\theta_c^h = h \cdot f_1 \cdot \theta_{slope} \quad (4.23)$$

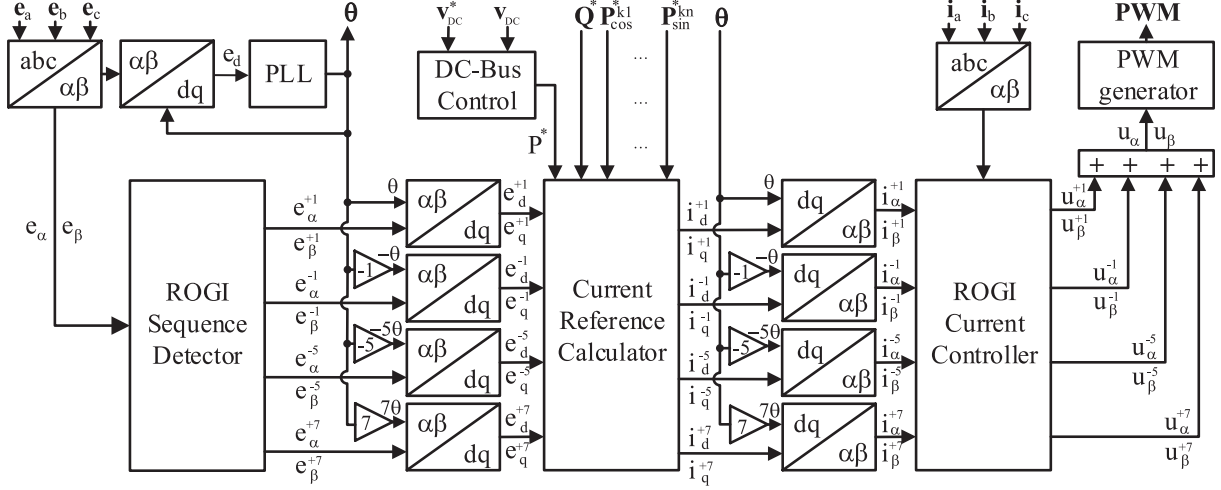


Figure 4.2: Graphical description of the whole system, including voltage sequence detector, *Current References Calculation (CRC)* method and current controller [58].

Once that the measurements have been properly corrected, the algorithm for reducing active power ripple can be carried out. The graphical description of the whole system can be seen in Fig. 4.2. First, the PCC voltage measurements (abc) are converted to the $\alpha\beta$ domain and the sequences are obtained. Then, each one of the interesting detected sequences are converted to the dq synchronous reference frame, all of them with $\theta = h \cdot \theta_{PLL}$. Then, the CRC is in charge of providing the current references to the current controller, for accomplishing the power requirements with the measured voltages. Current references are converted to $\alpha\beta$ and compared with the measured ones, the error is passed through the MROGI controller described in Section 3.5. Finally, the output is sent to the switches after proper modulation.

From the whole system, the CRC is the key part, regarding the required capability to be accomplished. Hereafter, four different strategies are analysed and compared.

- FPS current components (i_d^{+1}, i_q^{+1}) are employed, which can accomplish exclusively the active (P^*) and reactive (Q^*) power references.
- FPS and FNS current components ($i_d^{+1}, i_q^{+1}, i_d^{-1}, i_q^{-1}$) are employed, which is able to follow active (P^*) and reactive (Q^*) power references and eliminate one of the active power ripples (2nd).
- FPS, FNS and common harmonic current components ($i_d^{+1}, i_q^{+1}, i_d^{-1}, i_q^{-1}, i_d^{-5}, i_q^{-5}, i_d^{-7}, i_q^{-7}$) are employed, which is able to follow active (P^*) and reactive (Q^*) power references and eliminate up to three the active power ripples (2nd, 4th, 6th).
- Finally, the proposed method in this thesis, where also FPS, FNS and common harmonic current components ($i_d^{+1}, i_q^{+1}, i_d^{-1}, i_q^{-1}, i_d^{-5}, i_q^{-5}, i_d^{-7}, i_q^{-7}$) are employed. It is able to follow active (P^*) and reactive (Q^*) power references and eliminate instead of three active power ripples reduction (2nd, 4th, 6th), exclusively reduce the two most relevant

ones (2nd and 6th) and employ the remaining degree of freedom for THD currents reduction.

4.4.1. FPS current control without power ripple elimination

In the first current references calculation strategy, just the FPS (+1) current is calculated and controlled. In this way, as two independent currents are controlled (i_d^{+1}, i_q^{+1}), two degrees of freedom are available and as typically described, they can be employed in following P^* and Q^* references. This strategy is mathematically described in (4.24) and it is depicted in Fig. 4.3.

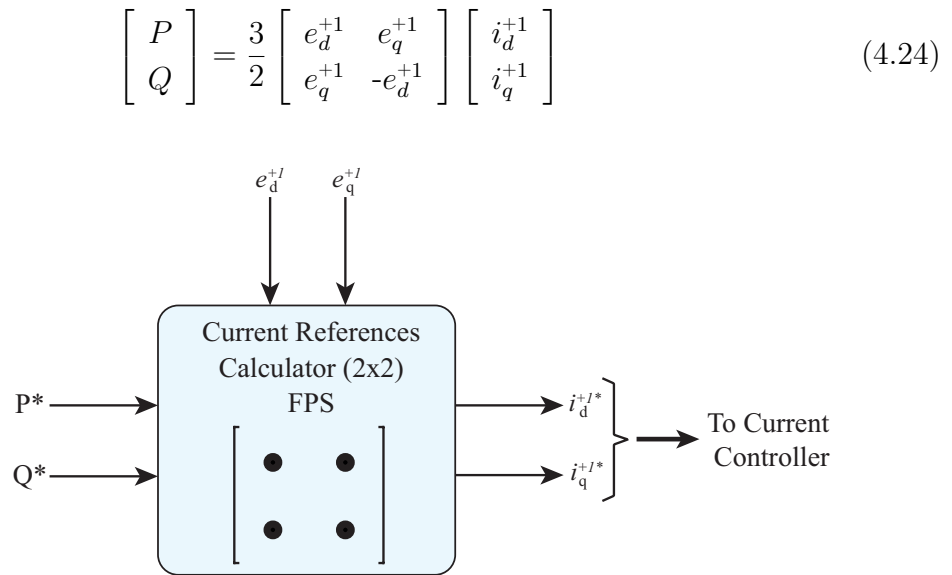


Figure 4.3: Current reference calculation for P and Q reference following, without controlling power fluctuations. Matrix of size 2×2 is required to calculate FPS (i_d^{+1}, i_q^{+1}) reference currents.

However, by the employment of this strategy, if harmonics or unbalance are present at the PCC voltage level, instantaneous active and reactive power would present ripple.

4.4.2. FPS and FNS current control for power ripple elimination

If any kind of unbalance is presented at the PCC (magnitude or phase) as previously described, it can be interpreted as FNS sequence. This voltage unbalance provokes a 2nd harmonic power ripple (combination of $h_1 = -1$ and $h_2 = 1$ in eq. 4.21). This ripple, as described before, is undesirable and its disappearance would be desirable. If unbalanced currents are injected (FNS), its combination with the voltage FPS component, also would result in power ripple at second harmonic (combination of $h_1 = +1$ and $h_2 = -1$ in eq. 4.20).

If the current reference is properly calculated, the first ripple could be compensated with the second one, resulting in a power ripple close to zero. In Fig. 4.4 and by the

employment of the inverse of 4×4 matrix described in (4.25), the current references for achieving P^* , Q^* and a zero second active power ripple (P_2^*) can be worked out, as seen in Fig. 4.4.

$$\begin{bmatrix} P \\ Q \\ P_2^c \\ P_2^s \end{bmatrix} = \frac{3}{2} \begin{bmatrix} e_d^{+1} & e_q^{+1} & e_d^{-1} & e_q^{-1} \\ e_q^{+1} & -e_d^{+1} & e_q^{-1} & -e_d^{-1} \\ e_d^{-1} & e_q^{-1} & e_d^{+1} & e_q^{+1} \\ e_q^{-1} & -e_d^{-1} & -e_q^{+1} & e_d^{+1} \end{bmatrix} \begin{bmatrix} i_d^{+1} \\ i_q^{+1} \\ i_d^{-1} \\ i_q^{-1} \end{bmatrix} \quad (4.25)$$

Figure 4.4: Current reference calculation for power ripple elimination (2nd). Matrix of size 4×4 is required to calculate FPS (i_d^{+1}, i_q^{+1}) and NFS (i_d^{-1}, i_q^{-1}) reference currents.

The topic of dealing with power ripple during voltage grid unbalances or voltage dips is of high interest and have been treated in recent works [104], [105], [106].

4.4.3. Multifrequency current control for power fluctuations elimination

In a similar way, as the previous currents calculation, the algorithm control can be extended for compensating the power ripple related with harmonics components. In an extension to the previous calculation, the appearance of harmonics components at the PCC voltage ($h_1 = [-5, +7, -11, +13, \dots]$), generates low order harmonic power ripples with the combination of current FPS. In a similar process as before, harmonic currents could be injected in order to provoke power ripples that makes the compensation of the first ones. Controlled harmonic currents are FPS, FNS, -5 and +7 sequences, and therefore 8 degrees of freedom are available ($i_d^{+1}, i_q^{+1}, i_d^{-1}, i_q^{-1}, i_d^{-5}, i_q^{-5}, i_d^{+7}, i_q^{+7}$). Two degrees of freedom are employed for following P^* and Q^* . For the complete elimination of each harmonic power component, two degrees of freedom are needed (P_{hs}, P_{hc}). This makes that with the controlled sequences a total of three harmonic components can be eliminated. In [107], different targets are pursued, and one of them is shown in Fig. 4.5, where the lower active power ripple harmonics are eliminated. For accomplishing that objective, the current calculation is obtained from the inverse of the 8×8 voltages matrix described in

eq. (4.26).

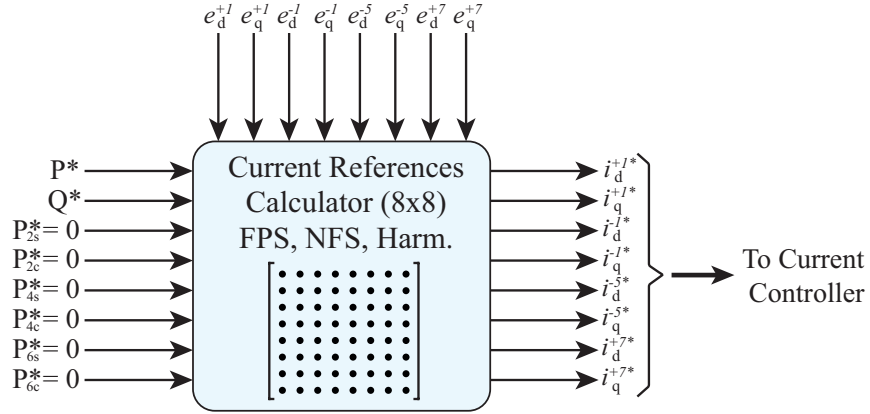


Figure 4.5: Current reference calculation for power ripple elimination (2nd, 4th, 6th). Matrix of size 8×8 is required to calculate FPS (i_d^{+1}, i_q^{+1}), NFS (i_d^{-1}, i_q^{-1}) and harmonic ($i_d^{+5}, i_q^{+5}, i_d^{+7}, i_q^{+7}$) reference currents.

$$\begin{bmatrix} P \\ Q \\ P_2^c \\ P_2^s \\ P_4^c \\ P_4^s \\ P_6^c \\ P_6^s \end{bmatrix} = \frac{3}{2} \begin{bmatrix} e_d^{+1} & e_q^{+1} & e_d^{-1} & e_q^{-1} & e_d^{+5} & e_q^{+5} & e_d^{+7} & e_q^{+7} \\ e_q^{+1} & -e_d^{+1} & e_q^{-1} & -e_d^{-1} & e_q^{+5} & -e_d^{+5} & e_q^{+7} & -e_d^{+7} \\ e_d^{-1} & e_q^{-1} & e_d^{+1} & e_q^{+1} & 0 & 0 & 0 & 0 \\ e_q^{-1} & -e_d^{-1} & -e_q^{+1} & e_d^{+1} & 0 & 0 & 0 & 0 \\ 0 & 0 & e_d^{+5} & e_q^{+5} & e_d^{-1} & e_q^{-1} & 0 & 0 \\ 0 & 0 & e_q^{+5} & -e_d^{+5} & -e_q^{-1} & e_d^{-1} & 0 & 0 \\ e_d^{+5}+e_q^{+7} & e_q^{+5}+e_d^{+7} & 0 & 0 & e_d^{+1} & e_q^{+1} & e_d^{+1} & e_q^{+1} \\ e_q^{+5}-e_d^{+7} & e_d^{+5}-e_q^{+7} & 0 & 0 & -e_q^{+1} & e_d^{+1} & e_q^{+1} & -e_d^{+1} \end{bmatrix} \begin{bmatrix} i_d^{+1} \\ i_q^{+1} \\ i_d^{-1} \\ i_q^{-1} \\ i_d^{+5} \\ i_q^{+5} \\ i_d^{+7} \\ i_q^{+7} \end{bmatrix} \quad (4.26)$$

However, although the three active power harmonic ripples can be reduced, it implies an increment of the injected harmonic currents. This effect is totally undesirable and implies the harmful effect that is also regulated by the standards [108]. In order to perform an optimization over the previous algorithm, a novel current references calculation technique that reduces the most important ripple components while injects the minimum current THD was proposed in [58].

4.5. CRC for Power Ripple elimination with THD optimization

During previous section, the main strategies depending on the number of controlled sequences were analysed. Strategies for exclusively FPS (2×2), with addition of FNS (4×4) and with the addition of harmonics sequences (-5 and +7 with 8×8) were shown. The last one is able to eliminate the three power ripple at the lowest frequencies (2nd, 4th, 6th). However, the amount of harmonic currents that is injected to the grid is really high, which implies difficulties to accomplish it in a way that meets the standards. In

this context, a new strategy is proposed and detailed during this section, where the least important ripple component of the reduced ones is released, and now the new available degrees of freedom are employed for reducing the THD [58]. The contribution detailed along this section has been published in [58].

The first step is to identify which power ripple components are the most important. In Table 4.1, the power ripple harmonic ($k = h_1 - h_2$) produced by the cross effect of coupling between different voltage and current harmonics are shown. In the table, the warmer colors are related with those components with higher magnitude (being +1 the highest). Then, the power ripple k for each two sequences is expressed, and again, the contribution of each summand is graphically expressed with warm colors.

Table 4.1: Power ripple from combination of different voltage and current sequences

Voltage (h_1) \ Current (h_2)	+1	-1	-5	+7	-11	+13
+1	0	+2	+6	-6	+12	-12
-1	-2	0	+4	-8	+10	-14
-5	-6	-4	0	-12	+6	-18
+7	+6	+8	+12	0	+18	-6
-11	-12	-10	-6	-18	0	-24
+13	+12	+14	+18	+6	+24	0

As it can be appreciated, the most important power harmonic ripple result from the combination of a non-fundamental sequence with the FPS (+1). It can be noted, that the enormous value of FPS, makes that second and sixth power ripples are generally more important than the rest (fourth, eighth and twelfth) that can be neglected.

Therefore, in the novel strategy, the two components that imply the greatest contribution to the ripple are reduced to zero (P_{2s} , P_{2c} , P_{6s} , P_{6c}). Then, the two released degrees of freedom will adopt a new functionality, from reducing the fourth harmonic ripple (P_{4s} , P_{4c}), to find the minimum *Harmonic Distortion* (HD) for the controlled currents. The HD provoked by the controlled harmonic currents (-5 and +7) can be described as:

$$HD = (i_d^{-5})^2 + (i_q^{-5})^2 + (i_d^{+7})^2 + (i_q^{+7})^2. \quad (4.27)$$

As expressed before, (4.27) wants to be minimized. Firstly, (4.26) can be rewritten, releasing P_4^c and P_4^s

$$\begin{bmatrix} P \\ Q \\ P_2^c \\ P_2^s \\ P_6^c \\ P_6^s \end{bmatrix} = \frac{3}{2} \begin{bmatrix} e_d^{+1} & e_q^{+1} & e_d^{-1} & e_q^{-1} & e_d^5 & e_q^5 & e_d^7 & e_q^7 \\ e_q^{+1} & -e_d^{+1} & e_q^{-1} & -e_d^{-1} & e_q^5 & -e_d^5 & e_q^7 & -e_d^7 \\ e_d^{-1} & e_q^{-1} & e_d^{+1} & e_q^{+1} & 0 & 0 & 0 & 0 \\ e_q^{-1} & -e_d^{-1} & -e_q^{+1} & e_d^{+1} & 0 & 0 & 0 & 0 \\ e_d^5 + e_q^7 & e_q^5 + e_d^7 & 0 & 0 & e_d^{+1} & e_q^{+1} & e_d^{+1} & e_q^{+1} \\ e_q^5 - e_d^7 & e_d^7 - e_q^5 & 0 & 0 & -e_q^{+1} & e_d^{+1} & e_q^{+1} & -e_d^{+1} \end{bmatrix} \begin{bmatrix} i_d^{+1} \\ i_q^{+1} \\ i_d^{-1} \\ i_q^{-1} \\ i_d^{-5} \\ i_q^{-5} \\ i_d^{-7} \\ i_q^{-7} \end{bmatrix} \quad (4.28)$$

where, the non-fundamental current components can be expressed in terms of known values and the FPS current components (i_d^{+1} and i_q^{+1}):

$$\underbrace{\begin{bmatrix} i_d^{-1} \\ i_q^{-1} \\ i_d^{-5} \\ i_q^{-5} \\ i_d^{-7} \\ i_q^{-7} \end{bmatrix}}_{I_{6 \times 1}} = \underbrace{\begin{bmatrix} e_d^{-1} & e_q^{-1} & e_d^5 & e_q^5 & e_d^7 & e_q^7 \\ e_q^{-1} & -e_d^{-1} & e_q^5 & -e_d^5 & e_q^7 & -e_d^7 \\ e_d^{+1} & e_q^{+1} & 0 & 0 & 0 & 0 \\ -e_q^{+1} & e_d^{+1} & 0 & 0 & 0 & 0 \\ 0 & 0 & e_d^{+1} & e_q^{+1} & e_d^{+1} & e_q^{+1} \\ 0 & 0 & -e_q^{+1} & e_d^{+1} & e_q^{+1} & -e_d^{+1} \end{bmatrix}^{-1}}_{M_{6 \times 6}} \left(\frac{2}{3} \underbrace{\begin{bmatrix} P \\ Q \\ P_2^c \\ P_2^s \\ P_6^c \\ P_6^s \end{bmatrix}}_{S_{6 \times 1}} - \underbrace{\begin{bmatrix} e_d^{+1} \\ e_q^{+1} \\ e_d^{-1} \\ e_q^{-1} \\ e_d^5 + e_q^7 \\ e_q^5 - e_d^7 \end{bmatrix}}_{M_{6 \times 1b}} i_d^{+1} - \underbrace{\begin{bmatrix} e_q^{+1} \\ -e_d^{+1} \\ e_q^{-1} \\ -e_d^{-1} \\ e_q^5 + e_d^7 \\ e_d^7 - e_q^5 \end{bmatrix}}_{M_{6 \times 1c}} i_q^{+1} \right) \quad (4.29)$$

Now, (4.29) can be also written as a more general expression, with constant part, and two coefficient matrix for i_d^{+1} and i_q^{+1} :

$$I_{6 \times 1} = A_{6 \times 1} + B_{6 \times 1} \cdot i_d^{+1} + C_{6 \times 1} \cdot i_q^{+1} \quad (4.30)$$

where the constant part is $A_{6 \times 1} = 2/3 \cdot M_{6 \times 6}^{-1} \cdot S_{6 \times 1}$ and the coefficient matrix for i_d^{+1} and i_q^{+1} are $B_{6 \times 1} = -M_{6 \times 6}^{-1} \cdot M_{6 \times 1b}$ and $C_{6 \times 1} = -M_{6 \times 6}^{-1} \cdot M_{6 \times 1c}$, respectively. Each current component (each element of $I_{6 \times 1}$) can be described as

$$i_k = a_k + b_k i_d^{+1} + c_k i_q^{+1} \quad (4.31)$$

where a_k , b_k and c_k ($k = \{1 \dots 6\}$) are each one of the corresponding indexed values of $A_{6 \times 1}$, $B_{6 \times 1}$ and $C_{6 \times 1}$ matrices. Then, previous equation (4.27) can be rewritten in terms of elements of (4.31):

$$HD = \sum_{k=3}^6 \left(a_k + b_k i_d^{+1} + c_k i_q^{+1} \right)^2. \quad (4.32)$$

As it has been stated before, the objective of the proposed reference calculation strategy

is to minimize the HD. Therefore, the local minimums and maximums can be found with the partial derivations of (4.32) with respect to i_d^{+1} and to i_q^{+1} :

$$\frac{\partial HD}{\partial i_d^{+1}} = \sum_{k=3}^6 2b_k (a_k + b_k i_d^{+1} + c_k i_q^{+1}) = 0 \quad (4.33)$$

$$\frac{\partial HD}{\partial i_q^{+1}} = \sum_{k=3}^6 2c_k (a_k + b_k i_d^{+1} + c_k i_q^{+1}) = 0 \quad (4.34)$$

For knowing now if (4.33) and (4.34) state for a minimum or a maximum, the second derivatives are worked out:

$$\frac{\partial^2 HD}{\partial (i_d^{+1})^2} = \sum_{k=3}^6 2(b_k)^2 \quad (4.35)$$

$$\frac{\partial^2 HD}{\partial (i_q^{+1})^2} = \sum_{k=3}^6 2(c_k)^2 \quad (4.36)$$

where they would always result in a positive value, which implies that when (4.33) and (4.34) are equalled to zero, a minimum THD is found. Besides, as the equation system composed by (4.33) and (4.34) are of first order, just one solution (minimum) can be found, which implies that the local minimum found is an absolute minimum.

Therefore, the two new equations (4.33) and (4.34), can take the place leaved by the ones employed for the reduction of the fourth order ripple. The new proposed system is depicted in Fig. 4.6 and the new optimized references calculations are expressed in (4.37).

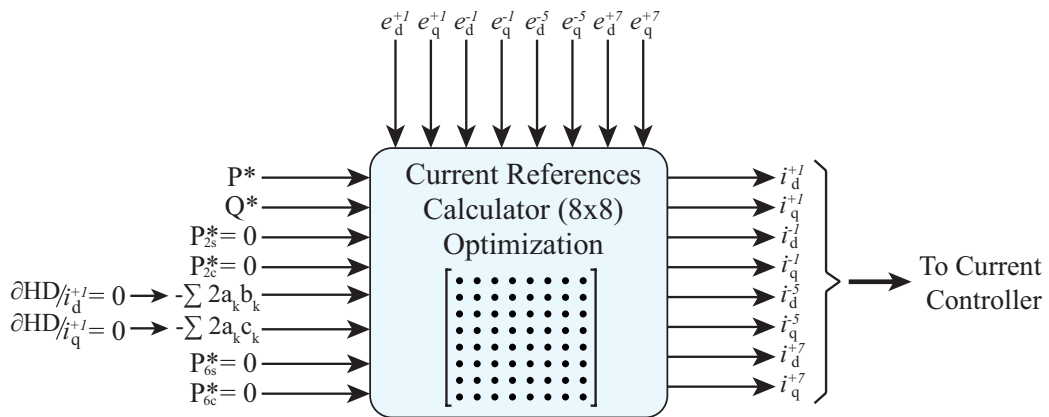


Figure 4.6: Current reference calculation for the most critical power ripple elimination (2nd, 6th) and THD reduction. Matrix of size 8×8 is required to calculate FPS (i_d^{+1}, i_q^{+1}), NFS (i_d^{-1}, i_q^{-1}) and harmonic ($i_d^{-5}, i_q^{-5}, i_d^{+7}, i_q^{+7}$) reference currents.

$$\begin{bmatrix} P \\ Q \\ P_2^c \\ P_2^s \\ -\sum 2a_k b_k \\ -\sum 2a_k c_k \\ P_6^c \\ P_6^s \end{bmatrix} = \frac{3}{2} \begin{bmatrix} e_d^{+1} & e_q^{+1} & e_d^{-1} & e_q^{-1} & e_d^5 & e_q^5 & e_d^7 & e_q^7 \\ e_q^{+1} & -e_d^{+1} & e_q^{-1} & -e_d^{-1} & e_q^5 & -e_d^5 & e_q^7 & -e_d^7 \\ e_d^{-1} & e_q^{-1} & e_d^{+1} & e_q^{+1} & 0 & 0 & 0 & 0 \\ e_q^{-1} & -e_d^{-1} & -e_q^{+1} & e_d^{+1} & 0 & 0 & 0 & 0 \\ \sum 2b_k^2 & \sum 2b_k c_k & 0 & 0 & 0 & 0 & 0 & 0 \\ \sum 2b_k c_k & \sum 2c_k^2 & 0 & 0 & 0 & 0 & 0 & 0 \\ e_d^5 + e_d^7 & e_q^5 + e_q^7 & 0 & 0 & e_d^{+1} & e_q^{+1} & e_d^{+1} & e_q^{+1} \\ e_q^5 - e_q^7 & e_d^7 - e_d^5 & 0 & 0 & -e_q^{+1} & e_d^{+1} & e_q^{+1} & -e_d^{+1} \end{bmatrix} \begin{bmatrix} i_d^{+1} \\ i_q^{+1} \\ i_d^{-1} \\ i_q^{-1} \\ i_d^{-5} \\ i_q^{-5} \\ i_d^{+7} \\ i_q^{+7} \end{bmatrix} \quad (4.37)$$

4.6. Simulation Results

In order to test the proposed reference currents calculation method a simulation environment is employed. The simulated system is composed by a NPC converter connected to the grid through an LC filter ($L = 750 \mu\text{H}$ and $C = 100\mu\text{F}$). The sampling time is equal $200 \mu\text{s}$ and the switching frequency equal to 5 kHz . For having power oscillations, the grid is set distorted with an FNS of 0.5% ($h = -1$) and 5% and 2% for the fifth ($h=-5$) and seventh ($h=+7$) components, respectively. The different parameters for the simulation have been collected in Table 4.2.

Table 4.2: Power oscillation control: simulation parameters description

Parameter category	Parameter	Parameter Value
Grid Voltage	Grid frequency (f_1)	50 Hz
	FPS 230 V ($h=+1$)	1.00 pu
	FNS ($h=-1$)	0.005 pu
	harmonic sequence ($h=-5$)	0.05 pu
	harmonic sequence ($h=+7$)	0.02 pu
Filter	Inductance (L)	750 μH
	Capacitor (C)	100 μF
Control references	DC-Bus voltage	750 V
	Q reference	35 kVAr
Frequencies	Sampling frequency (f_s)	5 kHz
	Switching frequency (f_{sw})	5 kHz

The test consists on switching the current references calculation algorithm between the different previously described ones in Section 4.4 and the one proposed in Section 4.5. The grid distortion previously described implies that if it is not compensated, power oscillation will appear. As depicted in Fig. 4.7 when just the fundamental frequency is taken into account (2x2 and 4x4), a sixth harmonic fluctuation appears in the instantaneous active power. Meanwhile, if the (8x8) matrix is employed, the power oscillation at the sixth harmonic is reduced.

In the same way, the reduction of active power oscillations also imply the reduction over the dc-bus voltage. The FFT for the dc-bus voltage is shown in 4.8.

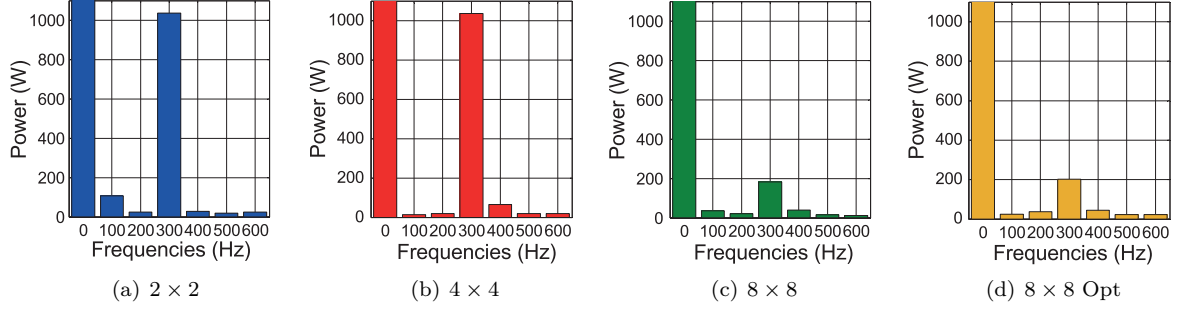


Figure 4.7: FFT of instantaneous active power with the different methods of current references calculation.

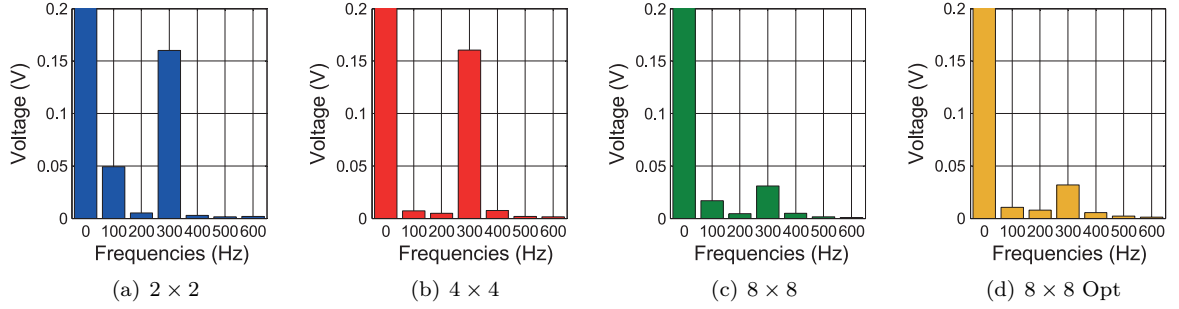


Figure 4.8: FFT of dc-bus voltage with the different methods of current references calculation.

As previously stated, the benefit of reducing those harmonic components in instantaneous active power and in dc-bus voltage presents two disadvantages. The first disadvantage is the increment of the computational runtime. The second one is that in order to eliminate these power and dc-bus oscillations, the injection of harmonic currents is required. With the optimization presented the most critical components (2^{nd} and 6^{th}) are reduced with the minimum delivered THD. The fundamental and harmonic components delivered with each method are shown in Fig. 4.9.

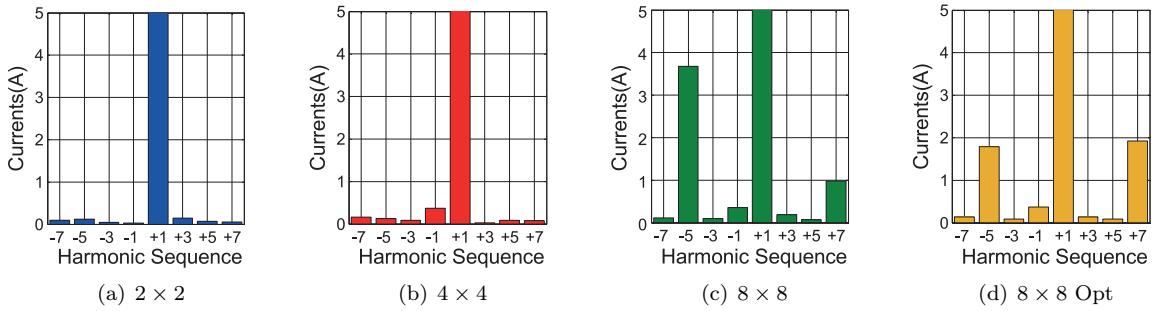


Figure 4.9: Complex FFT of exchanged currents ($\vec{i}_{\alpha\beta}$) with different CRC methods.

The obtained results are collected in Table 4.3:

The obtained results show how the 2^{nd} harmonic is reduced with the 4×4 and 8×8 methods. The 6^{th} harmonic is also eliminated with the 8×8 strategies. Finally, it can be appreciated how the optimized proposed 8×8 matrix reduces the THDi in 30 %, for the presented case. The THDi reduction is of great importance as contemplated on [108], where a maximum of 5 % is allowed over the whole THD current injection. As counterpart

Table 4.3: Simulation results

Parameter	Power oscillations [W]			DC-Bus [mV]			HD
Control	\hat{P}_2	\hat{P}_4	\hat{P}_6	\hat{V}_2	\hat{V}_4	\hat{V}_6	h<11*
2x2	108.1	24.50	1037	49.4	5.2	160	1.25 %
4x4	13.64	19.42	1036	7.2	4.9	160	1.31 %
8x8	36.20	21.49	182.0	16.7	4.6	31.0	5.14 %
8x8 Opt	24.43	37.05	203.2	10.5	8.0	31.7	3.46 %

with the proposed CRC, the 4th harmonic is not controlled. Anyhow, its presence is not high due to it is provoked by the interaction between 5th and 7th harmonic currents and voltages.

4.7. Conclusions

In this chapter the different CRC techniques for instantaneous power oscillation compensation have been described. It has been explained how a distorted grid provokes oscillation over the instantaneous power and the dc-bus. Although the injection of harmonic currents are penalized by different standards, the proper amount of them can compensate the instantaneous power oscillations.

Different CRC have been analysed for eliminating the 2nd power harmonic with unbalanced currents injection (4×4 matrix) and the 2nd, 4th and 6th harmonics elimination with the harmonic currents injection (8×8 matrix).

A new CRC method has been proposed where the reduction of the 4th harmonic ripple has been released and the remaining degree of freedom has been employed for the THD reduction. Finally, simulation results show the performance of the proposed CRC in comparison with the other ones.

Chapter 5

Current controller saturators under multifrequency operation

5.1. Introduction

The main objective of three-phase VSCs is to perform a flow of energy between the ac and dc side. However, the amount of energy that a specific converter can exchange is limited and it needs to be taken into account during the converter design process. These limitations are usually contained into two different dimensions:

- Voltage limitations
- Current limitations

First, the ac voltage that can be generated at the ac side of a VSC is limited by the dc-bus. The possible ac voltage that can be generated without exceeding the linear modulation range is directly related with the dc voltage of the VSC. At first view, it could seem that the problem can be easily solved with just increasing the voltage level. However, the increment of V_{dc} is not trivial. The maximum dc bus voltage is reaching a technological limitation. Sometimes, it is needed to employ strategies where the voltage to block is divided between several switches connected in series (multilevel topology). Another option is to employ semiconductors that are able to block higher voltages, which usually implies higher switching losses [109].

Furthermore, if the dc bus voltage is much higher than the required one for the desired output ($m_a \ll 1$), a higher THD is delivered [110]. Despite in some cases, as in PV applications, the dc bus is variable, and the same occurs with batteries, where the voltage levels is related with the *State of charge (SOC)* [111]. In the particular case of PV, when a higher dc voltage is needed, for example to deliver a high capacitive reactive power, the MPPT can be abandoned, in order to reach a point with a higher dc voltage [112].

In this regard, the actuation signal that comes out from the current controller needs to be kept within the limitations imposed by the input dc voltage. In order to accomplish it, an actuation saturator is placed after the current controller that maintains the actuation signal within the linear range. The description of the current controller saturators are detailed in this chapter. Section 5.2 describes the limitations of the actuation regarding the DC voltage, in section 5.3 the difficulties when multifrequency control is employed are analysed. Finally, in section 5.4 a new multifrequency saturation is proposed and compared with the available multifrequency saturators up to date.

Second, the maximum current that a VSC can exchange with the grid is determined by the maximum current allowed by the different elements that compose the VSC. Between these elements, switches and inductances are the most important ones within the current limitation. The switches are designed for a maximum *Root Mean Square (RMS)* current and the same occurs with the inductances, which can reach the core saturation. The current nominal values are well known and are provided by the manufacturers [113] [114].

Meanwhile, the current that the VSC exchanges with the grid is determined by the reference currents (input parameter of the current controller). In order not to overcome the previously described current limitations, as they are known, they can be consequently avoided. This functionality is achieved after the CRC, through a current references saturator, which is explained during section 5.5.

In Fig. 5.1, an schematic with the current and voltage saturators is depicted. The position of each saturator inside the current control is also showed.

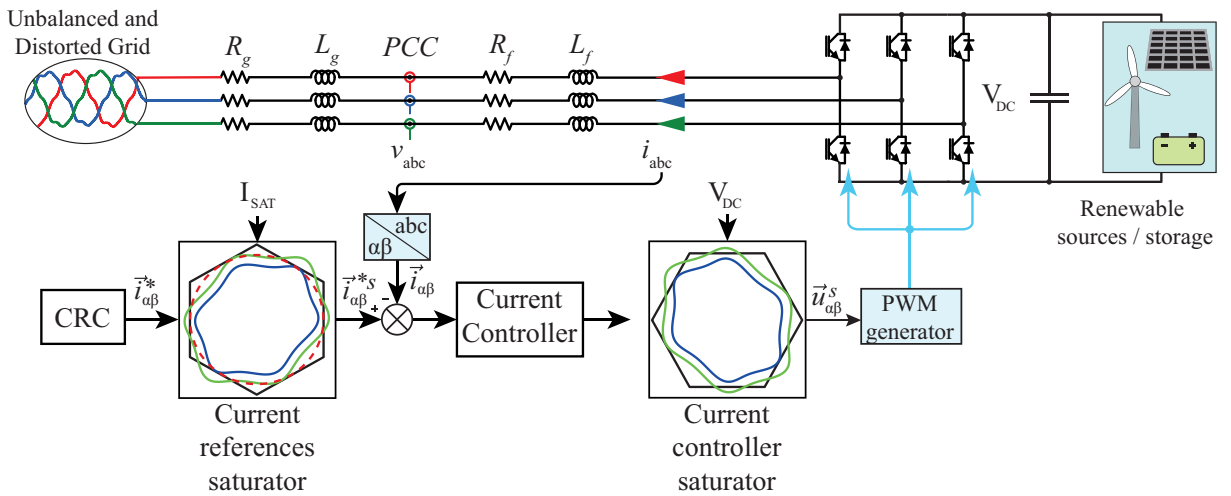


Figure 5.1: Schematics of current and voltage saturators in a current control.

5.2. VSC DC voltage limitations

VSC, as depicted in Fig. 5.2, provides a three-phase voltage signal depending on the switches states. As the switches on the same leg cannot be conducting at the same time, each phase can be connected to $+\frac{V_{DC}}{2}$ or to $-\frac{V_{DC}}{2}$. Assuming the possible combinations of the 3 different arms, each of them can be connected to $+\frac{V_{DC}}{2}$ (1) or to $-\frac{V_{DC}}{2}$ (0). Then, a total of 8 different possible combinations are reachable.

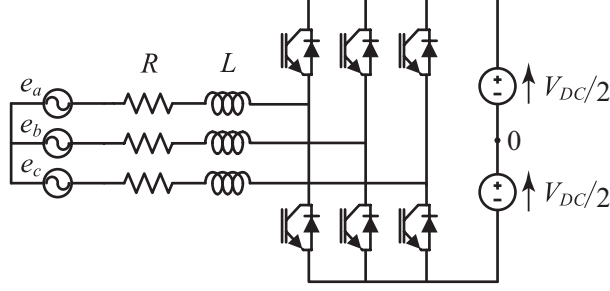


Figure 5.2: 2-levels VSC

The three phase voltages for each phase can be easily transformed to the $\alpha\beta$ stationary reference frame by applying the amplitude invariant Clarke transformation as described in Eq. 5.1.

$$T_{abc \rightarrow \alpha\beta\gamma} = \frac{2}{3} \begin{bmatrix} 1 & -\frac{1}{2} & -\frac{1}{2} \\ 0 & \frac{\sqrt{3}}{2} & -\frac{\sqrt{3}}{2} \\ \frac{1}{\sqrt{2}} & \frac{1}{\sqrt{2}} & \frac{1}{\sqrt{2}} \end{bmatrix} \quad (5.1)$$

The different reachable states with their correspondent voltage values per phase and in $\alpha\beta$ reference frame are collected in Table 5.1.

Table 5.1: Voltage values depending on state

State	u_a	u_b	u_c	u_α	u_β	$\vec{u}_{\alpha\beta}$
000	$-V_{DC}/2$	$-V_{DC}/2$	$-V_{DC}/2$	0	0	$0.000 + j0.000$
100	$+V_{DC}/2$	$-V_{DC}/2$	$-V_{DC}/2$	$\frac{2V_{DC}}{3}$	0	$\frac{2V_{DC}}{3} + j0.000$
110	$+V_{DC}/2$	$+V_{DC}/2$	$-V_{DC}/2$	$\frac{V_{DC}}{3}$	$\frac{V_{DC}}{\sqrt{3}}$	$\frac{V_{DC}}{3} + j\frac{V_{DC}}{\sqrt{3}}$
010	$-V_{DC}/2$	$+V_{DC}/2$	$-V_{DC}/2$	$-\frac{V_{DC}}{3}$	$\frac{V_{DC}}{\sqrt{3}}$	$-\frac{V_{DC}}{3} + j\frac{V_{DC}}{\sqrt{3}}$
011	$-V_{DC}/2$	$+V_{DC}/2$	$+V_{DC}/2$	$-\frac{2V_{DC}}{3}$	0	$-\frac{2V_{DC}}{3} + j0.000$
001	$-V_{DC}/2$	$-V_{DC}/2$	$+V_{DC}/2$	$-\frac{V_{DC}}{3}$	$-\frac{V_{DC}}{\sqrt{3}}$	$-\frac{V_{DC}}{3} - j\frac{V_{DC}}{\sqrt{3}}$
101	$+V_{DC}/2$	$-V_{DC}/2$	$+V_{DC}/2$	$\frac{V_{DC}}{3}$	$-\frac{V_{DC}}{\sqrt{3}}$	$\frac{V_{DC}}{3} - j\frac{V_{DC}}{\sqrt{3}}$
111	$+V_{DC}/2$	$+V_{DC}/2$	$+V_{DC}/2$	0	0	$0.000 + j0.000$

The last column gives the expression for each state as a complex value. Those expressions could be represented in a complex plane. In this complex plane u_α is the real part and u_β is the imaginary one (*Space Vector Modulation (SVM)*). It can be noted that two states (000 and 111) remains at the origin while the other six states fix the limits of the converter, as depicted in Fig. 5.3. The six states can be seen as the vertices of the hexagon where any of the vectors inside could be reached by a combination of the three closest states.

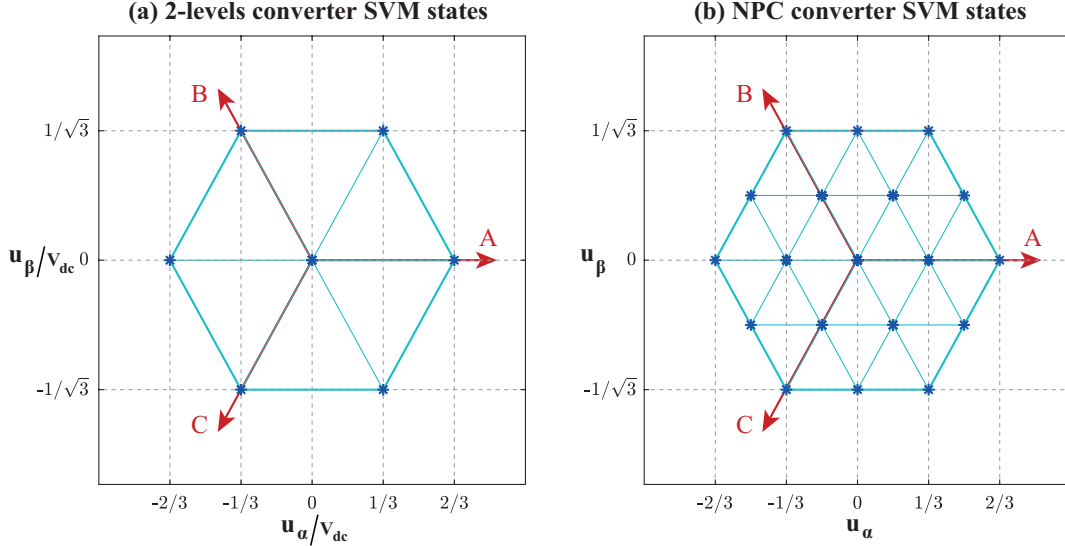


Figure 5.3: (a) 2-levels and (b) 3-levels NPC converters states and limiting hexagon.

In Fig. 5.3.b, it can be seen that when the number of levels is increased, the number of switching states also increases (n^3) and the same occurs with the number of triangles ($6[n - 1]^2$) [115]. Anyhow, the new states are included between the same limitation hexagon that the one for the two levels converter (Fig. 5.3.a). The same limiting hexagon can be appreciated for other higher levels converters as *Modular Multilevel Converter (MMC)*, if balanced dc-bus voltages are assumed.

At the same time, the output of the current controller provides the voltage in $\alpha\beta$ -stationary reference frame (maybe after dq to $\alpha\beta$ transformation). When the most common current sequences (+1, -1, -5, +7, etc) want to be controlled, these sequences will be also present at ac voltage of the converter ($\vec{v}_{\alpha\beta}$).

In steady state situation, the set of all the different values that $\vec{u}_{\alpha\beta}$ takes for the different instants, during the natural period, describe a trajectory in the $\alpha\beta$ plane. This plane goes from the simplest circular trajectory when just +1 sequence is controlled; passing by the ellipse trajectory when +1 and -1 sequences are controlled; and to complex epitrochoids or hypotrochoids when harmonic sequences (usually -5 and +7) are added to the control. The complexity of the trajectory increases with the number of controlled sequences, as depicted in Fig. 5.4.

Therefore, the trajectory size increases with the number of required capabilities (harmonic control, capacitive Q deliver). Regardless of the trajectory shape, always that it remains within the limiting hexagon, the converter is modulating in the linear modulation range. If at any moment, the trajectory exceeds the zone delimited by the available DC voltage hexagon, that part of the trajectory turns unreachable and in the SVM context, it would be seen, as following the closest hexagon edge. This effect is called overmodulation and it implies the appearance of low order harmonic voltage components (-5, +7, -11, +13) [116], which is undesirable.

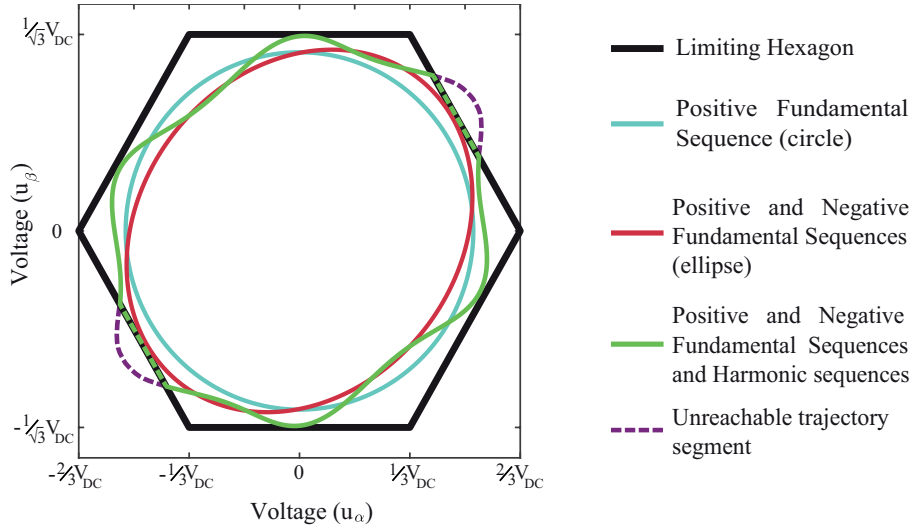


Figure 5.4: Different $\vec{u}_{\alpha\beta}$ trajectories including different positive and negative sequences [47].

Therefore, the above technical limitations conducts to a situation, where the linear modulation zone cannot be easily expanded and if the trajectory is desired to be inside this zone, it would need to be reduced. Therefore, the employed techniques consist on limiting the control actuation signals. Usually, those saturation techniques, can be divided into two main categories [59]: scalar and vector techniques.

On one hand, scalar saturation technique is the immediate saturation strategy, where each of the independent components (a,b,c) of the modulating signals are limited to the maximum reachable value [60]. By this saturation strategy, the maximum voltage can be obtained from the dc voltage (following hexagon edges), with the counterpart of injecting distorted currents with low order harmonics.

On the other hand, vector saturation techniques treat the different components as just one vector. Therefore, in the case that limitations are needed, they are applied over the vector, affecting all the components together.

5.3. Harmonic trajectory shapes

Here, the trajectories resulted from the combination between the different harmonic components are compared with the known mathematical curves [117].

An epitrochoid is defined as the curve traced by a point, inside of a first circle, which radius is equal to r , rolling outside a second fixed circle of radius equal to R . The distance from the point to the center of the first circle is defined as d . The special case, where d is equal to r is known as epicycloid. The trajectory is defined by:

$$x(\theta) = (R + r) \cos(\theta) + d \cos\left(\frac{R + r}{r} \cdot \theta\right) \quad (5.2)$$

$$y(\theta) = (R + r) \sin(\theta) + d \sin\left(\frac{R + r}{r} \cdot \theta\right). \quad (5.3)$$

Meanwhile, a hypotrochoid is also a curve defined by the movement of a point inside of a first circle (of radius r), but in this case, the circle is rolling inside a second circle of radius R . As before, the distance from the point to the center of the first circle is defined as d and in this case, the special case where d is equal to r is known as hypocycloid. The trajectory is defined by:

$$x(\theta) = (R - r) \cos(\theta) + d \cos\left(\frac{R - r}{r} \cdot \theta\right) \quad (5.4)$$

$$y(\theta) = (R - r) \sin(\theta) - d \sin\left(\frac{R - r}{r} \cdot \theta\right). \quad (5.5)$$

Examples of epitrochoid and hypotrochoid trajectories are represented in Fig. 5.5.a and 5.5.b, respectively. In the following, the generated trajectories by the combined addition of fundamental components and harmonic components, are compared with these trajectories.

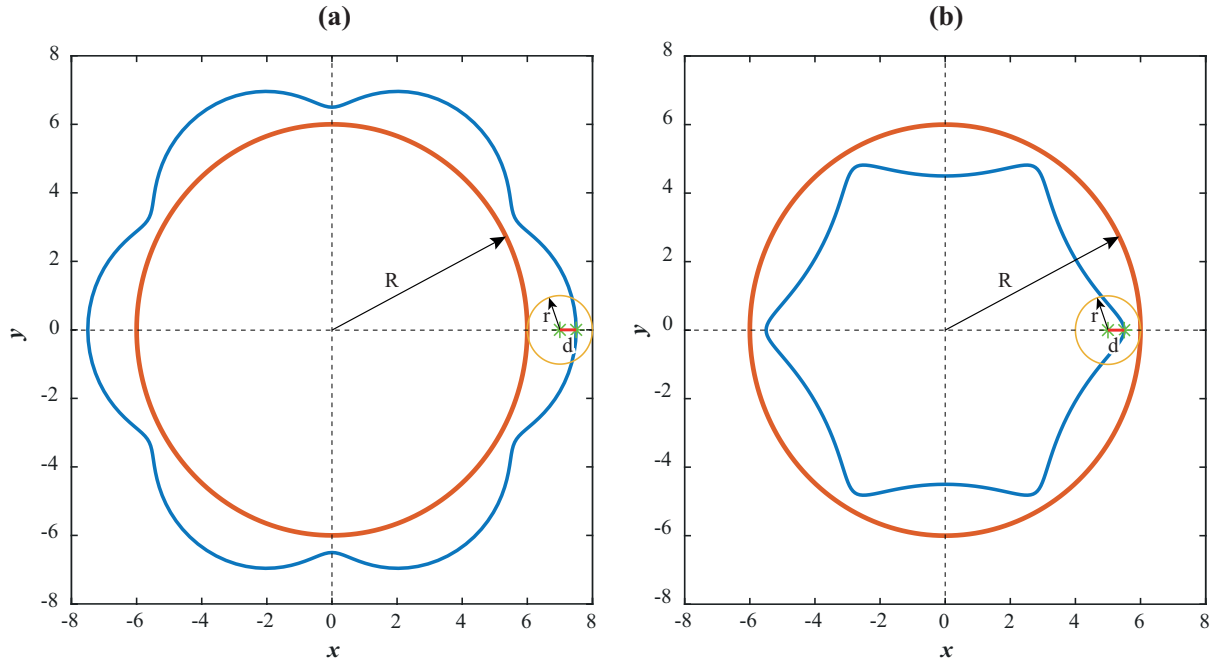


Figure 5.5: Examples of two different types of roulette: (a) Epitrochoid and (b) Hypotrochoid. Both of them with $R=6$, $r=1$ and $d=0.5$

Firstly, it is assumed the combined effect of the FPS and the +7 harmonic sequence, the trajectory would be described as:

$$x(\theta) = U_1 \cos(\theta) + U_4 \cos(7\theta) \quad (5.6)$$

$$y(\theta) = U_1 \sin(\theta) + U_4 \sin(7\theta) \quad (5.7)$$

where, by comparison with (5.2) and (5.3), it can be stated that $d = U_4$, $(R + r) = U_1$ and $\frac{R+r}{r} = 7$. It can be seen that the trajectory is equal to the one for describing the epitrochoid, as it can be appreciated in Fig. 5.6.a.

Now the combined effect of the FPS and the -5 harmonic sequence is analysed, the trajectory results in:

$$x(\theta) = U_1 \cos(\theta) + U_3 \cos(-5\theta) = U_1 \cos(\theta) + U_3 \cos(5\theta) \quad (5.8)$$

$$y(\theta) = U_1 \sin(\theta) + U_3 \sin(-5\theta) = U_1 \sin(\theta) - U_3 \sin(5\theta) \quad (5.9)$$

where, by comparison with hypotrochoid at (5.4) and (5.3), it can be stated that $d = U_3$, $(R - r) = U_1$ and $\frac{R-r}{r} = 5$. It can be seen that the trajectory is equal to the one for describing the hypotrochoid, as it can be appreciated in Fig. 5.6.b.

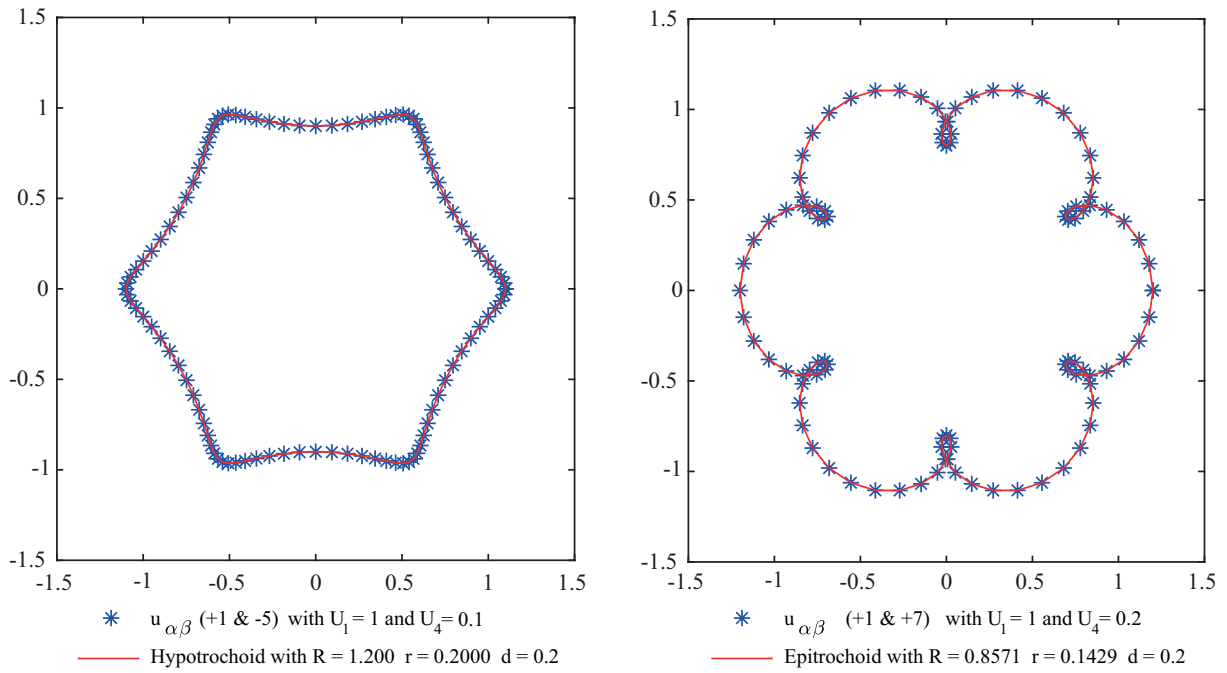


Figure 5.6: Comparison of mathematical curves with the $\vec{u}_{\alpha\beta}$ trajectory: (a) An hypotrochoid fits the trajectory described by the addition of FPS and fifth harmonic. (b) Epitrochoid fits the trajectory described by the addition of FPS and seventh harmonic.

The periodicity in both cases is equal to 6, and it can be worked out as $\frac{R}{r}$, where for the case of FPS and fifth harmonic, where $r = \frac{U_1}{5}$ and $R = U_1 + r$:

$$\frac{R}{r} = \frac{\frac{5U_1 + U_1}{5}}{\frac{U_1}{5}} = 6 \quad (5.10)$$

Regarding to the case of FPS and seventh harmonic, where $r = \frac{U_1}{7}$ and $R = U_1 - r$:

$$\frac{R}{r} = \frac{\frac{7U_1 - U_1}{7}}{\frac{U_1}{7}} = 6 \quad (5.11)$$

5.4. Multifrequency Current Controller Saturators

As it has been described in previous section, when more sequences are included into the control algorithm, it results in more complex trajectories. When different functionalities are required to the inverter, the trajectory can exceed the linear modulation range and in order to avoid undesirable effects, it should be brought back. Multifrequency distortion free saturators are in charge of reducing the trajectory and avoiding overmodulation and windup. Different multifrequency saturators are analysed and a new one, which is able to instantaneously calculate the optimal reduction gain (with minimum THDi), is proposed.

5.4.1. Distortion Free Equally weighted Saturator

The described multifrequency saturator along this section was introduced in [64]. This saturator, consisted on an algorithm that was able to deal with the different sequences at the same time.

The current controller employed in the described is based in a PRC, with ROGIs which resonant frequencies are equal to the interesting controlled frequencies (+1, -1, -5 and +7) plus the proportional component [31]. The output actuation signal, that comes from the current controller can therefore be described as:

$$\vec{u}_{\alpha\beta} = \vec{u}_{\alpha\beta}^{+1} + \vec{u}_{\alpha\beta}^{-1} + \vec{u}_{\alpha\beta}^{-5} + \vec{u}_{\alpha\beta}^{+7} + \vec{u}_{\alpha\beta}^p \quad (5.12)$$

The trajectory composed by $\vec{u}_{\alpha\beta}$ should not exceed the delimited linear modulation area. For accomplishing that objective, as soon as $\vec{u}_{\alpha\beta}$ exceeds the hexagon, it starts to subtract the exceeding current in order to bringing back the trajectory inside the hexagon, as depicted in Fig 5.7.

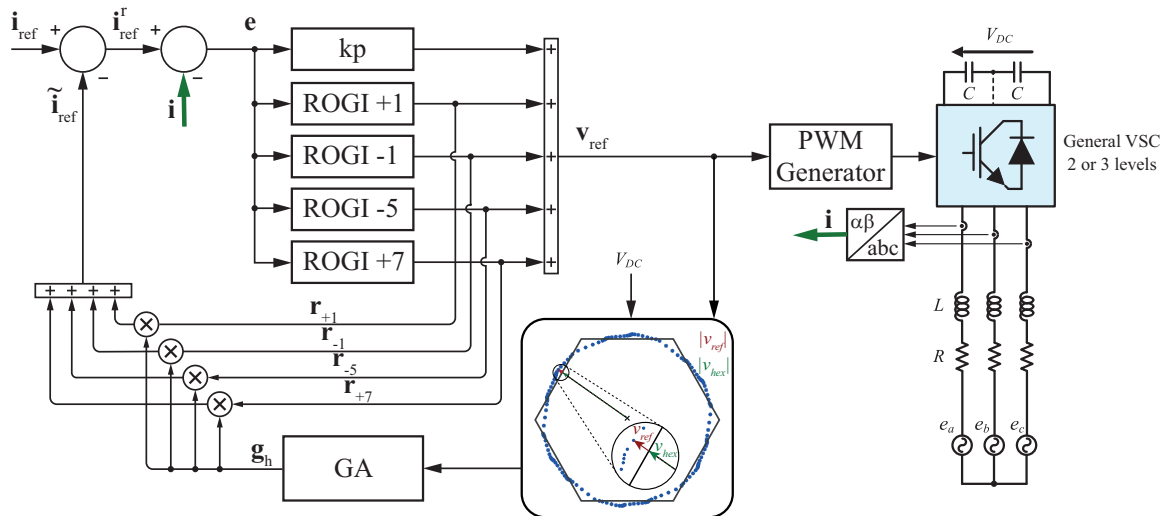


Figure 5.7: Distortion Free Equally weighted Saturator algorithm representation.

For knowing if the trajectory is exceeding the hexagon, for each instant k , the module of the trajectory ($|\vec{u}_{\alpha\beta}|$) is obtained. Then, for the same angle of the trajectory ($\angle \vec{u}_{\alpha\beta}(k)$) the module of the hexagon ($|\vec{v}_{hex}|$) is worked out, and both modules are compared.

If δ is lower than 0, it implies that the analysed point of the trajectory is contained inside the linear modulation zone. However, if δ gets a higher value than 1, it implies that the studied point is exceeding the linear range, and it needs to be corrected. If distortion-free saturator wants to be implemented, it is not just enough by bringing the external points inside the linear modulation range, however, the whole trajectory would need to be reduced until all the individual points are contained inside. For accomplishing that, for the whole period (T_1), the maximum value of δ is employed:

$$\delta_k = \max [|\vec{u}_{\alpha\beta}(k)| - |\vec{v}_{hex}(k)|]_{kT_1}^{(k-1)T_1}. \quad (5.13)$$

The discrete signal obtained in (5.13) is converted to a continuous signal through a discrete-to-continuous ZOH:

$$\delta = \text{ZOH}_{T_1}(\delta_k). \quad (5.14)$$

A new parameter γ is now employed that slowly increases or decreases depending on the value adopted by δ . The integration output is saturated to the interval $[0, \gamma_{\max}]$:

$$\gamma = \left[\int \frac{\alpha_g \delta}{V_{base}} dt \right]_0^{\gamma_{\max}} \quad (5.15)$$

where, α_g is in charge of determining the dynamics of the parameter γ . As it is explained later, the faster the parameter γ changes, the sooner the trajectory is brought back into the linear zone. However, the dynamics need to be slow enough in comparison with the control loop, concretely with the inner current control loop, and therefore it is recommended that:

$$\alpha_g \leq \frac{\omega_1}{4\pi}. \quad (5.16)$$

The key part of the algorithm comes now, where the exceeding part of $\vec{u}_{\alpha\beta}$ is estimated as: the multiplication of the recent calculated parameter γ by each actuation signal that comes out from each ROGI (r_h). This exceeding voltage can be expressed as an exceeding current \tilde{i}_{refh} and subtract it from the original reference in previous instant:

$$i_{refh}^r = i_{refh} - \underbrace{\frac{\gamma r_h}{\hat{Z}(j\hbar\omega_1)}}_{\tilde{i}_{refh}} \quad (5.17)$$

5.4.2. Maximum Power Distortion Free Saturator

A different distortion free multifrequency saturation strategy was developed in [66]. In this case, based on the multifrequency saturator described in [64], a partial harmonic compensator in the case of saturation is described. Firstly, the natural current harmonic $\mathbf{i}_{DQh,nat}$ is described as the harmonic current produced when no harmonic voltage is generated at the ac side of the converter, in order to perform a compensation.

$$\mathbf{i}_{DQh} = \frac{\mathbf{u}_{DQh} - \mathbf{e}_{DQh}}{Z(j\omega h)} \rightarrow \mathbf{i}_{DQh,nat} = -\frac{\mathbf{e}_{DQh}}{Z(j\omega h)} \quad (5.18)$$

Therefore, the natural harmonic currents, namely $\mathbf{i}_{DQ5,nat}$ and $\mathbf{i}_{DQ7,nat}$ can be easily worked out. Then, once that the natural harmonic currents are initially worked out, the harmonic references currents need to be selected. If the natural currents are selected as references, no voltage would be generated at the output of the VSI. However, in the opposite side, if \mathbf{i}_{DQh} is equalled to zero, the harmonic current would be completely eliminated, due to that, the needed voltage component \mathbf{u}_{DQh} is applied.

However, the rise of \mathbf{u}_{DQh} provokes an increment over the total ac voltage component to be applied at the ac side of the VSC:

$$\mathbf{v}_{ref} = \mathbf{u}_{DQ} = \mathbf{u}_{DQ1} + \mathbf{u}_{DQ5} + \mathbf{u}_{DQ7} \quad (5.19)$$

This increment could provoke that the trajectory followed by \mathbf{v}_{ref} could at some point exceed the delimited linear modulation zone. In order to avoid this, due to the fact that the natural currents are known, the reference currents in this saturation algorithm are worked out as

$$\mathbf{i}_{DQh,ref} = \lambda_h \cdot \mathbf{i}_{DQh,nat} \rightarrow \arg(\mathbf{i}_{DQh,ref}) = \arg(\mathbf{i}_{DQh,nat}). \quad (5.20)$$

Therefore, depending exclusively from the λ_h parameter, it would be decided how far the compensation is achieved. If $\lambda = 0$ is selected, a total harmonic compensation would be achieved (implying the generation of $\mathbf{u}_{DQh} = \mathbf{e}_{DQh}$). If $\lambda = 1$ is selected, no harmonic current compensation would be achieved at all (implying no generation of \mathbf{u}_{DQh} and reducing the trajectory size). Therefore, several intermediate values are available among those extremes ($\lambda_h \in [0, 1]$).

The key part of the algorithm is how to properly select the λ_h parameter, in critical situations, for achieving the maximum possible current compensation, without exceeding the linear modulation range. In an analogous strategy to the one employed in [64], a comparison between the module of \mathbf{v}_{ref} and the module of the vector with the same argument as \mathbf{v}_{ref} that traces the hexagon ($|\mathbf{v}_{hex}|$), is carried out.

In the same way as before (although in a different conceptual implementation), when $|\mathbf{v}_{ref}|$ is greater than $|\mathbf{v}_{hex}|$, parameter λ_h needs to be increased in order to reduce com-

pensated current and reduce the harmonic voltage component \mathbf{u}_{DQh} . Then, the maximum value for the whole trajectory is worked out in order to achieve distortion free saturation:

$$\delta_k = \max [|\mathbf{v}_{ref}(k)| - |\mathbf{v}_{hex}(k)|]_{kT_1}^{(k-1)T_1}. \quad (5.21)$$

Finally, by the integration of the previously calculated δ , the λ parameter can be obtained. In this case the integrator output is saturated between 0 and 1:

$$\lambda = \left[\int \frac{\alpha_g \delta}{V_{base}} dt \right]_0^1. \quad (5.22)$$

The graphical representation of the method described in [66] is depicted in Fig. 5.8.

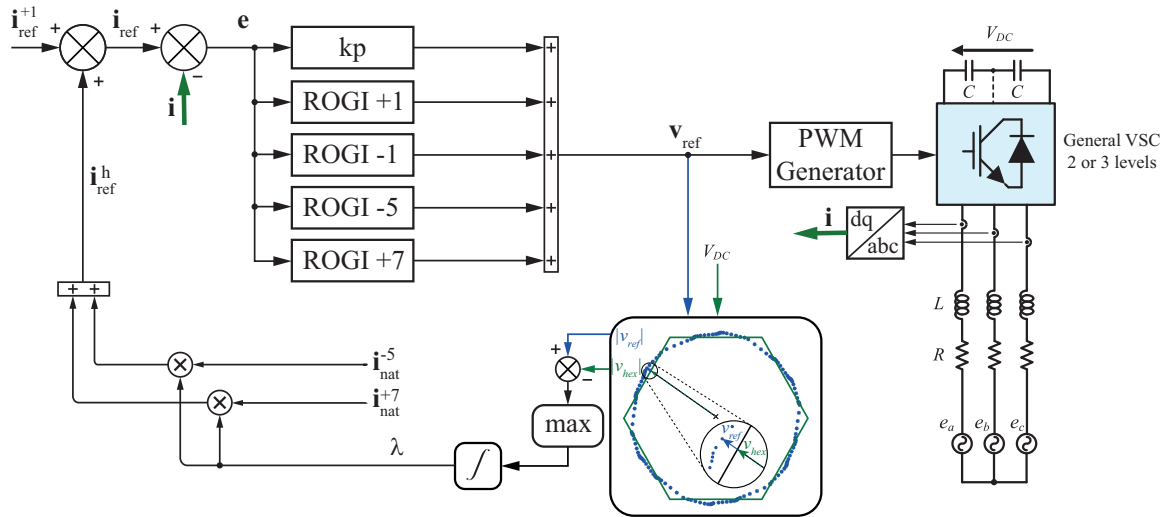


Figure 5.8: Maximum Power Distortion Free Saturator algorithm representation.

5.4.3. Distortion free Instantaneous Multifrequency Saturator (DFIMS)

During this section, the proposed algorithm for instantaneous saturation (DFIMS) is described. This algorithm implies an advance in multifrequency saturation. The proposed DFIMS is able to analyse for each instant the following points of the trajectory, and apply the necessary reduction to achieve a new trajectory. This new trajectory accomplishes the distortion free requirements.

Firstly, a simplest version of DFIMS can be implemented for cases where exclusively positive and negative sequences are dealt with. Finally, the complete version of DFIMS is described, where the harmonic sequences are included.

5.4.3.1. DFIMS with positive and negative sequences

Assuming a control system where positive and negative sequences are employed, the output of the current controller in stationary reference frame would be the sum of two complex vector voltage signals. The positive fundamental sequence rotates at an angular frequency of ω while the negative fundamental component rotates at $-\omega$. Knowing the two instantaneous complex voltage values at an instant $(u_\alpha^{+1} + ju_\beta^{+1}, u_\alpha^{-1} + ju_\beta^{-1})$, it is possible to obtain the magnitude (hereafter U_1 for FPS and U_2 for FNS) and the phasor angle (hereafter ϕ_1 for FPS and ϕ_2 for FNS).

Knowing the magnitudes and phasor for both components at an instant, the trajectory that the voltage signal would depict (if no changes occur) is described by the following equation

$$\vec{u}_{\alpha\beta} = U_1 \cdot e^{j\omega t + \phi_1} + U_2 \cdot e^{-j\omega t + \phi_2}. \quad (5.23)$$

If the complete trajectory remains inside of the hexagon, which delimits linear modulation zone, all the trajectory vectors would be reachable and the signal will not present any distortion. However, if the trajectory goes out of the hexagon at certain points (Fig. 5.9.a), the trajectory cannot be completed without distortion. In that case, it could be desirable to reduce the trajectory by multiplying both sequence magnitudes by a gain k_{12} . The new trajectory would be described by (5.24) and it contains the same sequences but inside the hexagon, as depicted in Fig. 5.9.b.

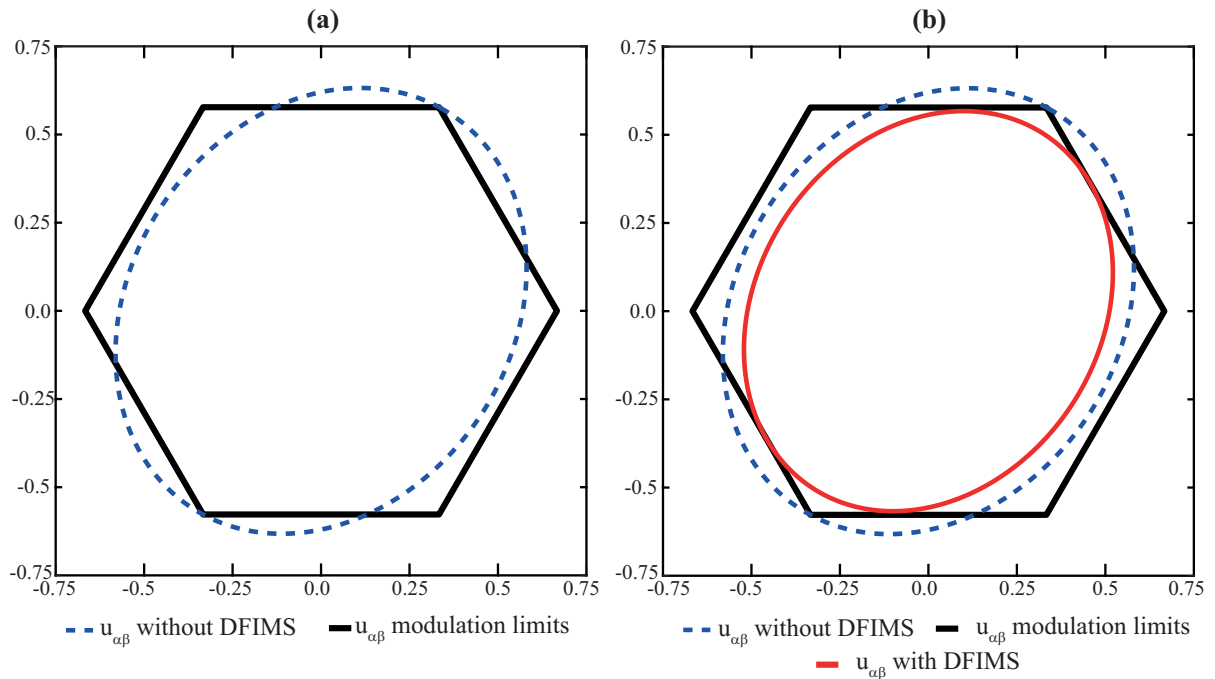


Figure 5.9: (a) Positive and negative overmodulation trajectory example and (b) Reduced positive and negative trajectory after DFIMS application.

$$\vec{u}_{\alpha\beta} = k_{12} \cdot U_1 e^{j\omega t + \phi_1} + k_{12} \cdot U_2 \cdot e^{-j\omega t + \phi_2}. \quad (5.24)$$

In order to get closer to a planar representation, (5.24) could be expanded and rewritten in cartesian form as:

$$\vec{u}_{\alpha\beta} = k_{12} \cdot u_1 \cdot \cos(\omega t + \phi_1) + j \cdot k_{12} \cdot u_1 \cdot \sin(\omega t + \phi_1) + k_{12} \cdot u_2 \cdot \cos(-\omega t + \phi_2) + j \cdot k_{12} \cdot u_2 \cdot \sin(-\omega t + \phi_2). \quad (5.25)$$

Now, from (5.25), two equations can be obtained, if the equation is divided in real and imaginary parts in a complex plane:

$$x = k_{12} \cdot u_1 \cdot \cos(\omega t + \phi_1) + k_{12} \cdot u_2 \cdot \cos(-\omega t + \phi_2) \quad (5.26)$$

$$y = k_{12} \cdot u_1 \cdot \sin(\omega t + \phi_1) + k_{12} \cdot u_2 \cdot \sin(-\omega t + \phi_2) \quad (5.27)$$

Working now with the sum angles formulas:

$$\sin(\hat{A} + \hat{B}) = \sin(\hat{A}) \cdot \cos(\hat{B}) + \cos(\hat{A}) \cdot \sin(\hat{B}) \quad (5.28)$$

$$\cos(\hat{A} + \hat{B}) = \cos(\hat{A}) \cdot \cos(\hat{B}) - \sin(\hat{A}) \cdot \sin(\hat{B}) \quad (5.29)$$

Previously described (5.26) and (5.27) can be rewritten as:

$$x = k_{12} [\cos(\omega t)(u_1 \cos(\phi_1) + u_2 \cos(\phi_2)) - \sin(\omega t)(u_1 \sin(\phi_1) + u_2 \sin(\phi_2))] \quad (5.30)$$

$$y = k_{12} [\sin(\omega t)(u_1 \cos(\phi_1) - u_2 \cos(\phi_2)) + \cos(\omega t)(u_1 \sin(\phi_1) + u_2 \sin(\phi_2))] \quad (5.31)$$

The trajectory of $\vec{u}_{\alpha\beta}$ would be inside the hexagon always that the absolute value of the trajectory for each of the ωt instants, is lower than the value for the hexagon at that phase value. Checking this mathematically, brings difficult equations which would be very difficult to solve in the computational times that are available for a commercial DSP. However, taking advantage on the ellipse symmetry and on the ease to the ellipse rotation, a new method is proposed here.

Firstly, attending only to the top and bottom hexagon edges, they can be easily described as the constant function

$$y = \pm \frac{V_{DC}}{\sqrt{3}}. \quad (5.32)$$

The proposed method here, compares the ellipse y coordinate with the y constant function of the top and bottom edges of the hexagon. In this way, if the ellipse goes out of those limits, a gain k_{12} is obtained for placing the outermost point over the threshold. Therefore, only the equation for the y ellipse value is needed (5.31). By differentiating this equation, the maximum and minimum values can be found solving the following equation:

$$k_{12} [(U_{C1} - U_{C2}) \cdot \omega \cdot \cos(wt) - (U_{S1} + U_{S2}) \cdot \omega \cdot \sin(wt)] = 0 \quad (5.33)$$

where U_{C1} and U_{S1} stands for $U_1 \cdot \cos \phi_1$ and $U_1 \cdot \sin \phi_1$ and U_{C2} , and U_{S2} stands for $U_2 \cdot \cos \phi_2$ and $U_2 \cdot \sin \phi_2$ where all of them are known values. Solving now (5.33), the maximum and minimum values are found as:

$$wt = \arctan \left(\frac{U_{C1} - U_{C2}}{U_{S1} + U_{S2}} \right) \quad (5.34)$$

and there would exist two solutions for the problem in the $[0-2\pi)$ interval. For each of the two solutions a value of the k_{12} can be obtained equalling (5.31) to the threshold in (5.42) both in absolute value:

$$|k_{12} [\sin(wt)(U_{C1} - U_{C2}) + \cos(wt)(U_{S1} + U_{S2})]| = \left| \frac{V_{DC}}{\sqrt{3}} \right|. \quad (5.35)$$

The lowest value of k_{12} that also is lower than the unity, would be taken as one of the three possible values of k_{12} . In this way, the limits with the top and bottom edges have been easily studied as threshold.

For checking with the other four hexagon edges, it could be performed through two rotations of 60° applied over the ellipse and obtaining both k_{12} as described in the process explained before. Applying a 60° rotation over the ellipse is as easy as adding $\frac{\pi}{3}$ to ϕ_1 and ϕ_2 for the first rotation and $-\frac{\pi}{3}$ to ϕ_1 and ϕ_2 for the second rotation. The process is depicted in Fig. 5.10.

The smallest k_{12} for the three rotations is selected as the k_{12} for the saturation. This makes that the current value and the next ones (if no input variation exists) would be inside of the delimited linear modulation zone.

5.4.3.2. Multifrequency sequences saturator

The proposed DFIMS explained during this section, is in charge of accomplishing multifrequency application, without abandoning at any moment the linear modulation range zone. The main objective of this saturator is to inject the minimum possible current harmonic distortion.

Here, the actuation signal that comes out of the current controller in stationary reference frame ($\alpha\beta$) would be the sum of the different complex vector voltage signals.

$$\vec{u}_{\alpha\beta} = \vec{u}_{\alpha\beta}^{+1} + \vec{u}_{\alpha\beta}^{-1} + \vec{u}_{\alpha\beta}^{-5} + \vec{u}_{\alpha\beta}^{+7} \quad (5.36)$$

The goal to accomplish with DFIMS algorithm, is to keep $\vec{u}_{\alpha\beta}$ at any moment, instantaneously inside of the space vector composed by the hexagon determined by the dc bus. In

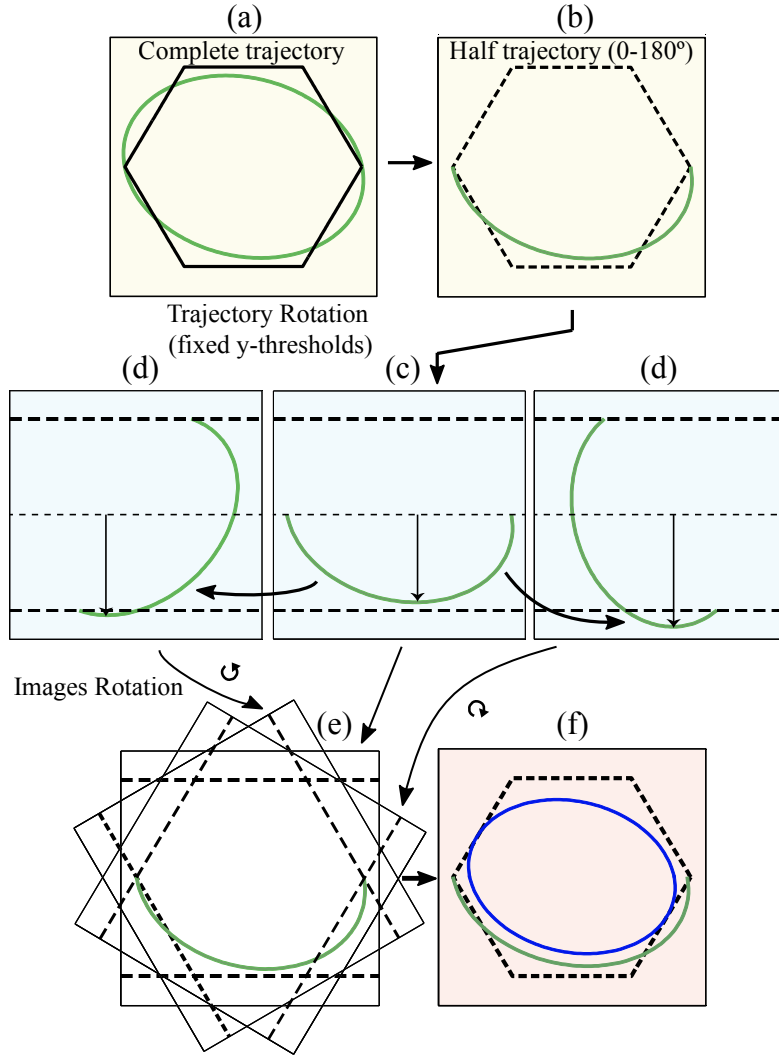


Figure 5.10: Trajectory rotation process example.

a general way, $\vec{u}_{\alpha\beta}$ can be written as the combined effect of the FPS and the components that are in charge of unbalance and harmonic distortions (grid perturbations):

$$\vec{u}_{\alpha\beta} = \underbrace{U_1 e^{j(\omega t + \phi_1)}}_{\text{Fundamental}} + \underbrace{\sum_{h \in H} U_h e^{j(h\omega t + \phi_h)}}_{\text{Perturbations}} \quad (5.37)$$

where H is composed by the n controlled sequences $[\dots, -11, -5, -1, +7, +13, \dots]$. The representation of the complex variable $\vec{u}_{\alpha\beta}$ in a complex plane depicts a trajectory that, in steady state, it is repeated periodically every fundamental period T_1 . This trajectory needs to be graphically compared against the hexagon limited zone, as in Fig. 5.10.a. The trajectory would remain inside the delimited zone, always that for each value adopted for ωt , the module of the trajectory is smaller than the module of the hexagon for that phase. As described in the previous multifrequency saturation algorithms, this comparison can be made and then, through a progressive reduction of the trajectory, reach back the linear modulation range.

However, when that reduction wants to be instantaneously achieved, as it is proposed here, difficult equations come out in order to mathematically work out the exact gain that brings the trajectory inside the delimited hexagon. It needs to be taken into account that the gain must not just be calculated for bringing the $\vec{u}_{\alpha\beta}$ value for the studied instant inside the hexagon. The strategy estimates where the following points would be expected to be and the proper gain calculation needs to be instantaneously calculated in order to bring the studied (k) and all the following points (up to $k + T_1$) within the hexagon. To achieve this, the outermost point is taken within the limits (in order to go as far as possible without reaching overmodulation).

5.4.3.2.1. DFIMS Algorithm Description: With the novel algorithm, in the case of the actuation vector exceeds the linear modulation range, the trajectory is instantaneously reduced for not reaching overmodulation. However, this algorithm needs to be accomplished within the computational times available for commercial DSPs.

In order to be able to accomplish instantaneousness and performing it in a suitable computational time for the available DSPs, the new algorithm is developed. This algorithm instead of obtaining high order equations, taking into advantage the trajectory symmetry and the ease of trajectory rotation, the equations complexity is reduced.

Firstly, as previously explained, reduction gains need to be worked out for the whole trajectory. As the calculation will be made at an instant k , the next points can be estimated with the individual information available for each sequence ($u_{\alpha\beta}^{+1}$, $u_{\alpha\beta}^{-1}$, $u_{\alpha\beta}^{-5}$, $u_{\alpha\beta}^{+7}$).

The rotating angular frequency for each component is described as $h\omega$ (typically ω , $-\omega$, -5ω and $+7\omega$). Knowing the instantaneous complex voltage values at an instant (u_{α}^{+1} , u_{β}^{+1} , u_{α}^h , u_{β}^h), it is possible to obtain the magnitude (hereafter U_1 for positive fundamental sequence and U_h for the rest of sequences) and the phasor angle (hereafter ϕ_1 for positive fundamental sequence and ϕ_h for unbalance and distortion components).

As the magnitudes and phase for all the components at an instant are known, the following points trajectory that the voltage signal would depict are extrapolated by the following equation

$$\vec{u}_{\alpha\beta} = U_1 \cdot e^{j\omega t + \phi_1} + \sum_{h \in H} U_h \cdot e^{-j\omega t + \phi_h}. \quad (5.38)$$

The same method of the positive and negative fundamental sequence saturator can be applied, where just the y coordinate of the complex plane will be employed. Extracting just the complex part (y coordinate of complex plane) from (5.38), the following equation is obtained:

$$y = k_F(U_1 \cdot \sin(\omega t + \phi_1)) + \sum_{h \in H} (k_h U_h \cdot \sin(h\omega t + \phi_h)) \quad (5.39)$$

Working now with the sum angles formulas, (5.39) can be expressed as:

$$y = k_F [U_{S1} \cdot \cos(\omega t) + U_{C1} \cdot \sin(\omega t)] + \sum_{h \in H} k_h [U_{Sh} \cdot \cos(h\omega t) + U_{Ch} \cdot \sin(h\omega t)] \quad (5.40)$$

where $U_{S1} = U_1 \cdot \sin(\phi_1)$, $U_{C1} = U_1 \cdot \cos(\phi_1)$, $U_{Sh} = U_h \cdot \sin(\phi_h)$ and $U_{Ch} = U_h \cdot \cos(\phi_h)$. As it was described in previous section, it is needed to find the maximum and the minimum values of the y function. For this, the differentiation respect to ωt is done and the resulting equation needs to be solved for $\frac{dy}{d\omega t} = 0$:

$$\frac{dy}{d\omega t} = k_F [U_{S1} \cdot \sin(\omega t) - U_{C1} \cdot \cos(\omega t)] + \sum_{h \in H} k_h \cdot h [U_{Sh} \cdot \sin(h\omega t) + U_{Ch} \cdot \cos(h\omega t)] = 0. \quad (5.41)$$

Once that the maximum and minimum values for the y function has been obtained, they are compared with the maximum allowed value (y_{max}) for the linear modulation range:

$$y_{max} = \pm \frac{V_{DC}}{\sqrt{3}}. \quad (5.42)$$

Then, (6.48) can be expressed in order to find the gains for placing the outermost point in the maximum admissible edge (Fig. 5.10.c):

$$\pm \frac{V_{DC}}{\sqrt{3}} = k_F [U_{S1} \cdot \cos(\omega t) + U_{C1} \cdot \sin(\omega t)] + \sum_{h \in H} k_h [U_{Sh} \cdot \cos(h\omega t) + U_{Ch} \cdot \sin(h\omega t)]. \quad (5.43)$$

Equations (5.41) and (5.43), performs a system of equations with numerous variables (all the independent sequences gain and the phase angle ($\omega t = \theta$)). However, in order to find solutions a deterministic system needs to be obtained.

5.4.3.2.2. Deterministic system obtainment For the obtainment of a deterministic system, new equations need to be defined in order to perform a relationship between the gains. Usually, for the harmonic components, the same priority is assigned in the gain calculation. Therefore, the reduction gain for each harmonic component can be set to the same k_H :

$$k_H = k_{-5} = k_{+7} = k_{-11} = k_{+13} \quad (5.44)$$

Then, the reduction priority of the ($h=-1$) FNS component (unbalance for the fundamental component) needs to be related with the harmonic and the FPS components. In this concern, it will be assumed that as the harmonic components and the unbalanced are determined by the grid standards, both of them would have the same priority reduction ($k_{-1} = k_H$). It needs to be noted that this is just the decision taken in this approach. Depending on the desired functionality, the same priority can be given to the FNS and FPS ($k_{-1} = k_F$) or a different relation can be set among them.

At this point just two gain variables are remained (k_F and k_H). In order to reach the deterministic system, a decision on which functionality is more important needs to be made.

If fundamental gain is the most important component, as in applications where the maximum active or reactive power are required, the last one to be reduced is the fundamental gain (k_F) and the reduction priority is always done from the harmonic components (k_H). An example of this saturation strategy can be found in [66] for permanent magnets synchronous machines.

An intermediate solution can be found where the same reduction factor is assigned to FPS gain (k_F) and to the rest of components (k_H). This strategy would not completely accomplish with the THD reduction, but the diminution in active and reactive powers is not great. This approach is the one described in [64].

Finally, the proposed strategy in this thesis is to always meet the harmonic and unbalance requirements, assigning the minimum reduction priority to (k_H). In this case a small amount of active and reactive powers is reduced for avoiding overmodulation, while the standards are always accomplished. For performing this, the fundamental gain k_F is first obtained assuming that k_H is equal to 1. In the difficult case that with the complete reduction of FPS, the actuation still goes out of the limiting hexagon k_H would be calculated. This one is the strategy published in [47] and is the one followed hereafter.

5.4.3.2.3. Algorithm Completion: Then, once that the gains have been reduced to two (k_F and $\theta = \omega t$), they will be calculated for the case where just the top and bottom hexagon edges are taken into account. In the case that at any point the y coordinate is higher than $\frac{V_{DC}}{\sqrt{3}}$ or lower than $-\frac{V_{DC}}{\sqrt{3}}$, the reduction gain k_F is calculated for bringing all the trajectory points within these limits. Then, in order to make the comparison of the trajectory with the rest of the edges, a rotation is applied over the trajectory and the process is again carried out for the trajectory with the same constant axis, as depicted in Fig. 5.10.d.

The new trajectory with $\pm 60^\circ$ rotations is determined as:

$$\vec{u}_{\alpha\beta} = U_1 \cdot e^{j\omega t + \phi_1 + \phi_r} + \sum_{h \in H} U_h \cdot e^{j\omega t + \phi_h + \phi_r} \quad (5.45)$$

where ϕ_r is added to the original phase of each sequence (ϕ_1 or ϕ_h). The modification of the original phases (ϕ_x) into a new angle (ϕ'_x), results in a modification of U_{Cx} and U_{Sx} values:

$$U_{Cx} = U_x \cos(\phi_x + \phi_r) = U_{\alpha x} \cdot \cos(\phi_r) + U_{\beta x} \cdot \sin(\phi_r) \quad (5.46)$$

$$U_{Sx} = U_x \sin(\phi_x + \phi_r) = U_{\beta x} \cdot \cos(\phi_r) + U_{\alpha x} \cdot \sin(\phi_r) \quad (5.47)$$

Then, by solving equations (5.41) and (5.43) for $\phi_r = \{-60^\circ, 0^\circ, +60^\circ\}$, the minimum k_F is selected. With the reduction of the FPS sequence (k_F), the trajectory would be completely contained inside the limiting hexagon, as depicted in Fig. 5.10.f.

5.4.3.2.4. Simplified implementation: As previously explained, with the DFIMS saturator for the desired functionality, a reduction of k_F is applied in order to keep the whole trajectory in the linear modulation range, while the harmonics and unbalance standards are always accomplished. In this way, it will be assumed that the harmonic and unbalance components would not be able to saturate by themselves allowing to set $k_H = 1$.

Then, the fundamental reduction gain can be worked by solving the following system of equations:

$$\begin{cases} \pm \frac{V_{DC}}{\sqrt{3}} = k_F [U_{S1} \cdot \cos(\omega t) + U_{C1} \cdot \sin(\omega t)] + \sum_{h \in H} [U_{Sh} \cdot \cos(h\omega t) + U_{Ch} \cdot \sin(h\omega t)] \\ k_F [U_{S1} \cdot \sin(\omega t) - U_{C1} \cdot \cos(\omega t)] + \sum_{h \in H} h \cdot [U_{Sh} \cdot \sin(h\omega t) + U_{Ch} \cdot \cos(h\omega t)] = 0. \end{cases} \quad (5.48)$$

In the previous system of equations, if the most common harmonics are dealt with, a total of six non linear functions ($\cos(\omega t)$, $\sin(\omega t)$, $\cos(-5\omega t)$, $\sin(-5\omega t)$, $\cos(7\omega t)$, $\sin(7\omega t)$) are presented. It requires a high computational effort to solve an equation system with non-linear functions.

Chebisev polynomial formulas for the multiple angle expression of the sine and cosine can be applied in order to convert the equations in terms of $\cos(\theta)$, $\cos(h\theta)$, $\sin(\theta)$, $\sin(h\theta)$ to high order equations in terms of $\sin(\theta)$, $\cos(\theta)$. Finally, $\sin(\theta)$, $\cos(\theta)$ could be replaced by

$$\frac{2\theta'}{(\theta')^2 + 1}, \quad \text{and} \quad -\frac{(\theta')^2 - 1}{(\theta')^2 + 1}, \quad (5.49)$$

respectively, where $\theta' = \tan(\theta)$. This strategy allows to treat the problem in terms of θ' instead of working with the circular trigonometric functions. Anyhow, in order to solve the system of equations it still would require a huge computational time due to the high order of equations.

As computational time is critical for equation solving, instead of trying to accurately solve the system of equations (5.48), an approximation of those functions could be worked out, which will reduce the execution time. The approximation consist on finding the closest third order polynomial to every non linear function in 30° intervals, as shown in Fig. 5.11.

Table 5.2: Coefficients for polynomial approximation of non linear functions

Function	0° - 30°				30° - 60°			
	x_3	x_2	x_1	x_0	x_3	x_2	x_1	x_0
$\cos(\omega t)$	-0.1604	-0.0028	1.0004	-0.000	0.1174	-0.6283	0.0627	0.9886
$\sin(\omega t)$	0.0430	-0.5143	0.0016	1.0000	-0.1174	-0.0752	1.0424	-0.0084
$\cos(-5\omega t)$	18.2143	-17.1492	0.4332	0.9912	-13.3338	39.1863	-33.3642	7.7924
$\sin(-5\omega t)$	4.8805	6.7799	-5.8399	0.0209	-13.3338	23.6477	-8.9564	-0.3933
$\cos(7\omega t)$	45.3383	-30.7023	0.1384	1.0056	-33.1899	64.7976	-35.5217	4.6880
$\sin(7\omega t)$	12.1484	-27.8519	10.3128	-0.0799	-33.1899	91.6062	-77.6325	19.8646

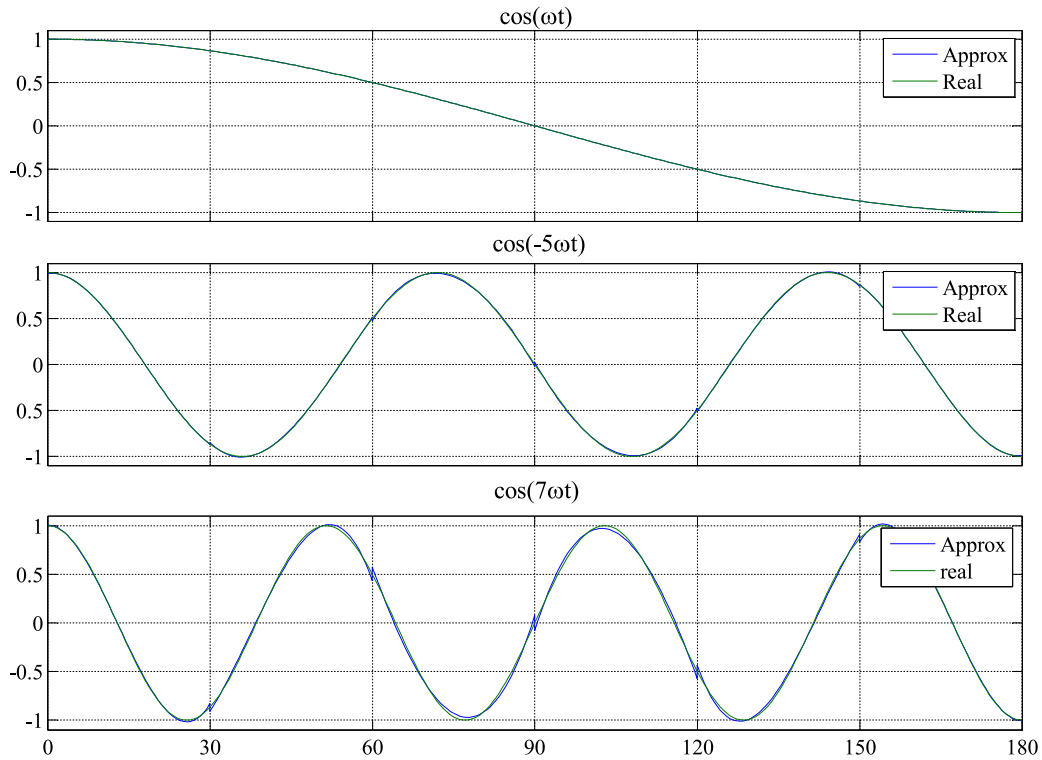


Figure 5.11: Approximation to the non-linear functions by third order polynomial.

Substituting the non-linear functions by the approximated polynomial, the equation would result in two cubic polynomial equations that still require a high computational time.

A third alternative passes through not trying to solve the system of equations (5.48). In this way, as the control of VSC is implemented in discrete domain, a limited number of samples are available. Instead of calculating which θ would corresponds to the maximum or minimum y coordinate value, the required gain value for each θ could be worked out, taking advantage of the fast calculations of sum and multiplication of the DSP.

In this way, if a T_s of 200 μs is employed, a total of 100 points would shape the trajectory during the fundamental period (20 ms). With the trajectory symmetry, the number of points to be checked could be reduced to just 50. Then, the smallest k_F lower than the unity needs to be selected. The k_F corresponding to each point could be calculated as:

$$k_F = \frac{\pm \frac{2V_{DC}}{\sqrt{3}} - \sum [U_{Sh} \cdot \cos(h\omega t) + U_{Ch} \sin(h\omega t)]}{[U_{S1} \cdot \sin(\omega t) - U_{C1} \cdot \cos(\omega t)]} \quad (5.50)$$

As the division takes additional computational time, it is not needed to carry out 50 divisions in order to obtain all the different gains and then decide which is the smallest one. Instead, the numerator and denominator for each point are obtained and the comparison is made before making the division. In this way, the numerator and denominator that results in the smallest gain are obtained and finally, the division is made for obtaining the optimal fundamental gain (k_F). The whole process is depicted in Fig. 5.12.

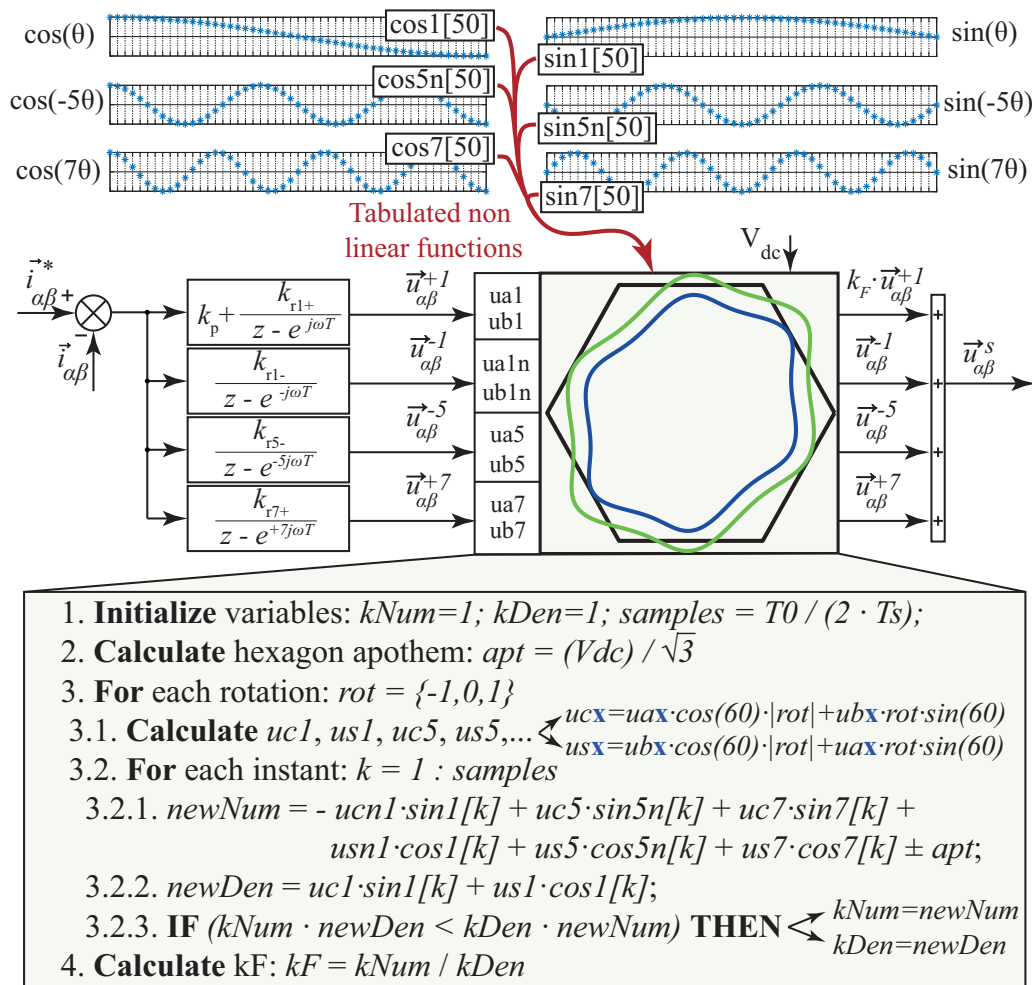


Figure 5.12: Graphical description of simplified implementation of DFIMS. Non-linear functions are tabulated and the gain is evaluated for every instant.

5.4.3.2.5. Antiwindup algorithm description: As it has been previously highlighted, saturation is carried out over the FPS component of the output voltage ($\vec{u}_{\alpha\beta}^{+1}$). The reduction of this output voltage components implies a reduction of the FPS component of current exchanged with the grid ($\vec{i}_{\alpha\beta}^{+1}$). In some way, this reduction over the current reference can be understood as an indirect saturation over the current references, topic that is addressed in Section 5.5. While the saturator is actuating, the reference FPS current cannot be reached and therefore an steady-state signal error exists between reference and measured signals. This steady state error signal is a complex sinusoidal that would bring the output of the ROGI ($h = +1$) to infinite.

Therefore, if this situation wants to be avoided, the FPS current reference needs to be reduced. Ideally, the amount of current that should be reduced from the reference is the amount that is not possible to deliver due to the saturation. In [64], the amount of voltage that is not given due to the saturation, is calculated and it is transformed to the amount of current that is not being exchanged with the grid. This transformation is made through the nominal values of the filter impedances for the corresponding sequence.

However, in the proposed algorithm, a step further is taken and antiwindup system is applied at the origin of the saturation. One of the capabilities that commonly takes the trajectory out of the dc-bus limitation is delivering capacitive reactive power. If the reduction is directly done over the FPS reference current component ($\vec{i}_{\alpha\beta}^{+1*}$) the reduction is indirectly carried out over both active and reactive powers. However, the active power reference achievement (P^*) is more important than the reactive power reference achievement (Q^*) and in addition, its influence over the voltage output is not as high as the one for (Q^*). In this way, the adopted strategy for the antiwindup in this application is to reduce as far as possible from the reactive power reference (Q^*) and then just in case that it cannot be further reduced, reduce from the active power reference (P^*).

Assuming a VSI connected to the grid through an L-filter, the relation between the output ac-voltage and the exchanged grid current for the FPS is described as:

$$\vec{u}_{\alpha\beta}^{+1} - \vec{e}_{\alpha\beta}^{+1} = \vec{i}_{\alpha\beta}^{+1} \cdot (R + j\omega L) \quad (5.51)$$

where R and L are the nominal filter resistance and inductance values and $\vec{e}_{\alpha\beta}^{+1}$ is the FPS grid voltage. When the output voltage component ($\vec{u}_{\alpha\beta}^{+1}$) is out of the limitations, the FPS voltage output is saturated ($\vec{u}_{\alpha\beta}^{+1s}$), resulting in a reduced delivered current:

$$\vec{u}_{\alpha\beta}^{+1s} - \vec{e}_{\alpha\beta}^{+1} = \vec{i}_{\alpha\beta}^{+1} \cdot (R + j\omega L) \quad (5.52)$$

The difference of delivered current can be written as:

$$\vec{i}_{\alpha\beta}^{+1} - \vec{i}_{\alpha\beta}^{+1s} = \Delta \vec{i}_{\alpha\beta}^{+1} = \frac{\Delta \vec{u}_{\alpha\beta}^{+1}}{(R + j\omega L)} \quad (5.53)$$

where $\Delta \vec{u}_{\alpha\beta}^{+1} = \vec{u}_{\alpha\beta}^{+1} - \vec{u}_{\alpha\beta}^{+1s}$ and $\Delta \vec{i}_{\alpha\beta}^{+1} = \vec{i}_{\alpha\beta}^{+1} - \vec{i}_{\alpha\beta}^{+1s}$. Therefore, the amount of not provided current ($\Delta \vec{i}_{\alpha\beta}^{+1}$) can be expressed as the components for P^* and Q^* :

$$\begin{bmatrix} \Delta P^* \\ \Delta Q^* \end{bmatrix} = \begin{bmatrix} e_{\alpha}^{+1} & e_{\beta}^{+1} \\ e_{\beta}^{+1} & -e_{\alpha}^{+1} \end{bmatrix} \begin{bmatrix} \Delta i_{\alpha}^{+1} \\ \Delta i_{\beta}^{+1} \end{bmatrix}. \quad (5.54)$$

The reduction when saturation starts is carried out over the reactive power reference Q^* . In this way, the origin of the saturation is tackled. The reduction is therefore made over constant variables, which helps to avoid the phase shifting problem related with time variant signals. Antiwindup schematics are depicted in Fig. 5.13.

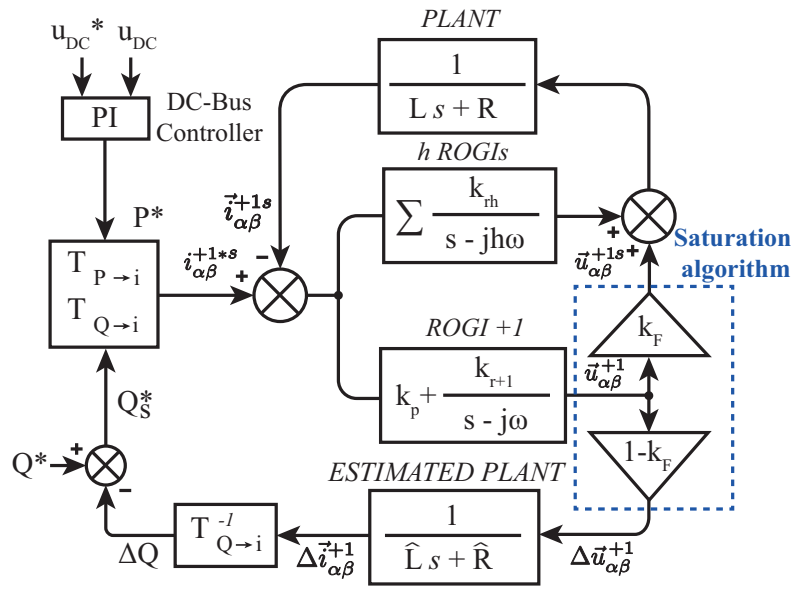


Figure 5.13: Scheme of the antiwindup plus saturator algorithm.

5.4.3.2.6. DFIMS transient analysis: In the last part of the DFIMS proposal, the dynamics analysis when the saturator plus antiwindup algorithms are actuating is carried out. As previously depicted in Fig. 5.13, the saturator can be interpreted as a gain (k_F) that multiplies the voltage component ($\vec{u}_{\alpha\beta}^{+1}$) resulting in a saturated voltage output component ($\vec{u}_{\alpha\beta}^{+1s} = k_F \cdot \vec{u}_{\alpha\beta}^{+1}$). Meanwhile, the exceeding voltage can be expressed as ($\Delta \vec{u}_{\alpha\beta}^{+1} = \vec{u}_{\alpha\beta}^{+1} - \vec{u}_{\alpha\beta}^{+1s} = (1 - k_F) \cdot \vec{u}_{\alpha\beta}^{+1}$). Then, the remaining control actuation is subtracted through the antiwindup algorithm. First, as previously explained, the exceeding control actuation ($\Delta \vec{u}_{\alpha\beta}^{+1}$) is transformed to the exceeding current ($\Delta \vec{i}_{\alpha\beta}^{+1}$) and it can be expressed as an exceeding ΔQ ($\Delta \vec{i}_{\alpha\beta}^{+1*} = \Delta Q^* \cdot T_{Q \rightarrow i}^{-1}$). Therefore, assuming no variation in the active power reference, the total feedback current can be expressed as $\vec{i}_{\alpha\beta}^{+1} = \Delta \vec{i}_{\alpha\beta}^{+1} + \vec{i}_{\alpha\beta}^{+1s}$. If the total FPS current reference ($\vec{i}_{\alpha\beta}^{+1*}$) is taken as input and the total FPS measured current ($\vec{i}_{\alpha\beta}^{+1}$) as output, the closed loop transfer function can be expressed as:

$$\frac{\vec{i}_{\alpha\beta}^{+1}}{\vec{i}_{\alpha\beta}^{+1*}} = \frac{\hat{G} \cdot C_{+1} \cdot (1 - k_F) + G \cdot C_{+1} \cdot k_F + G \cdot \sum C_h}{1 + \hat{G} \cdot C_{+1} \cdot (1 - k_F) + G \cdot C_{+1} \cdot k_F + G \cdot \sum C_h} \quad (5.55)$$

where G is the real plant, \hat{G} the estimated plant, and C_{+1} (FPS) plus C_h (FNS and harmonics) the ROGI controllers. In the case that $\hat{L} = L$ and $\hat{R} = R$, the effect of the saturation would have no effect on the global system dynamics, as shown in Fig. 5.14.

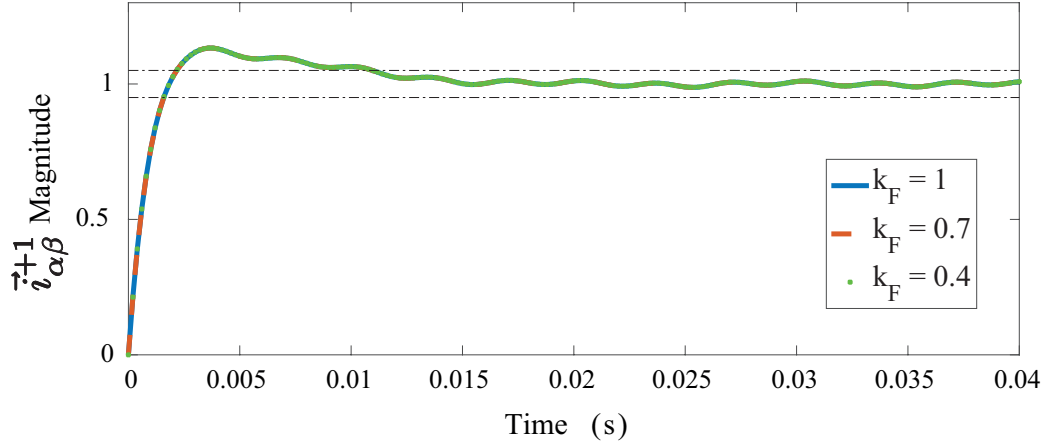


Figure 5.14: Step response of closed loop transfer function with different saturation gains ($k_F = 1$, $k_F = 0.7$, $k_F = 0.4$), with $\hat{L} = L$ and $\hat{R} = R$.

On the contrary, even when estimated parameters highly vary from the real ones (in both underestimation and overestimation), the only effect over the control loop during saturation is a slightly variation over the settling time (Fig. 5.15).

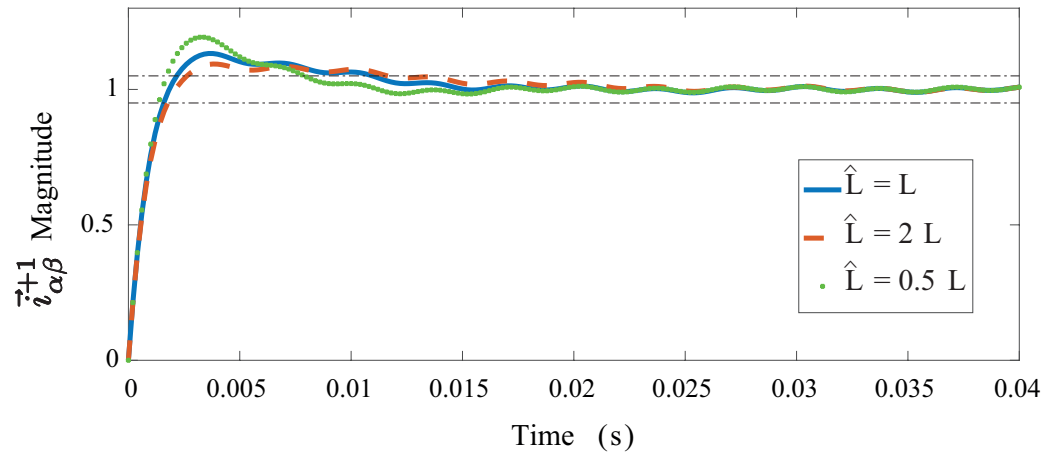


Figure 5.15: Step response of closed loop transfer function with $k_F = 0.4$, and with $\hat{L} = 0.5L$, $\hat{L} = L$ and $\hat{L} = 2L$

5.5. VSC current references saturators

As previously described, the current controller of the VSC needs to take into account that the current reference cannot exceed the limitation imposed by the different components. Usually, the shunt VSC is designed for being able to exchange a nominal power with the grid. This power rating can be expressed as a nominal RMS current (I_N) that can pass across the converter. In any case, the elements that compose the converter presents a maximum admissible current (I_{MAX}) value that necessarily is higher than the current nominal value. In order to protect the elements of the converter, different protections are set. These protections are usually based on software and hardware current protections that in case of overcurrent stop the converter. Overcurrent is considered when the measured current at one phase is higher than a software (I_{SW}) or hardware (I_{HW}) threshold.

$$I_N < I_{SW} < I_{HW} < I_{MAX} \quad (5.56)$$

The idea is therefore, to try to keep the current reference always below the protection threshold. The previously described saturators for the output of the current controller indirectly limit the delivered current. However, the maximum reference current could be directly limited. For this objective, a current value for saturation needs to be selected (I_{SAT}). If at any moment the current references exceed the selected maximum value, the reference currents is limited through the current references saturator. The value of I_{SAT} needs to be selected as an abnormal high value above the nominal current and below the protection values:

$$I_N < I_{SAT} < I_{SW} < I_{HW} < I_{MAX} \quad (5.57)$$

Typically, when exclusively the FPS component is taken into account, the limitation of the current reference can be worked out as a circle. It does not make any difference if the saturation is carried out over the RMS current or over the current amplitude signal. In a similar way, the same limitation circle, would determine if the reference is or not within the safety region in stationary or synchronous reference frame.

However, with the addition of sequences, the trajectory is not as simple as a circle and there not exists a direct correspondence between RMS current and maximum amplitude per phase. Therefore, with the inclusion of harmonic sequences, the current could exceed RMS value or the maximum amplitude independently. In this regard, the current saturator can be implemented in order not to exceed the RMS current the maximum amplitude or both.

5.5.1. RMS current Saturator

With the addition of controlled sequences, the reference current is defined in stationary reference frame as follows:

$$\vec{i}_{\alpha\beta}^* = \vec{i}_{\alpha\beta}^{+1*} + \vec{i}_{\alpha\beta}^{-1*} + \vec{i}_{\alpha\beta}^{-5*} + \vec{i}_{\alpha\beta}^{+7*}. \quad (5.58)$$

Meanwhile, the RMS value of the total reference current ($\vec{i}_{\alpha\beta}^*$) can be worked out as:

$$I_{\text{RMS}} = \sqrt{(i_{\alpha}^{+1*})^2 + (i_{\beta}^{+1*})^2 + \sum [(i_{\alpha}^{h*})^2 + (i_{\beta}^{h*})^2]} \quad (5.59)$$

The total RMS reference current value should not exceed the saturation current threshold I_{SAT} . In the case that this occurs, the different current references components should be reduced in order to get a total current smaller than the saturation limit. This reduction should be made without modification of the phase corresponding to each sequence. In order to achieve this, a gain is multiplied by each component:

$$\vec{i}_{\alpha\beta}^* = k_1 \cdot \vec{i}_{\alpha\beta}^{+1*} + k_2 \cdot \vec{i}_{\alpha\beta}^{-1*} + k_3 \cdot \vec{i}_{\alpha\beta}^{-5*} + k_4 \cdot \vec{i}_{\alpha\beta}^{+7*}. \quad (5.60)$$

Different strategies could be taken in order to determine which ones should be more or less reduced when saturation is reached. As in [59] occurred with the FPS and NFS, gain optimizations can be carried out in order to enhance different parameters. In this case, the different optimizations are out of the scope and the proportional saturation will be employed. Following this strategy in case of reaching RMS saturation, all the components will be reduced with the same priority ($k = k_1 = k_2 = k_3 = k_4$):

$$\vec{i}_{\alpha\beta}^* = k \left(\vec{i}_{\alpha\beta}^{+1*} + \vec{i}_{\alpha\beta}^{-1*} + \vec{i}_{\alpha\beta}^{-5*} + \vec{i}_{\alpha\beta}^{+7*} \right). \quad (5.61)$$

Resulting in a simple equation for calculating the gain k that brings the value of I_{RMS} equal to the threshold saturation current value I_{SAT} :

$$k = \frac{I_{\text{SAT}}}{\sqrt{(i_{\alpha}^{+1*})^2 + (i_{\beta}^{+1*})^2 + \sum_{h \in H} [(i_{\alpha}^{h*})^2 + (i_{\beta}^{h*})^2]}} \quad (5.62)$$

where if k is higher or equal than 1, the reference current is smaller than the threshold and no action needs to be carried out. Otherwise, if k is smaller than the unity, all the current reference sequences would be reduced by the k parameter. In this case, if the current references come from a previous controller, it needs to be stopped in order to avoid the continuous increment of references.

5.5.2. Maximum peak current value Saturator

Meanwhile, the current saturator can be implemented with the objective of avoiding that any of the instantaneous phase currents could exceed the saturation value. The hardware protections are usually implemented by thermal magnetic circuit breakers that are able to detect an overcurrent or short-circuit in any of the phases and make a physical disconnection in times of milliseconds. This protection needs to be set as a complementary protection for an extreme situation where the control alarms have failed. If an abnormal situation occurs, a lower level software alarm needs to be implemented in the control algorithm. In this concern during the current measurements of each phase, if the measured value exceed the selected threshold, the control needs to be stopped and the system disconnected. In this regard, the software alarm will stop the system resulting in less working hours of the converter.

Although this alarm needs to exist and it is the first one in being checked, an additional saturation limit could be set that prevents the reference currents to be out of the limits. In this context, a threshold (I_{SAT}) is set below the software alarm threshold (I_{SW}). In this way, if any of the phases from the reference currents exceed the threshold (I_{SAT}) the reference currents are recalculated before the current controller, avoiding the software alarm activation.

In stationary frame the current references (i_α^* and i_β^*) can be written in three-phase signals (i_a^* , i_b^* , i_c^*) through the invariant amplitude Clarke transformation:

$$\begin{bmatrix} i_a^* \\ i_b^* \\ i_c^* \end{bmatrix} = \begin{bmatrix} 1 & 0 \\ -\frac{1}{2} & \frac{\sqrt{3}}{2} \\ -\frac{1}{2} & -\frac{\sqrt{3}}{2} \end{bmatrix} \begin{bmatrix} i_\alpha^* \\ i_\beta^* \end{bmatrix}. \quad (5.63)$$

From previous equation, several conclusions can be extracted, in order to do not exceed I_{SAT} by any of the phases. For example, if the maximum value that i_a^* can adopt is I_{SAT} it implies that i_α^* cannot exceed $\pm I_{SAT}$. Assuming that i_α^* is now equal to $-I_{SAT}$, i_β^* could not exceed $I_{SAT}/\sqrt{3}$ in order to keep $i_b^* < I_{SAT}$. Therefore, the first limiting point can be found in $(I_{SAT}, \frac{I_{SAT}}{\sqrt{3}})$. In a similar way, the six points could be worked out and they are collected in Table 5.3 and the hexagon that is shaped with the limiting points is represented in Fig. 5.16.

Table 5.3: Limiting $\vec{i}_{\alpha\beta}$ values

Limiting vertices	1	2	3	4	5	6
i_α^*	$-I_{SAT}$	$-I_{SAT}$	$+I_{SAT}$	$+I_{SAT}$	0	0
i_β^*	$+\frac{I_{SAT}}{\sqrt{3}}$	$-\frac{I_{SAT}}{\sqrt{3}}$	$+\frac{I_{SAT}}{\sqrt{3}}$	$-\frac{I_{SAT}}{\sqrt{3}}$	$+\frac{2 \cdot I_{SAT}}{\sqrt{3}}$	$-\frac{2 \cdot I_{SAT}}{\sqrt{3}}$

Therefore, in a general way, if the amplitudes of the three phase currents want to be kept below a desired threshold in any situation, the trajectory depicted by the current

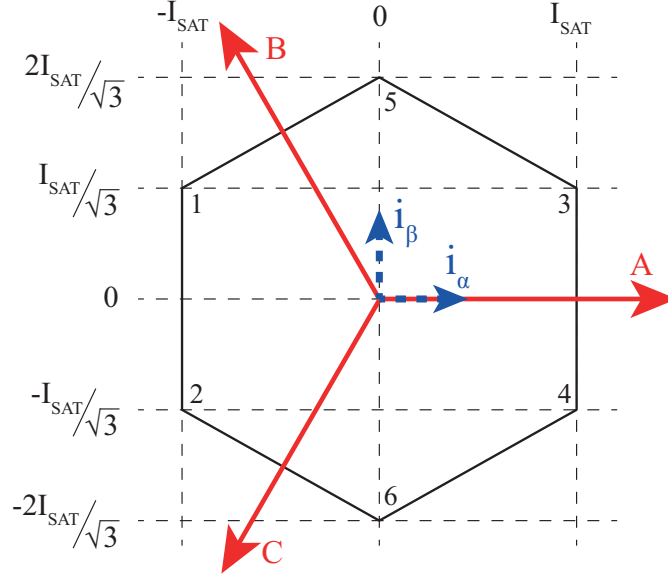


Figure 5.16: Current limitations in stationary $\alpha\beta$ axis for amplitude saturation.

references $\vec{i}_{\alpha\beta}$ needs to be contained inside the hexagon. The trajectory depicted by the reference current is defined by:

$$\vec{i}_{\alpha\beta}^* = \vec{i}_{\alpha\beta}^{+1*} + \vec{i}_{\alpha\beta}^{-1*} + \vec{i}_{\alpha\beta}^{-5*} + \vec{i}_{\alpha\beta}^{+7*} \quad (5.64)$$

Therefore, the problem resides on keeping a trajectory inside the limits of an hexagon. Although the beginning of the problem comes from a completely different nature, the reader could appreciate that geometrically it is similar to the already solved problem for dc bus voltage saturation in current controller saturators. Actually, geometrically the only difference with the previous approach is the rotation of the hexagon by 90° . Following the previous methodology, the trajectory could be written as:

$$\vec{i}_{\alpha\beta}^* = \underbrace{I_1^* e^{j(\omega t + \phi_1)}}_{\text{Fundamental}} + \underbrace{\sum_{h \in H} I_h^* e^{j(h\omega t + \phi_h)}}_{\text{Perturbations}}. \quad (5.65)$$

In order to keep the trajectory inside the linear modulation range, independent gains multiply each one of the current reference sequences. These gains that can adopt a value between 0 and 1 are the reduction factors that need to be calculated. With the inclusion of the saturation gains, the trajectory could be rewritten as:

$$\begin{aligned} \vec{i}_{\alpha\beta} = i_\alpha + j \cdot i_\beta = & k_F I_1 \cos(\theta + \phi_1) + j \cdot k_F I_1 \sin(\theta + \phi_1) \\ & + \sum_{h \in H} [k_h I_h \cos(h\theta + \phi_h) + j \cdot k_h I_h \sin(h\theta + \phi_h)]. \end{aligned} \quad (5.66)$$

Taking into account its representation on a complex plane, the trajectory can be divided into x and y coordinates:

$$x = k_F I_1 \cos(\theta + \phi_1) + \sum_{h \in H} k_h I_h \cos(h\theta + \phi_h) \quad (5.67)$$

$$y = k_F I_1 \sin(\theta + \phi_1) + \sum_{h \in H} k_h I_h \sin(h\theta + \phi_h). \quad (5.68)$$

On the contrary of current controller saturator, in this case the constant function is located in the x axis. Therefore, when DFIMS saturator is applied, the x coordinate of $\vec{i}_{\alpha\beta}$ needs to be compared with the left and right hexagon edges at $\pm I_{SAT}$.

For calculating the independent gains, the same process as described for DFIMS employed for the current saturation. The process consists on detecting the most external trajectory point from the left and right edges and calculating the gains that would bring it at the limit of the hexagon. For solving the equations, the priority of reduction among sequences needs to be set in order to obtain a deterministic system. Then, the trajectory is rotated $\pm 60^\circ$, and for each one, a gain is obtained, for checking the trajectory with the whole hexagon. Finally, for ending with the saturation process, the smaller gain value smaller than the unity is selected as the reduction factor.

As the saturation is applied over the reference currents, if they are obtained from a previous controller with integration part, it needs to be stopped as soon as the saturation is reached.

5.6. Simulation Results

In order to test the proposed current controller DFIMS, the distorted grid and a NPC converter has been simulated in Matlab/Simulink R2016b. The grid and converter parameters are described in Table 5.4.

Table 5.4: Simulation parameters description

Parameter category	Parameter	Parameter Value
Grid Voltage	Grid frequency (f_1)	50 Hz
	FPS 230 V ($h=+1$)	0.91 pu \rightarrow 1.06 pu
	FNS ($h=-1$)	0.03 pu
	harmonic sequence ($h=-5$)	0.06 pu
	harmonic sequence ($h=+7$)	0.05 pu
Filter	Inductance (L)	750 μ H
Control references	DC-Bus voltage	675 V
	Q reference	110 kVar
Frequencies	Sampling frequency (f_s)	5 kHz
	Switching frequency (f_{sw})	5 kHz

The converter is working as a *Static Compensator (STATCOM)* and 110 kVar capacitive reactive power is requested (Q^*). The high requested value of reactive power is

reachable when the grid voltage is lower than the nominal (0.91 pu). However, if the grid voltage rises to a higher value (1.06 pu), the requested capacitive reactive power value becomes unreachable. This occurs because the needed voltage at the ac side of the converter for delivering the requested Q^* is out of the limits for the available dc-bus voltage. Therefore, when this occurs, three different alternatives are tested.

In the first one, no distortion free saturator nor antiwindup are applied in the control algorithm. With this strategy, overmodulation is reached and as the requested input is not satisfied, the control increases the actuation request, until reaching an unstable situation. This case is depicted in Fig. 5.17.a.

In the second case, the literature distortion free saturator proposed in [64] is implemented. In this situation, when the requested output voltage goes beyond the limitations, it starts to decrease until bringing all the ac voltage values within the dc limitations (hexagon). This process takes some time until bringing the whole trajectory to the linear modulation range and during this time overmodulation occurs. As a consequence, during this transient, high levels of harmonic sequences are injected into the grid, as depicted in Fig. 5.17.b. The second important fact of this saturator is that for achieving the reduction of the trajectory, all the different voltage components are reduced in the same amount. As reduction is also carried out over the harmonic components, it implies that our converter is not generating the harmonic voltage components for reducing the electric potential difference between grid and converter, generating harmonic currents. This effect is depicted in Fig. 5.17.c where harmonic currents are exchanged at the controlled harmonic components (5^{th} and 7^{th}).

Finally, in the third case, the proposed DFIMS is tested under the same described circumstances. In this case, the proposed DFIMS algorithm allows to calculate the optimal gain that keeps the trajectory within the limitations. It is calculated as soon as the steady state is reached and the settling time is the one defined by the current control loop. In this regard, as it has been proved and as it can be observed in Fig. 5.17.d, the saturation is performed several times sooner than in the other saturation algorithms. In addition, this saturator always delivers the minimum distortion to the grid by generating the requested harmonic voltage to compensate the electric potential difference.

The obtained results of the simulation test for the three different cases are collected in Table 5.5.

Table 5.5: Simulation Results

Strategy	Overmodulation	Literature Sat.	Proposed DFIMS
Q delivered	109 kVAr (unstable)	41.5 kVAr	34.7 kVAr
i_g THD ($h < 50$)	10.23 %	3.40 %	1.40 %
$\hat{i}_g(h = 1)$	209.2 A	80.6 A	66.6 A
$\hat{i}_g(h = 5)$	11.87 A	1.55 A	0.33 A
$\hat{i}_g(h = 7)$	4.56 A	1.09 A	0.27 A

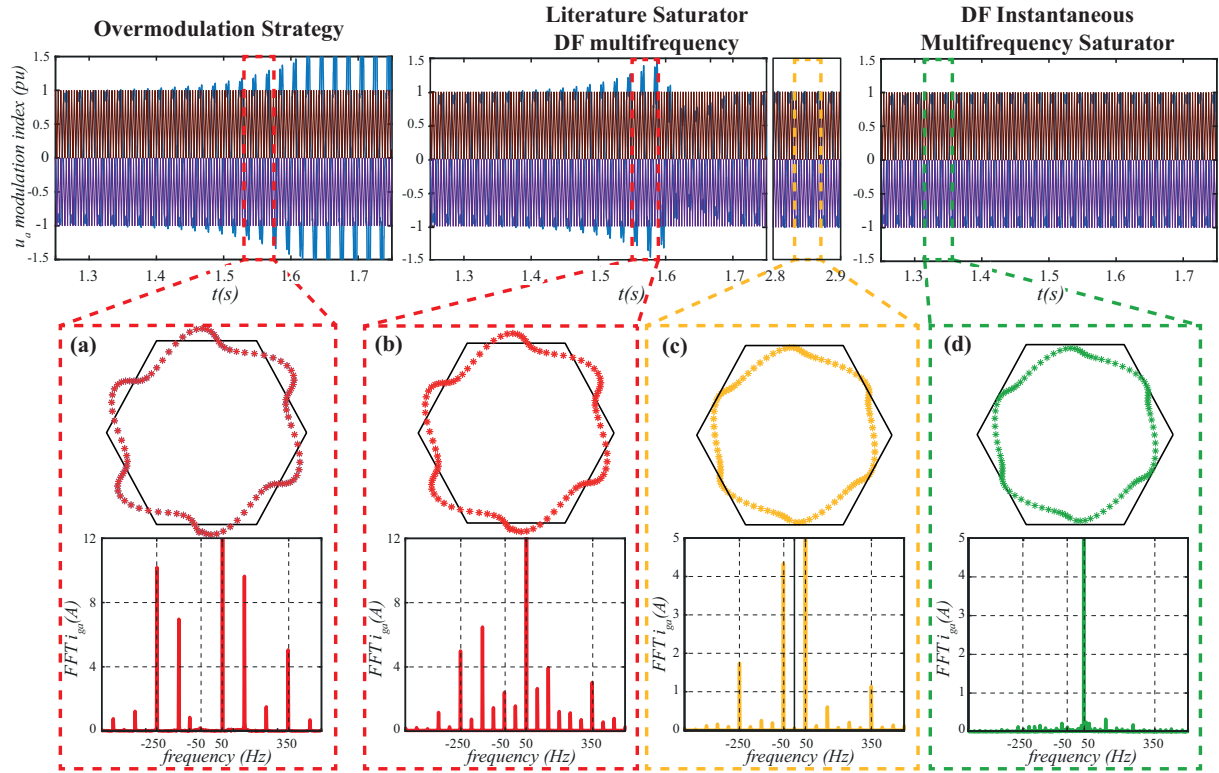


Figure 5.17: Comparison between the different strategies in a simulated environment (Grid voltage = 1.06 pu, Q increasing until 110 kVar). The transition of the modulator signal for phase a (u_a) is depicted above. The $\vec{u}_{\alpha\beta}$ trajectory for each situation and the FFT of the signals are also depicted. The overmodulation is depicted before reaching instability and for the literature saturator, the transient and the steady state performance are shown.

In order to test the transient response of the proposed saturator, a different test was carried out. For this test a step is applied in the reactive power reference (Q^*). This test is carried out into three different scenarios. In the first scenario, a high value of dc-bus voltage is set and the desired reactive power value is reachable without overmodulation. As the saturator algorithm does not actuate in this scenario, the time until the reactive power reaches the Q^* value corresponds to the current control loop settling time. For the second and the third tests the dc-bus voltage is set to a lower value. The final value of the step is unreachable and therefore, the saturator actuates. For the second test, the literature saturator is employed and for the third test the one employed is the proposed DFIMS. In these two cases, the time until the reactive power reaches the Q^* value corresponds to the settling time of both, saturator plus current controller. The results and the different settling times can be seen in Fig. 5.18.

As it was analyzed during the previous section, the DFIMS does not increase the current controller settling time. However, it can be seen how the literature saturators increase the settling time. This fact makes the proposed DFIMS the fastest saturator up to date.

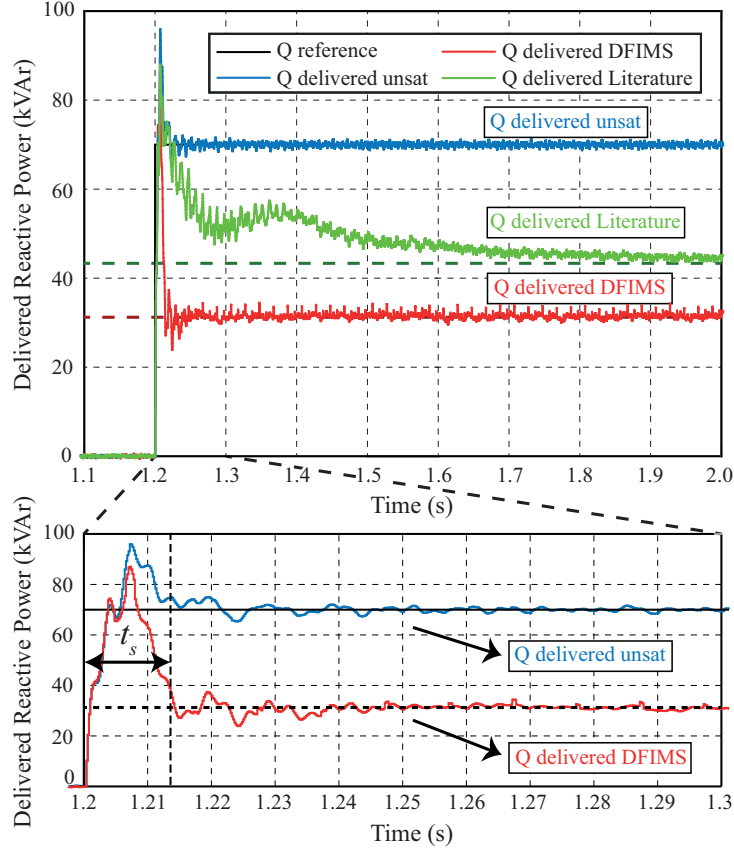


Figure 5.18: Dynamic response with a step of Q^* : without saturation (higher dc bus voltage) and when literature saturator and DFIMS actuate. Same t_s is achieved with DFIMS and without saturation.

5.7. Conclusions

Multifrequency control of power converters is gaining importance due to the necessity of controlling the harmonic currents exchanged with the grid. While different goals want to be met with fundamental and harmonic components, the converter could reach its physical limitations. These limitations are divided into currents and voltages. When harmonic components are dealt with, the voltage limitation becomes crucial.

If this limitation is not prevented, injection of low order current harmonics to the grid occurs. In order to avoid this problem, different saturators have been proposed in the literature. In this chapter, those saturators have been described and analysed. A new DFIMS saturator has been proposed that is able to instantaneously calculate the optimal reduction factors for avoiding this issue.

The proposed algorithm always delivers the minimum current THD meeting the IEEE standards. In addition the saturation is carried out instantaneously. As a disadvantage, when saturation occurs, in order to avoid overmodulation with the proposed algorithm the reactive capacitive power reference is slightly reduced.

The novel proposed DFIMS is compared with the previous multifrequency saturator in simulation. It shows the benefits in both, dynamics improvement and THD reduction.

Chapter 6

Multifrequency control for PCC voltage distortion compensation

6.1. Introduction

As it has been described along the document, between the different multi-frequency applications, harmonic sequences current references can be calculated following different strategies:

- Harmonic current references can be calculated in order to deliver the active power as constant as possible, as described in Chapter 4. Additionally, some optimizations can be performed, as to reduce the current THD while the main ripple components are reduced, as in Section 4.5.
- Harmonic current references can be set to zero in order to do not exchange harmonic currents with the grid and getting the minimum current THD. An example of this strategy is shown for testing the proposed saturator in Chapter 5.
- The last of the strategies falls on calculating the current reference in order to deliver the needed harmonic current that the non-linear loads are demanding and reducing at the same time the voltage harmonic presence at the PCC.

Different types of loads are commonly connected to the grid. Most common loads are linear loads(resistive loads, inductive loads and capacitive loads). Anyhow, in the last years the number of non-linear loads has increased. Non-linear loads provoke an exchange of harmonic currents with the grid, which is considered undesirable. This harmonic current exchange also affects the voltage harmonic components at the PCC, especially with weak grids.

In order to increase the capabilities of the VSIs and make them more attractive through grid support, they can face the problem of compensation of the harmonic currents con-

sumed by non-linear loads. The problem can be faced at two stages that are analysed along the chapter:

- In the first stage, the VSI can be connected close to the non-linear load and deliver the harmonic currents required by it. With this solution, the currents are not consumed from the grid. Therefore, the harmonic currents are not propagated along the power network, avoiding harmonic voltages appearance. This functionality has been usually accomplished by APFs.
- In the second stage, the VSI is connected at any point of the grid (PCC). The voltage measurements at the PCC are a reflection of the harmonic currents consumed by different non-linear loads. Here, it will be pursued to inject enough harmonic currents in order to compensate the harmonic voltages at the PCC and enhance grid power quality.

6.2. VSC with Active Power Filter (APF) functionality

In the first strategy, in some scenarios where non-linear loads are connected to the grid or a considerable amount of harmonic are consumed from it, APF appears as the right solution [67]. Active power filters are power converters, which are in charge of compensating these current harmonics through power conversion. These devices measure the current consumed by non-linear load and inject the enough currents in order to compensate them and consume a cleaner total current from the grid, as depicted in Fig. 6.1.

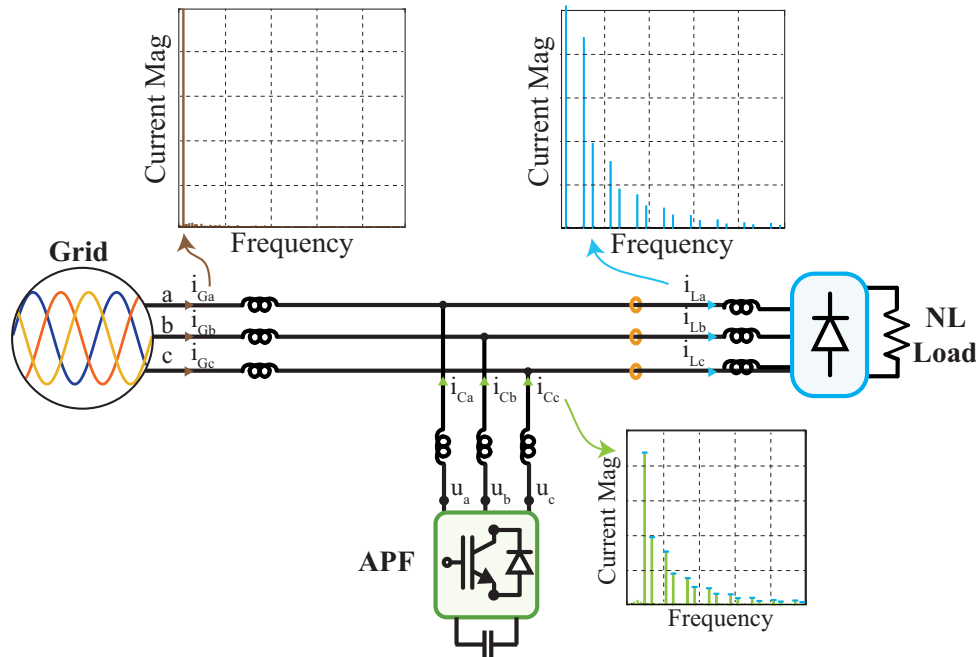


Figure 6.1: Typical scheme of an APF compensating the harmonic current consumed by a non-linear load, in order to consume a clean current from the grid.

Commercial APFs are commonly shunt connected and they measure the current consumption of the load ($\vec{i}_{\alpha\beta L}$) or the total consumption from the grid ($\vec{i}_{\alpha\beta G}$) [68]. Control algorithms employ those measurements in order to obtain the reference currents ($\vec{i}_{\alpha\beta C}^*$) that the APF needs to exchange ($\vec{i}_{\alpha\beta C}$) for compensation of harmonic current and power factor.

APFs are usually employed in different industries: metallurgy, petrochemicals, mechanical, paper, plastic processing and textile industries (rectifiers, rolling mills, electric arc furnaces), transportation industries (rectifiers and inverters for electric vehicles, electric motorcycles), telecommunication, medical and construction industries.

Therefore, these industries are requiring more and more from APFs, making that sometimes a high rated compensation current could be demanded, and a decision is needed between installing a greater APF or installing several APFs.

6.2.1. VSIs for Distributed generators with APF capabilities

Regarding to active power filter functionality, the VSI associated with the distributed generators, are physically similar to the one employed for standalone active power filter [118]. Then, in order to increase the interest and the benefits of installing new distributed generators, the VSI associated to these generators could accomplish secondary goals in addition to the main task of active power injection. Among those secondary goals, active power filter functionality can be included. As counterpart, the inclusion of different capabilities under the same VSI, could reach the converter limitations.

It needs to be noted, that in most cases, a distributed generator VSI would not be able to perform the same compensation as an APF, due that the APF has the compensation as its exclusive task. Anyhow, it is the combined operation of both, energy injection and compensation what make them so interesting. However, the inclusion of new capabilities implies to require an additional effort to VSIs which can push it to the limit.

The mentioned limitations can be reached in different ways. Firstly, the addition of the different current components, FPS ($\vec{i}_{\alpha\beta}^{+1}$), FNS ($\vec{i}_{\alpha\beta}^{+1}$) and harmonic components (usually, $\vec{i}_{\alpha\beta}^{-5}$ and $\vec{i}_{\alpha\beta}^{+7}$) could exceed the RMS current converter limitation or the power limitations [50].

However, when the issue of harmonic current compensation is faced, another limitation needs to be taken into account. Usually, for current compensation, the same current that is consumed by the non-linear loads, needs to be provided by the controlled inverter. The injected harmonic currents are described as follows:

$$\vec{i}_{\alpha\beta}^h = \frac{\vec{u}_{\alpha\beta}^h - \vec{e}_{\alpha\beta}^h}{R + j\omega h L}. \quad (6.1)$$

The effect of the inductance part over the total impedance is predominant and especially when harmonics are controlled. In order to inject a small amount of current, the needed output voltage ($\vec{u}_{\alpha\beta}^h$) drastically increases with the harmonic order.

Therefore, the addition of the different voltage sequences that are needed at the output could reach the voltage output limitations determined by the input dc-bus voltage. These limitations, and the control implementation in order to obtaining the maximum from the inverter without exceeding them, in a multifrequencial context, were analysed during chapter 5.

Firstly, it needs to be noticed that in case of reaching limitations, the converter will not be able to satisfy all the capabilities. If all the capabilities want to be achieved at all times, two different strategies could be followed. On the one hand, an oversized inverter could be employed, with a higher rated power and a high dc-bus voltage. On the other hand, a solution that has gained interest along the last years, is to work with different VSIs with lower rated power and in a cooperative way, accomplishing the required capabilities.

6.2.2. Parallel operation of VSIs for DGs with APF capabilities

As the number of non-linear loads is increasing, more APF applications are being required. The capacity of the employed converters could be increased in order to meet the requirements. Another possibility is the alternative, where several inverters with lower capacity are connected in parallel. This option is gaining more interest, due to the increment of flexibility and reliability in operation [69].

In this context, the control strategies for parallel APFs are gaining attention for harmonic and reactive power compensation in distribution grid. Among the different control strategies suitable for parallel APFs:

- Frequency splitting
- Power Splitting
- Master Slave Control
- THD based cooperative Control
- Droop Control for APF

6.2.3. Proposed strategy for maximum power extraction during Parallel operation of VSIs for DGs with APF capabilities

As previously explained, the increment of non-linear loads has made that the local compensation of harmonic currents has gained more interest. The similar electronic topology of APFs and inverters associated to DGs has made that the last ones can also achieve

harmonic currents compensation. As the main task of VSIs associated to DGs is to deliver power, harmonic compensation can be accomplished until reaching limitations (as a secondary goal). In order to accomplish these objectives, the limitations, especially the output voltage limitation can make that capabilities just could be perfectly addressed with an oversized converter or, what is being preferred due to flexibility, cooperative satisfaction of the task within converters.

Regarding to that point, a new strategy is proposed here. This strategy, when dc voltage saturation is reached for any of the inverters, the harmonic compensation would be completed by the rest of inverters. The compensation of harmonics is desired to be achieved as local as possible. It means that if constraints are not reached, the closest inverter to the load should be the first in compensating harmonics, if it is not able to compensate all the harmonic currents by just itself, the total harmonic current would try to be compensated by the closest and the second closest, and in this way, successively. With this strategy, harmonic currents propagation is avoided and therefore harmonic voltage distortion is prevented.

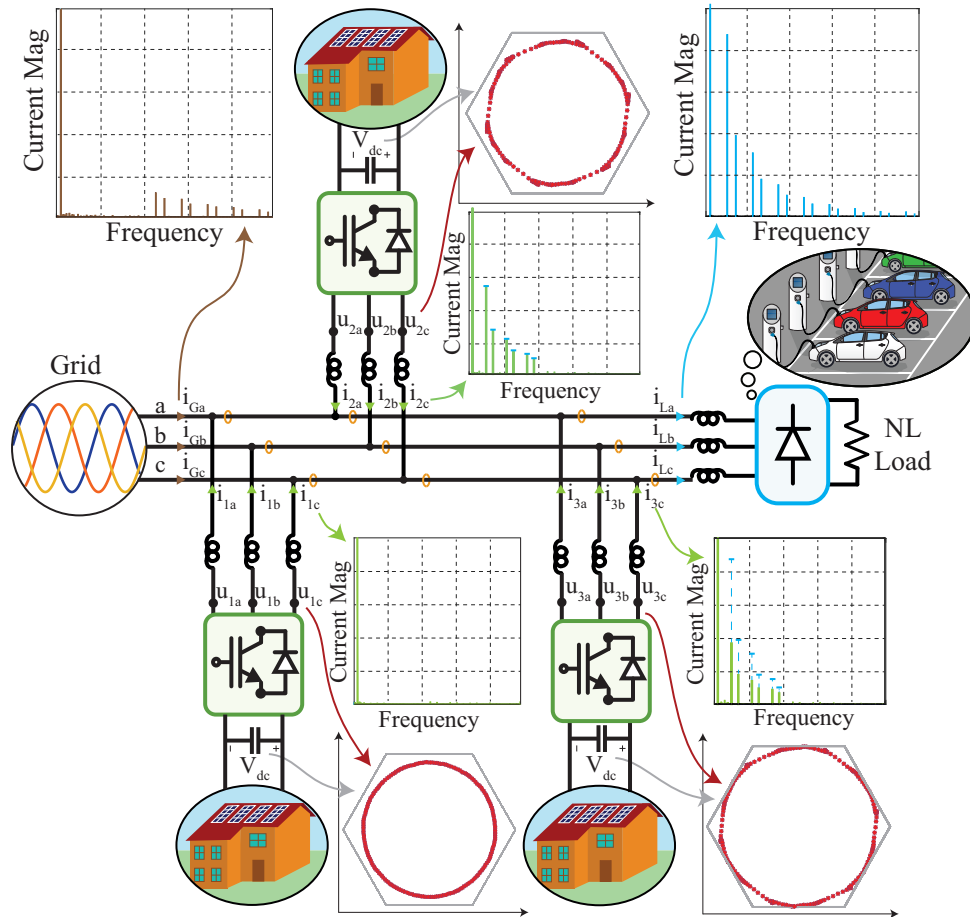


Figure 6.2: Application of Parallel VSIs with APF Capabilities.

Therefore, as shown in Fig. 6.2, the proposed strategy actuates when the demanded output voltage is too high, and the linear range is about to be abandoned. This strategy

deliver the enough harmonic current (i_2) in order to achieve the remaining compensation of ($i_L + i_1$).

Although the method, is valid for n converters, in order to simplify the explanation of the strategy, the number of inverters will be reduced to two and the closest inverter to the load will receive the name of “Load VSI” and the closest one to the grid will be named as “Grid VSI”.

For the control of the inverter, as the currents are measured downstream of the VSI, the harmonic currents that the inverter would need to deliver are well-known. First, it is needed to make a decomposition of the harmonic currents for precisely knowing each one of the harmonic sequences. For doing this, a similar system that the ones employed for the voltage synchronization and sequences detection can be now employed for the currents decomposition [30] [41].

The structure of the sequences detector is based on multiple ROGIs where each one presents a pole at the interesting frequency. In this way, for completing the closed loop, the feedback is generated as the sum of the different outputs from each ROGI. Therefore, taking into account FPS, FNS and the most common harmonic sequences (-5 & +7) the measured load current can be decomposed as:

$$\vec{i}_{\alpha\beta L} = \vec{i}_{\alpha\beta L}^{+1} + \vec{i}_{\alpha\beta L}^{-1} + \vec{i}_{\alpha\beta L}^{-5} + \vec{i}_{\alpha\beta L}^{+7} \quad (6.2)$$

To obtain accurately each one of the components is essential for the proper accomplishment of the algorithm. Especially, for the harmonic components, which generate the harmonic reference components that the inverter needs to provide:

$$\vec{i}_{\alpha\beta}^{-5*} = -\gamma \cdot \vec{i}_{\alpha\beta L}^{-5} \quad (6.3)$$

$$\vec{i}_{\alpha\beta}^{+7*} = -\gamma \cdot \vec{i}_{\alpha\beta L}^{+7} \quad (6.4)$$

where γ stands for the applied reduction factor in the case that saturation is reached and that will be described later. On the contrary, references for FPS ($\vec{i}_{\alpha\beta}^{+1}$) and FNS ($\vec{i}_{\alpha\beta}^{-1}$) are worked out in order to control reactive and active power. Those components would be reduced in the case that the harmonics components have been completely reduced ($\gamma = 0$), and in that way, the maximum active power will be always delivered. Then, the total reference current is calculated as:

$$\vec{i}_{\alpha\beta}^* = \vec{i}_{\alpha\beta}^{+1*} + \vec{i}_{\alpha\beta}^{-1*} + \vec{i}_{\alpha\beta}^{-5*} + \vec{i}_{\alpha\beta}^{+7*}. \quad (6.5)$$

Therefore, the total error signal ($e = \vec{i}_{\alpha\beta}^* - \vec{i}_{\alpha\beta}$) passes through the MROGI current controller. There, each ROGI is in charge of generating the proper actuation signal $\vec{u}_{\alpha\beta}^h$ that reduces the error for the tuned frequency. The total actuation signal that would be

in charge of the switches switching after the PWM generation is described as:

$$\vec{u}_{\alpha\beta} = \vec{u}_{\alpha\beta}^{+1} + \vec{u}_{\alpha\beta}^{-1} + \vec{u}_{\alpha\beta}^{-5} + \vec{u}_{\alpha\beta}^{+7} \quad (6.6)$$

However, under some circumstances it could occur that the whole trajectory followed for the different instants is not completely inside the limiting hexagon shaped by the dc-bus. Now, the reduction factor γ can be worked out as in [66]. In this way, the magnitude to be applied at the output of the inverter $|\vec{u}_{\alpha\beta}|$ ($|\vec{u}_{ref}|$) is compared with the magnitude of the hexagon for that phase $|\vec{v}_{hex}|$:

$$\delta = \max(|\vec{u}_{ref}| - |\vec{v}_{hex}|). \quad (6.7)$$

Finally, for obtaining the proper value of γ , which is in charge of reducing the current references with respect to the measured harmonic load currents δ is integrated and limited within the interval $[0,1]$.

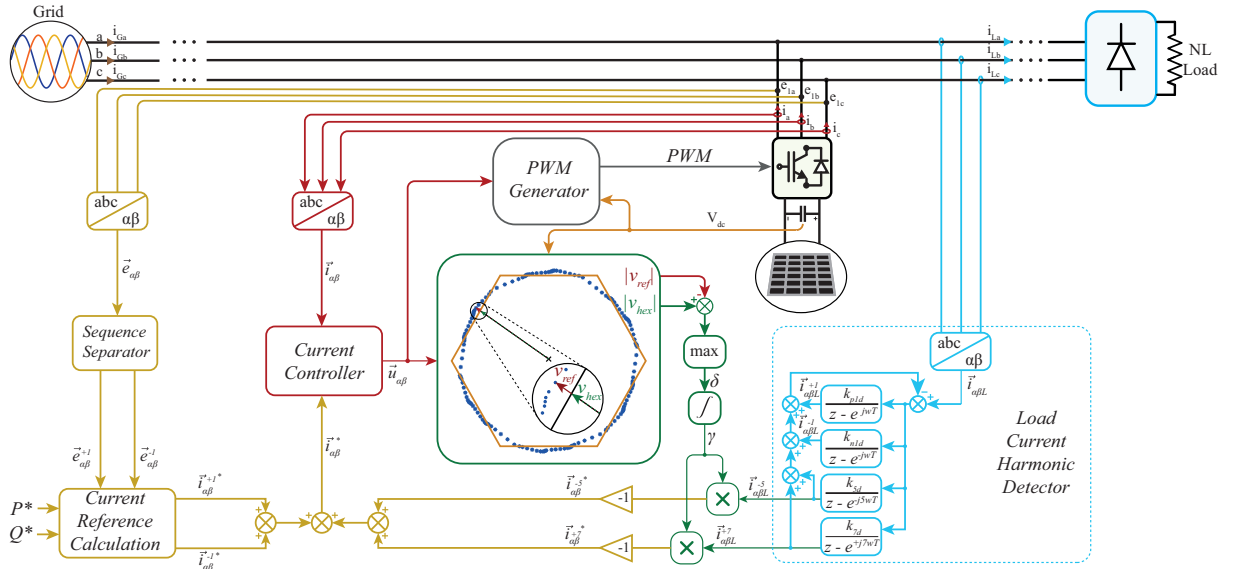


Figure 6.4: Scheme of the employed saturation strategy for parallel connected distributed generators.

Then, as previously specified, if the saturation algorithm needs to act, γ will be different to 1 and therefore, the total harmonic currents would not be completely compensated. In this case, is where the harmonic current that the next inverter measures ($\vec{i}_{\alpha\beta L}^{-5}$ and $\vec{i}_{\alpha\beta L}^{+7}$) would be different to zero and therefore, harmonic components references would not be zero, reaching the compensation in a cooperative way.

6.3. Harmonic PCC voltage reduction

As previously described the harmonic currents can be measured and compensated, when non linear loads are locally connected. However, two main disadvantages appear in this context:

- The location of the non-linear load needs to be close to the inverter.
- Additional current sensors are needed.

Therefore, a second strategy appears, which consists into perform compensation without employing measurements of harmonic currents consumed by non-linear loads. On contrary to the previous strategy, what it will be pursued here is to compensate the grid harmonics in an indirect way, through the voltage measurements at the PCC. In this way, if harmonic voltages are presented at the PCC, it indicates that grid distortion exists. This grid distortion is due to the harmonic current consumption of non-linear loads that have not been locally compensated and that have been propagated along the grid.

For analysing PCC harmonic voltage compensation, a general case where different non-linear loads are connected up and downstream is analysed in Fig. 6.5.a. Firstly, as the complete grid is too complex to analyse, at some point the rest of the grid needs to be assumed as a voltage power supply (which could be slightly distorted within the standards limitations) with a grid impedance.

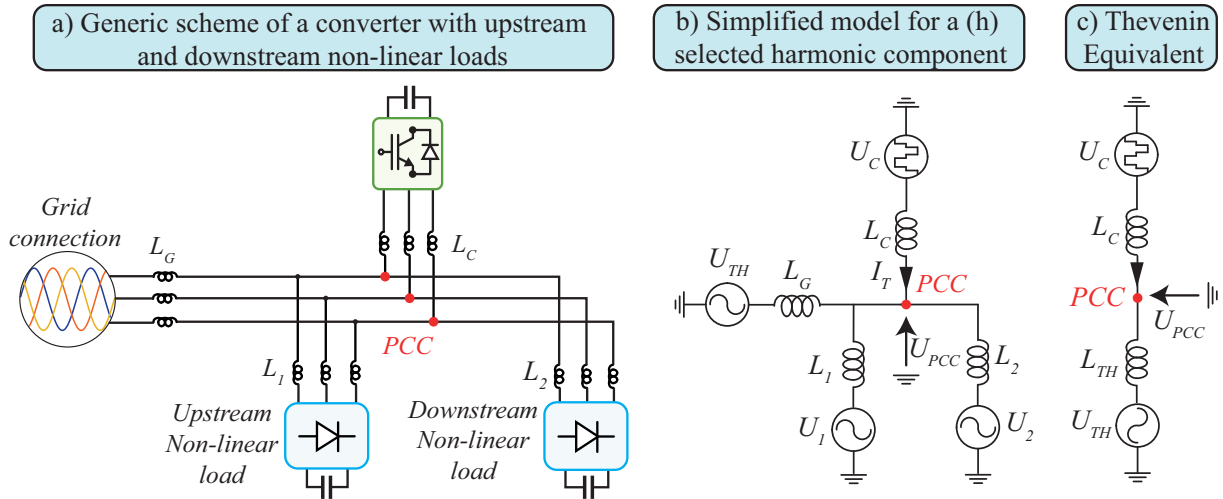


Figure 6.5: General case with non-linear loads up and downstream from the PCC and its equivalence.

Then, assuming exclusively a single harmonic component (h) the model can be simplified as depicted in Fig. 6.5.b. In this case, the non-linear load can be represented as harmonic voltage sources. The pursued objective is that through generating a certain voltage at the converter output (U_C), a compensation can be performed that reduces to zero the harmonic voltage component at the PCC (U_{PCC}).

However, although a variation in the converter output voltage (U_C) results into different currents distribution, it would be simplified through the Thevenin's theorem. As far as the PCC is concerned, the rest of the elements including the grid connection could be reduced to an equivalent impedance (Z_{TH} , simplified as an inductance) and an equivalent voltage power supply (V_{TH}), as depicted in Fig. 6.5.c.

Therefore, the voltage at the PCC could be described as:

$$U_{PCC}^h = U_{TH}^h - \frac{U_{TH}^h - U_c^h}{\omega h L_{TH} + \omega h L_C} \cdot (\omega h L_{TH}) = U_{TH}^h - U_{TH}^h \cdot \frac{L_{TH}}{L_{TH} + L_C} + U_c^h \cdot \frac{L_{TH}}{L_{TH} + L_C}. \quad (6.8)$$

Assuming now that the harmonic PCC voltage wants to be completely reduced ($U_{PCC}^h = 0$) and naming the relationship among inductances q_L ($q_L = \frac{L_{TH}}{L_{TH} + L_C}$), U_C can be worked out as:

$$U_C = -U_{TH} \cdot \frac{1 - q_L}{q_L}. \quad (6.9)$$

From this last equation, different conclusions can be derived, when PCC voltage harmonic compensation wants to be achieved in different situations. Here, situations with grid distortion and with or without non-linear loads connected up and downstream are analysed and the obtained results are depicted in Fig. 6.6.

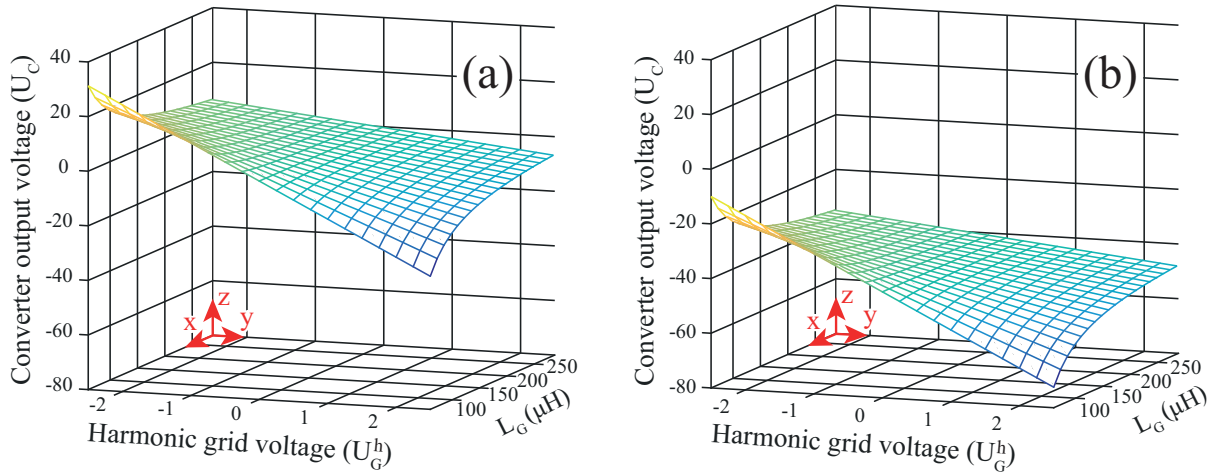


Figure 6.6: Required converter output voltage (U_C) values are obtained with variation of grid inductance ($L_G = \{60 \mu\text{H}, 260 \mu\text{H}\}$) and harmonic grid voltage ($U_G^h = \{-2.5\text{V}, 2.5\text{V}\}$) in two different scenarios. In a) without local non-linear load, b) two local non-linear loads: one placed upstream ($U_1^h = 5 \text{ V}$ and $L_1 = 200 \mu\text{H}$) and another downstream ($U_2^h = 3 \text{ V}$ and $L_2 = 100 \mu\text{H}$)

In Fig. 6.6.a, a situation without local non-linear loads is studied. In this case, the PCC harmonic components are due to U_G , exclusively. If $U_G = 0$ no harmonic compensation is needed and $U_C = 0$. If harmonic distortion exists, compensation need to be carried out injecting a voltage with the opposite phase. It can be seen that the voltage magnitude is related with the value of L_G . In the case of a high L_G , e.g $L_G = 260 \mu\text{H}$ the PCC can be

easier compensated. However, in the case of small grid inductance, e.g. $L_G = 60\mu\text{H}$, a high magnitude is needed in order to perform the compensation.

In Fig. 6.6.b, local non linear loads are connected. First, it is considered no harmonic grid distortion ($U_G = 0 \rightarrow y = 0$). Following the schematic shown in Fig. 6.5, the two non-linear load up (NL1: $U_1^h = 5\text{ V}$ and $L_1 = 200\mu\text{H}$) and downstream (NL2: $U_2^h = 3\text{ V}$ and $L_2 = 100\mu\text{H}$) can be compensated with a constant converter voltage ($U_C = -41.25\text{ V}$). It should be noted that in this particular case, if the upstream load NL1 is disconnected, the same functionality than an APF is achieved, without any additional sensor. In addition, if non-linear loads are connected, they could be compensated in the same way with the followed strategy, overtaking APF capabilities. In addition as previously described, theoretically, the PCC voltage can be reduced to zero even when the grid is distorted.

Even with all the presented enhancements of this harmonic voltage compensator functionality, it is not typically employed by shunt connected VSCs. If voltage needs to be compensated at the PCC, the most typical employed device is the *Dynamic Voltage Restorer (DVR)* [120]. As it is a series connected device, it is a more efficient device in order to modifying the voltage. Anyhow, as the predominant inverters along the grid are parallel connected, it would be an interesting idea to add the described compensation functionality to them. However, two are the main obstacles that prevent the described system for being widely employed:

- In difference with APF the compensation is made in a global way, i.e. it is not possible to differ if the harmonic at the PCC are provoked by local or external non-linear loads and all of them would be tried to be compensated without differentiation. From the PCC onwards, everything is simplified to a Thevenin grid impedance and a Thevenin equivalent voltage. This is analysed along subsection 6.3.1 and depicted in Fig. 6.7.
- The required voltage that the converter needs to provide at its output in order to perform the compensation, can be extremely high. This is one of the main impediments for implementing DVR functionality in a shunt DG interfacing inverter [89]. Even when this topic has been dealt up to date, a limit needs to be pre-set for being far from overmodulation [77]. In this thesis, with the employment of the proposed DFIMS saturator, this problem will be tackled. It is analysed during section 6.3.2.

6.3.1. Grid Impedance

Assuming the point of view of a VSC working as the interface between a distributed generator and the grid, there exists many parameters that could be of interest. Among these different parameters, knowing what occurs beyond the PCC is a key knowledge in some applications. One of the most extended applications is to detect if the Distributed

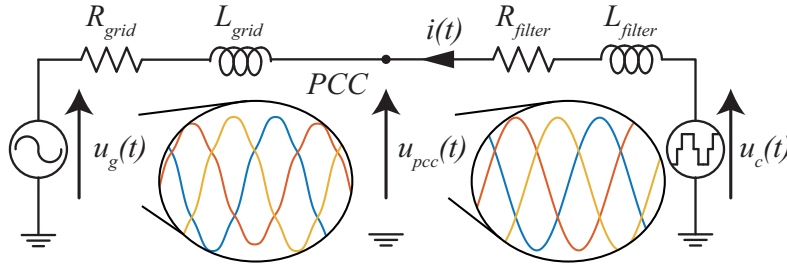


Figure 6.7: PCC Harmonic voltage control representation.

Generator is operating in islanding mode and immediately disconnect [121]. Islanding is a special condition that occurs when the power grid for any reasons cannot maintain the electric supply.

Although passive methods could be enough for detecting the majority of islanding situations some cases are not detected. These methods are based on monitoring the grid conditions and detect sudden changes. However, it could occur that even with grid disconnection, conditions are maintained and islanding is not detected. This situation is known as non-detection zone (NDZ).

In this context, passive methods are not considered reliable and active methods are necessary. Active methods provoke a small disturbance in the grid and analyse the resulting effects. Therefore, with these methods NDZ are minimized. Between these active methods, new ones appeared in order to detect sudden changes in the grid impedance. Grid impedance is known as the equivalent impedance seen from the PCC. Therefore, if the grid impedance is estimated, an islanding mode could easily be detected. The German standards [122] has increased the interest in this type of islanding detection related with the grid impedance estimation. The main impedance detection methods can be divided into:

- Current Spike injection and FFT analysis [80] [81].
- Reference current phase angle alteration and grid reaction analysis [82].
- Active (P) and reactive (Q) power variations [83] [84] [85] [86].
- Frequency tone injection [87] [88].

In advantage, these methods allows not only to precisely detect if the distributed generator is working in islanding mode but also precisely employ the value of the grid impedance for further goals. The knowledge of this value, in addition to the previously islanding detection functionality is also important in current [123] [124] and voltage control [125].

As the grid impedance is the result of the Thevenin equivalent of all the different devices connected to the grid, two different types are differentiated:

- Strong grid (*Short-circuit Ratio (SCR)* $= 1/Z_{pu} > 5$)
- Weak grid ($SCR = 1/Z_{pu} < 3$)

Firstly, the consideration of a strong grid is analyzed. In Fig. 6.8, an example of strong grid is depicted. Strong grids are usually defined by the presence of big conventional generators with small impedance. Even when different non-linear loads or distributed generators are connected, the Thevenin grid impedance will be small and it will remain constant during time. Usually, regarding the design of the current controller for a VSI, the magnitude of the grid impedance could be neglected, due to the fact that the impedance presented by the VSI filter is commonly greater than the one measured upstream. However, in PCC voltage control, two different statements need to be taken into account. As an advantage, a strong grid implies that the harmonic currents consumed by non linear load would not generate excessive harmonic voltages. As a disadvantage, if harmonic voltage at the PCC exists, the value of currents that are needed to be injected to compensate harmonic voltage is high enough to reach VSI overmodulation.

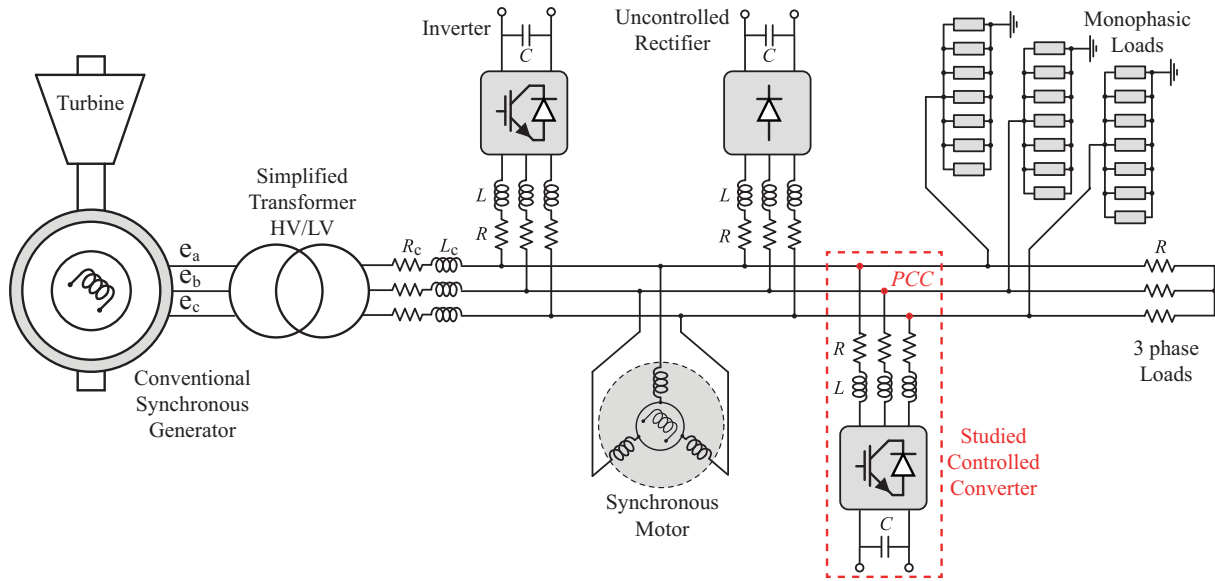


Figure 6.8: Different loads and distributed generators connected to strong grid formed by conventional generators.

Secondly, in some cases, those big conventional generators may not be present at the grid. Therefore, the equivalent Thevenin grid impedance would not be as small as before. This equivalent impedance would be highly modified by the connection or disconnection of new equipment. This type of grid is described as a weak grid. When this occurs, the grid impedance value is high, and in addition its value can change with time, due to the connection or disconnection of different devices to the grid. That fact implies several concerns:

- Stability problems in current and voltage control.

- Harmonic currents consumed by non-linear loads turn into voltage distortion at the PCC.

On contrary, as an advantage, the higher value of the grid impedance would make easier to perform the harmonic PCC compensation. Due to the injected harmonic currents are transformed into voltage compensation at the PCC. This type of grid can be commonly found in islands and also in low-developed areas in remote locations, where low power transformers and long wires are employed to feed the loads [126] [127].

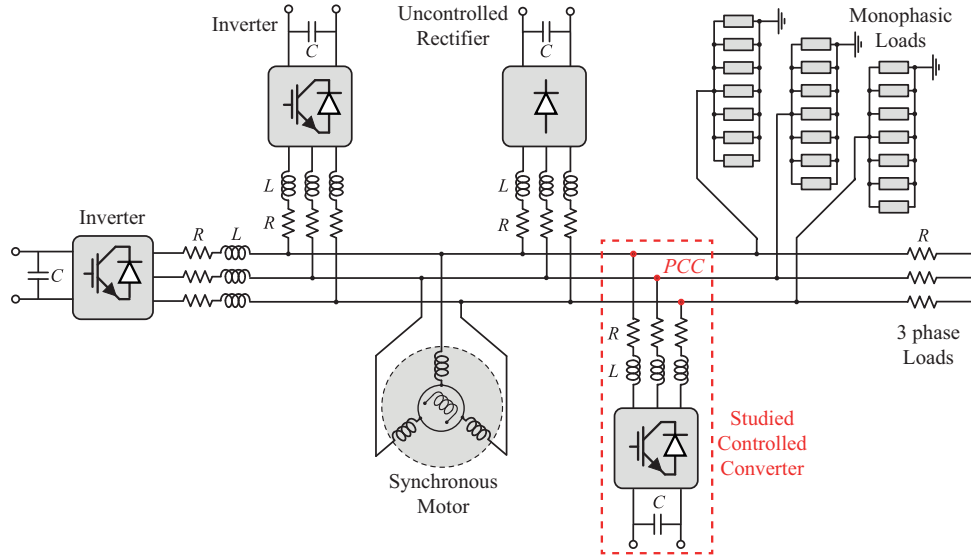


Figure 6.9: Different loads and distributed generators connected to a weak grid.

Therefore, the parameter of grid inductance is significant for the PCC harmonic compensation and its identification is of high importance.

6.3.1.1. Grid impedance in multifrequency context

As previously explained, the grid impedance is the equivalent impedance seen from the PCC. This equivalent impedance could be made up of the combination of different elements such as resistances, inductances, capacitors. Following the Thevenin's theorem, the equivalent grid impedance is the impedance seen from the PCC if all the independent sources are deactivated [128].

For knowing the equivalent impedance an estimation is done, due to the difficulty to properly make an impedance calculation with all the different connected devices and the dependent sources. In this way, several methods have been already mentioned for the estimation. In addition, for the desired goal of harmonic PCC compensation, the impedance at those harmonic frequencies is desired to be known. However, the grid impedance varies with the frequency and the variation is not always linear (inductive behavior).

As previously expressed, the harmonic compensation wants to be carried out over the most common harmonics at the grid. Those harmonics are the lowest odd harmonics, which are not multiple of three (typically $5^{th} \rightarrow 250$ Hz and $7^{th} \rightarrow 350$ Hz). Therefore, the interesting frequencies for knowing the grid impedance are the ones at 250 Hz and 350 Hz. Typically, the grid impedance can be modelled as $Z_g = R_g + L_g s$ and even the resistance term could be neglected for harmonics resulting in $Z_g = L_g s$. The simplicity of this model has been criticized in [125], due to the disregard of the capacitors. According to this paper, the impedance would be necessary to be calculated for each one of the interesting frequencies, in order to obtain a more accurate impedance value. Although this statement is completely right, in practice the perturbations over the grid at those frequencies could lead to interaction with the resonance of current controllers (PRC).

In this context, in some approaches as in the one proposed here that is further described in subsection 6.3.1.2 a different strategy is taken. A perturbation is provoked at a specific frequency (frequency of the injected harmonic) and the grid impedance at this frequency is obtained through the voltage and currents measurements. Then, the grid impedance obtained for that frequency is extrapolated to estimate the interesting frequencies at 250 Hz and 350 Hz.

However, the frequency of the injected harmonic needs to be carefully selected not only for not interfering with the resonant controllers, but also for being far from the resonant frequency [129]. Although the resonant frequency can be within a wide range, it is usually designed for not interfering with the background distortion or switching frequencies (typically $10 \cdot f_0 < f_r < f_{sw}/2$).

Therefore, as it occurs in [87], the frequency selected for the harmonic injection is between 400 and 600 Hz. In this regard, the main components of background distortion and the resonant frequency are typically avoided. As the grid behaviour is mainly inductive, the extrapolation for obtaining the impedance value ($Z = s \cdot L$) at the interesting frequencies are acceptable. Even in worst cases where several capacitors are connected and the resonant frequency gets really lower, the obtained values can be accepted assuming the extrapolation error, as depicted in Fig. 6.10.

6.3.1.2. Grid Inductance estimation based on Generalized Integrators (GIGI)

During this section, the proposed Grid Inductance estimation based on Generalized Integrators (GIGI) proposed method is described. In this method during a short period of time, a harmonic component is added to the output of the current controller. In this way, the switches would generate this harmonic voltage component at the ac side of the converter.

The harmonic selected for the inductance estimation needs to fulfil a bunch of requirements:

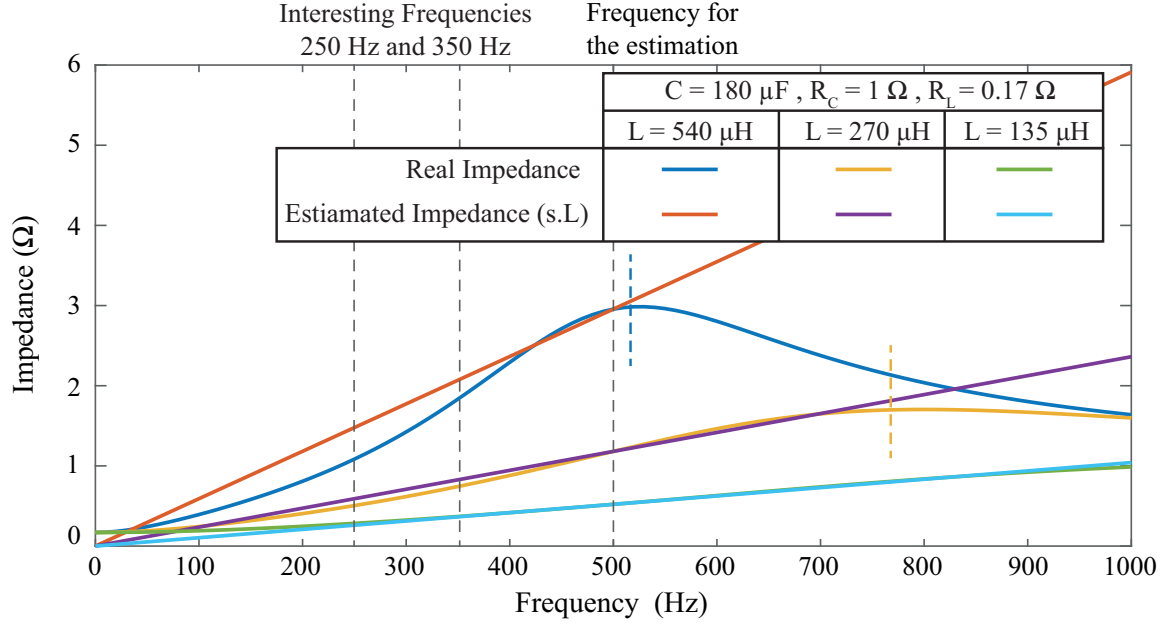


Figure 6.10: Grid estimation in worst scenario: connected capacitors results in low resonant frequencies. Comparison is made between impedance estimation at desired frequencies (250 & 350 Hz) [125] and obtaining the impedance at 500 Hz and extrapolating for the interesting frequencies [87] [88].

- The selected harmonic must not appear at the grid (6.11).
- The harmonic needs to be high enough in order to neglect the resistive part.
- The frequency should not be in the resonant frequency of the controllers.
- It needs to be lower than the resonant frequency (if resonance effects).
- It also needs to be lower than the Nyquist frequency for the sampling time.

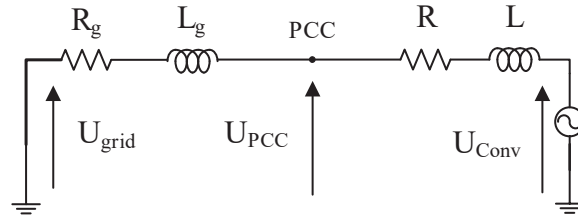


Figure 6.11: Electrical scheme for a provoked harmonic that is not present in the grid voltage [88].

The electrical scheme including grid and converter at the injected harmonic component is depicted in Fig. 6.11. With the previous requirements, the voltage presence at the grid for the injected harmonic should be approximately 0V. Then, by taking the voltage and current measurements at the PCC the grid impedance would be determined by:

$$Z_{gh} = \frac{V_h}{I_h} = R_g + j\omega h L_g \approx \omega h L_g \quad (6.10)$$

where Z_{gh} represents the grid impedance at the injected frequency and V_h and I_h stands for the harmonic (h) voltage and current components measured at the PCC, respectively. Balanced phases are assumed and therefore, the measurements of only one phase are taken. Then, it is needed to identify the voltage and current components for the injected harmonic. For achieving that, SOGIs tuned at the injected frequency are employed as band filter. Then, the harmonic voltage and current amplitudes are detected through a *Moving Average Filter (MAF)*. The global process, through the employment of those well known tools, optimized for its implementation in a *Digital Signal Processor (DSP)* and it is depicted in Fig. 6.12.

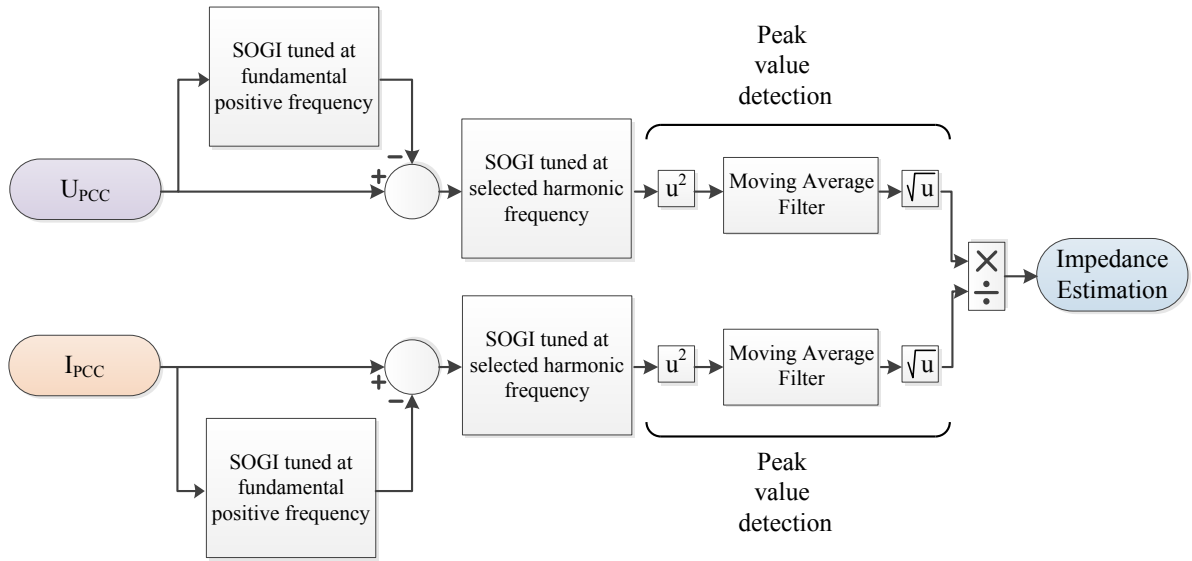


Figure 6.12: GIGI system graphical description. [88].

Following the previously described scheme, the first step is to receive the measurements of voltages and currents at the PCC of one single phase. These measurements contains all the different components that are present at the grid (fundamental and background distortion) plus the injected component:

$$x(t) = X_1 \cdot (\sin(\omega \cdot t + \phi_1)) + X_3 \cdot (\sin(3\omega \cdot t + \phi_3)) + X_5 \cdot (\sin(5\omega \cdot t + \phi_5)) \\ + X_7 \cdot (\sin(7\omega \cdot t + \phi_7)) + X_9 \cdot (\sin(9\omega \cdot t + \phi_9)) + X_h \cdot (\sin(h\omega \cdot t + \phi_h)) \quad (6.11)$$

where x stands for both current (i) or voltage (v) and the injected harmonic is described as h . In the second step, the harmonic current and voltage components ($X_h \cdot (\sin(h\omega t + \phi_h))$) are wanted to be separated from the rest of the measured signal. For this purpose the SOGI is employed as band filter. SOGI transfer function is described as

$$\frac{y(s)}{x(s)} = \frac{2k \cdot s}{s^2 + \omega_0^2} \quad (6.12)$$

where $s = j\omega$. If ω_0 is replaced by $h \cdot \omega$, the SOGI presents an infinite gain at the injected harmonic frequency. It can be seen in the right part of Fig. 6.13 where h is set to 10. The value of the SOGI gain (k) plays a fundamental role in its behaviour. The lower k is selected the more selectivity is achieved for the rest of components. However, the lower is the k the slower is the filtration. As the filtering process wants to be achieved as fast as possible, a high gain is desired. However, the differences in the components magnitudes makes that reducing the selectivity could not completely eliminate the undesired components. This fact especially occurs with the FPS component, which is hundreds of times bigger than the injected one. In this context, a previous SOGI with a gain that allows fast detection is employed for extracting the FPS components and eliminate it from the complete measured signal. This is shown in the left side of Fig. 6.13. Then, after this previous SOGI, a bigger gain can be assigned to the second SOGI in order to reduce the filtering time and knowing that the selectivity reduction would not imply the appearance of FPS in the output.

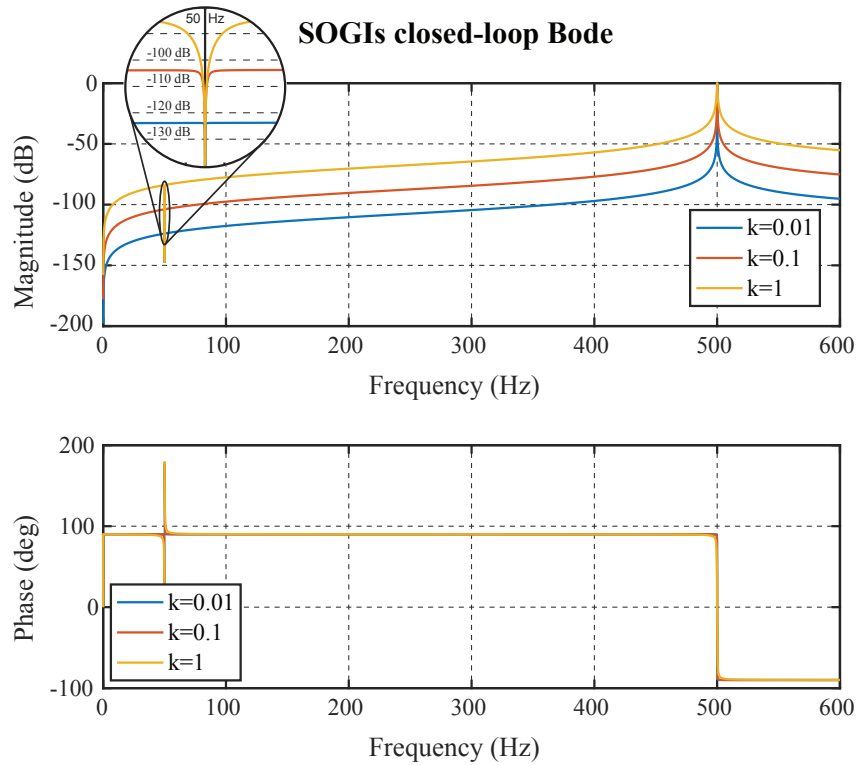


Figure 6.13: GIGI SOGIs closed loop transfer function in terms of magnitude and phase. The magnitude shows the rejection to the non desired fundamental frequency. [88].

During the third step, once that the desired harmonic component signals have been extracted, the objective is to obtain their amplitudes. If the amplitudes are obtained, the impedance magnitude would be simply calculated as $|Z_h| = \frac{|V_h|}{|I_h|}$. Therefore, for completing this step and obtaining the magnitudes, a simple product detector and a MAF for filtering purposes are employed.

The extracted signal after the SOGIs filtering can be expressed as:

$$y(t) = |Y_h| \cdot \sin(h\omega t + \phi_h) \quad (6.13)$$

where $|Y_h|$ is the peak value that wants to be obtained. The previous signal is multiplied by itself:

$$y_2(t) = y(t) \cdot y(t) = \frac{|Y_h|^2}{2} [1 - \cos(2h\omega t + 2\phi)]. \quad (6.14)$$

Therefore, the extracted harmonic signal in (6.13) is converted in a signal with two components, one at zero frequency and the other component at twice the harmonic frequency. Then, the oscillating part is eliminated through the MAF, exclusively remaining the constant part. MAF is a kind of filter that allows the pass of constant signals and presents a complete rejection to those components that are multiple of the selected frequency, as depicted in Fig. 6.14. MAF is determined by the following equation:

$$y_o(t) = \frac{1}{n} (y_2(k) + y_2(k-1) + \dots + y_2(k-n+1)) = \frac{1}{n} \sum_{i=0}^{n-1} y_2(k-i) \quad (6.15)$$

which in discrete domain can be expressed as:

$$Y_o(z) = \left(\frac{1}{n} \sum_{i=0}^{n-1} z^{-i} \right) Y_2(z) = \frac{1}{n} \cdot \frac{1 - z^{-n}}{1 - z^{-1}} \cdot Y_2(z). \quad (6.16)$$

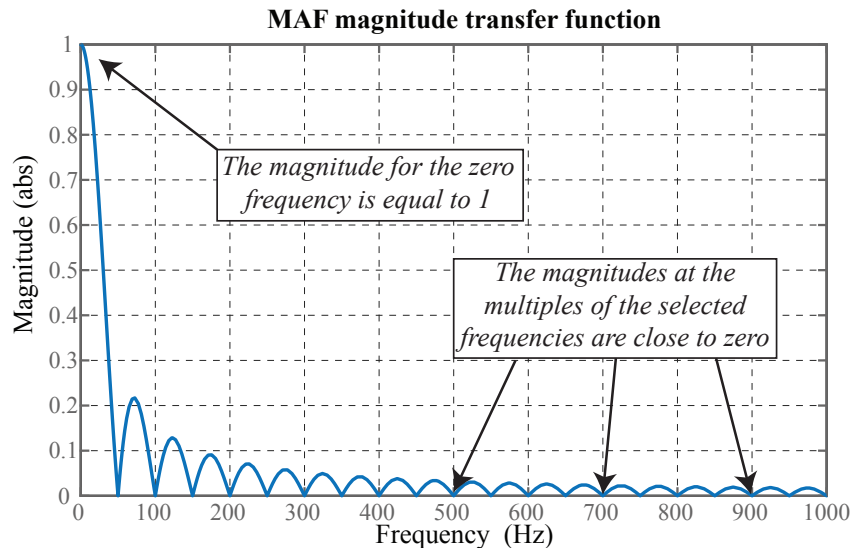


Figure 6.14: MAF transfer function in terms of magnitude. The magnitude shows the rejection to the multiples of the natural frequency (50Hz) and the gain equal to 1 for the constant signal part. [88].

In order to obtain the magnitude ($|Y_h|$), a factor correction of 2 needs to be applied, describing the MAF transfer function as:

$$\frac{Y_o(z)}{Y_2(z)} = \frac{2}{n} \cdot \frac{1 - z^{-n}}{1 - z^{-1}} \quad (6.17)$$

Finally, the square root of the output completes the process of harmonic voltage or current magnitude calculation ($|Y_h| = \sqrt{Y_o(z)}$) as depicted in Fig. 6.12. As the impedance at the calculated harmonic is assumed to be of inductive effect, the grid inductance estimation is approximately calculated as:

$$L_g \simeq \frac{\hat{V}_{PCC}}{\hat{I}_{PCC} \cdot \omega \cdot h} \quad (6.18)$$

Once that the detection process has been described, the process for the harmonic injection is explained. Before describing the algorithm, it needs to be decided which harmonic will be selected for the harmonic injection and the consequently detection. In this case, a frequency of 500 Hz ($h=10$) was selected. This harmonic component meets all the previous conditions. It is an even harmonic with a negligible presence at the grid and it is high enough for considering that the impedance is due exclusively to the inductive effect. Furthermore, the sampling frequency (5 kHz) is several times greater than the injected and the harmonic component is higher than the controlled harmonics (250 Hz and 350 Hz) and lower than the resonant frequency (≈ 1 kHz).

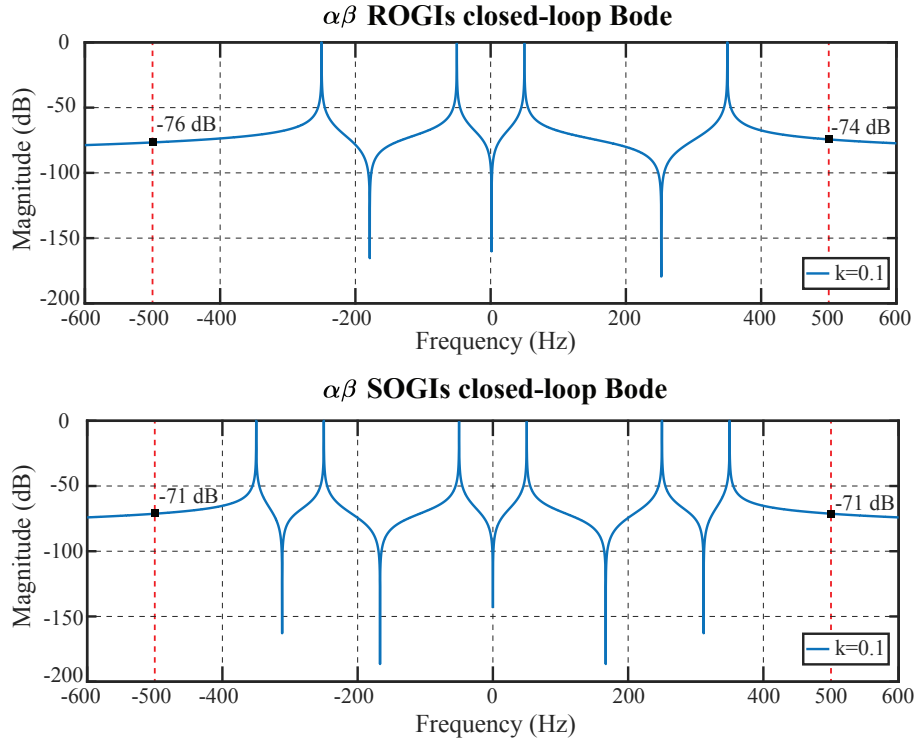


Figure 6.15: Bode response of current controller based in stationary reference frames for multiple ROGIs and multiple SOGIs. Different rejection rate is observed for ROGIs, where negative sequence of the injected harmonic presents a higher rejection rate than the positive one [88].

For the control algorithm, it was decided to employ the stationary reference frame

$\alpha\beta$. In this way for the current control it could be not needed to work out θ reducing some computational time associated with its detection and with transformations. In this context, for achieving zero error at the controlled frequencies, typically fundamental and -5 and +7 sequences PRC are needed. In this specific case, the employment of ROGIS at -5 and +7 imply a reduction of -76 dB for $h = -10$ and a reduction of -74 dB for $h = +10$. A similar effect to the ROGIs could be obtained if synchronous reference frame (dq) are employed and ± 6 SOGIs are employed. However, as the premise is to avoid the θ calculation and its associated transformations if SOGIs are employed at ± 5 and ± 7 the reduction factor would be -71 dB for $h = \pm 10$, as depicted in Fig. 6.15.

Although it has been decided that the tenth harmonic is the desired one for the harmonic injection, it can be seen that with the MROGI current controller the rejection is higher for the negative sequence. In this case, as the injection is generated by the inverter, a negative sequence can be easily generated with pre-stored values for each instant and added to the output of the current controller, as depicted in Fig. 6.16.

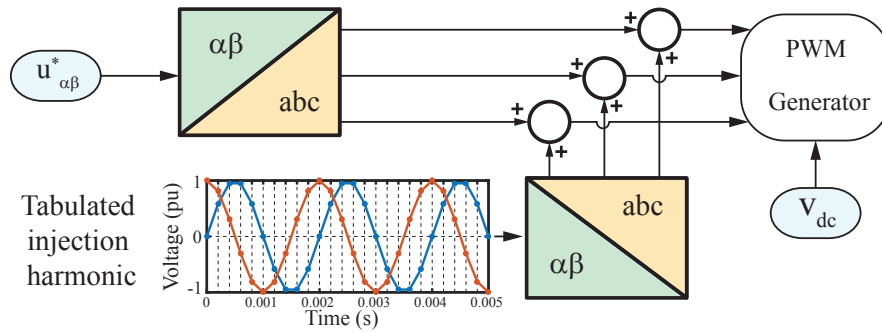


Figure 6.16: Negative sequence harmonic injection. The selected harmonic component is added to the output of the current controller. Then the PWM is generated in order to provoke that voltage at the AC-side of the converter [88].

The GIGI proposed method has been tested in a simulation developed over Matlab/Simulink 2016. A three levels NPC is connected to the grid through an L filter ($L = 750 \mu\text{H}$). Two impedances of $40 \mu\text{H}$ and a resistive part of 0.025Ω are employed (after the PCC) for simulating a variation of the grid impedance from $40 \mu\text{H}$ to $80 \mu\text{H}$. Voltage $\alpha\beta$ signals are added to the output of the current controller. These signals has an amplitude of 8V and a negative sequence of tenth harmonic. The results of detection of grid inductance when grid impedance is changed at 1.4s are depicted in Fig. 6.17.

In the bottom part of Fig. 6.17 it can be appreciated a constant error which is associated with the assumption that the grid is purely inductive. Anyhow, this error can be disregarded for our purposes. The selected L filter ($750 \mu\text{H}$) and the small value of grid inductances ($40 \mu\text{H}$ or $80 \mu\text{H}$ simulating a strong grid) performs a voltage divider:

$$U_{PCC}^h = U_C^h \cdot \frac{L_g}{L_g + L_f}. \quad (6.19)$$

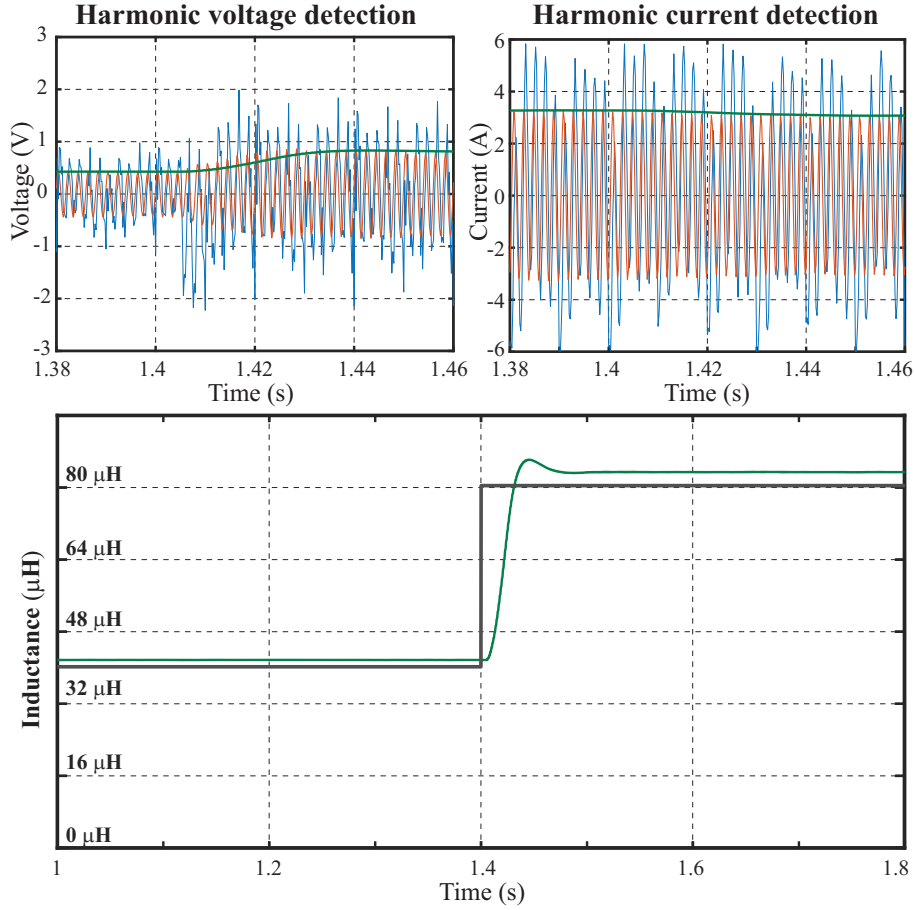


Figure 6.17: Harmonic current and voltage detection. Measurements without the main component (blue), harmonic SOGI filtered signal (red) and detected amplitude (orange) are shown in top figures. The real grid inductance (red) and the estimated inductance (blue) are shown at the bottom figure. [88].

In the simulation case, the SOGI gains for the harmonic filtering have been set to 1.0 for the FPS and to 0.05 for the harmonic injection filter. Meanwhile, the MAF filter has been configured to 100 samples. The configuration of this parameters allow the detection of a grid impedance change in 0.05 s, as depicted in Fig. 6.17. Anyhow, depending on the application and the pursued objective, these parameters can be modified in order to improve accuracy or detection time.

6.3.2. Saturation for harmonic PCC voltage

As previously described, the compensation of harmonic voltage distortion at the PCC with parallel connected converters is not a trivial task. The background distortion and the influence of the grid impedance usually makes that a complete compensation is unreachable. During this section, the multifrequency current control applied to voltage harmonic compensation is described. In addition, the adaptation of the novel saturation strategies, as the DFIMS, for this specific purpose is analysed.

6.3.2.1. PCC harmonic voltage mathematical model

As described in Fig. 6.7, for each phase, the voltage at the output converter is described as:

$$u_c(t) = R_g \cdot i(t) + L_g \cdot \frac{di(t)}{dt} + R_f \cdot i(t) + L_f \cdot \frac{di(t)}{dt} + e(t). \quad (6.20)$$

Therefore, the voltage at the PCC, where the harmonic voltages are desired to be compensated can be defined as:

$$\begin{aligned} v_a(t) &= R_{ga} \cdot i_a(t) + L_{ga} \cdot \frac{di_a(t)}{dt} + e_a(t) \\ v_b(t) &= R_{gb} \cdot i_b(t) + L_{gb} \cdot \frac{di_b(t)}{dt} + e_b(t) \\ v_c(t) &= R_{gc} \cdot i_c(t) + L_{gc} \cdot \frac{di_c(t)}{dt} + e_c(t) \end{aligned} \quad (6.21)$$

and if a three phase balanced system is assumed and through the employment of the $\alpha\beta$ -stationary reference frame, the previous equations can be rewritten as:

$$v_\alpha(t) = R_g \cdot i_\alpha(t) + L_g \cdot \frac{di_\alpha(t)}{dt} + e_\alpha(t) \quad (6.22)$$

$$v_\beta(t) = R_g \cdot i_\beta(t) + L_g \cdot \frac{di_\beta(t)}{dt} + e_\beta(t) \quad (6.23)$$

employing now the Park transformation,

$$\vec{s}_{dq}(t) = T_{\alpha\beta \rightarrow dq} \cdot \vec{s}_{\alpha\beta}(t) = \begin{bmatrix} \cos(h \cdot \theta) & \sin(h \cdot \theta) \\ -\sin(h \cdot \theta) & \cos(h \cdot \theta) \end{bmatrix} \begin{bmatrix} s_\alpha(t) \\ s_\beta(t) \end{bmatrix}, \quad (6.24)$$

the equations can be written in the synchronous reference frame, where the PCC voltages can be described as:

$$v_d(t) = v_\alpha(t) \cdot \cos(h \cdot \theta) + v_\beta(t) \cdot \sin(h \cdot \theta) \quad (6.25)$$

$$v_q(t) = -v_\alpha(t) \cdot \sin(h \cdot \theta) + v_\beta(t) \cdot \cos(h \cdot \theta). \quad (6.26)$$

by the substitution of (6.22) and (6.23) in (6.25) the following equation is obtained:

$$v_d(t) = \left(R_g i_\alpha(t) + L_g \frac{di_\alpha(t)}{dt} + e_\alpha(t) \right) \cos(h \cdot \theta) + \left(R_g i_\beta(t) + L_g \frac{di_\beta(t)}{dt} + e_\beta(t) \right) \sin(h \cdot \theta) \quad (6.27)$$

$$v_d(t) = R_g i_d(t) + e_d(t) + L_g \left(\frac{di_\alpha(t)}{dt} \cdot \cos(h \cdot \theta) + \frac{di_\beta(t)}{dt} \cdot \sin(h \cdot \theta) \right) \quad (6.28)$$

$$v_d(t) = R_g i_d(t) + e_d(t) + L_g \left(\frac{di_\alpha(t) \cdot \cos(h \cdot \theta)}{dt} + i_\alpha(t) \cdot \omega \cdot \sin(h \cdot \theta) + \frac{di_\beta(t) \cdot \sin(h \cdot \theta)}{dt} - i_\beta(t) \cdot \omega \cdot \cos(h \cdot \theta) \right) \quad (6.29)$$

$$v_d(t) = R_g i_d(t) + L_g \cdot \frac{di_d(t)}{dt} - \omega \cdot L_g \cdot i_q + e_d(t). \quad (6.30)$$

In a similar way the equation for v_q can be described as:

$$v_q(t) = R_g i_q(t) + L_g \cdot \frac{di_q(t)}{dt} + \omega \cdot L_g \cdot i_d + e_q(t). \quad (6.31)$$

Therefore the plant of the system, seeing the PCC voltage (v_d and v_q) as the output and the injected current (i_d and i_q) as input, could be described from (6.30) and (6.31) as:

$$v_d - e_d = (R_g + L_g \cdot s) \cdot i_d + L_g \cdot h \cdot \omega \cdot i_q \quad (6.32)$$

$$v_q - e_q = (R_g + L_g \cdot s) \cdot i_q - L_g \cdot h \cdot \omega \cdot i_d. \quad (6.33)$$

Then, the scheme of the plant model and the controller structure in order to control the PCC harmonic voltages are depicted in Fig. 6.18. The controller is in charge of obtaining the current references that will be controlled by the inner current control loop.

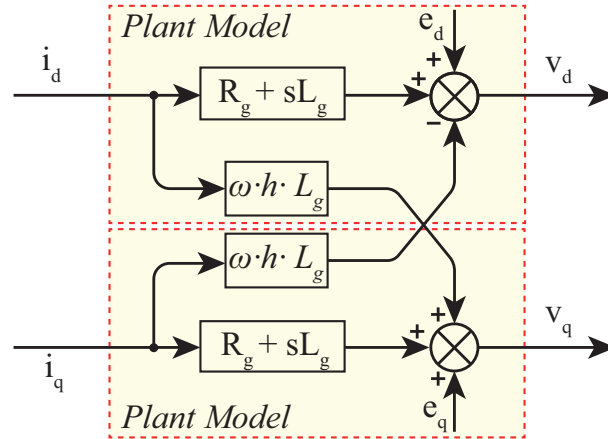


Figure 6.18: PCC voltage plant model with grid resistance and grid inductance.

6.3.2.2. PCC harmonic voltage controller

During this part of the section the design of the PCC harmonic voltage controller is analysed and tuned. As previously described, the variables are referred to the dq-synchronous reference frame in order to obtain a simpler system. It means that for each harmonic sequence, a conversion from $\alpha\beta$ to dq is required. Therefore, the electric parameter θ needs to be accurately calculated.

As it can be seen in Fig. 6.18, the voltage at the PCC depends on the two current components (i_d and i_q). In this regard, the effect of the i_d component over v_d and the effect of i_q over v_q could be neglected by the two following reasons:

- First, the summand described by sL_g performs the derivation of the current signal in dq synchronous reference frame (dc signal) and resulting in a value close to zero.
- Second, after neglecting the sL_g term, two proportional terms are multiplying the current signals. R_g is the coefficient that relates the same axes voltage and current (i_d for v_d and i_q for v_q). Meanwhile $\omega h L_g$, is the coefficient that relates the coupling among axes (i_q for v_d and i_d for v_q). As the term $\omega h L_g$ is several times higher than R_g , the R_g term can be disregarded.

With these premises, the plant depicted in Fig. 6.18 can be simplified to the plant depicted in Fig. 6.19.

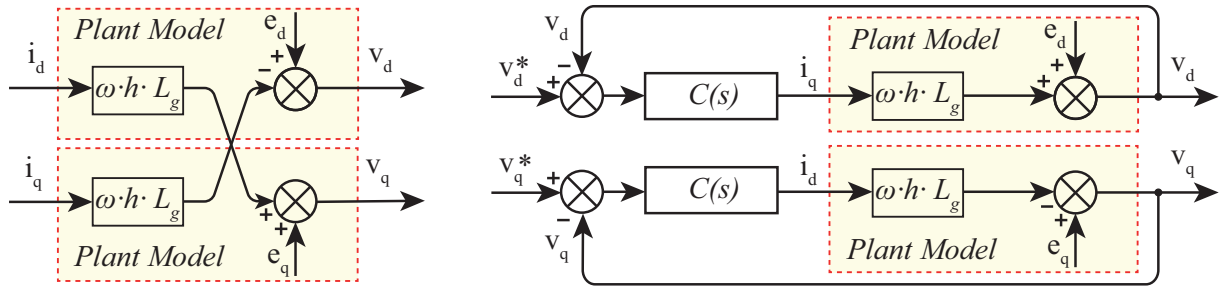


Figure 6.19: Simplified PCC voltage plant model with grid resistance and grid inductance. Simplified plant model and harmonic voltage controller.

Analysing the plant representation, it can be appreciated that the variation of v_d is related with i_q , and in the same way, v_q is related with i_d through a proportional plant. The proportional plant is described exclusively by the harmonic frequency and the grid inductance. This case is an example of the importance related with the grid impedance/inductance estimation as described in Section 6.3.1. The different variables are expressed in dq -synchronous reference frame (dc signals) and the plant is described as a zero order proportional plant. In this context, for the achievement of a zero error in steady state, the controller needs to be provided with an integration part. For controlling the proportional plant described as:

$$T(s) = \frac{v}{i} = \omega \cdot h \cdot L_g, \quad (6.34)$$

a PI controller is employed:

$$C(s) = \frac{i}{v^*} = \frac{k_p s + k_i}{s}. \quad (6.35)$$

The total transfer function for d and q voltage control is described as:

$$\frac{v}{v^*} = \frac{(k_p \cdot \omega \cdot h \cdot L_g)s + k_i \cdot \omega \cdot h \cdot L_g}{s [(1 + k_p \cdot \omega \cdot h \cdot L_g)s + k_i \cdot \omega \cdot h \cdot L_g]}. \quad (6.36)$$

If a step input (R_o) is applied over the transfer function, the output in time domain is determined by the following equation:

$$c(t) = R_o - R_o \left(\frac{1}{1 + k_p \cdot \omega \cdot h \cdot L_g} \right) \cdot e^{\frac{-k_i \cdot \omega \cdot h \cdot L_g}{1 + k_p \cdot \omega \cdot h \cdot L_g} \cdot t}. \quad (6.37)$$

Analysing this equation, it can be seen that the value that the output takes initially in pu ($c(0)$) can be configured by the parameter k_p :

$$k_p = \frac{c(0)}{\omega \cdot h \cdot L_g \cdot (1 - c(0))} \quad (6.38)$$

Then, the parameter k_i is the one related with the settling time (t_s). Assuming that the desired settling time for achieving the 98% of the reference is known, k_i can be selected as:

$$k_i = -\frac{1 + k_p \cdot \omega \cdot h \cdot L_g}{t_s \cdot \omega \cdot h \cdot L_g} \cdot \lg [0.02 + 0.02 \cdot k_p \cdot \omega \cdot h \cdot L_g] \quad (6.39)$$

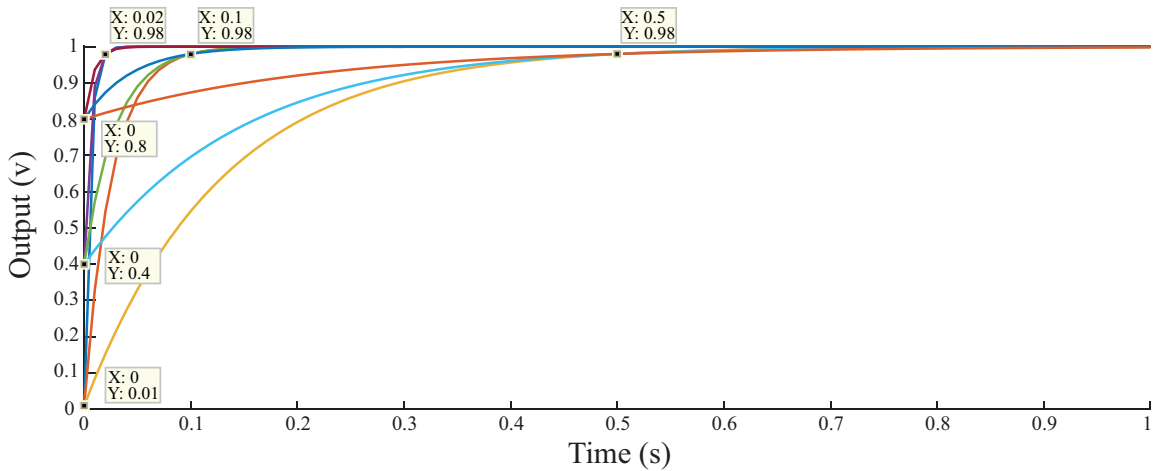


Figure 6.20: Output voltage signal obtained by means of controllers with different integral and proportional gains.

In Fig. 6.20 the output for an step of 1 V is depicted for different controllers. The different controllers are designed for achieving different settling times (0.02 s, 0.1 s and 0.5 s) and for starting from different initial outputs (0.01 V, 0.4 V and 0.8 V).

Meanwhile, in Fig. 6.21 the actuation current signal needed for achieving the 1 V compensation is depicted. Taking into account the different settling times and starting points, it can be concluded that as the plant is of proportional type, in no case with a PI controller would exist overshoot. Therefore, it would not incur in any excess of actuation for reaching the steady state, avoiding additional problems for saturation in the inner control loop.

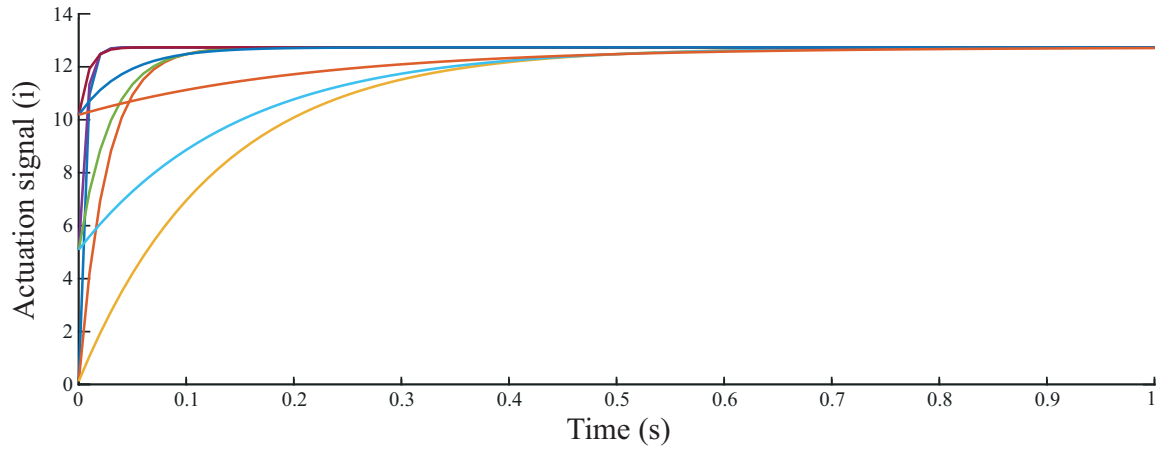


Figure 6.21: Actuation currents signal required for the accomplishment of 1 V compensation with a grid inductance of 250 μH .

6.3.2.3. PCC harmonic voltage saturation algorithm

As previously described, when the control of PCC harmonic voltage is pursued, the main concern resides on the overmodulation problems. The grid inductance value determines the amount of harmonic current needed to perform the compensation. In order to obtain these reference currents, the inner current controller loop is in charge. However, there exists the problem, that for delivering a harmonic current component, a great actuation is needed. That can lead to a situation where the voltage needed at the output of the converter cannot be provided due to the dc voltage limitation. If this occurs, overmodulation is reached and it is not difficult to lead an instability situation if a proper saturation algorithm is not implemented. It needs to be noted that in this case, the voltage harmonic components are several times more limiting than the harmonic currents limitation. Therefore, RMS current limitation is not usually reached within the PCC harmonic control, and an indirect current limitation is performed through the voltage output saturation.

In harmonic PCC voltage control, the ac output voltage is very limiting, as described in [77] or even in the most recent works as in [89], where the PCC voltage control function-

ality is discarded from shunt connected converters. However, a different vision is provided in this thesis. In this part of the section, the key part for making the desired PCC control functionality feasible is described. In this regard, in the case that the limit of output voltage is reached, it needs to be instantaneously saturated providing the maximum possible compensation within the allowed range. For this purpose, the instantaneous multifrequency saturator proposed in previous chapter (DFIMS) is view from a new perspective and modified in order to deal with the desired functionality. This makes DFIMS the first multifrequency saturator that is able to guarantee stability during harmonic saturation.

The system as depicted in Fig. 6.22 is composed by the previously described PCC harmonic voltage compensator and the value of the grid inductance needs to be previously estimated. The ROGI based multifrequency controller and the modified DFIMS algorithm plus antiwindup complete the proposed scheme for the compensation of harmonic voltages.

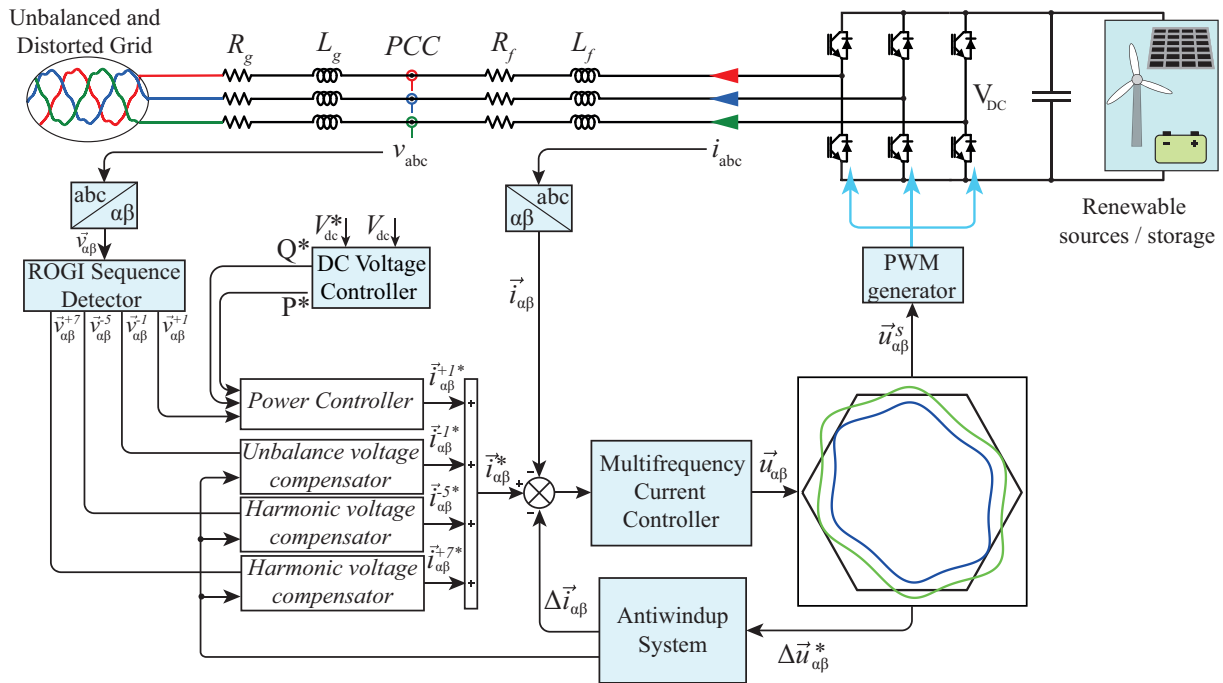


Figure 6.22: Schematics of control of PCC voltage containing the different subsystems.

As it has been mentioned, the DFIMS algorithm proposed in Chapter 5 appears as the desired solution for avoiding overmodulation and ensure stability. This saturation algorithm calculates the optimal reduction gains instantaneously and in addition, independent priorities can be assigned for the reduction of each sequence.

As it was previously mentioned, the voltage that the VSC needs to provide at the ac side is determined by the output of the inner current controller ($\vec{u}_{\alpha\beta}$). The value that this parameter can take is limited by the dc voltage, graphically depicted by a hexagon. In the case that it is needed, $\vec{u}_{\alpha\beta}$ can be reduced by the diminution of the different components:

$$\vec{u}_{\alpha\beta} = k_F \cdot U_1 \cdot e^{j\omega t + \phi_1} + \sum_{h \in H} k_h \cdot U_h \cdot e^{jh\omega t + \phi_h} \quad (6.40)$$

where k_F is the reduction gain for the FPS component and k_h stands for the independent gain for each of the rest of sequences ($h = -1, -5, +7$). As previously seen, the complex equation described in (6.40) can be expressed by exclusively the imaginary part. In a complex plane, the imaginary part corresponds with the y axis.

$$y = k_F \cdot U_1 \cdot \sin(\omega t + \phi_1) + \sum_{h \in H} k_h \cdot U_h \cdot \sin(h\omega t + \phi_h) \quad (6.41)$$

The objective of DFIMS is to calculate the optimal gains in order to keep the whole trajectory inside the limiting hexagon, which apothem is described as:

$$a = y_{\max} = \frac{1}{\sqrt{3}} V_{DC} \quad (6.42)$$

The comparison is made by obtaining the maximum value for the y component and calculating the gain for being equal to the hexagon apothem. In order to perform the comparison of the whole trajectory with the whole hexagon, two rotations of $\pm 60^\circ$ are carried out. In this case the priorities for the gains calculation varies from the one described in the original DFIMS. In this case, voltage harmonic compensation is desired (U_{-5} and U_{+7}). However, in most cases it cannot be completely achieved. Therefore, this functionality should be partially accomplished within the remaining dc bus capability until reaching the limitations. The same gain is assigned to the different harmonic components k_H . As previously described in DFIMS description, a decision needs to be made over the priority assigned to the gain of the FNS.

For the harmonic PCC compensation, the FNS component is not too high under normal conditions (usually smaller than the 3 %) and the FNS current injection does not imply high voltage generation that could lead to overmodulation. Therefore, the same component is assigned to the first FPS component and the second FNS component (k_{12}). It is the first gain to be worked out, and then if there exists dc bus margin, the harmonic sequences gain (k_H) is calculated (on contrary, it is directly set to 0).

For calculating the first gain k_{12} it is assumed that there is not any harmonic component. Then 6.41 can be expressed as:

$$y = k_{12} [\sin(\omega t)(U_1 \cos(\phi_1) - U_2 \cos(\phi_2)) + \cos(\omega t)(U_1 \sin(\phi_1) + U_2 \sin(\phi_2))] \quad (6.43)$$

The trajectory of $\vec{u}_{\alpha\beta}$ if only FPS and FNS are taken into account is described by an ellipse. This ellipse would be inside the hexagon always that the absolute value of the trajectory for each of the ωt instants, is lower than the value for the hexagon at that phase value. Checking this mathematically, it brings difficult equations which would be very difficult to solve in the computational times that are available for a commercial DSP.

Therefore, comparing the ellipse y coordinate with the y constant function of the top and bottom edges of the hexagon, the computational time is reduced. In this way, if the

ellipse goes out of those limits, a gain k_{12} is obtained for placing the outermost point over the threshold. The derivation of (6.43) determines the maximum and minimum values of y coordinate.

$$\frac{dy}{dt} = k_{12}[(U_{C1} - U_{C2}) \cdot \omega \cdot \cos(\omega t) - (U_{S1} + U_{S2}) \cdot \omega \cdot \sin(\omega t)] = 0 \quad (6.44)$$

where U_{C1} and U_{S1} stands for $U_1 \cdot \cos \phi_1$ and $U_1 \cdot \sin \phi_1$ and U_{C2} and U_{S2} stands for $U_2 \cdot \cos \phi_2$ and $U_2 \cdot \sin \phi_2$ where all of them are known values. By solving (6.44) the maximum and minimum values are found as:

$$\omega t = \arctan\left(\frac{U_{C1} - U_{C2}}{U_{S1} + U_{S2}}\right) \quad (6.45)$$

and there would exist two solutions for the problem in the $(0-2\pi)$ domain. For each of the two solutions a value of k_{12} can be worked out by comparing equation 6.43 to the threshold in (6.42) both in absolute value:

$$|k_{12}[\sin(\omega t)(U_{C1} - U_{C2}) + \cos(\omega t)(U_{S1} + U_{S2})]| = \left|\frac{V_{DC}}{\sqrt{3}}\right|. \quad (6.46)$$

The lowest value of k_{12} that also is lower than the unity, would be taken as one of the three possible $k_{12}s$. In this way the limits with the top and bottom edges have been easily studied as threshold.

For checking with the other four hexagon edges, it could be performed in the same way by rotations of $\pm 60^\circ$ applied over the ellipse and obtaining both k_{12} as described in the process explained before. Applying a $\pm 60^\circ$ rotation over the ellipse is as easy as adding $\frac{\pi}{3}$ to ϕ_1 and ϕ_2 for the first rotation and $-\frac{\pi}{3}$ to ϕ_1 and ϕ_2 for the second rotation.

Once that the reduction gain for the FPS and NFS has been worked out (k_{12}), the turn is for the calculation of the reduction gain for the harmonic components (k_H). It needs to be noted that if the value of k_{12} is smaller than one, it means that the limitation has been already reached by just the fundamental components and the margin for the harmonic components is narrow.

Anyhow, after the completion of the previous process, k_{12} is known and k_H can be worked out. The equation is described in the same way as the previous one for the y coordinate with the inclusion of harmonic sequences:

$$y = k_{12} [\sin(\omega t)(U_{C1} - U_{C2}) + \cos(\omega t)(U_{S1} + U_{S2})] + k_{34} [U_{C3} \cdot \sin(-5\omega t) + U_{S3} \cdot \cos(-5\omega t) + U_{C4} \cdot \sin(7\omega t) + U_{S4} \cdot \cos(7\omega t)] \quad (6.47)$$

As it was described in previous chapter, it is needed to find the maximum and the

minimum of the y function. For this, the differentiation respect to wt is done and equalled to zero:

$$\begin{aligned} \frac{dy}{d\omega t} &= k_{12} [\cos(\omega t)(U_{C1} - U_{C2}) - \sin(\omega t)(U_{S1} + U_{S2})] + \\ k_{34} [-5 \cdot U_{C3} \cdot \cos(-5\omega t) + 5 \cdot U_{S3} \cdot \sin(-5\omega t) + 7 \cdot U_{C4} \cdot \cos(7\omega t) - 7 \cdot U_{S4} \cdot \sin(7\omega t)] &= 0 \end{aligned} \quad (6.48)$$

In previous equation, a total of six non linear functions ($\cos(\omega t)$, $\sin(\omega t)$, $\cos(-5\omega t)$, $\sin(-5\omega t)$, $\cos(7\omega t)$, $\sin(7\omega t)$) are presented. The reduction gain k_H is calculated by solving this non linear equation system or through the computational algorithm that is described in Chapter 7 for reducing computational time.

In conclusion, k_{12} and k_H are calculated for each time step and taking into account an estimation of the whole trajectory. Through the described process the trajectory that comes out from the inner current loop controller can be reshaped as desired in order not to exceed the limitations. However, as the output is reduced, the reference would be not accomplished resulting in a higher output requirement by the ROIGs. Consequently, a smaller gain is needed in order to keep the actuation within the limitations. This process would lead the reduction gains to zero. In order to prevent this situation an antiwindup system is required.

The basis of the antiwindup system consists on calculating the amount of output voltage that is not being applied at the ac terminals of the converter ($\Delta \vec{u}_{\alpha\beta}^h$). Then, the amount of current that is not being delivered ($\Delta \vec{i}_{\alpha\beta}^h$) is calculated through the converter voltage reduction. Finally, this amount of current is subtracted from the reference currents ($\vec{i}_{\alpha\beta}^{*h}$) that are the input of the current control loop. This antiwindup system was already proposed in [64].

It is known that the delivered current can be described as:

$$\vec{i}_{\alpha\beta}^h = \frac{\vec{u}_{\alpha\beta}^h - \vec{e}_{\alpha\beta}^h}{R + jh\omega L} \quad (6.49)$$

where $\vec{e}_{\alpha\beta}^h$ stands for the grid voltage harmonic sequence. Then, if instead of $\vec{u}_{\alpha\beta}^h$ the output is saturated to $\vec{u}_{\alpha\beta}^{hs}$, the delivered current results in:

$$\vec{i}_{\alpha\beta}^{hs} = \frac{\vec{u}_{\alpha\beta}^{hs} - \vec{e}_{\alpha\beta}^h}{R + jh\omega L} \quad (6.50)$$

and the undelivered current can be calculated as:

$$\Delta \vec{i}_{\alpha\beta}^h = \vec{i}_{\alpha\beta}^h - \vec{i}_{\alpha\beta}^{hs} = \frac{\vec{u}_{\alpha\beta}^h - \vec{e}_{\alpha\beta}^h}{R + jh\omega L} - \frac{\vec{u}_{\alpha\beta}^{hs} - \vec{e}_{\alpha\beta}^h}{R + jh\omega L} = \frac{\vec{u}_{\alpha\beta}^h - \vec{u}_{\alpha\beta}^{hs}}{R + jh\omega L} = \frac{\Delta \vec{u}_{\alpha\beta}^h}{R + jh\omega L} \quad (6.51)$$

and $\Delta \vec{i}_{\alpha\beta}^h$ can be expressed for FPS and NFS as:

$$\Delta \vec{i}_{\alpha\beta}^h = (1 - k_{12}) \cdot \frac{\vec{u}_{\alpha\beta}^h}{R + jh\omega L}. \quad (6.52)$$

Meanwhile, for the harmonic sequences $\Delta \vec{i}_{\alpha\beta}^h$ can be expressed as:

$$\Delta \vec{i}_{\alpha\beta}^h = (1 - k_H) \cdot \frac{\vec{u}_{\alpha\beta}^h}{R + jh\omega L}. \quad (6.53)$$

Finally, for avoiding the windup in the inner current control loop, the undelivered current needs to be subtracted from the reference currents, resulting in a new saturated current reference:

$$\vec{i}_{\alpha\beta}^{hs*} = \vec{i}_{\alpha\beta}^{h*} - \Delta \vec{i}_{\alpha\beta}^h. \quad (6.54)$$

It needs to be noted the difficulty of subtraction of harmonic complex signals. For example, if a sampling time of 200 μs , a variation of θ between to consecutive instants of 18° appear for the 5th harmonic and of 25.2° for the 7th. That variation can be considered excessive, and resulting in phase shifting problems. In this way, it is recommended to employ lower sample times that reduces the uncertainty. As minimum, the employment of 100 μs as sample time is required.

Once that the antiwindup for the inner loop has been detailed, it needs to be dealt with the outer pcc voltage controller loop during saturation. While saturation, as the output is constrained, the voltage PCC harmonic compensation could not be completely achieved. As the compensation is not achieved, the error input would not be zero and the PI controllers, would continuously increase the output ($\vec{i}_{\alpha\beta}^{h*}$).

In order to avoid this behaviour, the strategy followed consists on two steps:

- The PCC harmonic voltage controller should start from an output close to zero and gradually increasing towards the complete compensation.
- At the time that the inner control loop detects saturation, the integral actuation of the PI needs to be stopped.

The gradual increment on the outer control needs to pass through all the values from 0 to the final output for performing compensation (that might not be reached). For achieving this, during the design of the PCC harmonic voltage controller, a low initial point ($c(0)$) needs to be selected when k_p is calculated in (6.38). As a consequence, it can be perfectly identified when the harmonic voltage compensation has reached to its maximum. Then the calculation of k_i for the PCC harmonic voltage loop in (6.39) needs to be done with a settling time that is at least ten times higher than the settling time

Then, as soon as the occurrence of saturation is detected the integration of each PI controller is stopped. It is achieved by the logical parameter γ that multiplies the PI integrator input:

$$\gamma = (k_H == 1). \quad (6.55)$$

The modified DFIMS and the antiwindup system for the PCC voltage control is depicted in Fig. 6.23

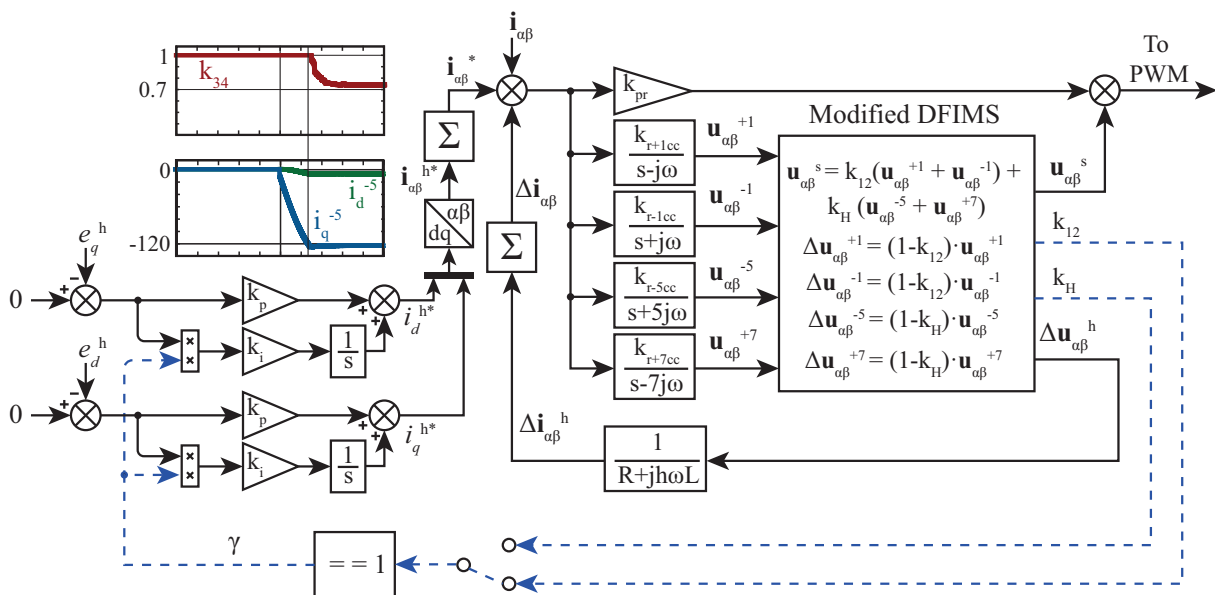


Figure 6.23: Scheme of PCC Harmonic control with DFIMS saturator plus antiwindup.

6.4. Simulation Results

The simulation results are divided in the two different strategies proposed in order to prevent the PCC voltage distortion. In the first strategy, the functionality of APF filter is studied for the compensation of local non-linear loads in order to prevent the propagation of harmonic voltages by locally compensating the harmonic currents. In the second strategy, the harmonic voltage is measured at the PCC and the harmonic voltage presence is reduced by harmonic currents injection.

6.4.1. Parallel Active Power Filters

For testing the proposed algorithm, Matlab/Simulink R2016b is employed. The simulation set-up is composed by a grid without perturbations, two VSIs working as APFs

and a non-linear load. Both VSIs are the interface between distributed generators and grid. The main objective of the VSIs is to inject the maximum possible active power to the grid. As a secondary goal they are trying to compensate the local non-linear loads simplified as exclusively one non-linear load. One of the VSI is connected closer to the load (Load VSI) and the other one closer to the grid (Grid VSI). The compensation of the harmonic currents consumed by the non-linear load is preferred with the Load VSI in order to avoid the harmonics propagation. The parameters of the simulation test are collected in Table 6.1.

Table 6.1: Simulation parameters

Parameter	Value
V_{dc}	750 \rightarrow 690 V
V_{ac}	400 V_{rms}
L_{filter}	750 μH
P_{ref} (Load VSI)	50 kW
Q_{ref} (Load VSI)	120 kVar
NL load (Uncontr. Rect. + R)	6.4 Ω
T_s	100 μs

In Fig. 6.24 an example of working operation is shown. In this case, the first and second inverters are delivering a certain amount of active and reactive power ($P = 50$ kW, $Q = 120$ kVar). In this situation with a dc-bus of 750V, the Load VSI is able to deliver the desired amount of power and at the same time completely compensate the harmonic non-linear load. Assuming a dc-bus reduction, the Load VSI is not able to completely cope with both objectives. As two VSIs are parallel connected, the objectives could be achieved in a cooperative way.

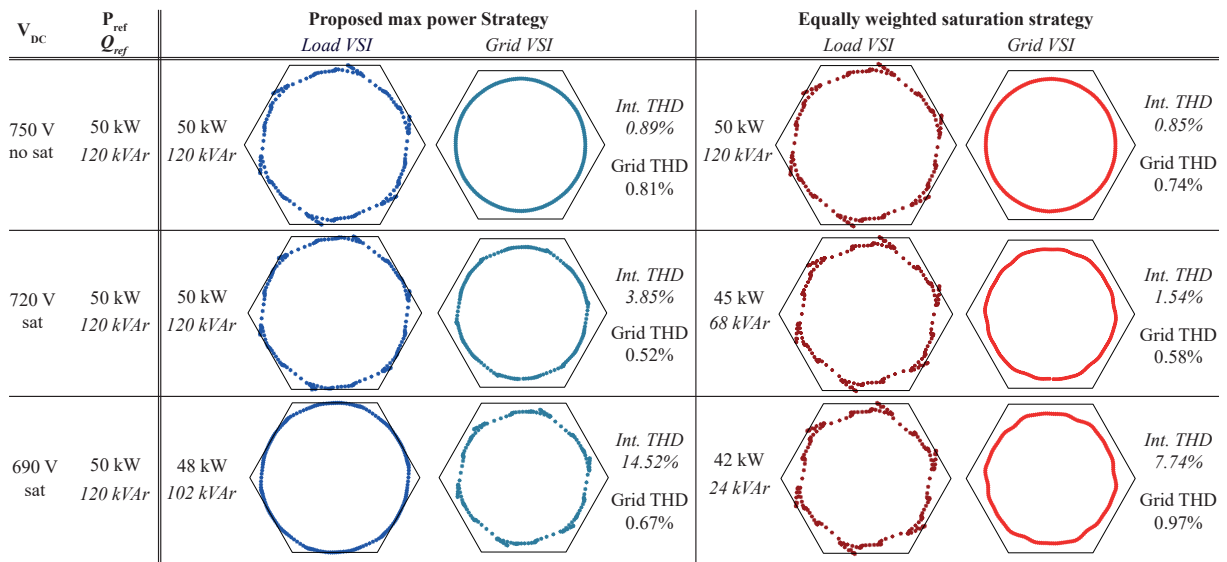


Figure 6.24: Comparison of the proposed maximum power strategy (reduction of harmonic compensation) and equally weighted compensation (reduction of power delivering and harmonic compensation).

The proposed strategy opts for delivering the maximum possible power (50 kW and 120 kVAr) and reduce from the harmonic compensation. Then, the Grid VSI is in charge of compensating the remaining harmonic currents that the Load VSI was not able to compensate.

Meanwhile, the proposed strategy is compared with a technique that opts for reducing all the different components with the same weight. In this case, a reduction over the delivered active power and reactive power is carried out which allows to perform a higher compensation with the Load VSI.

With the equally weighted saturation strategy when saturation occurs, a reduction is carried out over the different functionalities in order to do not exceed the voltage limitations. In this context, the reduction from P and Q allows a smaller reduction over the harmonic components than the proposed strategy. In this context, the currents that circulates between the converters present smaller distortion, and the Grid VSI completely compensates the harmonic currents in order to deliver clean currents to the grid.

However, in the proposed strategy, when saturation occurs, the harmonic currents are less compensated by the Load VSI. It results in harmonic current circulation at the line between the inverters. Anyhow, in the same way as before, the Grid VSI completes the compensation of those harmonic currents performing a deliver of clean currents to the grid.

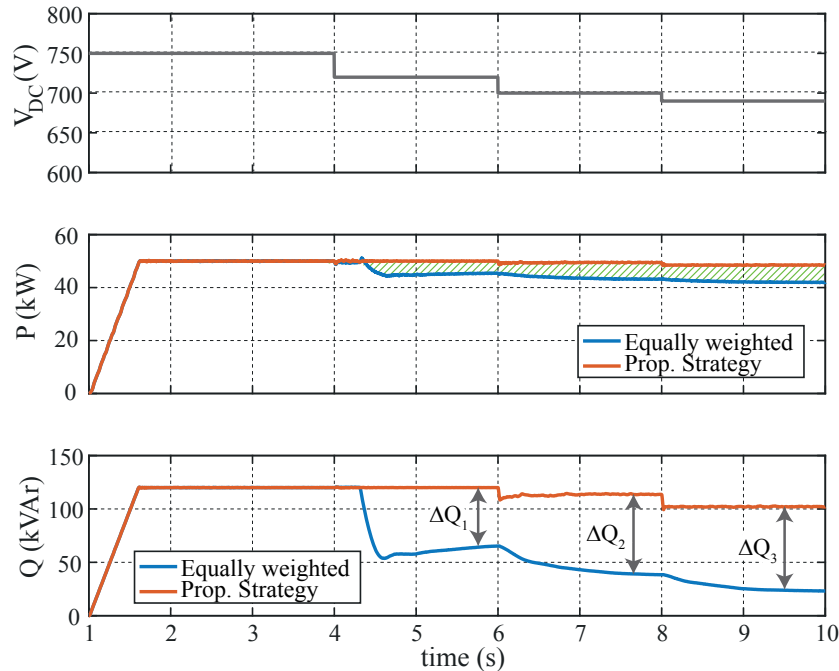


Figure 6.25: Comparison of active (P) and reactive (Q) powers with the proposed strategy and the equally weighted strategy.

Therefore, in both two cases the final result in terms of harmonic currents compensation is completely achieved. However, if the reduction is applied over active and reactive power

the total injection of energy and reactive power is smaller. In Fig. 6.25 it can be seen the difference of active and reactive power between the two strategies. This reduction implies lower economical return.

6.4.2. Harmonic PCC voltage reduction

This test aims to probe the proposed algorithm for the harmonic voltage reduction at the PCC. For this test Matlab/Simulink R2016b is employed. The employed VSC main objective is to deliver the maximum available power P and the required Q . Once that it has been satisfied, if there exists margin until the dc bus limitation, it tries to compensate the PCC harmonic voltages as maximum as possible.

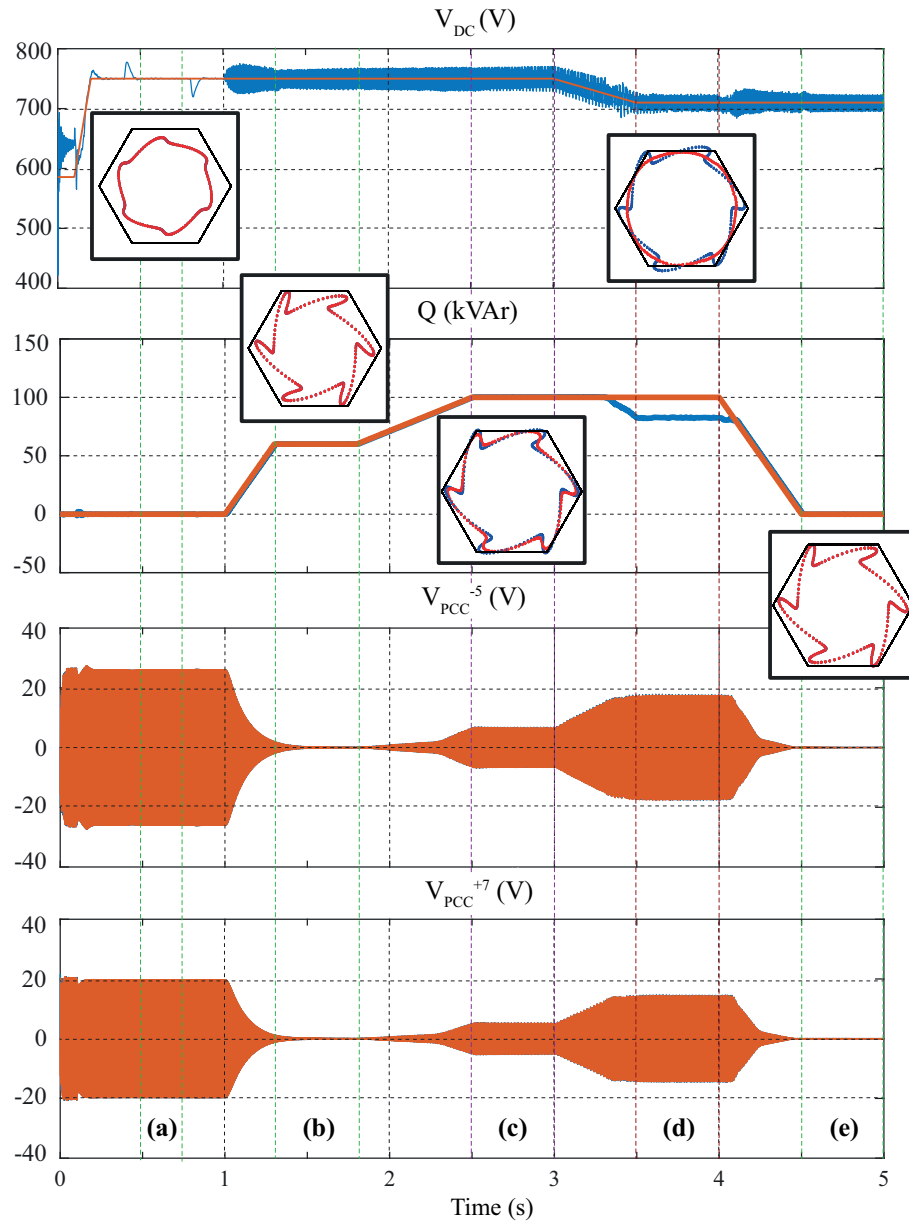


Figure 6.26: Harmonic PCC voltage control under different conditions.

For this test, an VSC with an L filter $750 \mu\text{H}$ is connected to a distorted grid. The distorted grid presents an inductance grid value of $250 \mu\text{H}$. With the previously mentioned objectives, different reactive power references and dc-bus voltage occurs, provoking the transition between saturated and unsaturated cases. The test is depicted in Fig. 6.26.

In the first time interval (0.5 - 0.75s), shown in Fig. 6.26.a the dc-bus is set to 750 V and $Q^* = 0$, without harmonic compensation (saturation is not reached $k_F = 1$, $k_H = 1$). Then, in the second time interval (1.3 - 1.8s), shown in Fig. 6.26.b, the PCC harmonic voltage compensation is carried out and Q^* is set to 60 kVAr (saturation is closer but it is not reached, $k_F = 1$, $k_H = 1$). In the third time interval (2.5 - 3s), shown in Fig. 6.26.c, Q^* rises to 100 kVAr. Saturation is reached and PCC harmonic voltage cannot be completely compensated ($k_F = 1$, $k_H \downarrow$). In the fourth time interval (3.5 - 4s), shown in Fig. 6.26.d, dc-bus is reduced to 710 V, saturation is higher now, and compensation of PCC harmonic voltage is almost abandoned and a diminution on the delivered Q occurs ($k_F \downarrow$, $k_H \downarrow\downarrow$). Finally, in the last time interval (4.5 - 5s), shown in Fig. 6.26.e, the Q^* reference is reduced to zero. In this conditions, the saturation state is abandoned and the PCC harmonic voltages are fully compensated ($k_F = 1$, $k_H = 1$).

6.5. Conclusions

During this chapter the compensation of harmonic voltages at the PCC is carried out. It has been studied as an additional functionality of shunt grid connected VSIs associated with distributed generators. In this context, two types of strategies has been studied: (1) VSI working as APF for compensating local non linear loads, preventing the propagation of the harmonic currents into harmonic voltages and (2) the measurement of harmonic voltages at the PCC and its compensation through harmonic currents injection.

For the first one, a contribution has been made when parallel APFs work in parallel and one of them reaches saturation. This strategy is based on always delivering to the grid the maximum available active power and the required reactive power. Then, the harmonic currents compensation is achieved in a cooperative way between the different VSIs.

For the second one, a control system for compensating the voltage harmonic at the PCC has been proposed. First, the importance of the grid impedance in the compensation is analysed and a novel method for the grid inductance detection is provided. Then, the problem of overmodulation in harmonic voltage compensation is faced. This problem has been mentioned in the literature and a new control system has been implemented with the previously proposed DFIMS. This approach appears as a solution for allowing the employment of shunt connected VSIs as PCC voltage compensators.

Finally, in the last part of the chapter, simulation tests validate the algorithms proposed for both strategies APF and harmonic voltage compensators.

Chapter 7

Experimental Results

7.1. Introduction

In the previous chapters presented in this thesis, the multifrequency control for VSCs has been studied. In some of this chapters, new algorithms are proposed that imply different contributions over the studied topics. Although these algorithms have been theoretically analysed and tested with simulation software, it has been also implemented for the control of real VSCs in order to validate the desired behaviour.

Depending on the application different experimental set-ups are employed in order to reach the desired results. The chapter is divided in a first section, where the employed experimental set-ups are described. Then, the next sections contain the experimental results for each one of the proposed algorithm. Each one of these sections describes the modifications of the set-up for the carried out test, explanations for the algorithm implementation at the control board and the obtained results and its comparison with different previous techniques.

7.2. Experimental set-up

For the experimental scenario, different equipment has been employed. The equipment can be divided into three different categories. The first category is the employed power converter. The second category is the control board where the algorithms are implemented. Finally, the third category describes the employed auxiliary equipment.

7.2.1. Power Converter

The converter employed for most of the experimental tests is the CONDOR converter. This converter is a back to back 150 kVA NPC. It is connected to the grid through an LCL filter composed by a grid side inductance of 250 μH , a capacitor of 100 μF and a converter side inductance of 500 μH . The filter topology can be modified in order to obtain the best

set-up for each test. LCL filter can be modified to an L filter ($750\ \mu\text{H}$) and to an LC filter ($750\ \mu\text{H}$ and $100\ \mu\text{F}$ or $300\ \mu\text{F}$, depending on star or triangle connection). The NPC voltage converter is shown in Fig. 7.1.

Although the CONDOR converter is composed by two VSCs, just the closest one to the grid is employed for testing the algorithms. In this context, for the proposed algorithms in this thesis, the converter is always working in STATCOM mode or as an interface for dc-sources and dc-loads.

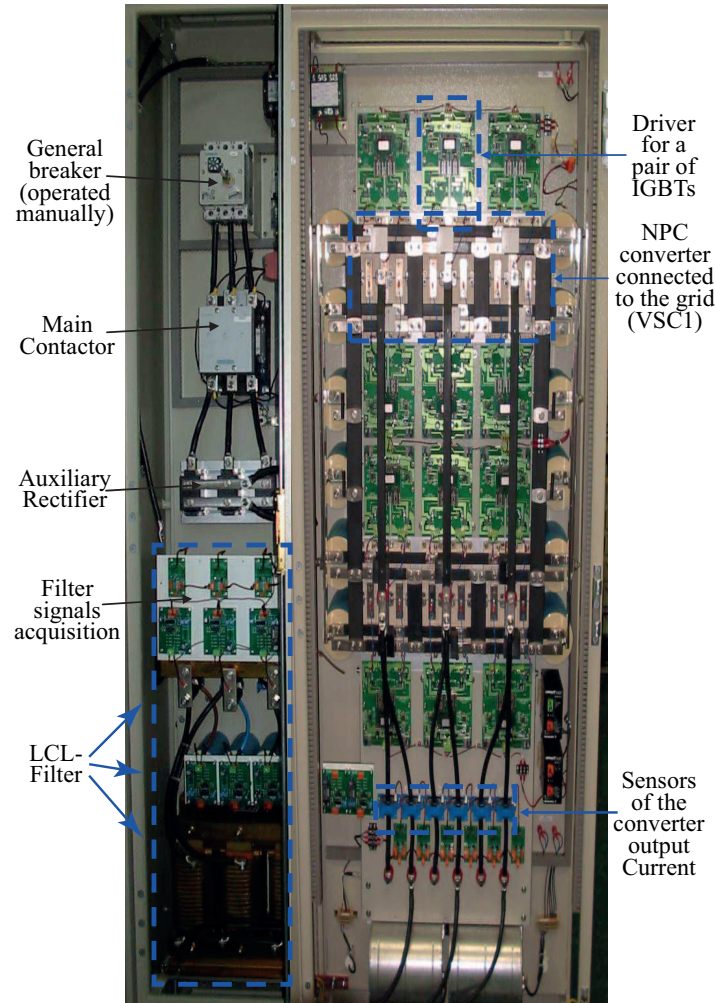


Figure 7.1: CONDOR Converter.

7.2.2. Control electronic system

The previously described CONDOR converter is controlled through a control electronic system. This system is in charge of acquiring the voltage and current measurements and generate the proper *Pulse-width Modulation (PWM)* signals for switching the IGBTs. Control electronic system is composed by a control card and a control host: the control platform is made up of a floating point DSP TMS320DSK6713 from Texas Instrument® and an FPGA SPARTAN 3 from Xilinx® [130], as shown in Fig. 7.2.

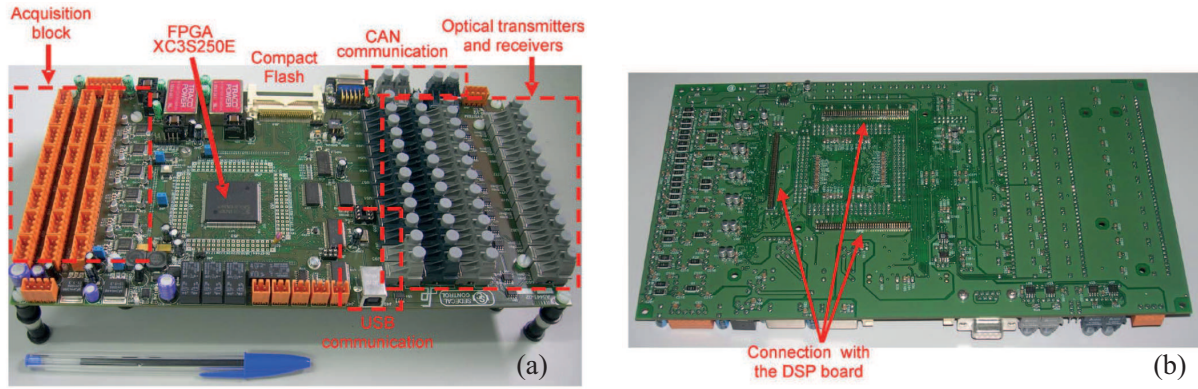


Figure 7.2: Control electronic system. (a) Top and (b) bottom views [130].

In addition, the control system is completed with an user-interface that is executed on a PC. The control card in real time, receives the references and control parameters from the interface and it sends the sampled variables to the PC. As seen in Fig. 7.3, the sampled variables can also be plotted in real time in the user interface.

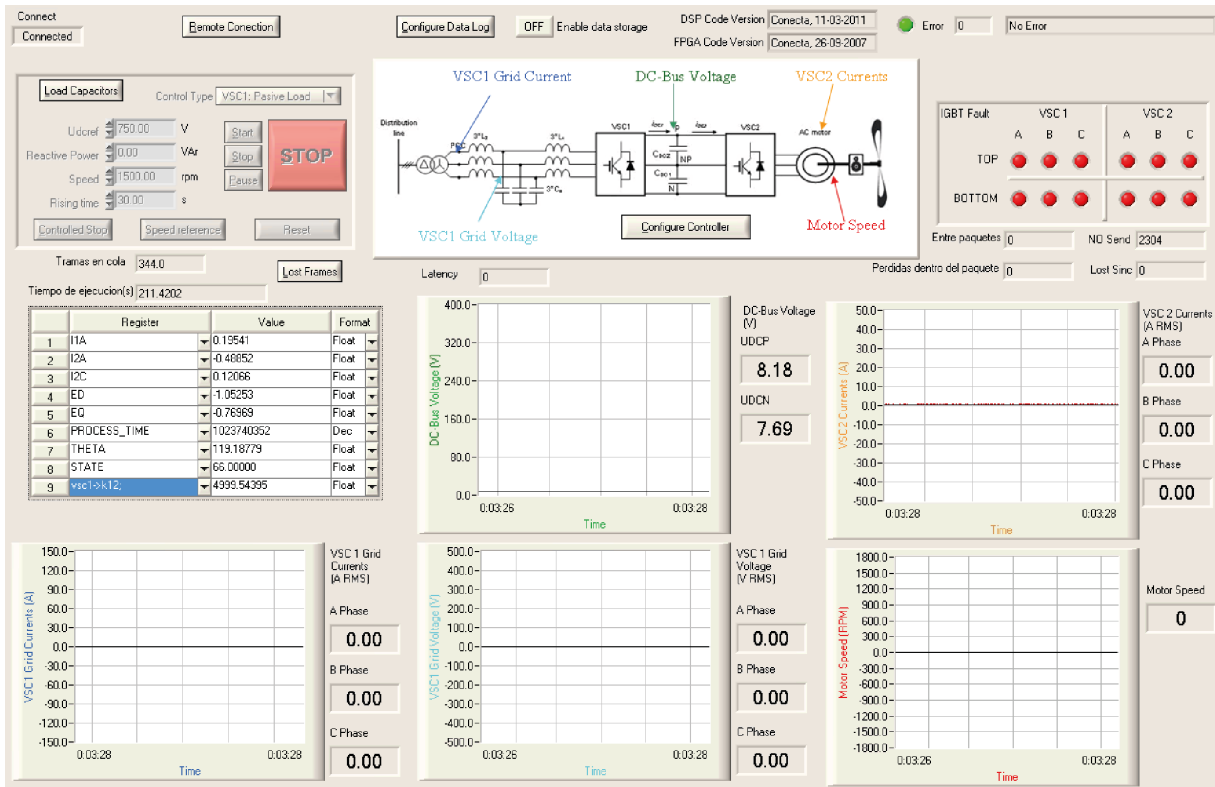


Figure 7.3: User interface for power converter [131].

7.2.3. Auxiliary equipment

In this subsection the complementary equipment employed for the different tested situations are introduced here. As the thesis is focused on the control of harmonic components, most of the tests are needed to be carried out with distorted grid conditions.

For this purpose a Regatron® Topcon ACS programmable power supply is employed, depicted in Fig. 7.4. This power source is able to work in the four quadrants. In addition, this power supply allows to generate distorted voltage waveforms with flexible harmonics amplitudes.



Figure 7.4: Regatron® TopCom ACS 3-phase programmable Power Supply.

Additional secondary equipment that has been also employed in different tests is a dc-source. In some tests, this dc-source is directly connected to the dc side of the power converter in order to fixing the dc voltage value. For this purpose the AMREL® SPS 800-18 power supply shown in Fig. 7.5 with a 800 V and 18 A voltage and current limits is employed.



Figure 7.5: AMREL® SPS 800-18 dc voltage source.

7.3. Instantaneous Active Power Multifrequency Control

The instantaneous active power oscillation reduction is experimentally tested in this section. The LC filter topology ($750 \mu\text{H}$, $100\mu\text{F}$) is employed for the test in order to reduce the high frequency components and avoid aliasing in the voltage measurements. The programmable power supply is configured to generate an unbalanced and distorted grid.

The proposed method of current reference calculation for mitigation of instantaneous active power fluctuations with minimum THDi is implemented in the electronic control system ($8 \times 8\text{Opt}$). In addition, other reference calculation methods are also implemented for comparison: (1) Without power oscillations reduction (2×2) matrix, (2) with reduction of the 2^{nd} power harmonic (4×4) and (3) with reduction of the 2^{nd} , 4^{th} and 6^{th} power harmonics without THD reduction (8×8). For the current references calculation, a system of linear equations needs to be solved. It requires a high computational time and the way of implementation is crucial in order to achieve a runtime lower than the sampling time. The runtime required for each one of the CRC methods are collected in Table 7.1 and the implementation approach is described in Subsection 7.3.1.

Table 7.1: Runtime for different CRC methods

CRC method	Controlled Parameters	Computational time
2×2	P, Q	$65.3 \mu\text{s}$
4×4	P, Q, P_2	$74.6 \mu\text{s}$
8×8	P, Q, P_2, P_4, P_6	$105 \mu\text{s}$
$8 \times 8 \text{ Opt}$	$P, Q, P_2, \text{HD}, P_6$	$145 \mu\text{s}$

The distorted and unbalanced voltage waveform generated by the programmable power supply is depicted in Fig. 7.6. The unbalance is provoked over the fundamental component (50Hz) with a magnitude and phase variation over phase B ($V_a = 230_{\angle 0^\circ} \text{ V}$, $V_b = 223_{\angle -115^\circ} \text{ V}$, $V_c = 230_{\angle 120^\circ} \text{ V}$). This distortion provokes FNS ($h=-1$) which if not controlled results in a 2^{nd} power harmonic. For the distortion, a 5 % (11.5 V) has been set for the fifth harmonic and 2% for the seventh harmonic. These values are within the allowed voltage harmonics by European Standards [132].

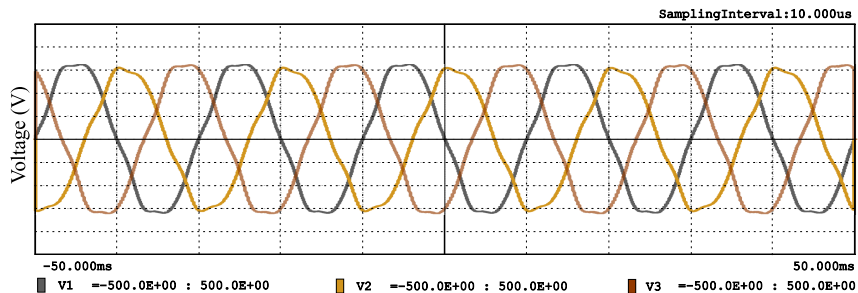


Figure 7.6: Generated unbalance and distorted grid voltage waveform [58].

With the described grid, a certain amount of active (P) and reactive (Q) powers are exchanged with the grid. This power request increases the FPS current component, which increases the power oscillations provoked by the combination of FPS current (\vec{i}_{+1}) with the non-fundamental voltage components (\vec{v}_{-1} , \vec{v}_{-5} , \vec{v}_{+7}). In this context, the different CRC methods are employed and the effect over the exchanged instantaneous power can be seen in Fig. 7.7 (waveform) and in Fig. 7.8 (FFT).

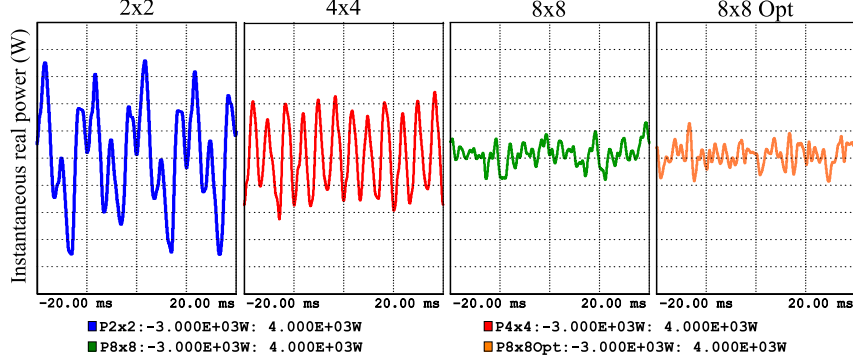


Figure 7.7: Filtered waveform of instantaneous active power (1kHz) when 2×2 (with second and sixth harmonics), 4×4 (with sixth harmonic) and 8×8 and 8×8 Opt (with no predominant harmonic) CRC methods are employed [58].

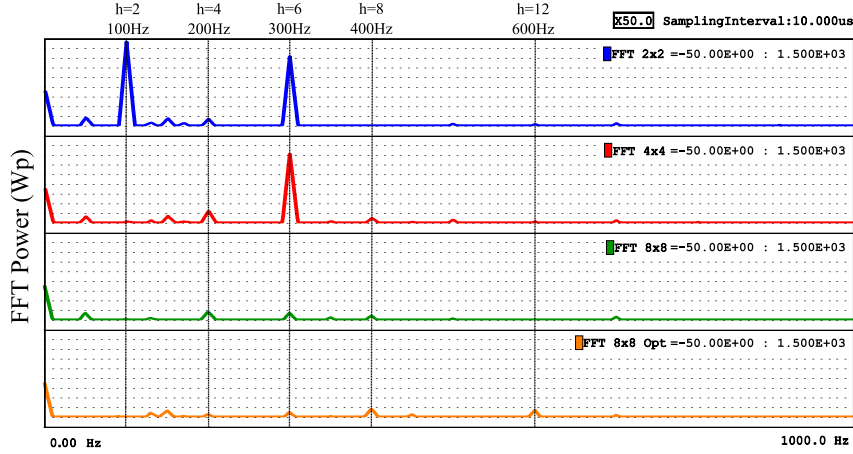
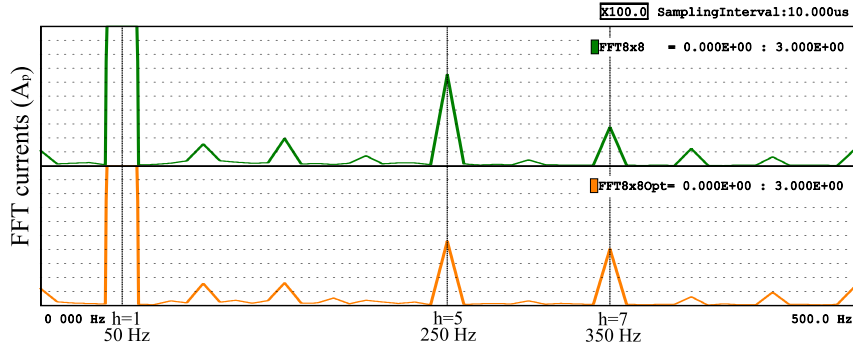


Figure 7.8: FFT of instantaneous active power for the different CRC methods [58].

It can be appreciated in both power instantaneous waveform and FFT how the 2nd harmonic elimination is reduced through the 4×4 CRC method. It can be also seen how the 6th harmonic is reduced with the 8×8 CRC method through the injection of harmonic currents to the grid (\vec{i}_{-5} and \vec{i}_{+7}). As it can be appreciated, the presence of the 4th harmonic is not significant and its reduction through the 8×8 CRC method is not relevant. However, it can be seen the benefits of employing this degree of freedom for current harmonic distortion minimization (8×8 Opt method), as depicted in Fig. 7.9.

It can be appreciated how the 5th current harmonic component is reduced and how the 7th harmonic current slightly increases. In the studied case, a 10 % THDi reduction and a 15 % HD reduction (5th and 7th harmonic currents) are achieved when the 8×8 Opt

Figure 7.9: FFT of exchanged currents with 8×8 and 8×8 Opt methods [58].

method is employed. Meanwhile, the instantaneous power 2^{nd} and 6^{th} harmonic are equally being reduced (85-90 % with both methodologies). The previously described experimental results are collected in Table 7.2.

Table 7.2: Instantaneous Active Power Experimental results

Parameter	Power spectrum (W_p)			HD	THD
Control	p_2	p_4	p_6	$h < 11$	$h < 50$
2x2	1347.3	135.86	1150.4	0.57 %	3.35 %
4x4	84.12	224.48	1143.3	0.56 %	3.42 %
8x8	88.78	150.6	157.66	3.70 %	5.02 %
8x8 Opt	134.48	83.86	122.70	3.18 %	4.54 %

7.3.1. Matrix LU Decomposition

As previously stated, the implementation of the CRC methods is essential for achieving a runtime lower than the sampling time. The complexity of the system comes from solving the system of linear equations, as expressed in (4.26) and (4.37):

$$\begin{pmatrix} P \\ Q \\ \dots \\ \dots \end{pmatrix}_{n \times 1} = \frac{2}{3} \begin{pmatrix} e_d^{+1} & e_q^{+1} & \dots & e_q^h \\ e_q^{+1} & -e_d^{+1} & \dots & -e_d^h \\ \dots & \dots & \dots & \dots \\ \dots & \dots & \dots & \dots \end{pmatrix}_{n \times n} \begin{pmatrix} i_{1d} \\ i_{1q} \\ \dots \\ i_{hq} \end{pmatrix}_{n \times 1}. \quad (7.1)$$

It should be noted, that the power references vector and the voltages matrix are known and the currents reference vector is the one that is desired to be obtained. Although the inverse of the voltage matrix could be calculated and the currents vector could be obtained with a matrices multiplication, the inverse calculation would be needed every sample instant. However, the greater the order of the matrix is, the more difficult to obtain its inverse.

In this way, a different strategy has been followed for solving the linear equation systems. The followed strategy is the matrix LU decomposition where a matrix is divided

in lower (L) and upper (U) triangular matrices [133]. Then, the vector can be solved by substitution.

In regard to the current reference calculation, the equation can be described as follows:

$$\vec{s}_{n \times 1} = \frac{2}{3} \cdot E_{n \times n} \cdot \vec{i}_{n \times 1}^* \rightarrow \vec{s}_{n \times 1} = A_{n \times n} \cdot \vec{i}_{n \times 1}^* \rightarrow \vec{s}_{n \times 1} = L_{n \times n} \cdot U_{n \times n} \cdot \vec{i}_{n \times 1}^* \quad (7.2)$$

Matrix A can be represented as the product of a lower diagonal matrix (L) by an upper diagonal matrix (U). The diagonal terms of the lower matrix are ones for making the system equation determined, as shown later:

$$\begin{pmatrix} a_{11} & a_{12} & \dots & a_{1n} \\ a_{21} & a_{22} & \dots & a_{2n} \\ \dots & \dots & \dots & \dots \\ a_{n1} & a_{n2} & \dots & a_{nn} \end{pmatrix}_{n \times n} = \begin{pmatrix} 1 & 0 & \dots & 0 \\ l_{21} & 1 & \dots & 0 \\ \dots & \dots & \dots & \dots \\ l_{n1} & l_{n2} & \dots & 1 \end{pmatrix}_{n \times n} \begin{pmatrix} u_{11} & u_{12} & \dots & u_{1n} \\ 0 & u_{22} & \dots & u_{2n} \\ \dots & \dots & \dots & \dots \\ 0 & 0 & \dots & u_{nn} \end{pmatrix}_{n \times n} \quad (7.3)$$

Now, all the different terms of the lower and upper diagonal matrices need to be found. Firstly, calculating the first row of matrix A as the multiplication of the first row of matrix L by the different columns of matrix U, the terms (u_{1j}) are calculated.

$$u_{1j} = a_{1j} \quad \text{where } j = [1, n] \quad (7.4)$$

Then, calculating the first column of matrix A (a_{j1}) as the multiplication of the different rows of L by the first column of U, the first column of L is obtained:

$$l_{j1} = a_{j1}/u_{11} \quad \text{where } j = [1, n] \quad (7.5)$$

The process follows with the same methodology, the second row of matrix U is obtained as:

$$u_{2j} = a_{2j} - u_{1j} \cdot l_{21} \quad \text{where } j = [2, n] \quad (7.6)$$

Then, the second column of matrix L can be obtained as:

$$l_{j2} = \frac{a_{j2} - l_{j1} \cdot u_{12}}{u_{22}} \quad \text{where } j = [2, n] \quad (7.7)$$

In this way, all the terms of L and U can be obtained in a optimized computational way. As previously described:

$$\vec{s}_{n \times 1} = A_{n \times n} \cdot \vec{i}_{n \times 1} = L_{n \times n} \cdot U_{n \times n} \cdot \vec{i}_{n \times 1} \quad (7.8)$$

It can be noted that $U \cdot \vec{i}$ returns a vector of dimensions $n \times 1$ which can be called $\vec{y}_{n \times 1}$, and therefore, the previous expression can be rewritten as:

$$\vec{s}_{n \times 1} = L_{n \times n} \cdot \vec{y}_{n \times 1} \quad (7.9)$$

where \vec{s} and L are known. As L is diagonal, \vec{y} can be easily obtained by substitution:

$$\begin{pmatrix} p_1 \\ p_2 \\ p_3 \\ \dots \\ p_n \end{pmatrix} = \begin{pmatrix} 1 & 0 & 0 & \dots & 0 \\ l_{21} & 1 & 0 & \dots & 0 \\ l_{31} & l_{32} & 1 & \dots & 0 \\ \dots & \dots & \dots & \dots & \dots \\ l_{n1} & l_{n2} & l_{n3} & \dots & 1 \end{pmatrix} \begin{pmatrix} y_1 \\ y_2 \\ y_3 \\ \dots \\ y_n \end{pmatrix}. \quad (7.10)$$

Therefore, all the items in \vec{y} can be easily obtained. Finally, for obtaining the desired currents vector (\vec{i}), it is enough to solve $\vec{y} = U_{n \times n} \cdot \vec{i}$:

$$\begin{pmatrix} y_1 \\ y_2 \\ y_3 \\ \dots \\ y_n \end{pmatrix} = \begin{pmatrix} u_{11} & u_{12} & u_{13} & \dots & u_{1n} \\ 0 & u_{22} & u_{23} & \dots & u_{2n} \\ 0 & 0 & u_{33} & \dots & u_{3n} \\ \dots & \dots & \dots & \dots & \dots \\ 0 & 0 & 0 & \dots & u_{nn} \end{pmatrix} \begin{pmatrix} i_1 \\ i_2 \\ i_3 \\ \dots \\ i_n \end{pmatrix}. \quad (7.11)$$

As U is diagonal, it is immediate to obtain the values for the current references, completing the CRC process.

7.4. Distortion Free Instantaneous Multifrequency Saturator

During chapter 5, the distortion free multi-frequency saturators are presented and analysed with simulation software. In this section, the proposed *Distortion Free Instantaneous Multifrequency Saturator (DFIMS)* is implemented and tested with the CONDOR converter. Then, the distortion free multifrequency saturator proposed in [64] (also referred to as “literature saturator”) is also implemented and a comparison is made between the two algorithms.

For this test, a distorted grid is required and in this context, the Regatron® Topcon ACS programmable power supply is employed. The setup for the test is described in Table 7.3.

In this situation, the converter (which is working as a STATCOM) is requested to deliver a high amount of reactive power (Q^*). This Q^* , which is reachable for a low grid

Table 7.3: Parameters for the instantaneous active power experimental test

Grid Voltage	Grid Frequency (f_1)	50 Hz
	FPS 230 V ($h = +1$)	1.06 pu
	FNS ($h=1$)	0.03 pu
	Harmonic Sequence ($h = -5$)	0.06 pu
	Harmonic Sequence ($h = +7$)	0.05 pu
Filter	Inductance (L)	750 μ H
Control references	DC-Bus voltage	650 V
	Q reference	110 kVAr
Frequencies	Sampling Frequency (f_s)	5 kHz
	Switching Frequency (f_{sw})	5 kHz

voltage condition, becomes unreachable when the grid presents a higher voltage. In this context, the grid is set to a high voltage value (1.06pu), with high harmonic presence.

When the Q^* is requested in order to avoid overmodulation and even instability, the saturator plus antiwindup algorithm actuates. As previously explained during chapter 5, the differences between the proposed DFIMS and the previous published DF-saturator in [64] are divided in two. First, when saturation is reached, some of the capabilities need to be reduced. DFIMS priority is to always accomplish the minimum possible THD injection, although that means Q^* reduction. Meanwhile, in the literature saturator, both capabilities are reduced in order to avoid overmodulation. The second difference between the literature and the proposed saturator is the saturator dynamics. The literature saturator consists on a saturation system with its own dynamics, which needs to be several times slower than the control algorithm. However, the proposed DFIMS presents a novel strategy that instantaneously works out the optimal reduction gain. As it was showed during simulation results, the dynamic of the global system during saturation is the same as if no saturation is applied.

For the presented case, the voltage and current waveforms are presented in Fig. 7.10. It can be appreciated that with the same grid configuration and the same Q^* of 110 kVAr, the exchanged grid currents are far less distorted with DFIMS saturator ($\text{THD} \approx 1.82$) than with literature saturator ($\text{THD} \approx 3.11$). The reduction over the controlled harmonic current components goes from 1.16 A to 0.17 A for the 5th current harmonic and from 0.69 A to 0.14 A for the 7th current harmonic. The counterpart is the reduction over the delivered Q from 40.619 kVAr to 35.706 kVAr.

The FFT of the currents for a single phase is depicted in Fig. 7.11. The peak values for each harmonic are shown for both literature saturator and DFIMS. Finally, the obtained results for the steady state test are collected in Table 7.4.

In addition to the steady state test, another test was carried out for showing the performance during transient state. In this test, the same grid conditions and dc-bus voltage are maintained. Then, the reactive power reference varies from 0 to 110 kVAr in 1s. The VSC reaches the saturation at the points showed before in Table 7.4 (40.62 kVAr for literature and 35.71 kVAr for DFIMS). This test is depicted in Fig. 7.12.a. Then,

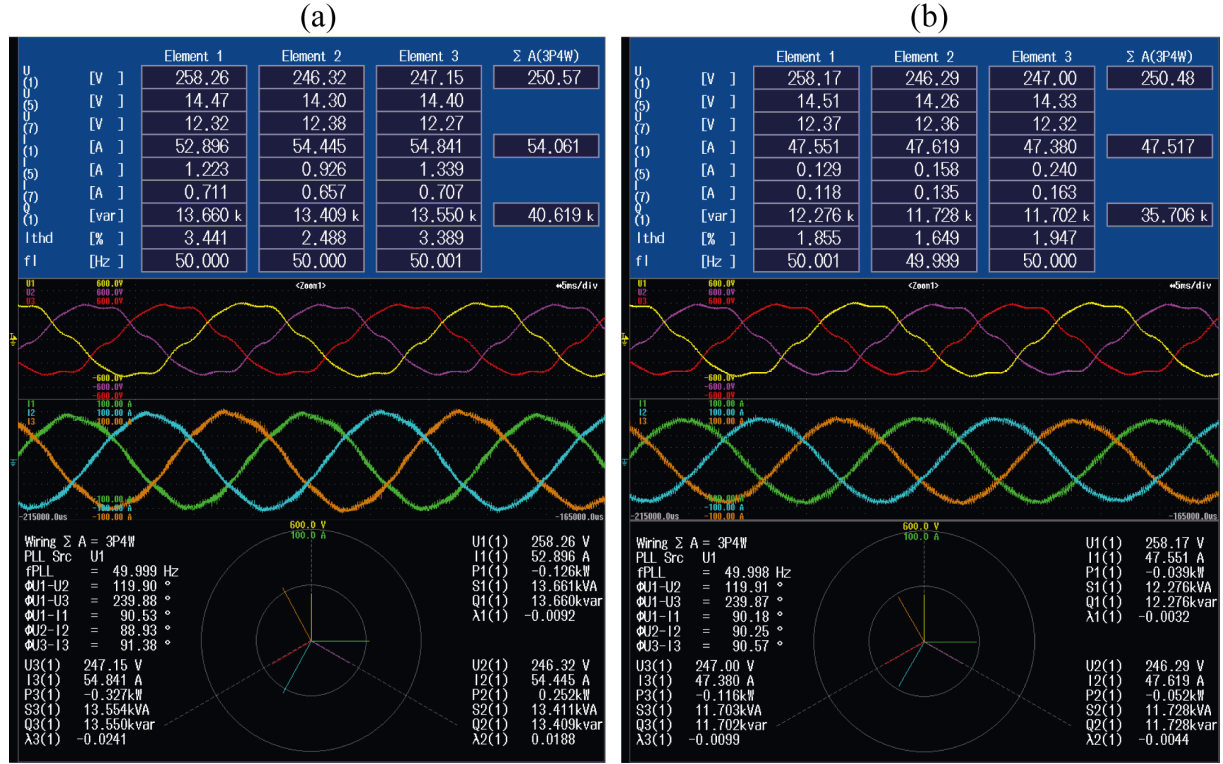


Figure 7.10: Voltage and currents waveforms obtained during experimental test during saturation with (a) Literature saturator and (b) DFIMS.

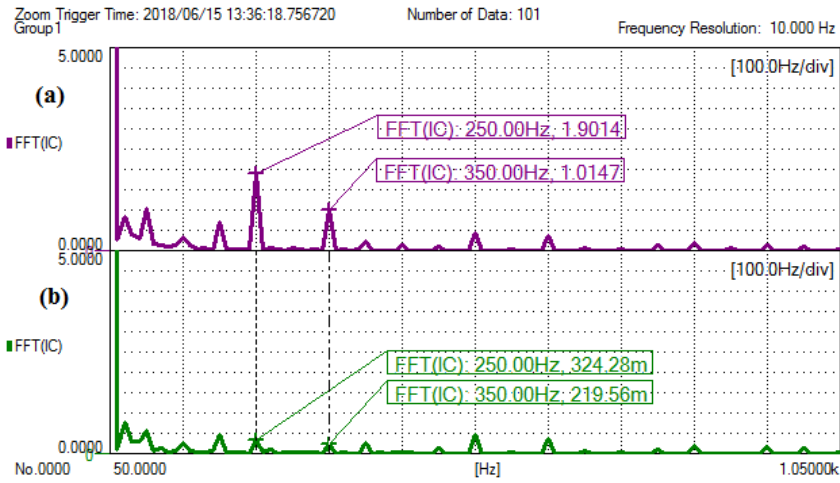
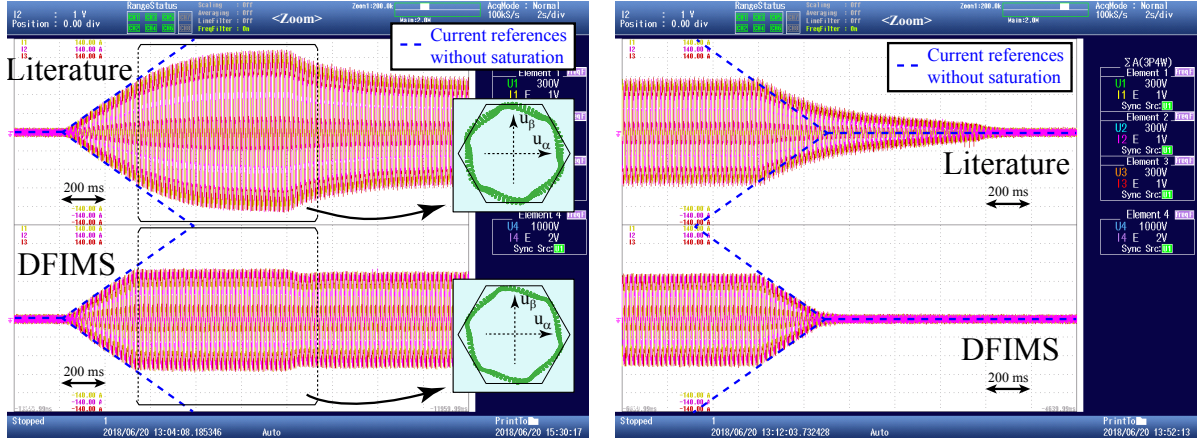


Figure 7.11: Current harmonic content comparing (a) the literature saturator and (b) the proposed DFIMS in steady state.

Table 7.4: Experimental Results for DFIMS and literature Saturators

Selected Saturation Strategy	Literature Saturator	Proposed DFIMS
Q delivered	40.62 kVAr	35.71 kVAr
i_g THD	3.106 %	1.817 %
$i_g(h = 1)$	76.45 A	67.20 A
$i_g(h = 5)$	1.644 A	0.248 A
$i_g(h = 7)$	0.978 A	0.196 A

a similar test is carried out when the reference reactive power goes from 110 kVAr to 0 kVAr, abandoning the saturation state. This test is depicted in Fig. 7.12.a.



(a) Transient with Q^* increment (saturation reached).

(b) Transient with Q^* diminution (saturation abandoned).

Figure 7.12: Transient state of the two different compared strategies (literature and DFIMS) in two different situations.

It can be seen how the proposed DFIMS follows the requested references and it detects the saturation as soon as it occurs. A small error occurs during the reference variation (ramp) related with the extrapolation of trajectory. When the reference remains constant, it can be seen how the steady state is reached in the external control settling time (100 ms for the dc-bus control). It also can be seen that when the saturation state is abandoned, the saturator instantaneously follows the reference values.

Meanwhile, it can be seen that with the literature saturator, while the ramp continues increasing the slow dynamics of the saturator allows the currents to increase. That incurs into overmodulation, as it can be appreciated in the trajectory depiction of $\vec{u}_{\alpha\beta}$. Then, once that the Q reference is kept constant, saturator takes time until reaching the steady state ($\approx 0.6s$). Finally, when the Q reference is taken to zero and the saturation state is abandoned, it can also be seen that the currents does not reach the current reference until 0.6s after.

Therefore, it can be concluded that it has been experimentally validated the proposed DFIMS advantages. First, it has been shown that the minimum THDi is always obtained, even under highly saturated situations (although the delivered Q^* is slightly reduced). Second, it has been proved the enhancements over the transient states in comparison with other literature saturators.

7.5. PCC Harmonic Voltage Control

During this section the experimental results corresponding to Chapter 6 are carried out. In this chapter the multifrequency control is employed for the reduction of grid harmonic

voltages. This can be achieved in two different ways: (1) indirectly, by compensating the harmonic currents consumed by local non-linear loads (APF functionality) or (2) directly, measuring the harmonic voltages at the PCC and injecting harmonic currents until the harmonic voltages at the PCC are compensated.

During this thesis, contributions have been made in both of them and therefore, experimental results are shown in Subsection 7.5.1 for the parallel operation of APFs under saturated situations and in Subsection 7.5.2 for the reduction of harmonic voltages for shunt connected VSIs.

7.5.1. Parallel Active Power Filters

This subsection focus on the experimental results for VSIs associated with distributed generators that try to compensate the harmonic currents consumed by non-linear loads. In this regard, it needs to be considered that an VSI might not be able to accomplish all the requested functionalities. The VSI has limitations that needs to be considered, specially dc-bus margin is of special importance when harmonic currents are dealt with. When this limitation is reached, both capabilities could not be fully accomplished, if linear modulation range wants to be maintained. In this regard, the proposed strategy when more than one VSIs are connected in parallel is two accomplish the harmonic load compensation in a cooperative way and try to always deliver the maximum power.

In order to perform the experimental test, a new setup is employed here. For this test, two VSIs are parallel connected, each one of them controlled through an independent TMS320F28335 Delfino microcontroller (150 MHz). For this test the employed inverter is connected to the grid through an L inductance of 3 mH. The test is carried out in two steps.

In the first step, the experimental setup (three-phase electric grid, two parallel connected inverters and a non-linear load) is simulated in OPAL-RT simulator. Meanwhile, the control algorithm is implemented in the same DSPs that will be employed in the second step of the test. As depicted in Fig. 7.13 the hardware in the loop simulation devices receives the PWM signals from both DSPs while delivers the voltage and currents simulated measurements.

The sampling time is equal to 100 μ s and the process is carried out in real time. This first step is used for testing the implemented code at the DSP. In this way, the implemented code is debugged for the second step, with real VSIs, preventing programming errors.

In the second step, the two real inverters are employed and a three phase programmable power supply (CSW 5550) is employed. As non-linear load, a resistor connected through an uncontrolled rectifier is employed. The whole experimental setup is shown in Fig. 7.14.

The two debugged DSPs are controlling in this test the real VSIs. In this case, the inputs are the real voltage and current measurements and the PWMs are directly applied

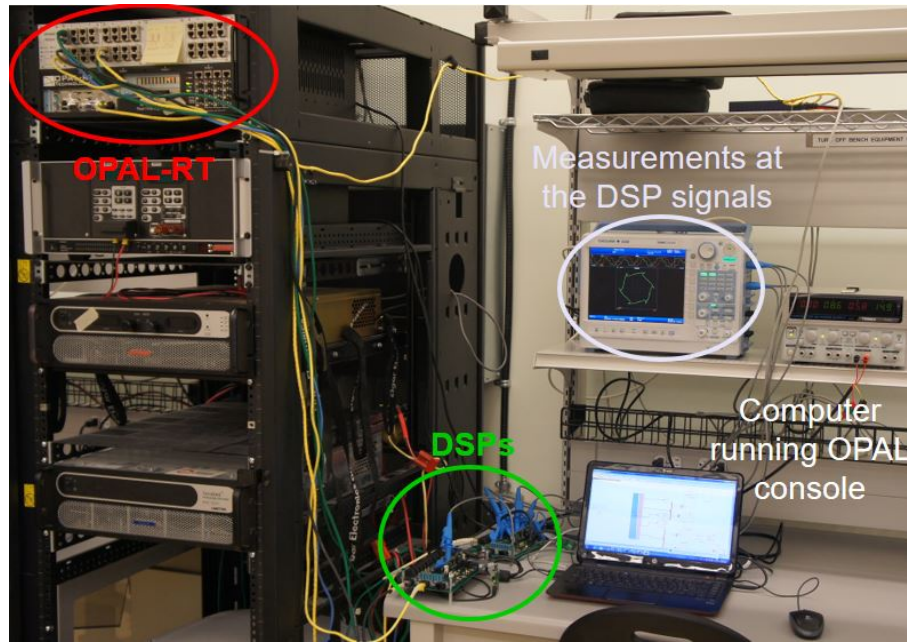


Figure 7.13: Hardware in the loop set-up composed by two DSPs and a real time simulator (which includes the grid, parallel VSIs and non-linear load).

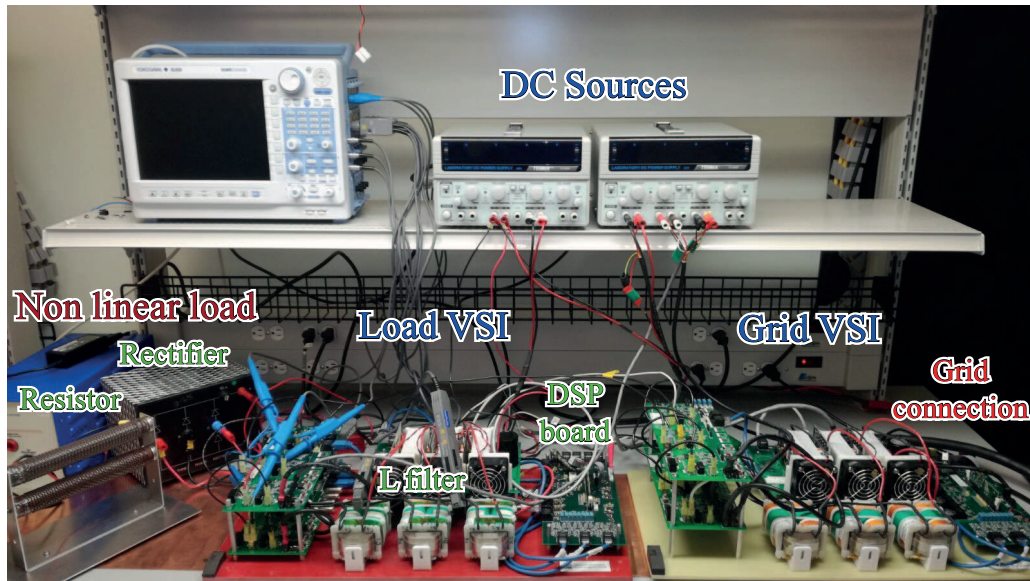


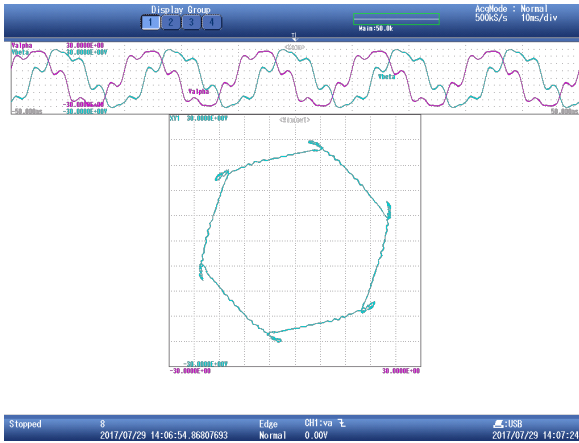
Figure 7.14: Experimental set-up for the parallel APFs strategy (VSIs, DSPs and Non-linear load).

over the drivers in charge of switching the transistors. The parameters of the grid and converter employed during the experimental test are collected in Table 7.5.

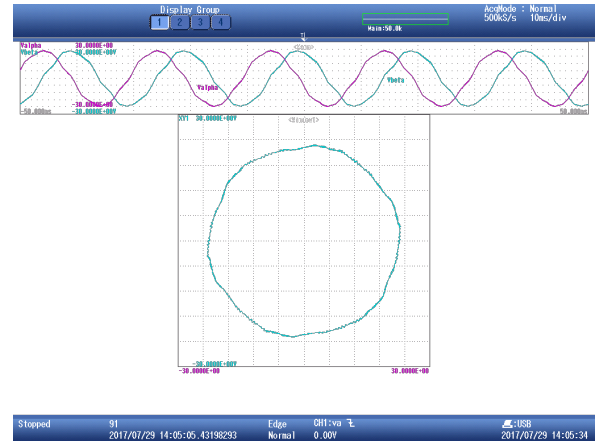
It can be seen how in this conditions, the VSI closer to the load (Load VSI) is taken to an overmodulation range if power and harmonic current compensation want to be simultaneously achieved by the Load VSI. Therefore, in order to keep the linear modulation range, in the proposed strategy the output voltage is exclusively reduced from the harmonic components. Meanwhile, the equally weighted strategy reduces from both of them. The output voltage references ($\vec{u}_{\alpha\beta}$) for each strategy are depicted in Fig. 7.15.

Table 7.5: Experimental set-up parameters for parallel APFs

Parameter	Value
V_{dc}	36 V
V_{ac}	12.5 V_{rms}
L_{filter}	3 mH
P_{ref} (Load VSI)	25 W
Q_{ref} (Load VSI)	20 VAR
NL load (Uncontr. Rect. + R)	10 Ω
T_s	100 μs



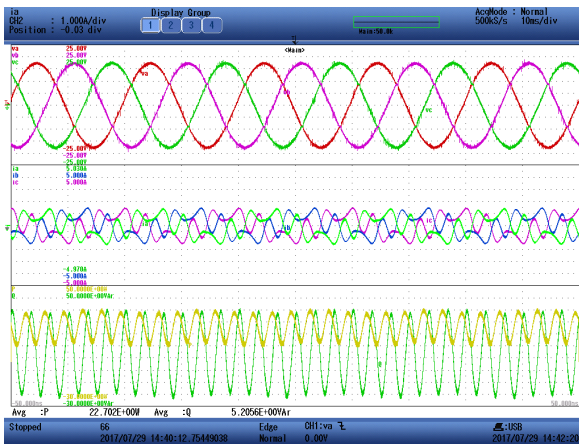
(a) Equally weighted saturation.



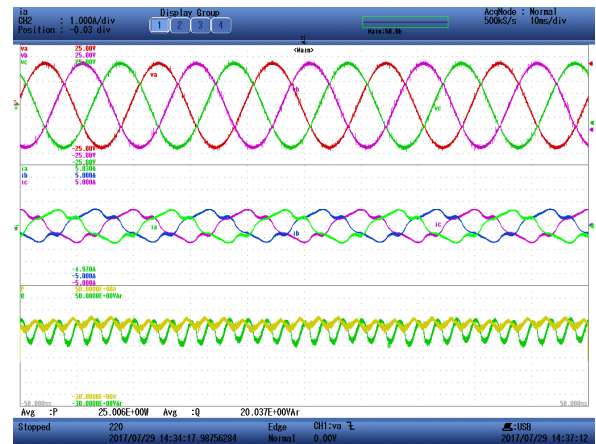
(b) Proposed maximum power strategy.

Figure 7.15: Comparison of reference output voltages ($\vec{u}_{\alpha\beta}$) during saturation. The smaller circle presented in the equally weighted strategy shows the reduction over the FPS component and therefore active and reactive power reduction.

The currents delivered by the Load VSI and the active (P) and reactive (Q) powers are depicted in Fig. 7.16.



(a) Equally weighted saturation.



(b) Proposed maximum power strategy.

Figure 7.16: Voltage (top), currents (middle) and active and reactive powers (bottom) measured at PCC for the VSI closer to the load. Active and reactive average powers are greater for the proposed strategy ($P = 25$ W and $Q = 20$ VAR) than for the equally weighted ($P = 22.7$ W and $Q = 5.2$ VAR).

It can be seen that the equally weighted strategy performs a less reduction over the harmonic components, which allows a greater harmonic currents compensation with the Load VSI. However, the delivered P and Q are reduced to 22.7 W and 5.2 VAR, respectively. Meanwhile, with the proposed strategy the reference P and Q powers are provided. However, the delivered harmonic currents do not fully compensate the harmonic currents load but this task will be completed by the grid VSI, as depicted in Fig. 7.17.

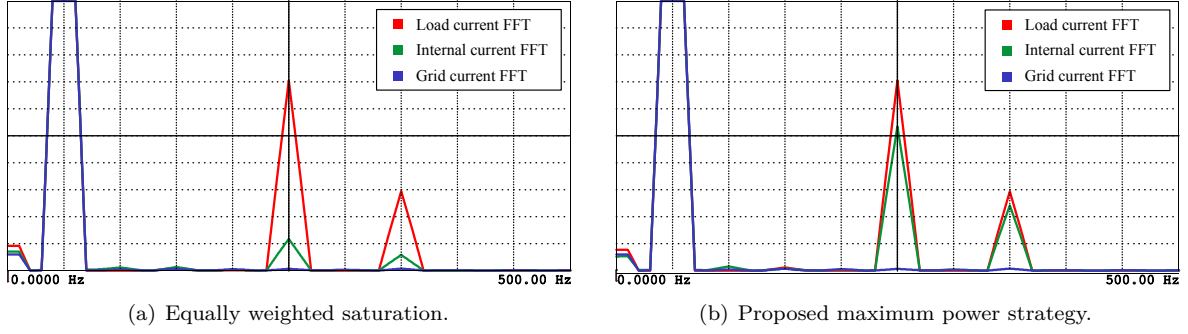


Figure 7.17: FFT of the different exchanged currents, the current consumed by the non-linear load (load current), the current after the compensation of the Load VSI (internal current) and the current delivered to the grid after the compensation of the Grid VSI (grid current).

7.5.2. PCC Harmonic Voltage Control

In this part of the chapter, the shunt connected VSC is in charge of directly compensating the voltage harmonic at the PCC. For this test, no additional current sensors are needed (as it occurred with APFs). Here, the PCC voltage is measured and its sequences are extracted. Then, harmonic currents are injected until the PCC voltage harmonics are reduced. The parameters employed for the experimental set-up are collected in Table 7.6

Table 7.6: Experimental parameters description for PCC control

Parameter category	Parameter	Parameter Value
Distorted Grid	Grid frequency (f_1)	50 Hz
	FPS ($h=+1$)	0.947 pu
	FNS ($h=-1$)	0.002 pu
	harmonic sequence ($h=-5$)	0.010 pu
	harmonic sequence ($h=+7$)	0.016 pu
Grid impedance	Inductance (L_g)	$250 + 40 \mu\text{H}$
Filter impedance	Inductance (L_f)	$750 \mu\text{H}$
	Capacitor (C_f)	$33 \mu\text{F}$
Control references	DC-Bus voltage	750 V
	Q reference	0 kVar
Frequencies	Sample frequency (f_s)	5 kHz
	Switching frequency (f_{sw})	2.5 kHz

One of the most important parameters for the control of harmonic voltages at the PCC is the grid inductance as expressed in Section 6.3.1. Following the described method in [88], the estimated grid inductance corresponds to a value of approximately $40 \mu\text{H}$. As the grid is strong and that would require a high amount of currents and output voltages,

an external equivalent inductance of $250\ \mu\text{H}$ (two parallel connected inductances of $500\ \mu\text{H}$) were connected between the grid and the PCC, as depicted in Fig. 7.18.

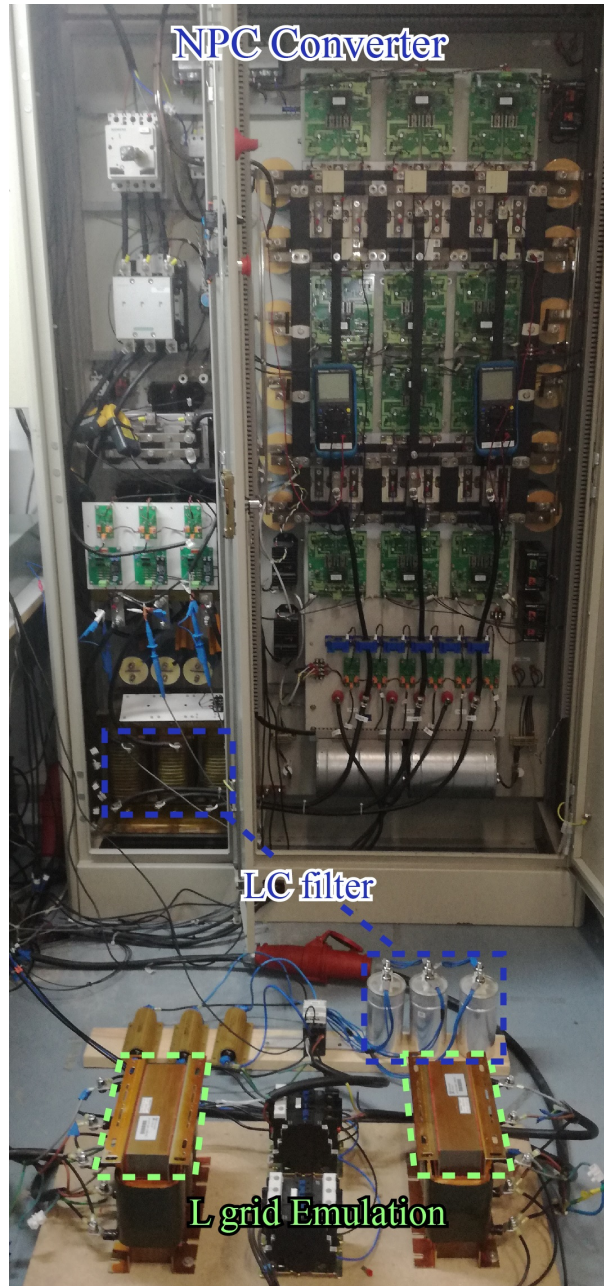


Figure 7.18: Experimental set-up for PCC harmonic voltage compensation with additional inductance for a weaker grid emulation [90].

In addition, some capacitors were added in order to perform an LC filter that avoids the aliasing effect of the commutation when a weak grid is employed. Then, the control strategy tries to reduce the harmonic voltage components at the PCC through the injection of harmonic currents. In Fig. 7.19 the detected non-fundamental voltage components at the PCC (v_{-1} , v_{-5} and v_{+7}) are depicted. The measurements are taken directly by the DSP and plotted in Matlab. It can be seen how with the proposed method, these components are taken to zero.

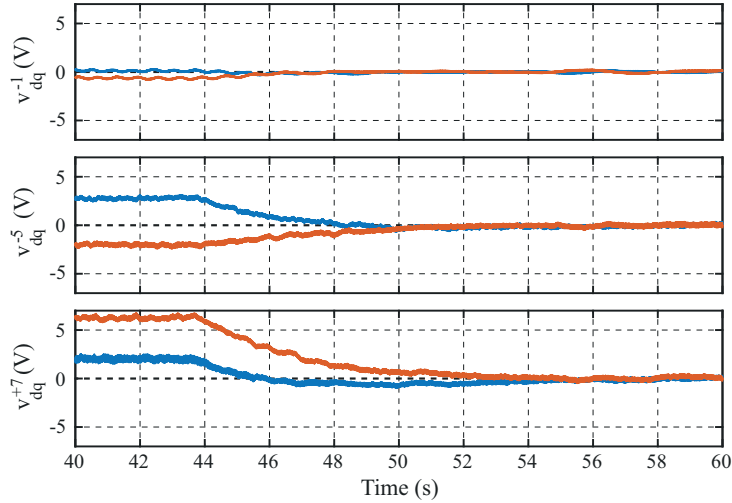


Figure 7.19: PCC Harmonic voltage sequences with PCC control [90].

Meanwhile, in Fig. 7.20 the PCC voltage waveform measured with the oscilloscope are shown when the PCC control algorithm is not employed and when it is activated. It can be appreciated how the power quality is improved and the results are collected in Table 7.7 where the voltage THD at the PCC presents a relative reduction of 57%.

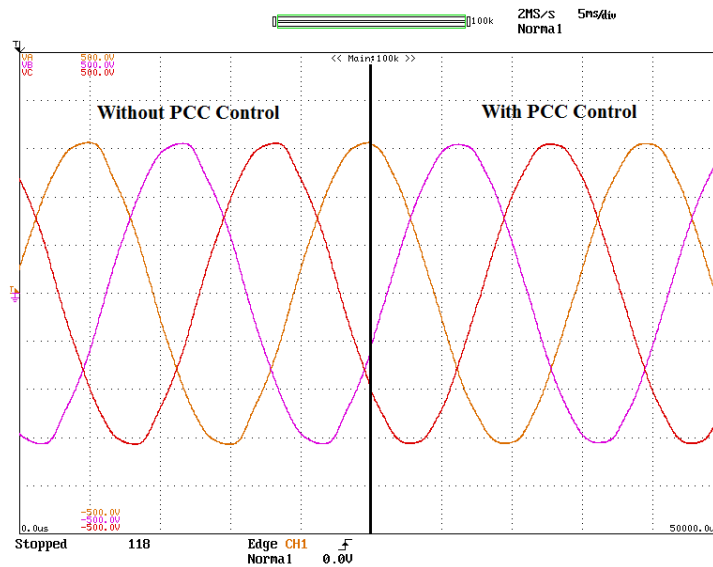


Figure 7.20: PCC voltage waveform comparison with and without PCC voltage harmonic control [90].

Table 7.7: Experimental Results of PCC control

Strategy	No v_{pcc} control	v_{pcc} control
v_{pcc} THD ($h < 10$)	2.22 %	0.97 %
$v_{pcc}^p(h = 5)$	3.34 V	0.57 V
$v_{pcc}^p(h = 7)$	5.34 V	0.14 V

7.6. Conclusions

In this chapter, all the algorithms that have been proposed along the thesis are experimentally tested. The experimental equipment employed for these tests is described.

First, the current reference calculation proposed in Chapter 4 for reducing the instantaneous active power ripple of the 2nd and 6th harmonic components is experimentally validated. This optimized calculation reduces the THD injection in comparison with other approaches. In the studied case THDi is reduced from 5.02 % to 4.54%.

Second, the proposed DFIMS described in Chapter 5 employed for overmodulation avoidance is compared with the most recent multifrequency saturators. It shows, for the studied case, a THDi reduction from 3.11 % to 1.82 % while the saturator is actuating in steady state. In the same way, the proposed DFIMS presents an enhanced transient response than the literature saturators.

Finally, the proposed algorithms for the grid harmonic voltages reduction in chapter 6 are analysed. First, the strategy proposed in section 7.5.1 where two or more VSIs for distributed generators compensate harmonic currents in a collaborative way is tested. It is shown that with the proposed strategy, under saturation circumstances higher P and Q values can be achieved. Then, the shunt harmonic compensator proposed in Section 7.5.2 is experimentally tested. It shows, for the studied case, a reduction in the harmonic voltage content at the PCC from 2.22 % to 0.97%.

Chapter 8

Conclusions and future works

8.1. Conclusions

During this thesis the different parts that involve the multifrequency control of shunt grid tied power converters are analysed and novel strategies are proposed in some of these fields. A new level of complexity is reached when in addition to the fundamental positive sequence (+50Hz) and fundamental negative sequence (unbalance), harmonic components are also dealt with.

This type of control implies challenges in the different parts of the control system, including synchronization, controllers, references calculations, limitations and applications. The different steps have been studied and in some of them new proposals have been made.

The increment of non-linear loads along the grid has increased the harmonic currents consumption and in this context, the propagation of these currents incurs into grid harmonic voltage distortion. When a distributed generator is connected to the grid, it is usually connected through a VSC. This VSC needs to be controlled in order to perform the desired functionality (typically the injection of the maximum P and the requested Q). However, the proliferation of those voltage harmonic components has opened a new dimension.

During Chapter 3, the controllers, which transfer functions are optimized for a single frequency control are introduced. Special interest has the novel ROGI controller that presents a complex transfer function and works with complex signals. A ROGI based sequence detector is proposed in this point in order to detect the voltage components sequences in the grid. Then, the multifrequency control with the employment of ROGIs and the different techniques for calculating the gains are presented. Some of this techniques are well-known (LQR, Ackermann) but some of them have been analysed and specifically employed for ROGIs in this thesis (plant pole cancellation).

Then, once that the multifrequency control and the harmonic voltage detection has been addressed, the contributions moved to a different part of the multifrequency con-

trol during chapter 4: current reference calculation. In this regard, the focus is placed on the calculation of current references for improving power filtering and power quality. The aforementioned presence of voltage harmonics implies that when current at the fundamental frequency is delivered (common case), the cross effect between the harmonic voltages and the fundamental current provokes oscillations over the exchanged instantaneous power. In this regard, different strategies have been proposed along the literature, which through the injection of harmonic currents, compensate the cross effect and reduce the instantaneous power ripple. In this chapter, a new CRC is proposed where the main harmonic components of the instantaneous power are reduced and at the same time the injected THDi is reduced. In this way, power filtering is achieved trying to enhance the power quality (reducing THDi). This method is validated and compared with the previous CRC methods in simulation (Section 4.6) and experimentally (Section 7.3).

A further step within the multifrequency control context is addressed in Chapter 5. In this case, the physical limitations of the VSCs are presented. The chapter is mainly focus over the limitation of the control actuation signals for multifrequency control. Some algorithms have been proposed in order to limit the control actuation signals without incurring into distortion (distortion free saturators). However, the presented distortion free multifrequency saturators offer slow dynamics. In this context, a new distortion free multi-frequency instantaneous saturator (DFIMS) is proposed here. DFIMS presents instantaneous dynamics with does not modifies the external control settling time. In addition, this saturator is focused on the minimum THDi injection, even when the grid is distorted. DFIMS has been validated in simulated experiments (Section 5.6) and it has been compared with the previous DF-saturators. Proposed DFIMS and literature saturator have been implemented and experimentally tested and compared in Section 7.4.

In the last part of the thesis, the root of the problem of harmonic voltage generation is directly tackled. In Chapter 6, the reduction of the harmonic PCC voltages is the main concern. As previously stated, the harmonic voltage presence is provoked by the propagation of the harmonic currents consumed by non-linear loads. In this context, the VSCs employed as the interface for distributed generators can use the remaining margin to perform this compensation. Two strategies are analysed: (1) locally compensating the harmonic currents consumed by non linear loads and avoiding propagation, (2) directly measuring the harmonics at the PCC voltage and inject harmonic currents until reducing these harmonic voltage sequences.

For the first strategy, a novel strategy is proposed in Section 6.2 where the harmonic current compensation of local non-linear load is carried out as a secondary task. In this strategy even under saturation situations the delivered active and reactive power references are as close as possible to the references and the harmonic compensation is achieved in a cooperative way among the close inverters. The proposed strategy is validated in simulation (Subsection 6.4.1) and experimentally (Subsection 7.5.1).

For the second strategy, a novel algorithm is proposed in Section 6.3, where the harmonic voltages at the PCC are detected and compensated through the injection of harmonic currents. In this strategy, additional current sensors are not required and the compensation is carried out upstream and downstream of the PCC connection. This implies that in most of the cases the harmonic voltages cannot be fully compensated and this strategy, where shunt connected VSI compensates harmonic voltages, had been discarded in several previous approaches. However, with the proposed DFIMS, this issue can be solved and the compensation can be carried out until reaching the saturation limitations. For the PCC voltage control design, the most important parameter is the grid inductance value, which is not a known value. In this context a novel method is also proposed for the grid inductance estimation that is enhanced for the pursued purpose here. The proposed strategy for harmonic voltage compensation is validated in simulation (Subsection 6.4.2) and experimentally (Subsection 7.5.2).

8.2. Future work

During this thesis, an extensive study and several contributions have been proposed within the multifrequency control of VSC. Nevertheless, there are some points that have been not addressed yet but they could be faced in the near future with the knowledge studied and developed during this thesis.

8.2.1. Fastest current controller

The design of multifrequency current controllers usually tries to accomplish requirements in terms of settling time and overshoot. Once that the proper gains for the accomplishment of these requirements have been obtained, the requirements are accomplished independently of the reference magnitude.

However, if the reference magnitude is too high or the dynamics are so demanding, the needed actuation goes out of the limitations. In this context, it has been considered a problem and the multifrequency control has been typically designed with LQR in order to reduce the cost gain and try to avoid over-modulation.

Then, with the new proposed DFIMS, faster controllers could be designed without worrying about overmodulation. Even they could be designed in order to accomplish low settling times and the real settling time would vary depending on the possible allowed actuation. In a future line it could also be tried to implement a dead-beat controller for the ROIGs multifrequency control.

8.2.2. Instantaneous Active Power

Regarding to the instantaneous active power, some improvements can be carried out. In this regard, a first improvement could be carried out in order to reduce the power oscillations at the dc-side. An assumption that the dc power is equal to the ac power has been made during this chapter. However, the instantaneous power consumed by the converter filter is not taken into account. An approach for improving even more the dc power filtering would be to consider this effect in the current references calculation matrix.

Another improvement could be to modify the proposed Saturator, in order to maintain the currents ratio that allows to continue reducing the power harmonics when saturation is reached.

Finally, due to the limited runtime and therefore, not all the harmonic power components can be reduced, an algorithm could be proposed for determining the most interesting components to be reduced at each moment.

8.2.3. Current Multifrequency Saturation

During this thesis, especially in Chapter 5, the importance of the actuation signal distortion free saturation has been stated. It can occurs that the actuation voltage signals goes out of the linear range and it needs to be properly solved.

A similar effect occurs with the current references. In several applications, the currents are limited and in order to not inject undesirable harmonics the reference currents need to be properly reduced. The current controller saturator can also be employed for the current references limitation as described in 5.5.

However, a deeper study could be carried out in this concern and it should be validated with simulated and experimental results. In addition, it needs to be taken into account the relationship between saturators and how the antiwindups are configured when simultaneously different saturators are employed.

8.2.4. PCC adaptative controller to L_g variations

Regarding to the reduction of harmonic voltages it has been mentioned that the grid inductance is a key parameter in order to set the voltage controller settling time. In this concern it is well known, specially for weak grid, that the value of the grid impedance can vary with time.

In this regard, the variation of the L_g parameter implies variation in the voltage controller settling time. This could even lead to a situation where the voltage settling time is too high (slow for the desired response) or too slow (excessively fast), which could lead to a control conflict with voltage and current controllers.

In this regard, a contribution could be made where the grid inductance estimated value is periodically updated. In this way, the gains for the PCC harmonic voltage controllers could be recalculated in order to meet the desired settling time and guarantee stability.

8.2.5. PCC harmonic voltage control with parallel shunt VSCs

As described in Section 6.3, a great contribution has been made during this thesis on the PCC harmonic voltage reduction through shunt connected VSCs. As it was described in the literature, one of the main issues is to reach overmodulation while the compensation is performed. In this thesis, with the employment of the proposed DFIMS, the harmonic voltage compensation can be taken as far as possible, within the linear modulation range.

Therefore, when this limit is reached, the harmonic voltage compensation cannot be fully achieved. It is also unthinkable that an only VSC is able to compensate the harmonic voltage distortion of the whole grid. It means that if fully compensation wants to be achieved by several VSCs must work in parallel. Therefore, different parallelization strategies could be studied for achieving the full compensation in a cooperative way. A good alternative could be to employ droop control in order to perform the compensation without control conflict between VSCs.

Bibliography

- [1] Enerdata, “Global Energy Statistical Yearbook 2017,” <https://yearbook.enerdata.net/total-energy/world-consumption-statistics.html>, online; accessed 30 July 2018.
- [2] J. Chontanawat, L. C. Hunt, and R. Pierse, “Does energy consumption cause economic growth?: Evidence from a systematic study of over 100 countries,” *Journal of Policy Modeling*, vol. 30, no. 2, pp. 209–220, 2008.
- [3] Christof Ruehl, “BP energy outlook 2030,” <http://www.eprg.group.cam.ac.uk/wp-content/uploads/2011/05/Keynote.pdf>, online; accessed 30 July 2018.
- [4] W. Hoffmann, *The economic competitiveness of renewable energy: pathways to 100% global coverage*. John Wiley & Sons, 2014.
- [5] European Commission, “A policy framework for climate and energy in the period from 2020 to 2030,” *Communication from the Commission to the European Parliament, the Council, the European Economic and Social Committee and the Committee of the Regions*, 2014.
- [6] International Energy Agency, “CO₂ emissions from fuel combustion - Highlights (2016 edition),” policy.nl.go.kr/cmmn/FileDown.do?atchFileId=157716&fileSn=36916, online; accessed 30 July 2018.
- [7] K. Clement-Nyns, E. Haesen, and J. Driesen, “The impact of charging plug-in hybrid electric vehicles on a residential distribution grid,” *IEEE Transactions on Power Systems*, vol. 25, no. 1, pp. 371–380, Feb 2010.
- [8] F. Beck and E. Martinot, “Renewable energy policies and barriers,” *Encyclopedia of energy*, vol. 5, no. 7, pp. 365–383, 2004.
- [9] C. Klessmann, A. Held, M. Rathmann, and M. Ragwitz, “Status and perspectives of renewable energy policy and deployment in the european union - what is needed to reach the 2020 targets?” *Energy Policy*, vol. 39, no. 12, pp. 7637 – 7657, 2011, clean Cooking Fuels and Technologies in Developing Economies. [Online]. Available: <http://www.sciencedirect.com/science/article/pii/S0301421511006355>
- [10] European Commission, “Energy for the future: Renewable sources of energy, white paper for a community strategy and action plan,” *Brussels*, 1997.

- [11] European Communities, “Directive 2001/77/EC of the European Parliament and of the Council of 27 September 2001 on the promotion of electricity produced from renewable energy sources in the internal electricity market,” *Official Journal of the European Communities*, vol. 44, no. 283, pp. 33 – 39, 2001.
- [12] M. Banja, F. Monforti-Ferrario, K. Bodis, A. Jaeger-Waldau, N. Taylor, J. F. Dallemand, N. Scarlat, “Renewable energy deployment in the european union, vol. 3,” *Publications Office of the European Union*, 2016.
- [13] European Commission, “Clean energy for all europeans,” *Brussels*, 2016.
- [14] M. Banja, F. Monforti-Ferrario, K. Bodis, A. Jaeger-Waldau, N. Taylor, J. F. Dallemand, N. Scarlat, “Renewable energy deployment in the european union, vol. 3,” *Publications Office of the European Union*, 2017.
- [15] T. Ackermann, G. Andersson, and L. Söder, “Distributed generation: a definition,” *Electric Power Systems Research*, vol. 57, no. 3, pp. 195 – 204, 2001.
- [16] G. Pepermans, J. Driesen, D. Haeseldonckx, R. Belmans, and W. D’haeseleer, “Distributed generation: definition, benefits and issues,” *Energy Policy*, vol. 33, no. 6, pp. 787 – 798, 2005.
- [17] P. Dondi, D. Bayoumi, C. Haederli, D. Julian, and M. Suter, “Network integration of distributed power generation,” *Journal of Power Sources*, vol. 106, no. 1, pp. 1 – 9, 2002, proceedings of the Seventh Grove Fuel Cell Symposium.
- [18] “IEEE Recommended Practice for Monitoring Electric Power Quality,” *IEEE Std 1159-2009 (Revision of IEEE Std 1159-1995)*, pp. c1–81, June 2009.
- [19] C. D. Schauder and R. Caddy, “Current control of voltage-source inverters for fast four-quadrant drive performance,” *IEEE Transactions on Industry Applications*, vol. IA-18, no. 2, pp. 163–171, March 1982.
- [20] P. Hsu and M. Behnke, “A three-phase synchronous frame controller for unbalanced load [inverter operation],” in *PESC 98 Record. 29th Annual IEEE Power Electronics Specialists Conference (Cat. No.98CH36196)*, vol. 2, May 1998, pp. 1369–1374 vol.2.
- [21] S. Park, S.-B. Han, B.-M. Jung, S.-H. Choi, and H.-G. Jeong, “A current control scheme based on multiple synchronous reference frames for parallel hybrid active filter,” in *Proceedings IPEMC 2000. Third International Power Electronics and Motion Control Conference (IEEE Cat. No.00EX435)*, vol. 1, 2000, pp. 218–223 vol.1.
- [22] Y. Sato, T. Ishizuka, K. Nezu, and T. Kataoka, “A new control strategy for voltage-type pwm rectifiers to realize zero steady-state control error in input current,” *IEEE Transactions on Industry Applications*, vol. 34, no. 3, pp. 480–486, May 1998.

- [23] G. Shen, X. Zhu, J. Zhang, and D. Xu, "A new feedback method for pr current control of lcl-filter-based grid-connected inverter," *IEEE Transactions on Industrial Electronics*, vol. 57, no. 6, pp. 2033–2041, June 2010.
- [24] E. Blanco, E. Bueno, F. Espinosa, S. Cobrecas, F. J. Rodriguez, and M. A. Ruiz, "Fast harmonics compensation in vses connected to the grid by synchronous-frame generalized integrators," in *Proceedings of the IEEE International Symposium on Industrial Electronics, 2005. ISIE 2005.*, vol. 2, June 2005, pp. 751–755 vol. 2.
- [25] W. C. Duesterhoeft, M. W. Schulz, and E. Clarke, "Determination of instantaneous currents and voltages by means of alpha, beta, and zero components," *Transactions of the American Institute of Electrical Engineers*, vol. 70, no. 2, pp. 1248–1255, July 1951.
- [26] L. Harnefors, "Modeling of three-phase dynamic systems using complex transfer functions and transfer matrices," *IEEE Transactions on Industrial Electronics*, vol. 54, no. 4, pp. 2239–2248, Aug 2007.
- [27] J. Holtz, "The representation of ac machine dynamics by complex signal flow graphs," *IEEE Transactions on Industrial Electronics*, vol. 42, no. 3, pp. 263–271, Jun 1995.
- [28] K. W. Martin, "Complex signal processing is not complex," *IEEE Transactions on Circuits and Systems I: Regular Papers*, vol. 51, no. 9, pp. 1823–1836, Sept 2004.
- [29] T. Crystal and L. Ehrman, "The design and applications of digital filters with complex coefficients," *IEEE Transactions on Audio and Electroacoustics*, vol. 16, no. 3, pp. 315–320, Sep 1968.
- [30] X. Guo, W. Wu, and Z. Chen, "Multiple-complex coefficient-filter-based phase-locked loop and synchronization technique for three-phase grid-interfaced converters in distributed utility networks," *IEEE Transactions on Industrial Electronics*, vol. 58, no. 4, pp. 1194–1204, April 2011.
- [31] C. A. Busada, S. G. Jorge, and J. A. Solsona, "Resonant current controller with enhanced transient response for grid-tied inverters," *IEEE Transactions on Industrial Electronics*, vol. PP, no. 99, pp. 1–1, 2017.
- [32] F. Blaabjerg, R. Teodorescu, M. Liserre, and A. V. Timbus, "Overview of control and grid synchronization for distributed power generation systems," *IEEE Transactions on Industrial Electronics*, vol. 53, no. 5, pp. 1398–1409, Oct 2006.
- [33] S.-K. Chung, "A phase tracking system for three phase utility interface inverters," *IEEE Transactions on Power Electronics*, vol. 15, no. 3, pp. 431–438, May 2000.

- [34] J. Svensson, M. Bongiorno, and A. Sannino, "Practical implementation of delayed signal cancellation method for phase-sequence separation," *IEEE Transactions on Power Delivery*, vol. 22, no. 1, pp. 18–26, Jan 2007.
- [35] P. Rodríguez, R. Teodorescu, I. Candela, A. V. Timbus, M. Liserre, and F. Blaabjerg, "New positive-sequence voltage detector for grid synchronization of power converters under faulty grid conditions," in *2006 37th IEEE Power Electronics Specialists Conference*, June 2006, pp. 1–7.
- [36] P. Rodriguez, A. Luna, I. Candela, R. Mújal, R. Teodorescu, and F. Blaabjerg, "Multiresonant frequency-locked loop for grid synchronization of power converters under distorted grid conditions," *IEEE Transactions on Industrial Electronics*, vol. 58, no. 1, pp. 127–138, Jan 2011.
- [37] F. Neves, H. Souza, E. Bueno, M. Rizo, F. Bradaschia, and M. Cavalcanti, "A space-vector discrete fourier transform for detecting harmonic sequence components of three-phase signals," in *2009 35th Annual Conference of IEEE Industrial Electronics*, Nov 2009, pp. 3631–3636.
- [38] F. A. S. Neves, H. E. P. de Souza, F. Bradaschia, M. C. Cavalcanti, M. Rizo, and F. J. Rodriguez, "A space-vector discrete fourier transform for unbalanced and distorted three-phase signals," *IEEE Transactions on Industrial Electronics*, vol. 57, no. 8, pp. 2858–2867, Aug 2010.
- [39] D. Yazdani, A. Bakhshai, G. Joos, and M. Mojiri, "A nonlinear adaptive synchronization technique for grid-connected distributed energy sources," *IEEE Transactions on Power Electronics*, vol. 23, no. 4, pp. 2181–2186, July 2008.
- [40] P. Rodriguez, A. Luna, I. Candela, R. Teodorescu, and F. Blaabjerg, "Grid synchronization of power converters using multiple second order generalized integrators," in *2008 34th Annual Conference of IEEE Industrial Electronics*, Nov 2008, pp. 755–760.
- [41] J. Moriano, E. Bueno, R. Martín, F. J. Rodríguez, and M. Rizo, "Multi-frequency stationary frame grid synchronization using multiple reduced order generalized integrators," in *IECON 2016 - 42nd Annual Conference of the IEEE Industrial Electronics Society*, Oct 2016, pp. 2349–2354.
- [42] S. Hu, X. Lin, Y. Kang, and X. Zou, "An improved low-voltage ride-through control strategy of doubly fed induction generator during grid faults," *IEEE Transactions on Power Electronics*, vol. 26, no. 12, pp. 3653–3665, Dec 2011.
- [43] J. Lopez, E. Gubia, E. Olea, J. Ruiz, and L. Marroyo, "Ride through of wind turbines with doubly fed induction generator under symmetrical voltage dips," *IEEE Transactions on Industrial Electronics*, vol. 56, no. 10, pp. 4246–4254, Oct 2009.

- [44] W. Libo, Z. Zhengming, and L. Jianzheng, "A single-stage three-phase grid-connected photovoltaic system with modified mppt method and reactive power compensation," *IEEE Transactions on Energy Conversion*, vol. 22, no. 4, pp. 881–886, Dec 2007.
- [45] K. J. Lee and R. Y. Kim, "An adaptive maximum power point tracking scheme based on a variable scaling factor for photovoltaic systems," *IEEE Transactions on Energy Conversion*, vol. 27, no. 4, pp. 1002–1008, Dec 2012.
- [46] P. Rioual, H. Pouliquen, and J. P. Louis, "Regulation of a pwm rectifier in the unbalanced network state using a generalized model," *IEEE Transactions on Power Electronics*, vol. 11, no. 3, pp. 495–502, May 1996.
- [47] J. Moriano, M. Rizo, E. J. Bueno, and R. Sendra, "Distortion-free instantaneous multifrequency saturator for thd current reduction," *IEEE Transactions on Industrial Electronics*, vol. pp, no. 99, pp. 1–9, Jan 2019.
- [48] M. Liserre, R. Teodorescu, and F. Blaabjerg, "Multiple harmonics control for three-phase grid converter systems with the use of pi-res current controller in a rotating frame," *IEEE Transactions on Power Electronics*, vol. 21, no. 3, pp. 836–841, May 2006.
- [49] C. Lascu, L. Asiminoaei, I. Boldea, and F. Blaabjerg, "Frequency response analysis of current controllers for selective harmonic compensation in active power filters," *IEEE Transactions on Industrial Electronics*, vol. 56, no. 2, pp. 337–347, Feb 2009.
- [50] D. Campos-Gaona, R. P. na Alzola, J. L. M. Morales, and M. Ordonez, "Dynamic mitigation of grid current harmonics using the power sphere concept in voltage source inverters," in *2016 IEEE 7th International Symposium on Power Electronics for Distributed Generation Systems (PEDG)*, June 2016, pp. 1–8.
- [51] T. Shimizu, T. Fujita, G. Kimura, and J. Hirose, "A unity power factor pwm rectifier with dc ripple compensation," *IEEE Transactions on Industrial Electronics*, vol. 44, no. 4, pp. 447–455, Aug 1997.
- [52] M. A. Brubaker, D. E. Hage, T. A. Hosking, H. C. Kirbie, and E. D. Sawyer, "Increasing the life of electrolytic capacitor banks using integrated high performance film capacitors," *Europe Power Conversion Intelligent Motion (PCIM)*, Aug 2013.
- [53] M. N. Hussain and V. Agarwal, "A new control technique to enhance the stability of a DC microgrid and to reduce battery current ripple during the charging of plug-in electric vehicles," in *Environment and Electrical Engineering (EEEIC), 2015 IEEE 15th International Conference on*, June 2015, pp. 2189–2193.
- [54] J. Shen, S. Schröder, J. Gao, and B. Qu, "Impact of DC-Link Voltage Ripples on the Machine-Side Performance in NPC H-Bridge Topology," *IEEE Transactions on Industry Applications*, vol. 52, no. 4, pp. 3212–3223, July 2016.

- [55] J. Klima, M. Chomat, and L. Schreier, "Analytical closed-form investigation of pwm inverter induction motor drive performance under dc bus voltage pulsation," *IET Electric Power Applications*, vol. 2, no. 6, pp. 341–352, Nov. 2008.
- [56] H. Xu, J. Hu, and Y. He, "Operation of Wind-Turbine-Driven DFIG Systems Under Distorted Grid Voltage Conditions: Analysis and Experimental Validations," *IEEE Transactions on Power Electronics*, vol. 27, no. 5, pp. 2354–2366, May 2012.
- [57] J. Hu, H. Xu, and Y. He, "Coordinated control of DFIG's RSC and GSC under generalized unbalanced and distorted grid voltage conditions," *IEEE Transactions on Industrial Electronics*, vol. 60, no. 7, pp. 2808–2819, July 2013.
- [58] J. Moriano, M. Rizo, E. J. Bueno, R. Martin, and F. J. Rodriguez, "A novel multi-frequency current reference calculation to mitigate active power fluctuations," *IEEE Transactions on Industrial Electronics*, vol. 65, no. 1, pp. 810–818, Jan 2018.
- [59] M. Rizo, M. Liserre, E. J. Bueno, F. J. Rodríguez, and A. Rodríguez, "Distortion-free saturators for power converters under unbalanced conditions," *IEEE Transactions on Power Electronics*, vol. 30, no. 6, pp. 3364–3375, June 2015.
- [60] J. Holtz, "Pulsewidth modulation-a survey," *IEEE Transactions on Industrial Electronics*, vol. 39, no. 5, pp. 410–420, Oct 1992.
- [61] M. N. Marwali and A. Keyhani, "Control of distributed generation systems-part i: Voltages and currents control," *IEEE Transactions on Power Electronics*, vol. 19, no. 6, pp. 1541–1550, Nov 2004.
- [62] R. Ottersten and J. Svensson, "Vector current controlled voltage source converter-deadbeat control and saturation strategies," *IEEE Transactions on Power Electronics*, vol. 17, no. 2, pp. 279–285, Mar 2002.
- [63] M. A. Zamani, A. Yazdani, and T. S. Sidhu, "A control strategy for enhanced operation of inverter-based microgrids under transient disturbances and network faults," *IEEE Transactions on Power Delivery*, vol. 27, no. 4, pp. 1737–1747, Oct 2012.
- [64] L. Harnefors, A. G. Yepes, A. Vidal, and J. Doval-Gandoy, "Multifrequency current control with distortion-free saturation," *IEEE Journal of Emerging and Selected Topics in Power Electronics*, vol. 4, no. 1, pp. 37–43, March 2016.
- [65] A. G. Yepes, J. Doval-Gandoy, and H. A. Toliyat, "Multifrequency current control including distortion-free saturation and antiwindup with enhanced dynamics," *IEEE Transactions on Power Electronics*, vol. 33, no. 9, pp. 7309–7313, Sept 2018.
- [66] J. Karttunen, S. Kallio, J. Honkanen, P. Peltoniemi, and P. Silventoinen, "Partial current harmonic compensation in dual three-phase pmsms considering the limited

- available voltage,” *IEEE Transactions on Industrial Electronics*, vol. 64, no. 2, pp. 1038–1048, Feb 2017.
- [67] H. Akagi, A. Nabae, and S. Atoh, “Control strategy of active power filters using multiple voltage-source pwm converters,” *IEEE Transactions on Industry Applications*, vol. IA-22, no. 3, pp. 460–465, May 1986.
- [68] Delta, “Delta Active Power Filter APF2000 Series,” <http://www.ferret.com.au/ODIN/PDF/Showcases/107154.pdf>, online; accessed 30 July 2017.
- [69] S. Khadem, M. Basu, and M. Conlon, “Parallel operation of inverters and active power filters in distributed generation system - a review,” *Renewable and Sustainable Energy Reviews*, vol. 15, no. 9, pp. 5155 – 5168, 2011.
- [70] M. Basu, S. P. Das, and G. K. Dubey, “Parallel converter scheme for high-power active power filters,” *IEE Proceedings - Electric Power Applications*, vol. 151, no. 4, pp. 460–466, July 2004.
- [71] T. Sürgevil, K. Vardar, and E. Akpınar, “Analysis of shunt active power filters using pscad for parallel operation,” in *2009 International Conference on Electrical and Electronics Engineering - ELECO 2009*, Nov 2009, pp. I–263–I–267.
- [72] D. Campos-Gaona, R. P. a Alzola, J. L. Monroy-Morales, M. Ordonez, O. Anaya-Lara, and W. E. Leithead, “Fast selective harmonic mitigation in multifunctional inverters using internal model controllers and synchronous reference frames,” *IEEE Transactions on Industrial Electronics*, vol. 64, no. 8, pp. 6338–6349, Aug 2017.
- [73] M. Routimo, M. Salo, and H. Tuusa, “Current sensorless control of a voltage-source active power filter,” in *Twentieth Annual IEEE Applied Power Electronics Conference and Exposition, 2005. APEC 2005.*, vol. 3, March 2005, pp. 1696–1702 Vol. 3.
- [74] H. Kawahira, Nahamura, and S. Nakazawa, “Active power filters,” in *Proceedings of the JIEE IPEC, Tokyo, Japan.*, 1983, pp. 981–992.
- [75] H. Akagi, “Control strategy and site selection of a shunt active filter for damping of harmonic propagation in power distribution systems,” *IEEE Transactions on Power Delivery*, vol. 12, no. 1, pp. 354–363, Jan 1997.
- [76] B. Renders, K. D. Gussem, W. R. Ryckaert, and L. Vandevelde, “Converter-connected distributed generation units with integrated harmonic voltage damping and harmonic current compensation function,” *Electric Power Systems Research*, vol. 79, no. 1, pp. 65 – 70, 2009. [Online]. Available: <http://www.sciencedirect.com/science/article/pii/S0378779608001557>

- [77] J. He, Y. W. Li, and M. S. Munir, "A flexible harmonic control approach through voltage-controlled dg-grid interfacing converters," *IEEE Transactions on Industrial Electronics*, vol. 59, no. 1, pp. 444–455, Jan 2012.
- [78] A. Burgio, G. Brusco, D. Menniti, A. Pinnarelli, and N. Sorrentino, "Design of a grid-connected photovoltaic system with grid ancillary services," in *2013 Africon*, Sept 2013, pp. 1–7.
- [79] A. Burgio, D. Menniti, N. Sorrentino, A. Pinnarelli, and G. Brusco, "An active resonance damper which avoids the estimation of the line characteristic impedance," *Electric Power Systems Research*, vol. 107, pp. 16 – 20, 2014. [Online]. Available: <http://www.sciencedirect.com/science/article/pii/S0378779613002447>
- [80] B. Palethorpe, M. Sumner, and D. W. P. Thomas, "Power system impedance measurement using a power electronic converter," in *Ninth International Conference on Harmonics and Quality of Power. Proceedings (Cat. No.00EX441)*, vol. 1, 2000, pp. 208–213 vol.1.
- [81] M. Sumner, B. Palethorpe, and D. W. P. Thomas, "Impedance measurement for improved power quality-part 1: the measurement technique," *IEEE Transactions on Power Delivery*, vol. 19, no. 3, pp. 1442–1448, July 2004.
- [82] M. Ciobotaru, V. Agelidis, and R. Teodorescu, "Accurate and less-disturbing active anti-islanding method based on pll for grid-connected pv inverters," in *2008 IEEE Power Electronics Specialists Conference*, June 2008, pp. 4569–4576.
- [83] M. Ciobotaru, R. Teodorescu, P. Rodriguez, A. Timbus, and F. Blaabjerg, "On-line grid impedance estimation for single-phase grid-connected systems using pq variations," in *2007 IEEE Power Electronics Specialists Conference*, June 2007, pp. 2306–2312.
- [84] A. V. Timbus, P. Rodriguez, R. Teodorescu, and M. Ciobotaru, "Line impedance estimation using active and reactive power variations," in *2007 IEEE Power Electronics Specialists Conference*, June 2007, pp. 1273–1279.
- [85] A. V. Timbus, R. Teodorescu, and P. Rodriguez, "Grid impedance identification based on active power variations and grid voltage control," in *2007 IEEE Industry Applications Annual Meeting*, Sept 2007, pp. 949–954.
- [86] S. Cobrecas, E. J. Bueno, D. Pizarro, F. J. Rodriguez, and F. Huerta, "Grid impedance monitoring system for distributed power generation electronic interfaces," *IEEE Transactions on Instrumentation and Measurement*, vol. 58, no. 9, pp. 3112–3121, Sept 2009.
- [87] M. Ciobotaru, R. Teodorescu, and F. Blaabjerg, "On-line grid impedance estimation based on harmonic injection for grid-connected pv inverter," in *2007 IEEE International Symposium on Industrial Electronics*, June 2007, pp. 2437–2442.

- [88] J. Moriano, V. Bermejo, E. Bueno, M. Rizo, and A. Rodriguez, "A novel approach to the grid inductance estimation based on second order generalized integrators," in *2017 IEEE Energy Conversion Congress and Exposition (ECCE)*, Oct 2017, pp. 1794–1801.
- [89] J. He, B. Liang, Y. W. Li, and C. Wang, "Simultaneous microgrid voltage and current harmonics compensation using coordinated control of dual-interfacing converters," *IEEE Transactions on Power Electronics*, vol. 32, no. 4, pp. 2647–2660, April 2017.
- [90] J. Moriano, E. Bueno, M. Moranchel, and M. Rizo, "Harmonic voltage compensation by grid supporting controlled distributed generators," in *2018 IEEE International Conference on Industrial Technology (ICIT)*, Feb 2018, pp. 1920–1925.
- [91] M. Ciobotaru, R. Teodorescu, and F. Blaabjerg, "A new single-phase pll structure based on second order generalized integrator," in *2006 37th IEEE Power Electronics Specialists Conference*, June 2006, pp. 1–6.
- [92] A. Ghosh and A. Joshi, "A new algorithm for the generation of reference voltages of a dvr using the method of instantaneous symmetrical components," *IEEE Power Engineering Review*, vol. 22, no. 1, pp. 63–65, Jan 2002.
- [93] J. Svensson, "Synchronisation methods for grid-connected voltage source converters," *IEE Proceedings - Generation, Transmission and Distribution*, vol. 148, no. 3, pp. 229–235, May 2001.
- [94] H.-S. Song, H.-G. Park, and K. Nam, "An instantaneous phase angle detection algorithm under unbalanced line voltage condition," in *30th Annual IEEE Power Electronics Specialists Conference. Record. (Cat. No.99CH36321)*, vol. 1, Aug 1999, pp. 533–537 vol.1.
- [95] S. M. Shinnars, *Modern control system theory and design*. John Wiley & Sons, 1998.
- [96] MathWorks, "Linear-quadratic regulator (LQR) design," <https://www.mathworks.com/help/control/ref/lqr.html>, online; accessed 30 July 2018.
- [97] H. Akagi, E. H. Watanabe, and M. Aredes, *Instantaneous power theory and applications to power conditioning*. John Wiley & Sons, 2017.
- [98] H. Akagi, Y. Kanazawa, and A. Nabae, "Instantaneous reactive power compensators comprising switching devices without energy storage components," *IEEE Transactions on Industry Applications*, vol. IA-20, no. 3, pp. 625–630, May 1984.
- [99] L. Gyugyi and B. R. Pelly, *Static Power Frequency Changers: Theory, Performance and Application*. Wiley, 1976.

- [100] F. Harashima, H. Inaba, and K. Tsuboi, "A closed-loop control system for the reduction of reactive power required by electronic converters," *IEEE Transactions on Industrial Electronics and Control Instrumentation*, vol. IECI-23, no. 2, pp. 162–166, May 1976.
- [101] L. Gyugyi and E. C. Strycula, "Active ac Power Filters," in *Proceedings IEEE Industrial Applications Annual Meeting*, vol. 19-C, 1976, pp. 529–535.
- [102] E. Clarke, *Circuit Analysis Of A-C Power Systems, Vol. I – Symmetrical and Related Components*. Wiley, 1943.
- [103] A. J. Roscoe, S. J. Finney, and G. M. Burt, "Tradeoffs Between AC Power Quality and DC Bus Ripple for 3-Phase 3-Wire Inverter-Connected Devices Within Microgrids," *IEEE Transactions on Power Electronics*, vol. 26, no. 3, pp. 674–688, Mar. 2011.
- [104] A. Camacho, M. Castilla, J. Miret, A. Borrell, and L. G. de Vicuña, "Active and Reactive Power Strategies With Peak Current Limitation for Distributed Generation Inverters During Unbalanced Grid Faults," *IEEE Transactions on Industrial Electronics*, vol. 62, no. 3, pp. 1515–1525, Mar. 2015.
- [105] F. Nejabatkhah, Y. W. Li, and B. Wu, "Control Strategies of Three-Phase Distributed Generation Inverters for Grid Unbalanced Voltage Compensation," *IEEE Transactions on Power Electronics*, vol. 31, no. 7, pp. 5228–5241, July 2016.
- [106] S. Alepuz, S. Busquets-Monge, J. Bordonau, J. A. Martinez-Velasco, C. A. Silva, J. Pontt, and J. Rodriguez, "Control Strategies Based on Symmetrical Components for Grid-Connected Converters Under Voltage Dips," *IEEE Transactions on Industrial Electronics*, vol. 56, no. 6, pp. 2162–2173, June 2009.
- [107] H. Xu, J. Hu, and Y. He, "Integrated Modeling and Enhanced Control of DFIG Under Unbalanced and Distorted Grid Voltage Conditions," *IEEE Transactions on Energy Conversion*, vol. 27, no. 3, pp. 725–736, Sept. 2012.
- [108] "IEEE Application Guide for IEEE Std 1547(TM), IEEE Standard for Interconnecting Distributed Resources with Electric Power Systems," *IEEE Std 1547.2-2008*, pp. 1–217, Apr. 2009.
- [109] K. Fujii, P. Koellensperger, and R. W. D. Doncker, "Characterization and comparison of high blocking voltage igbts and iegts under hard- and soft-switching conditions," *IEEE Transactions on Power Electronics*, vol. 23, no. 1, pp. 172–179, Jan 2008.
- [110] B. Wu and M. Narimani, *High-Power Converters and AC Drives: Second Edition*, 2017.

- [111] S. Lee, J. Kim, J. Lee, and B. Cho, "State-of-charge and capacity estimation of lithium-ion battery using a new open-circuit voltage versus state-of-charge," *Journal of Power Sources*, vol. 185, no. 2, pp. 1367 – 1373, 2008.
- [112] G. Tsengenes and G. Adamidis, "Investigation of the behavior of a three phase grid-connected photovoltaic system to control active and reactive power," *Electric Power Systems Research*, vol. 81, no. 1, pp. 177 – 184, 2011.
- [113] Torytrans S.L., "CATALOGO GENERAL v.4," https://www.torytrans.com/fileadmin/user_upload/Catalogo_General_v4_ES.pdf, online; accessed 30 July 2018.
- [114] Allied Electronics, "Bipolar Transistors Catalog," <https://www.alliedelec.com/transistors-modules/bipolar-transistors/>, online; accessed 30 July 2018.
- [115] A. K. Gupta and A. M. Khambadkone, "A space vector pwm scheme for multilevel inverters based on two-level space vector pwm," *IEEE Transactions on Industrial Electronics*, vol. 53, no. 5, pp. 1631–1639, Oct 2006.
- [116] K. Kondo and S. Doki, "Improvement of transient state characteristic for vector control system by using the inverter overmodulation range," in *2015 17th European Conference on Power Electronics and Applications (EPE'15 ECCE-Europe)*, Sept 2015, pp. 1–7.
- [117] E. Abbena, S. Salamon, and A. Gray, *Modern Differential Geometry of Curves and Surfaces with Mathematica, Third Edition*. Chapman and Hall / CRC, 2006.
- [118] T. L. Lee and P. T. Cheng, "Design of a new cooperative harmonic filtering strategy for distributed generation interface converters in an islanding network," *IEEE Transactions on Power Electronics*, vol. 22, no. 5, pp. 1919–1927, Sept 2007.
- [119] S. J. Chiang and J. M. Chang, "Parallel operation of shunt active power filters with capacity limitation control," *IEEE Transactions on Aerospace and Electronic Systems*, vol. 37, no. 4, pp. 1312–1320, Oct 2001.
- [120] J. Praveen, B. P. Muni, S. Venkateshwarlu, and H. V. Makthal, "Review of dynamic voltage restorer for power quality improvement," in *30th Annual Conference of IEEE Industrial Electronics Society, 2004. IECON 2004*, vol. 1, Nov 2004, pp. 749–754 Vol. 1.
- [121] A. Timbus, A. Oudalov, and C. N. M. Ho, "Islanding detection in smart grids," in *2010 IEEE Energy Conversion Congress and Exposition*, Sept 2010, pp. 3631–3637.
- [122] DIN-VDE, *Automatic disconnection device between a generator and the public low-voltage grid*. DIN-VDE Std. 0126-1-1, 2005.

- [123] M. Liserre, R. Teodorescu, and F. Blaabjerg, "Stability of grid-connected pv inverters with large grid impedance variation," in *2004 IEEE 35th Annual Power Electronics Specialists Conference (IEEE Cat. No.04CH37551)*, vol. 6, June 2004, pp. 4773–4779 Vol.6.
- [124] M. Liserre, R. Teodorescu, and F. Blaabjerg, "Stability of photovoltaic and wind turbine grid-connected inverters for a large set of grid impedance values," *IEEE Transactions on Power Electronics*, vol. 21, no. 1, pp. 263–272, Jan. 2006.
- [125] A. Tarkiainen, R. Pollanen, M. Niemela, and J. Pyrhonen, "Identification of grid impedance for purposes of voltage feedback active filtering," *IEEE Power Electronics Letters*, vol. 2, no. 1, pp. 6–10, March 2004.
- [126] M. P. Palsson, T. Toftevaag, K. Uhlen, and J. O. G. Tande, "Large-scale wind power integration and voltage stability limits in regional networks," in *IEEE Power Engineering Society Summer Meeting*, vol. 2, July 2002, pp. 762–769 vol.2.
- [127] J. O. G. Tande and K. Uhlen, "Wind turbines in weak grids - constraints and solutions," in *Proc. CIRED 2001*, vol. 4, June 2001, pp. 18–21.
- [128] J. E. Brittain, "Thevenin's theorem," *IEEE Spectrum*, vol. 27, no. 3, pp. 42–, March 1990.
- [129] J. H. R. Enslin and P. J. M. Heskes, "Harmonic interaction between a large number of distributed power inverters and the distribution network," *IEEE Transactions on Power Electronics*, vol. 19, no. 6, pp. 1586–1593, Nov 2004.
- [130] E. J. Bueno, A. Hernandez, F. J. Rodriguez, C. Giron, R. Mateos, and S. Cobrecas, "A dsp- and fpga-based industrial control with high-speed communication interfaces for grid converters applied to distributed power generation systems," *IEEE Transactions on Industrial Electronics*, vol. 56, no. 3, pp. 654–669, March 2009.
- [131] F. J. Rodriguez, C. Giron, E. J. Bueno, A. Hernandez, S. Cobrecas, and P. Martin, "Remote laboratory for experimentation with multilevel power converters," *IEEE Transactions on Industrial Electronics*, vol. 56, no. 7, pp. 2450–2463, July 2009.
- [132] "Voltage characteristics of electricity supplied by public distribution networks," *EN 50160:2010*, 2011.
- [133] E. Weisstein, "Lu decomposition," <http://mathworld.wolfram.com/LUDecomposition.html>, online; accessed 30 July 2018.